Addressing CO2 Electrolysis Challenges with Novel Ion-exchange Membranes

Petrov, K.V.

DOI
10.4233/uuid:0b200bcd-73a4-48f6-81ab-1af0ea8004b6

Publication date
2024

Document Version
Final published version

Citation (APA)
Petrov, K. V. (2024). *Addressing CO2 Electrolysis Challenges with Novel Ion-exchange Membranes*. [Dissertation (TU Delft), Delft University of Technology]. https://doi.org/10.4233/uuid:0b200bcd-73a4-48f6-81ab-1af0ea8004b6

Addressing CO_2 Electrolysis Challenges with Novel Ion-Exchange Membranes

Kostadin V. Petrov

Propositions

accompanying the dissertation

Addressing CO_2 Electrolysis Challenges with Novel Ion-Exchange Membranes

by

Kostadin Veselinov Petrov

1. Nanofluidic membranes with sufficiently small pore sizes (<8 nm) to achieve highly permselective ion-exchange are commercially available. (Chapter 2)
2. In electrochemical applications with low electrolyte concentrations, fixed ionic charges are imperative for a conductive ion-exchange membrane. (Chapter 3)
3. Although carbonate-rejecting membranes seem like a pragmatic solution for the cross-over problem in CO_2 electrolyzers, this concept is more challenging than converting carbonate back to CO_2. (Chapter 5)
4. Multi-layer membranes are a necessity for energy efficient CO_2 electrolysis. (Chapter 6)
5. Dense ion-exchange membranes are not really dense.
6. Given the urgency of addressing the climate and material depletion crises, no funds should be directed to non-urgent research, such as sports science.
7. The abundance of information is turning creativity and understanding into noise and fatigue.
8. Time and effort invested in academia-industry knowledge exchange should be reflected in research impact metrics to incentivize this practice.
9. "Magical" technological innovations, such as converting air-captured carbon into fuels, offer comprehensive solutions to our environmental challenges. However, their appeal should not distract us from more immediate solutions.
10. In the movie "The Lion King", Scar has the same goals as a typical human leader.

These propositions are regarded as opposable and defendable, and have been approved as such by the promotors prof. dr. B. Dam, and dr. ir. D.A. Vermaas.

Addressing CO_2 Electrolysis Challenges with Novel Ion-Exchange Membranes

ADDRESSING CO_2 ELECTROLYSIS CHALLENGES WITH NOVEL ION-EXCHANGE MEMBRANES

Dissertation

for the purpose of obtaining the degree of doctor
at Delft University of Technology,
by the authority of the Rector Magnificus prof. ir. T.H.J.J. van der Hagen,
chair of the Board of Doctorates,
to be publicly defended on
Wednesday 5th of June 2024 at 10:00 o'clock.

by

Kostadin Veselinov PETROV

Master of Science in Chemical and Biochemical Engineering,
NOVA University of Lisbon, Portugal,
born in Sofia, Bulgaria.

The dissertation has been approved by the promotors.

promotor: em. prof. dr. B. Dam
promotor: dr. ir. D.A. Vermaas

Composition of the doctoral committee:

Rector Magnificus,	chairperson
Em. prof. dr. B. Dam,	Delft University of Technology, promotor
Dr. ir. D.A. Vermaas,	Delft University of Technology, promotor
Independent members:	
Em. prof. dr. J.J.C. Geerlings	Delft University of Technology
Prof. dr. ir. W. de Jong	Delft University of Technology
Dr. R.M. Hartkamp	Delft University of Technology
Prof. dr. ir. R.G.H. Lammertink	University of Twente
Dr. D. Aili	Technical University of Denmark

This work is part of the research programme Towards large-scale electroconversion systems (TOeLS), financed by Shell and the Topsectors Chemistry, HTSM and Energy.

Keywords: CO_2 Electrolysis, Ion-exchange, Nanofluidic, Thin-film, Membranes

Printed by: Ridderprint

Cover by: K.V. Petrov, using elements from Freepik.com

ISBN 978-94-6384-594-6

An electronic version of this dissertation is available at
http://repository.tudelft.nl/.

За Дядо Коста.

CONTENTS

SUMMARY

As a response to climate change, substantial efforts are being made to achieve global net-zero greenhouse gas emissions by the year of 2050, as established by the Paris agreement. To decrease reliance on fossil fuels, we are transitioning to renewable energies and electrifying various sectors. However, certain segments of the global supply chain will still require carbon-based chemicals and energy carriers. CO_2 electrolysis allows the use renewable electricity to electrochemically reduce air-captured CO_2, producing chemical building blocks such as CO, ethylene and formate. These chemicals can then be converted into larger hydrocarbons, e.g. into synthetic diesel using the Fischer-Tropsch process. In this way, CO_2 electrolysis can aid in closing the carbon cycle by converting CO_2 emissions into valuable chemicals and fuels.

Despite its promise, a few hurdles still hamper the industrialization of CO_2 electrolysis. These are the relatively low energy efficiency, salt deposition, the inefficient use of CO_2 due to carbonate cross-over and the necessity of scarce iridium-based anode catalysts.

Most of the mentioned challenges can potentially be solved by novel, or optimized ion-exchange membranes (IEMs) - these have a pivotal role in the process since they provide a conductive medium to selectively transport ions between the electrodes. Increasing the IEM's ionic conductivity and permselectivity can increase the energy efficiency of the process and decrease cation cross-over and therefore salt deposition. Furthermore, an OH^- selective membrane which rejects other anions such as carbonate, can potentially solve the carbonate-cross over issue. In this way, the goal of this work is to develop novel IEMs to address each of the challenges tied with CO_2 electrolysis.

Chapter 2 and 3 explore nanofluidic membranes (NFMs), which are an emerging alternative to polymeric IEMs. NFMs are based on inorganic materials and their selectivity mechanism relies on charged nanopores instead of functional groups immobilized on a polymeric backbone. This mechanism has the opportunity to improve both the selectivity and conductivity.

In Chapter 2 we measured the permselectivity of commercial anodized aluminium oxide (AAO) membranes with different pore sizes, between different KCl concentrations. Our experiments reveal that membranes with 10-nm pores have permselectivities above 90%, comparable to those of polymeric IEMs, up to electrolyte concentrations of 0.15 vs. 0.75 M. To our knowledge, this is the highest reported ion selectivity for nanofluidic IEMs. Conversely, asymmetric AAO membranes featuring a thin selective layer, exhibited low permselectivity. Through simulations using the space-charge model, we delved into the influence of other parameters. Our numerical results indicate that pore size and surface potential are the most sensitive parameters for increasing selectivity. Additionally, a minimum pore length is required for good performance, although increasing it beyond the µm scale yields no significant result.

Chapter 3 deals with the optimization of the ionic conductance of NFMs. Although NFMs allow direct, non-tortuous ionic pathways for efficient ion transport, a conductive

NFM has not been demonstrated. We measured the ionic conductance of commercial AAO membranes with different pore sizes under different current densities and electrolyte concentrations. We also performed computational simulations of a nanopore channel with charged walls between two electrolyte reservoirs. Our findings indicate that electrolyte concentration is the main parameter that determines NFM conductance, with a linear dependence at least up to 1 M. The optimal pore length is between 0.5 to 5 μm considering the trade-off between selectivity and conductance. On the other hand, the conductance is not sensitive to the pore diameter. Conical nanopores are a way to increase conductance, but according to our results, this increase comes at the expense of selectivity.

Our findings suggest that NFMs can outperform polymeric IEMs in specific electrochemical applications, such as reverse electrodialysis. However, many challenges are tied to their use in CO_2 electrolyzers, suach as the influence of pH on surface charge and the lack of conductivity and mechanical strength. Therefore, the remaining chapters focus on improving polymeric IEMs.

Since the CO_2 reduction reaction consumes water, water management within a CO_2 electrolyzer is crucial to avoid salt deposition and maintain IEM hydration, which ensures its conductivity. In Chapter 4, a device architecture incorporating an anion-exchange membrane (AEM) with internal water channels to mitigate membrane dehydration is proposed and demonstrated. A two-dimensional continuum model is developed to assess water fluxes and local water content, as well as to determine the optimal channel geometry and composition. The modified AEMs are then fabricated and tested experimentally, demonstrating that the internal channels can both reduce K^+ cation crossover as well as improve conductivity and therefore overall cell performance. This work demonstrates the promise of these materials, and operando water-management strategies in general, in addressing some of the major hurdles in CO_2 electrolyzers operated at high current densities.

In Chapter 5, we attempt to tackle the carbonate cross-over issue in CO_2 electrolyzers by fabricating a thin-film composite membrane, with a selective layer to reject carbonate. The selective polyamide layers were synthesized on the surface of commercial AEMs. We studied the effect of different polyamide chemistries, the curing step and the monomer concentration on the CO_2 electrolysis process. Our preliminary experiments showed a significant increase in $OH^-/{CO_3}^{2-}$ selectivity, but this result was not reproduced with electrolysis-suitable AEMs as support. Nevertheless, we show that the ionic conductance of these membranes can be optimized by manipulating the organic phase-monomer concentration. Additionally, we unveiled other challenges related to the incorporation of TFCMs in CO_2 electrolyzers, such as the increased hydrogen production, and salt deposition. Our findings show that for some polyamide chemistries, these challenges can be avoided by introducing a catholyte layer.

Lastly, in Chapter 6 we argue that intrinsically stable and efficient CO_2 electrolysis without rare-earth metals is only possible using multilayer membrane systems, such as TFCMs or bipolar membranes (BPMs). While reverse- and forward-bias BPMs are both capable of inhibiting CO_2 cross-over, forward-bias fails to solve the rare-earth metals requirement at the anode. Unfortunately, reverse-bias BPM systems presently exhibit comparatively lower Faradaic efficiencies and higher cell voltages than AEM-based systems. To improve these metrics, optimizing the catalyst, reaction microenvironment and alkali

cation availability should be the primary areas of research. Furthermore, BPMs can be improved by using thinner layers and a suitable water dissociation catalyst. In this way, BPMs and TFCMs can become the primary membrane separator of choice, alleviating core remaining challenges in CO_2 electrolysis to bring this technology to industrial scale.

SAMENVATTING

Als antwoord op de klimaatverandering worden er aanzienlijke inspanningen geleverd om, in het jaar 2050, netto-nul emissies te bereiken zoals vastgelegd in het klimaatakkoord van Parijs. Om onze afhankelijkheid van fossiele brandstoffen te verminderen, schakelen we over op hernieuwbare energiebronnen en elektrificeren we verschillende sectoren. Bepaalde onderdelen van de wereldwijde toeleveringsketen zullen echter nog altijd koolstofhoudende chemicaliën en energiedragers nodig hebben. Met de elektrolyse van koolstofdioxide (CO_2) kan hernieuwbare elektriciteit gebruikt worden om afgevangen CO_2 elektrochemisch te reduceren naar chemische bouwstenen zoals koolstofmonoxide, ethyleen en formaat. Deze chemicaliën kunnen vervolgens worden omgezet in grotere koolwaterstoffen, zoals synthetische diesel met behulp van het Fischer-Tropsch proces. Op deze manier kan CO_2 elektrolyse bijdragen aan het sluiten van de koolstofkringloop door CO_2-uitstoot om te zetten in waardevolle chemicaliën en brandstoffen.

Ondanks de potentie van CO_2 elektrolyse zijn er nog een paar hindernissen die de industrialisatie van deze technologie in de weg staan, namelijk de relatief lage energie-efficiëntie, zoutafzetting, het inefficiënte gebruik van CO_2 door carbonaat cross-over en de noodzaak voor schaarse op iridium-gebaseerde anodekatalysatoren.

Van deze uitdagingen zouden mogelijk de meeste opgelost kunnen worden met nieuwe of geoptimaliseerde ionen uitwisselingmembranen (ion-exchange membranes, IEM's) - deze spelen een centrale rol in het proces omdat ze een geleidend medium bieden die ionen selectief transporteren tussen de elektrodes. Het verhogen van de ionengeleidbaarheid en permselectiviteit van het IEM kan de energie-efficiëntie van het proces verbeteren en de kation cross-over en resulterende zoutafzetting verminderen. Bovendien, kan een OH^--selectief membraan, dat andere anionen zoals carbonaat tegenhoudt, mogelijk het probleem van carbonaat cross-over oplossen. Het doel van dit werk is het ontwikkelen van nieuwe IEM's om de uitdagingen van CO_2 elektrolyse aan te pakken.

Hoofdstuk 2 en 3 gaan in op nanofluïdische membranen (NFM's), een opkomend alternatief voor polymere IEM's. NFM's bestaan uit anorganische materialen en hun selectiviteit komt van geladen nanoporiën in plaats van geïmmobiliseerde functionele groepen aan een polymeerketen. Dit mechanisme heeft de mogelijkheid om zowel de selectiviteit als geleidbaarheid te verbeteren.

In Hoofdstuk 2 hebben we de permselectiviteit gemeten van commerciële geanodiseerd aluminiumoxide (anodized aluminium oxide, AAO) membranen met verschillende poriegrootten, in verschillende KCl-concentraties. Uit onze experimenten blijkt dat membranen met 10-nm poriën een permselectiviteit van meer dan 90% hebben tot elektrolytconcentraties van 0.15 en 0.75 M in de twee omliggende compartimenten. Dit is vergelijkbaar met polymere IEM's en voor zover wij weten de hoogst gerapporteerde ionenselectiviteit voor nanofluïdische IEM's. Daarentegen vertoonden asymmetrische AAO-membranen met een dunne selectieve laag een lage permselectiviteit. Met behulp van simulaties en het space-charge model hebben we de invloed van andere parameters on-

derzocht. De numerieke resultaten geven aan dat poriegrootte en oppervlak-potentiaal de meest gevoelige parameters zijn voor het verhogen van de selectiviteit. Verder is een minimale porielengte vereist voor een goede werking, terwijl het vergroten voorbij de µm-schaal geen significante verbetering oplevert.

Hoofdstuk 3 behandelt de optimalisatie van de ionische geleiding van NFM's. Hoewel NFM's directe, niet-kronkelige ionische paden voor efficiënt ionentransport biedt, is een geleidend NFM nog niet gedemonstreerd. We hebben de ionische geleiding gemeten van commerciële AAO-membranen met verschillende poriegrootten onder verschillende stroomdichtheden en elektrolytconcentraties. Daarnaast hebben we simulaties uitgevoerd op een nanoporie met geladen wanden tussen twee elektrolytreservoirs. We hebben bepaald dat de elektrolytconcentratie de belangrijkste parameter is die de NFM-geleiding bepaalt, met een lineaire afhankelijkheid tot ten minste 1 M. De optimale poriegrootte ligt tussen 0.5 en 5 µm gezien de compromis tussen selectiviteit en geleiding. Anderzijds is de geleiding niet gevoelig voor veranderingen in de poriediameter. Conische nanoporiën zijn een manier om geleiding te verhogen, maar volgens onze resultaten gaat deze verhoging ten koste van de selectiviteit.

Onze bevindingen suggereren dat NFM's beter kunnen presteren dan polymere IEM's in specifieke elektrochemische toepassingen, zoals omgekeerde elektrodialyse. Er zijn echter veel uitdagingen verbonden aan hun gebruik in CO_2 elektrolyzers, zoals de invloed van pH op de oppervlaktelading en het gebrek aan geleidbaarheid en mechanische sterkte. Daarom richten de resterende hoofdstukken zich op het verbeteren van polymere IEM's.

Aangezien de CO_2 reductiereactie water verbruikt, is waterhuishouding binnen een CO_2 elektrolyzer cruciaal om zoutafzetting te voorkomen en de hydratatie en dus geleidbaarheid van de IEM te behouden. In Hoofdstuk 4 wordt een ontwerp voorgesteld en gedemonstreerd dat gebruik maakt van een anionen uitwisselingsmembraan (anion-exchange membrane, AEM) met interne waterkanalen om uitdroging van het membraan tegen te gaan. Een tweedimensionaal continuümmodel is ontwikkeld om de waterstromen en het lokale watergehalte te evalueren, evenals om de optimale kanaalgeometrie en samenstelling te bepalen. De aangepaste AEM's worden vervolgens vervaardigd en experimenteel getest, waaruit blijkt dat de interne kanalen zowel de K+ kation cross-over kunnen verminderen als de geleidbaarheid en daarmee de algehele celprestatie kunnen verbeteren. Dit werk toont de potentie van deze materialen, en operando-waterhuishoudingstrategieën in het algemeen, bij het mitigeren van de grootste obstakels voor het behalen van hoge stroomdichtheden in CO_2 elektrolyzers.

In Hoofdstuk 5 proberen we de carbonaat cross-over in CO_2 elektrolyzers aan te pakken door een dunne-laag samengesteld membraan (thin-film composite membrane, TCFM) te fabriceren met een selectieve laag die carbonaat tegenhoudt. De selectieve polyamidelagen werden gesynthetiseerd op het oppervlak van commerciële AEM's. We bestudeerden het effect van verschillende polyamidechemie, de uithardingsstap en de monomeerconcentratie op het CO_2 elektrolyseproces. Onze preliminaire experimenten toonden een significante toename in $OH^-/{CO_3}^{2-}$ - selectiviteit, maar dit resultaat werd niet gereproduceerd voor AEM's geschikt voor elektrolyse. Desalniettemin laten we zien dat de ionische geleiding van deze membranen geoptimaliseerd kan worden door het aanpassen van de monomeerconcentratie in de organische fase. Bovendien onthulden we

andere uitdagingen met betrekking tot de integratie van TFCM's in CO_2 elektrolyzers, zoals de verhoogde waterstofproductie en zoutafzetting. Onze bevindingen zijn dat voor sommige polyamidechemie deze uitdagingen vermeden kunnen worden door een katholytische laag te introduceren.

Ten slotte stellen we in hoofdstuk 6 dat intrinsiek stabiele en efficiënte CO_2 elektrolyse zonder zeldzame aardmetalen alleen mogelijk is met meerlaagse membranen, zoals TFCM's of bipolaire membranen (BPM's). Terwijl reverse- en forward-bias BPM's beide in staat zijn om CO_2 cross-over te voorkomen, lost een forward-bias BPM de noodzaak voor zeldzame aardmetalen niet op. Helaas vertonen reverse-bias BPM-systemen momenteel relatief lagere Faradaïsche efficiëntie en hogere cel-voltages dan systemen met een AEM. Om dit te verbeteren, moet het onderzoek zich in de eerste plaats richten op het optimaliseren van de katalysator, het reactiemilieu en de beschikbaarheid van alkali-kationen. Bovendien kunnen BPM's worden verbeterd door dunnere lagen en een geschikte waterdissociatie katalysator te gebruiken. Op deze manier kunnen BPM's en TFCM's de primaire optie voor membraan worden en de belangrijkste uitdagingen van het naar industriële schaal brengen van CO_2 elektrolyse aanpakken.

List of Acronyms

AAO anodized aluminum oxide

AEL anion-exchange layer

AEM anion-exchange membrane

AEMEA anion-exchange membrane-electrode assembly

BPM bipolar membrane

BPMEA bipolar membrane-electrode assembly

CEL cation-exchange layer

CEM cation-exchange membrane

CL catalyst layer

CO_2R CO_2 reduction

CO_2RR CO_2 reduction reaction

DI deionized

ED electrodialysis

EDL electrical double layer

FE Faradaic efficiency

FTIR Fourier-transform infra red

GC gas chromatograph

GDE gas-diffusion electrode

GO graphene oxide

HER hydrogen evolution reaction

IEM ion-exchange membrane

ITM Ion Transport in Membranes

MEA membrane-electrode assembly

MPD m-phenylenediamine

NF nanofiltration

NFM nanofluidic membrane

OER oxygen evolution reaction

PIP piperazine

PTFE polytetrafluoroethylene

PTL porous-transport layer

RED reverse electrodialysis

RHE reference hydrogen electrode

RO reverse-osmosis

SCM space-charge model

SEM scanning electron microscopy

SHE standard hydrogen electrode

TFCM thin-film composite membrane

TMC trimesoyl chloride

TEM transmission electron microscopy

WD water dissociation

1

General Introduction

1.1. Closing the Carbon Cycle

The persistent increase in carbon emissions is causing climate changes of unprecedented magnitude. We, as a part of nature, are putting ourselves in danger as our activities destroy vital ecosystems and alter the composition of the atmosphere.[1]

To address this ecological crisis and attenuate climate change, it is imperative to achieve global net-zero greenhouse gas emissions by the year of 2050, as established by the Paris agreement.[2] To achieve this ambitious goal, emission reduction strategies must be implemented in all sectors, thus great efforts and investments are being made to:

- Increase the global capacity for renewable energy sources.
- Enhance the scalability and capacity of energy storage technologies.
- Improve the electrical grid, and its international connections.
- Electrify transportation, industries and households.
- Transition toward circular technologies that minimize resource waste.
- Preserve and safeguard natural carbon sinks from further degradation.
- Develop carbon capture methods from the air and ocean.
- Develop alternative energy carriers and carbon utilization strategies.

This is an extensive list of tasks, and many efforts still need to be done to minimize reliance on fossil fuels. However, even as we transition towards renewable energy sources and electrify various sectors, certain segments of our global supply chain will still require a carbon source.[3, 4] However, the use of alternative carbon sources remains relatively undeveloped.[5] Although this point is as critical as the others, there is little progress into producing a carbon-based energy carrier which does not rely on fossil fuels. Recognizing this importance, we focus our research efforts into closing the carbon cycle and producing carbon-neutral fuels and chemicals.

Among the few sustainable carbon sources, environmental carbon capture stands out. If the captured carbon is converted, for example into a fuel, then used in transportation

and re-emitted, a cyclic process can be established (Figure 1.1).[6] Closing the carbon cycle will deter the increase of carbon concentration in the atmosphere and ocean.

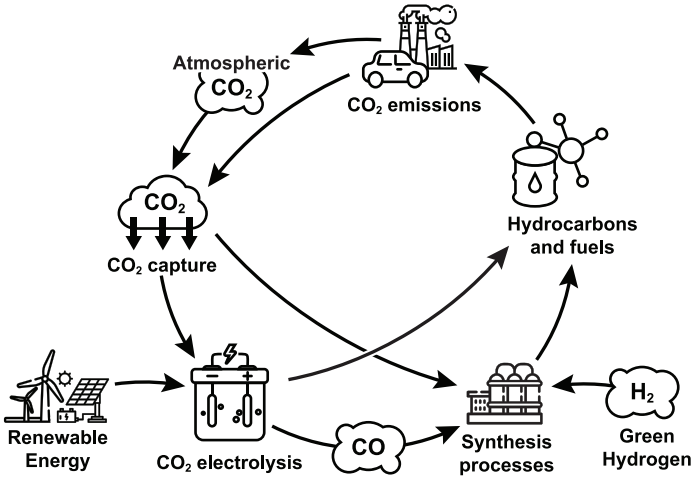

Figure 1.1: Proposed pathway to transition away from fossil fuels and close the carbon cycle.

To this end, carbon utilization technologies such as methanation, solid oxide CO_2 electrolysis and low temperature CO_2 electrolysis are being developed.[7–9] Our work focuses on the latter technology as it combines the advantage of using renewable electricity and mild operating conditions to convert carbon dioxide. Figure 1.1 shows how this technology can contribute to closing the carbon cycle.

1.2. CO_2 ELECTROLYSIS

By applying (green) electricity to an electrolyzer, CO_2 can be electrochemically reduced, synthesizing fuels or precursors to fuels, and therefore storing the energy in a chemical form. Depending on the used catalyst, the products of this process can be carbon monoxide (CO), formic acid (HCOOH), ethylene (C_2H_4), ethanol (C_2H_5OH), methane (CH_4), etc.[10] Techno-economical analyses have deemed CO, HCOOH and C_2H_4 as the most profitable products.[11, 12] These are building block molecules which are used in many chemical industries. A mixture of CO and hydrogen (H_2) is commonly referred to as syngas, which is used as a precursor for methanol, $C_2 - C_4$ olefins, synthetic natural gas and diesel, among others.[13, 14] Our work is aimed at the producton of CO, for which a silver catalyst is employed.

An electrolyzer comprises at least two electrically connected electrodes, where redox reactions are driven by applying a current. The electrodes are called cathode and anode, where reduction and oxidation reactions take place, respectively. In between the electrodes, a conductive medium must be present, to facilitate ion transport and close the electrical circuit. In CO_2 electrolysis, the following reactions occur (undesired reactions are highlighted in red):

- Cathode reactions:

$$CO_2 + H_2O + 2e^- \longrightarrow CO + 2OH^- \tag{1.1}$$

$$2H_2O + 2e^- \longrightarrow H_2 + 2OH^- \tag{1.2}$$

$$CO_2 + 2OH^- \longrightarrow {CO_3}^{2-} + H_2O \tag{1.3}$$

- Anode reactions:

$$2OH^- \longrightarrow \frac{1}{2}O_2 + H_2O + 2e^- \tag{1.4}$$

$$ {CO_3}^{2-} + H_2O \longrightarrow CO_2 + 2OH^- \tag{1.5}$$

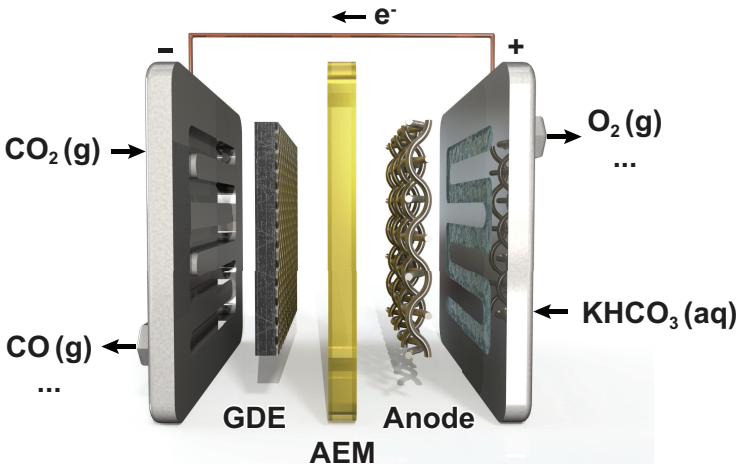

Figure 1.2: Schematic illustration of a typical laboratory scale CO_2 electrolyzer.

State-of-the-art electrolyzers operate in a zero-gap configuration, where porous electrodes are directly pressed against an ion-exchange membrane (IEM), to minimize transport losses.[15] Figure 1.2 depicts a schematic illustration of a laboratory-scale state of the art CO_2 electrolyzer. The specific configuration in this figure comprises:

- two current collectors with a flow field on either side. CO_2 is fed in gaseous state to the current collector behind the gas-diffusion electrode (GDE), and the anolyte is fed to the flow field of the current collector behind the anode.

- a GDE, which combines a gas-diffusion layer and a catalyst layer. The hydrophobic gas-diffusion layer, often made from carbon fibers infused with polytetrafluoroethylene (PTFE), allows the direct feed of gaseous CO_2 to the catalyst. The catalyst layer is immobilized on its surface. Together, they act as the cathode, where the CO_2 reduction reaction (CO_2RR) occurs (equation 1.1);

- the membrane, which is most commonly an anion-exchange membrane (AEM). It has the important role of providing an ion-conductive medium to selectively transport ions between the electrodes;
- on the right is typically a mesh or perforated plate electrode which serves as anode and catalyst for the oxygen evolution reaction (OER) (equation 1.4).

Despite its promise, CO_2 electrolysis is a technology that is currently mostly at research stage, since several challenges hinder its scale-up. These challenges are related to the suboptimal performance of certain components in the electrolyzer, and the complex nature of the underlying (electro)chemical reactions. Firstly, the process suffers from low energy efficiency, marked by large reaction overpotentials and significant ohmic losses in most systems.[16] Secondly, carbonate formation occurs at the cathode due to the alkaline medium (equation 1.3), causing salt deposition and CO_2 loss.[17] Potassium carbonate salts can deposit if K^+ ions migrate from the anolyte,[18] and when carbonate crosses the AEM to the anolyte, it lowers the pH and evolves into CO_2 (equation 1.5), resulting in an inefficient use of raw materials in the process.[19] In a less alkaline anolyte, the desired $NiFeO_x$ catalysts are not stable, forcing the process to use expensive rare-earth catalysts such as Ir.[20] Thirdly, product selectivity can also be a limiting factor. There is the undesired competing hydrogen evolution reaction (HER) (equation 1.2), and when using a copper catalyst, a mixture of various products is generated.[10] Finally, degradation of catalysts and GDEs, and loss of ion-exchange capacity of the IEM are also significant challenges.

Some of these issues can potentially be solved by improving and optimizing the IEM. Alkaline-stable AEMs would not suffer from degradation and loss of ion-exchange capacity.[21] More conductive membranes would enhance the energy efficiency of the process.[22] More selective membranes would prevent K^+ ions from crossing over and causing salt precipitation. An OH^- selective membrane could specifically inhibit carbonate migration, enabling the use of an alkaline anolyte. For these reasons, we aim to improve the IEMs for CO_2 electrolysis.

1.3. ION-EXCHANGE MEMBRANES

IEMs are already extensively used beyond CO_2 electrolysis. Various electrochemical processes aimed at water treatment, or which contribute to advancing the energy transition by facilitating green energy generation, energy storage, or energy conversion rely on IEMs for their selective ion conductivity.[23]

The majority of IEMs are thin films ($\approx$ 100 µm), and consist of a dense polymeric backbone structure with immobilized charged functional groups. The charged functional groups are responsible for the Donnan effect, rejecting ions with the same charge (co-ions) and allowing oppositely charged ions (counter-ions) to permeate.[24] Depending on the sign of the fixed ionic charges, the IEM can be selective for anions or cations. A membrane with negatively charged groups is classified as an cation-exchange membrane (CEM), and an IEM with positively charged groups is an AEM.[25]

The important benchmark metrics which define the performance of an IEM are its ionic conductance and its (perm)selectivity. Ionic conductance is the measure of the ability to transport ions under a driving force (e.g. concentration gradient or electric

field), measured in S/cm^2. The inverse of conductance is often reported - area resistance in Ωcm^2. Permselectivity is the ability of a membrane to allow oppositely charged ions (counter-ions) to permeate and reject ions of the same charge (co-ions). It is expressed in %, and calculated based on the transport numbers of the different ion species.[26]

Polymeric IEMs show a trade-off between these two properties. The hydrophilic nature of these membranes allows water to permeate through the membrane along with the ions, and the functional groups attached to the polymeric backbone can either hold a charge or be a point for cross-linking. Therefore, a highly cross-linked polymer can absorb less water as its chains are less mobile, and a highly charged polymer will be able to swell and absorb more water as its chains are mobile. In the first scenario, a larger driving force is required to conduct ions through the denser structure, but the selectivity will be relatively high. In the second scenario, since the cross linking is low the membrane can swell, increasing the free water volume inside the membrane, leading to an increased conductivity, but decreased selectivity (or increased co-ion transport).[27] In this way, the fixed charge density in fully hydrated membranes is limited, as illustrated in Figure 1.3.[28]

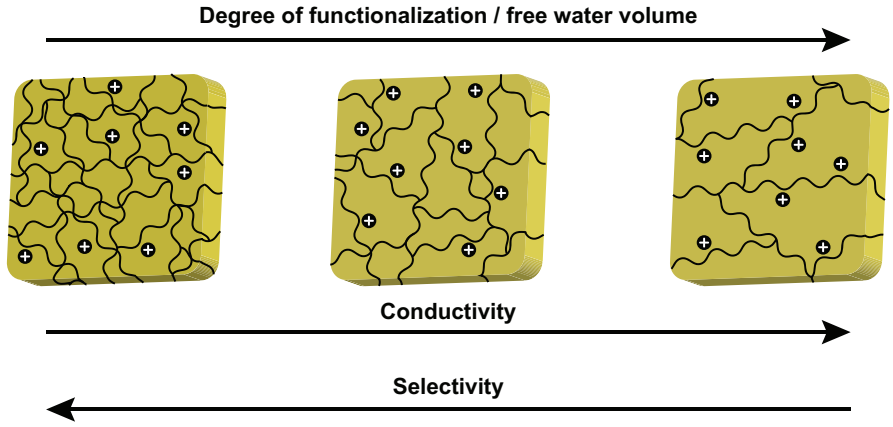

Figure 1.3: Illustration of the increasing degree of functionalization (decreasing cross-linking) in a hydrated IEM.

Other polymeric IEM disadvantages are related to the relatively high ionic resistance due to the steric hindrance for ion transport, and ageing due to chemical degradation in harsh environments.[29–31]

1.4. THESIS SCOPE AND OUTLINE

The shortcomings of polymeric IEMs mentioned in the previous section hamper the scale-up of certain electrochemical processes, such as reverse electrodialysis and redox flow batteries. In CO_2 electrolysis, the membrane and its contact with the catalyst can significantly reduce the energy efficiency of the process, and the low selectivity of membranes promotes K^+ migration through the AEM and salt deposition.

In this work, we aim to overcome the existing challenges in CO_2 electrolysis through different innovative ion-exchange membranes. The primary objectives are to enhance the membrane selectivity and conductivity, in order to boost the direct energy efficiency and

mitigate salt deposition by reducing cation cross over; and to prevent carbonate cross over to boost the overall energy efficiency by improving carbon usage.

Chapters 2 and 3 explore an alternative to polymeric IEMs - the nanofluidic IEM. These membranes are based on inorganic materials which do not have a polymeric backbone with immobilized functional groups, but rely on charged nanopores for the Donnan effect. Therefore, they have the potential to break the selectivity and conductivity trade-off. However, since it is a relatively novel concept and has not yet been applied in electrolysis, we will study how different parameters and properties affect the membrane performance. Chapter 2 is focused on enhancing the selectivity of nanofluidic membranes, and Chapter 3 focuses on the conductivity. An extended discussion on their potential use for CO_2 electrolysis can be found in Chapter 6. In both of these studies we used commercial anodized aluminium oxide membranes because of their dense array of cylindrical nanopores. We measured the permselectivity and conductivity of membranes with different pore sizes, between two compartments with different KCl concentrations and ratios. The parameters that could not be varied experimentally were simulated using the space-charge model.

Nanofluidic IEMs still need quite some development before they can be incorporated in an energy-efficient electrolyzer. Therefore, the remaining chapters focus on improving polymeric membranes for CO_2 electrolysis. Chapter 4 is focused on improving the conductivity of the polymeric AEM by maximizing its hydration. Since the CO_2RR consumes water, the membrane surface near the cathode tends to dry-out or reduce its water content at high current densities. Consequently, its conductivity is also reduced. We fabricated a membrane with internal microchannels and studied their effect in practical CO_2 electrolysis. The impact of water or different electrolyte concentrations on the current density and salt deposition was evaluated. Additionally, different channel geometries and placements were modelled in COMSOL Multiphysics.

In Chapter 5, a membrane that can reject carbonate is explored. A thin-film composite membrane is created by modifying an existing AEM with an additional selective layer. This polyamide layer is similar to what is used in the reverse osmosis and nanofiltration processes and in theory rejects carbonate ions, but allows OH^- ions to permeate. This can potentially solve the carbonate crossover issue which is the biggest hurdle for the CO_2 reduction technology. We investigated the effect of the monomer concentrations which are used to create the selective polyamide layers, and the impact of integrating them in a CO_2 electrolyzer.

In Chapter 6, we provide a summary of the conclusions drawn throughout this thesis, discuss the implications of the research and offer insights into the directions the field should take for membrane improvement. We argue that bipolar membranes (BPMs) can be the solution for many of the intrinsic limitations of the CO_2 electrolysis technology, since these membranes facilitate a carbon-efficient operation, while ensuring a stable alkaline anolyte.

BIBLIOGRAPHY

1. Intergovernmental Panel on Climate Change (IPCC). *Climate Change 2022: Impacts, Adaptation and Vulnerability* 3–33. ISBN: 9781009325844 (Cambridge University Press, Cambridge, UK and New York, USA, 2022).
2. *Paris Agreement* UN Treaty. United Nations, 2015.
3. Ahlgren, W. L. The Dual-Fuel Strategy: An Energy Transition Plan. *Proceedings of the IEEE* **100,** 3001–3052 (2012).
4. Galimova, T. *et al.* Global trading of renewable electricity-based fuels and chemicals to enhance the energy transition across all sectors towards sustainability. *Renewable and Sustainable Energy Reviews* **183,** 113420 (2023).
5. Stork, M., De Beer, J., Lintmeijer, N. & Den Ouden, B. Chemistry for climate: acting on the need for speed. Roadmap for the Dutch chemical industry towards 2050. *Ecofys, Berenschot* (2018).
6. Zhang, J., Sewell, C. D., Huang, H. & Lin, Z. Closing the Anthropogenic Chemical Carbon Cycle toward a Sustainable Future via CO_2 Valorization. *Advanced Energy Materials* **11,** 2102767 (2021).
7. Ferrari, J. in *Electric Utility Resource Planning* (ed Ferrari, J.) 109–138 (Elsevier, 2021). ISBN: 978-0-12-819873-5.
8. Song, Y., Zhang, X., Xie, K., Wang, G. & Bao, X. High-Temperature CO_2 Electrolysis in Solid Oxide Electrolysis Cells: Developments, Challenges, and Prospects. *Advanced Materials* **31,** 1902033 (2019).
9. Endrődi, B. *et al.* High carbonate ion conductance of a robust PiperION membrane allows industrial current density and conversion in a zero-gap carbon dioxide electrolyzer cell. *Energy & Environmental Science* **13,** 4098–4105 (2020).
10. Sassenburg, M. *et al.* Characterizing CO_2 Reduction Catalysts on Gas Diffusion Electrodes: Comparing Activity, Selectivity, and Stability of Transition Metal Catalysts. *ACS Applied Energy Materials* **5,** 5983–5994 (2022).
11. Shin, H., Hansen, K. U. & Jiao, F. Techno-economic assessment of low-temperature carbon dioxide electrolysis. *Nature Sustainability* **4,** 911–919 (2021).
12. Jouny, M., Luc, W. & Jiao, F. Correction to "General Techno-Economic Analysis of CO_2 Electrolysis Systems". *Industrial & Engineering Chemistry Research* **59,** 8121–8123 (2020).
13. Steynberg, A., Espinoza, R., Jager, B. & Vosloo, A. High temperature Fischer–Tropsch synthesis in commercial practice. *Applied Catalysis A: General* **186,** 41–54 (1999).
14. Rostrup-Nielsen, J. R. New aspects of syngas production and use. *Catalysis Today* **63,** 159–164 (2000).
15. Burdyny, T. & Smith, W. A. CO_2 reduction on gas-diffusion electrodes and why catalytic performance must be assessed at commercially-relevant conditions. *Energy Environtal Science* **12,** 1442–1453 (2019).

16. Hansen, K. U., Cherniack, L. H. & Jiao, F. Voltage Loss Diagnosis in CO_2 Electrolyzers Using Five-Electrode Technique. *ACS Energy Letters* **7,** 4504–4511 (2022).

17. Cofell, E. R., Nwabara, U. O., Bhargava, S. S., Henckel, D. E. & Kenis, P. J. A. Investigation of Electrolyte-Dependent Carbonate Formation on Gas Diffusion Electrodes for CO_2 Electrolysis. *ACS Applied Materials & Interfaces* **13,** 15132–15142 (2021).

18. Sassenburg, M., Kelly, M., Subramanian, S., Smith, W. A. & Burdyny, T. Zero-Gap Electrochemical CO_2 Reduction Cells: Challenges and Operational Strategies for Prevention of Salt Precipitation. *ACS Energy Letters* **8,** 321–331 (2023).

19. Liu, Z., Yang, H., Kutz, R. & Masel, R. I. CO_2 Electrolysis to CO and O_2 at High Selectivity, Stability and Efficiency Using Sustainion Membranes. *Journal of The Electrochemical Society* **165,** J3371–J3377 (2018).

20. Vass, Á., Kormányos, A., Kószo, Z., Endrődi, B. & Janáky, C. Anode Catalysts in CO_2 Electrolysis: Challenges and Untapped Opportunities. *ACS Catalysis* **12,** 1037–1051 (2022).

21. Hugar, K. M., Kostalik, H. A. I. & Coates, G. W. Imidazolium Cations with Exceptional Alkaline Stability: A Systematic Study of Structure–Stability Relationships. *Journal of the American Chemical Society* **137.** PMID: 26062959, 8730–8737. eprint: https://doi.org/10.1021/jacs.5b02879 (2015).

22. Salvatore, D. A. *et al.* Designing anion exchange membranes for CO_2 electrolysers. *Nature Energy* **6,** 339–348 (2021).

23. Varcoe, J. R. *et al.* Anion-exchange membranes in electrochemical energy systems. *Energy & Environmental Science* **7,** 3135–3191 (2014).

24. Donnan, F. G. Theorie der Membrangleichgewichte und Membranpotentiale bei Vorhandensein von nicht dialysierenden Elektrolyten. Ein Beitrag zur physikalisch-chemischen Physiologie. *Zeitschrift für Elektrochemie und angewandte physikalische Chemie* **17,** 572–581 (1911).

25. Sata, T. & Jones, G. N. *Ion Exchange Membranes* X001–X004. ISBN: 978-0-85404-590-7 (The Royal Society of Chemistry, 2004).

26. Giorno, L., Drioli, E. & Strathmann, H. in *Encyclopedia of Membranes* (eds Drioli, E. & Giorno, L.) 1490–1493 (Springer Berlin Heidelberg, Berlin, Heidelberg, 2016). ISBN: 978-3-662-44324-8.

27. Kamcev, J. Reformulating the permselectivity-conductivity tradeoff relation in ion-exchange membranes. *Journal of Polymer Science* **59,** 2510–2520 (2021).

28. Kitto, D. & Kamcev, J. The need for ion-exchange membranes with high charge densities. *Journal of Membrane Science* **677,** 121608 (2023).

29. Zhang, Z., Wen, L. & Jiang, L. Nanofluidics for osmotic energy conversion. *Nature Reviews Materials* **6,** 622–639 (2021).

30. Merle, G., Wessling, M. & Nijmeijer, K. Anion exchange membranes for alkaline fuel cells: A review. *Journal of Membrane Science* **377,** 1–35 (2011).

31. Ghalloussi, R. *et al.* Ageing of ion-exchange membranes in electrodialysis: A structural and physicochemical investigation. *Journal of Membrane Science* **436,** 68–78 (2013).

2

DESIGN CRITERIA FOR SELECTIVE NANOFLUIDIC MEMBRANES

Polymeric ion-exchange membranes (IEMs) are key to many electrochemical processes, but their intrinsic selectivity limitations restrict scale-up possibilities. Nanofluidic IEMs, based on inorganic rigid materials and charged nanopores, offer a promising alternative. We present design criteria for scalable and selective nanofluidic membranes. We used commercial anodized aluminum oxide (AAO) membranes with varying pore sizes to measure permselectivity between different KCl concentrations. Our experiments reveal that membranes with 10-nm pores have permselectivities above 90%, comparable to those of polymeric IEMs, up to electrolyte concentrations of 0.15 vs. 0.75 M. To our knowledge, this is the highest reported ion selectivity for nanofluidic IEMs. Conversely, asymmetric AAO membranes featuring a thin selective layer, exhibited low permselectivity. We explored the influence of other parameters through simulations using the space-charge model. Our numerical results indicate that pore size and surface potential are the most sensitive parameters for increasing selectivity. Additionally, pore length has a minimum requirement for good performance although increasing it beyond the µm scale yields no significant result. This study highlights nanofluidic IEMs as a promising alternative to polymeric IEMs and their capability to improve performance of many electrochemical processes, especially those involving low electrolyte concentrations on at least one membrane side.

This chapter has been published as "Design criteria for selective nanofluidic ion-exchange membranes" by K.V. Petrov, M. Mao, A. Santoso, I. I. Ryzhkov and D.A. Vermaas, Journal of Membrane Science, **688**, 122156 (2023).

2.1. INTRODUCTION

Depletion of drinking water across dry regions and the global energy transition toward renewable sources has boosted the relevance of electrochemical processes aimed at water treatment, energy storage, and energy conversion.[1–3] Examples of emerging or industrially established processes include electrodialysis (ED),[4–6] ion-exchange membrane bioreactors,[7] reverse electrodialysis (RED),[8, 9] fuel cells,[10, 11] redox flow batteries,[12, 13] the chlor-alkali process,[14] and water and CO_2 electrolysis [15–17]. In all these processes, ion-exchange membranes (IEMs) are key components because of their selective ion conductivity.

The vast majority of IEMs are based on a polymeric matrix with immobilized charged functional groups.[18] These groups are responsible for the Donnan effect, rejecting ions with the same charge (co-ions) and allowing oppositely charged ions (counter-ions) to permeate.[19] Yet there is a conductivity-to-selectivity trade-off. This arises from challenges related to the flexible polymeric backbone and charged polymers groups, such as swelling,[20, 21] which leads to free water volume inside the matrix and limits the density of immobilized charges. Volume in the polymeric matrix grows with increasing degree of functionalization, which increases conductivity but decreases selectivity.[22, 23] Since most IEMs have a charge density of 0.5 to 3 M, polymeric IEM selectivity is very limited in high electrolyte concentrations.[24–27] Many IEMs with sufficient conductivity have selectivity around 90% at 1 M electrolyte concentrations. This limits their potential usage for applications that, for example, employ brine solutions, such as power generation via RED.[28] The trade-off between membrane selectivity and conductivity as well as the intrinsic limits in charge density hamper improvement of traditional IEMs.[3, 29–34] Additionally, polymeric IEMs suffer from steric hindrance, leading to a relatively high resistance to ion transport,[35] and ageing due to chemical degradation in harsh environments.[36, 37]

Nanofluidic membranes (NFMs) (illustrated in Figure 2.1) are alternative IEMs whose selectivity mechanism does not rely on charged functional groups, but on the surface charge within the nanopore.[38–40] The radii of these nanopores is close in magnitude to the thickness of the electrical double layer (EDL). Therefore, the EDL covers the majority or the entirety of the nanopore, charging the fluid inside. This allows the NFM to reject co-ions and allow counter-ions to permeate; the NFM hence functions as an IEM.[41] Based on rigid materials without swelling issues, NFMs offer new possibilities in chemical stability and can be made ultrathin, thus enhancing ionic conductance.

Various fields apply single charged nanopores, such as nanofluidics and biosensing,[42, 43] but sheets with a large nanopore density, such as NFMs, have only recently been used for power generation.[41] The main reason is that most nanoporous materials are not easily scalable.[38] They have been produced using techniques such as focused ion beam,[44, 45] electron beam,[35] and ion-track etching,[46, 47] none of which yet exist on a commercial scale.[38] Moreover, nanofluidic IEMs are a novel concept; as such, we lack understanding of how different parameters affect their selectivity.

Anodized aluminum oxide (AAO) is a commercially available material that can be produced with different pore geometries. It has a considerable surface charge even at neutral pH and perfectly arrayed cylindrical pores with a high pore density.[48, 49] Being one of the few materials that combines these properties, it is widely studied, but selectivities that

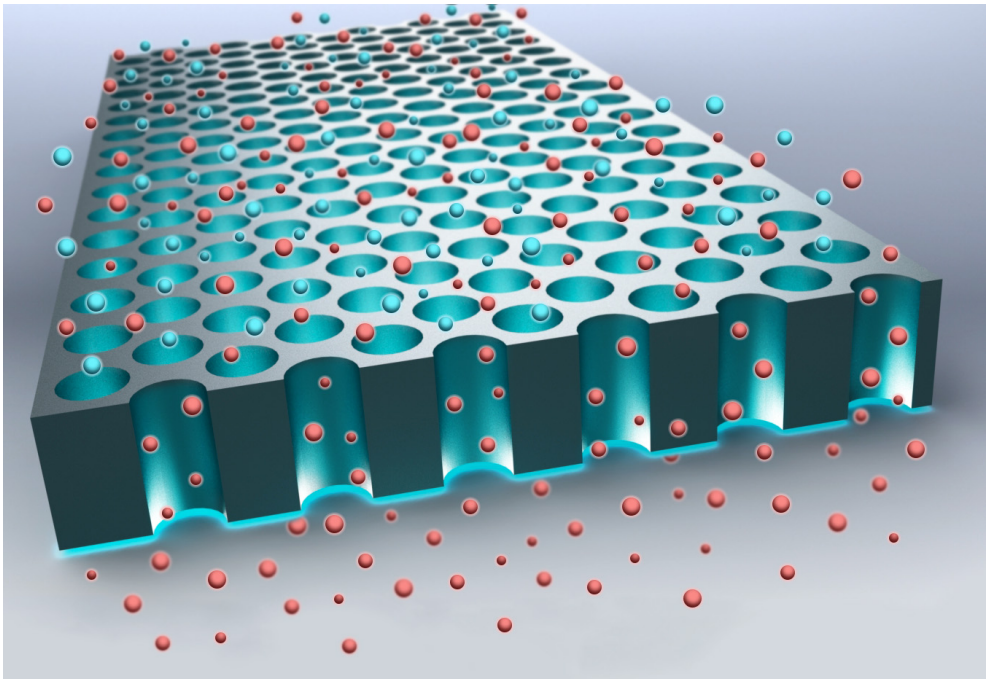

Figure 2.1: Illustration of the selectivity mechanism of an NFM. Counter-ions are shown in red, and co-ions are shown in blue.

can compete with polymeric IEMs have so far not been achieved. Kim et al.[50] achieved an apparent permselectivity of 60% by fabricating wide slits with a 4-nm height, while Kim et al.[51] achieved similar selectivity values using cylindrical pores with a 20-nm diameter. Using an asymmetric AAO membrane with two different pore diameters – the smaller being 2 nm – Lee et al.[52] achieved a permselectivity of approximately 100% at very low electrolyte concentrations, with a sharply decreasing selectivity with increasing concentration. These results, along with those documented in previous literature,[53] prove that pore geometry greatly impacts counter-ion selectivity of these membranes. Additionally, it is important to note that extrapolating existing findings from single nanochannels to NFMs might not be straightforward due to other potential factors, such as concentration polarization. Despite theory suggesting that lower pore diameter should increase selectivity, controlling pore size is challenging when dealing with very small pores. Optimization of NFM pore geometry is therefore essential to achieve peak performance in practical fluid applications.

This article aims to elucidate design criteria for inorganic nanoporous IEMs and investigate, both experimentally and numerically, to what extent AAO sheets can act as selective IEMs. For this study, we used commercial AAO membranes with different pore sizes to experimentally determine their permselectivity and simulated further parameters using the space-charge model (SCM). Our results suggest that these membranes can compete with polymeric IEMs in terms of permselectivity.

2.2. THEORETICAL BACKGROUND

The EDL is the ionic structure formed in the vicinity of a charged surface when immersed in an electrolyte. The electrochemical potential that arises at the solid-liquid interface causes the structure to form. It comprises two layers: the Stern layer, which is compact and very close to the surface, where ions are typically stagnant or have a very reduced mobility; and the diffuse layer, in which the concentration of counter-ions exponentially decreases in function of the distance to the surface until it reaches the bulk concentration.[54] Within the EDL, there is no electroneutrality as the counter-ion species is present in much higher concentration than the co-ion. The EDL thickness is characterized by the Debye length (λ_D), expressed as:

$$\lambda_D = \sqrt{\frac{\varepsilon \varepsilon_0 R_g T}{2 \cdot F^2 C_B}} \tag{2.1}$$

where ε is the relative permittivity, ε_0 is the permittivity of free space, R_g is the gas constant ($\mathrm{Jmol^{-1}K^{-1}}$), T is the absolute temperature (K), F is the Faraday constant (C/mol), and C_B is the bulk electrolyte concentration (mM).[55] Since λ_D depends on the bulk concentration (Equation 2.1), high selectivities can be achieved with low concentrations or narrower pores.

Evidence also shows that selectivity is determined by the Dukhin number (Du), rather than the Debye length. The Dukhin number (Equation 2.2) is the ratio between the surface conductivity induced by the charge on the pore walls and the bulk conductivity, which can be simplified as:

$$Du = \frac{|\sigma|}{F C_B R_p} \tag{2.2}$$

where σ is the surface charge density ($\mathrm{C/m^2}$) and R_p is the pore radius (m).[56, 57] The increased concentration of ions in the EDL, close to the surface, leads to an increased conductivity in this part of the solution. This effect is called surface conductance.[58] When a driving force is applied across the membrane, ion transport occurs through the most conductive regions, which is the vicinity of the charged walls (the EDL), especially when the bulk concentration is low. This explains selectivities observed for pore sizes larger than the Debye length and the relationship between surface charge density and selectivity.[44, 51] A $Du > 1$ indicates ionic selectivity for the nanopores.[56]

It is notable that the surface charge density itself can vary according to the environment. This depends on a material's surface potential, which in turn is dependent on the pH and on the electrolyte concentration.[59] The Grahame equation provides a relationship between the surface potential of a flat surface, and the surface charge density as:[60]

$$\sigma = \sqrt{8 C_B \varepsilon \varepsilon_0 k_B T} \sinh \frac{z e \phi_0}{2 k_B T} \tag{2.3}$$

where k_B is the Boltzmann constant (J/K), z is the ion valence, e is the elementary charge, and ϕ_0 is the pore wall potential. Since no transport occurs in the Stern layer, the ζ-potential is used as a boundary condition for surface potential (ϕ_0) and ion transport calculations.[60]

Although Du gives a good indication of the membrane's selectivity, more complex situations (such as distinct electrolyte concentration on either side) are usually solved using numerical simulations. Ion transport in nanochannels is often described by the space-charge model, initially developed by Morrison and Osterle.[61] This model considers a single nanopore, assuming an axisymmetric cylinder of length L and radius R_p, with x being the axial (longitudinal) coordinate and r being the radial coordinate. The pore connects two reservoirs of electrolytes with different concentrations, C_{low} and C_{high}. The pressure in the reservoirs is equal. Ion flux (J_i) is described by the Nernst-Planck equation as:

$$J_i(x,r) = c_i(x,r)u(x,r) - D_i\nabla c_i(x,r) - D_i\frac{z_i c_i F}{R_g T}\nabla\phi(x,r) \tag{2.4}$$

where u is the velocity of the fluid (m/s), D_i is the diffusion coefficient of the ion species i (m^2/s), z_i is the valence of ion i, and ϕ is the electric potential (V). The first term on the equation's right hand-side describes convective flow, the second accounts for diffusion, and the last accounts for migration. Electric potential and concentration profiles are described by the Poisson equation as:

$$\nabla^2\phi = -\frac{\rho_e}{\varepsilon\varepsilon_0} = -\frac{F}{\varepsilon\varepsilon_0}\left(c_+(x,r) - c_-(x,r)\right) \tag{2.5}$$

where ρ_e is the charge density (C/m^3) within the pore. To simplify the model, it is often assumed that local equilibrium is present in the radial direction (r) since the pore is much longer than its width. This leads to the assumption that ion flux and fluid velocity in the radial direction are 0. This allows us to insert Equation 2.5 into the r-component of Equation 2.4, which results in:

$$\frac{\partial c_i(x,r)}{\partial r} = -\frac{F z_i c_i(x,r)}{R_g T}\,\frac{\partial\phi_r(x,r)}{\partial r} \tag{2.6}$$

This can be integrated into the Boltzmann distribution as:

$$c_i(x,r) = c_v(x)\,\exp\left(-\frac{z_i F}{R_g T}\,\phi_r(x,r)\right) \tag{2.7}$$

We use the subscript v to represent "virtual" quantities expressing the principle of local equilibrium.

These equations can be solved using the boundary conditions of fixed wall potential and considering the cylindrical symmetry as:

$$\phi_r(x,R_p) = \phi_0 - \phi_v(x) \tag{2.8}$$

$$\frac{\partial\phi_r(x,0)}{\partial r} = 0 \tag{2.9}$$

where ϕ_0 is the potential at the pore wall, for which we used the ζ-potential value.

Finally, the velocity profiles within the pore can be obtained by the Navier-Stokes equation as:

$$\mu\nabla^2 u(x,r) - \nabla p_h(x,r) - \rho(x,r)\nabla\phi(x,r) = 0 \tag{2.10}$$

$$\nabla u(x,r) = 0 \tag{2.11}$$

where μ is the viscosity (Pa.s) and p_h is the hydrostatic pressure (Pa). The boundary conditions for velocity involve assuming a no-slip boundary condition and that the wall is impermeable to both fluids and ions, expressed as:

$$u\left(x, R_p\right) = 0 \tag{2.12}$$

The governing equations of the space-charge model (Equations 2.4, 2.5, 2.10, and 2.11) are highly coupled to each other, making it very complicated to solve even for simple geometries.[62] Consequently, the solution is typically obtained through numerical methods.

2.3. METHODS

2.3.1. PERMSELECTIVITY EXPERIMENTS

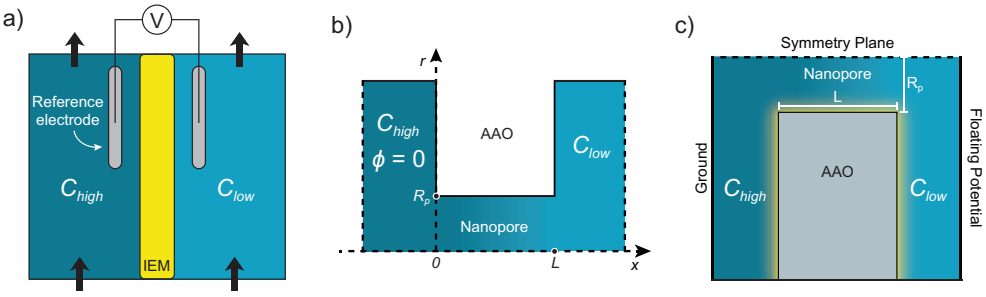

Figure 2.2: a) A schematic shows the permselectivity setup. b) The geometry modeled in the ITM software. c) The geometry modeled in COMSOL Multiphysics.

The two-compartment setup shown in Figure 2.2 allowed us to experimentally measure the permselectivity of a membrane. We placed the membrane between two compartments (150 mL each) of electrolyte solutions with different concentrations and then measured the electrical potential difference between them using two double-junction Ag/AgCl reference electrodes connected to an Autolab PGSTAT 128N potentiostat (Metrohm, Switzerland). The tested membranes were AAO discs with a diameter of 1.3±0.1 cm and an array of straight cylindrical nanopores of different pore sizes (InRedox, Colorado, USA), which act as an anion exchange membrane at neutral pH. We tested two sets of membranes: symmetric membranes with pore sizes of 10, 20, and 50 nm (in diameter); and asymmetric ones with a 150-nm pore size throughout the majority of the membrane thickness, and a 1.5-µm thick selective layer with a branched structure with a pore size of 3 ± 2 nm or 5 ± 2 nm (Figure S2.1). The membranes were used as delivered without any pretreatment. We placed the membranes in a holder between two flat O-rings, leaving 0.64 cm^2 of open area, which we then placed between the two electrolyte compartments. KCl was our chosen electrolyte for these measurements because K^+ and Cl^- ions have approximately the same mobilities, and therefore the measured potential is not affected by dif-

fusion potentials - only the Donnan potential would be detected. 500 mL of electrolyte were used to reduce the potential impact of concentration changes. The electrolyte in the compartments was kept flowing at 40 mL/min using a peristaltic pump to minimize concentration polarization. To avoid pH changes due to CO_2 dissolution from the air during the experiment, we bubbled a small amount of N_2 gas in the electrolyte reservoirs. Before measuring membrane potential, we kept the solutions flowing for at least three hours to ensure equilibration with the membrane. The potential was then taken as an average of at least 120 seconds. After obtaining three measurements, we rinsed and swapped the reference electrodes and took three more measurements. By averaging the six measurements, we ensured no effect of possible drift of the potential of the reference electrodes. We obtained the activity coefficients using Visual MINTEQ 3.1 software. The Cl^- concentrations in the two compartments were measured right after the experiment using an 881 IC pro ion chromatograph with a 150-mm A Supp 5/4.0 column (Metrohm, Switzerland). These concentrations were then used to calculate the Nernst potential.

An adapted version of the Nernst equation (Equation 2.13), which can be written for a 1:1 salt, and the measured membrane potential (E_M) enabled us to obtain the transport numbers within the membrane: t_-^m and t_+^m for counter-ions (anions) and co-ions (cations), respectively. If the transport number for counter-ions is 1, then the equation just equals the classical Nernst equation, which would be our ideal measured potential ($E_{M_{ideal}}$), expressed as:

$$E_M = \frac{RT}{F}\left(t_-^m - t_+^m\right)\ln\frac{a_1}{a_2} \tag{2.13}$$

We calculated the apparent permselectivity as follows:

$$\varphi = \frac{\frac{E_M}{E_{M_{ideal}}} + 1 - 2t_i}{2t_j} \approx \frac{E_M}{E_{M_{ideal}}} \tag{2.14}$$

where t_i and t_j stand for the transport numbers in the bulk of counter-ions and co-ions, respectively. In this case, they are approximately the same since KCl was used as the electrolyte.

2.3.2. MEMBRANE CHARACTERIZATION

To characterize surface morphology, we used focused ion beam scanning electron microscopy (FIB-SEM, FEI Helios G4 CX). Since this tool requires a conductive surface, we deposited gold nanoparticles on the AAO samples. We used 30 seconds of deposition time for imaging and 300 seconds for FIB cutting. The image was obtained using three different detectors, depending on the best-obtained contrast: an Elstar in-lens secondary electrons detector (TLD-SE), an Everhart-Thornley detector (ETD), and a high-performance ion conversion detector (ICE) at a beam current of 18-86 pA and electron energy of 10-30 keV. A complementary image was obtained using field emission scanning electron microscopy (FESEM, Hitachi Regulus SU8230) at a beam current of 1-5 μA and electron energy of 10-15 keV. We used the FIB for cutting a part of the sample to observe the cross-section with transmission electron microscopy (TEM). A JEOL JEM 3200FS microscope enabled us to obtain the TEM images at 150,000× magnification.

Image-processing the microscopy pictures enabled us to make pore size distributions from both TEM and SEM analysis. Further details on the image-processing methodology are available in the supporting information (Figures S2.2 and S2.3).

Using TriStar II 3020 equipment (Micromeritics), we measured nitrogen adsorption-desorption isotherms at 77 °K. Before the analysis, we degassed 23 mg of AAO material under vacuum at 250°C for 16 hours. The Brunauer–Emmett–Teller (BET) surface area of the membranes was measured at 46.06 ± 0.08 m^2/g. The Barrett, Joyner, and Halenda (BJH) method for the desorption cumulative volume of the pores up to 300 nm showed a volume of 0.252 cm^3/g. We fit these cumulative curves to obtain a pore size distribution by having incremental volumes at even steps and correcting this volume to obtain a relative frequency of each pore size interval (see Figure S2.4).

We also measured the water permeability of our membranes, but the permeability of the AAO membranes was too low to accurately measure. Details can be found the supporting information (Figure S2.5).

2.3.3. SIMULATIONS

Professor Ilya I. Ryzhkov, who collaborated with us on this work, developed a software called Mathematical Modelling of Ion Transport in Membranes (ITM) software.[53, 63] The software numerically solves the space-charge model (SCM), which describes the ion transport through cylindrical nanopores with a known surface potential. The pores connect two electrolyte tanks (Figure 2.2b) and permit inclusion of a Stern layer and a diffusion boundary layer outside the pores. In our simulations, pore size, pore length, electrolyte concentration, and surface potential were varied while remaining parameters were kept constant (summarized in Table S2.1). Unlike other models, the ITM software allows the use use a constant surface potential (instead of surface charge density) as a boundary condition. Pore size was kept above 3 nm because below that value, the continuum assumption becomes questionable.[56] The diffusion coefficients for K^+ and Cl^- were taken as 1.957×10^{-9} m^2/s and 2.032×10^{-9} m^2/s, respectively. Fluid viscosity was 0.888×10^{-3} Pa.s. The temperature was 298.15 °K. For the entirety of the nanopore, we used the relative permittivity of water, taken as 78.49. The boundary condition used for surface potential in the modeling was the ζ-potential, which is measured at the shear plane of the EDL.[64] Therefore, the pore size was corrected after the modeling to include the Stern layer thickness which was considered to be 0.5 nm. The effective pore size for ion transport is 1 nm smaller than what is reported in our simulation results.

Another model was created in COMSOL to assess the effect of the surface around the entrance of the nanopore, which was not possible to do with the ITM software. The COMSOL model used the Poisson-Boltzmann and Nernst-Planck equations in a 2D axysymmetrical geometry (Figure 2.2c) with four domains: two electrolyte tanks with defined concentration on the edge farther from the membrane; a membrane with a specific surface potential and no ion-flow across the walls; and a channel under the influence of this surface charge connecting the two reservoirs. The simulations evaluated the effect of including or not including the surface of the membrane, as opposed to solely applying the boundary conditions to the pore walls.

2.4. RESULTS AND DISCUSSION

2.4.1. PERMSELECTIVITY EXPERIMENTS

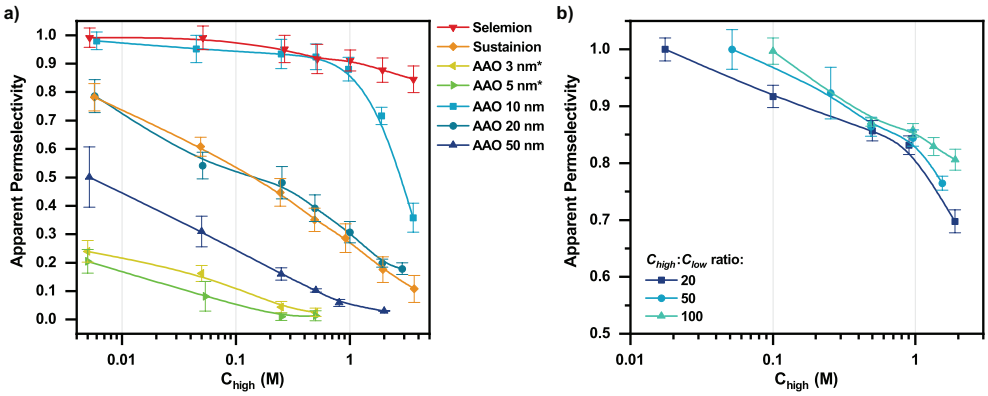

Figure 2.3: a) Apparent permselectivity of two polymeric IEMs – Selemion AMV and Sustainion X37 – and five AAO membranes with different pore sizes (3–50 nm) placed between two reservoirs with a concentration ratio of 5.*3-nm and 5-nm pores are asymmetric membranes with only a thin selective layer. b) Apparent permselectivity results showcase the effect of concentration and concentration ratio on permselectivity of the AAO membrane with 10-nm pores. Note that the figures have different scales.

We measured the apparent permselectivity of different IEMs between two compartments with different KCl concentrations. Figure 2.3a shows the apparent permselectivity vs. concentration at a fixed concentration ratio C_{low}:C_{high}, of 1:5. The general trend of decreasing selectivity for higher electrolyte concentration was expected from the Donnan equilibrium theory. The AAO selectivity was benchmarked against two polymeric membranes: Selemion AMV, developed for electrodialysis and one of the most selective commercial anion exchange membranes,[65] and Sustainion X37, geared for electrolysis.[66] Figure 2.3a shows that the AAO membrane with 10-nm pores had an apparent permselectivity of above 90% and was comparable with Selemion AEMs up to concentrations of approximately 0.7 M. Although its permselectivity rapidly decreased after this value, it was considerably more permselective than Sustainion in the whole concentration range. To our knowledge, this the highest permselectivity reported for NFMs.

The AAO membrane with 20-nm pores had a permselectivity comparable to that of Sustainion membranes, with an 80% permselectivity at 5 mM, which decreases with increasing concentration. The membranes with 50-nm pores showed poor selectivity, below 50% for the entire tested concentration range. This further evidenced the relationship between pore size and selectivity, where higher permselectivities are observed at lower pore sizes.

Finally, the anisotropic AAO membranes, which have a thin selective layer (1.5 µm thickness) of 3 ± 2-nm or 5 ± 2-nm pores on top of a support layer with 150-nm pores, also exhibited a poor permselectivity, comparable to that of a membrane with 50-nm pores. We hypothesize that the limited pore length of the fine pore layer caused the poor selectivity. Additionally, since diffusion flux is inversely proportional to thickness, a more pronounced concentration polarization was present, notably internally – in the section with

150-nm pores. Concentration polarization due to diffusion resulted in a lower concentration gradient over the membrane. This suggested that a certain pore length was required to achieve high selectivities. These samples have a branched type of structure at the end (Figure S2.1), whereby narrow pore size is achieved for a very limited length. The results in Figure 2.3a show that this branched structure was not enough to establish a selective layer, thereby urging further study of the effect of pore length (see section 2.4.3).

Figure 2.3b displays the apparent permselectivity of an AAO membrane with 10-nm pores for different concentrations and ratios of concentrations. The results showed that for all ratios, there was a decrease in permselectivity for increased concentration. Permselectivity was higher for higher ratios in concentrations when plotted against the C_{high}. When plotted against the C_{low}, we observed the opposite effect (Figure S2.6). Both concentrations on the two sides of the membrane therefore had an effect on selectivity. To better understand the high permselectivities for AAO membranes with 10-nm pores and the potential for further tuning its properties, we thoroughly characterized the membranes and built a model explaining the relationship between pore geometry, the different parameters, and permselectivity.

2.4.2. MEMBRANE CHARACTERIZATION

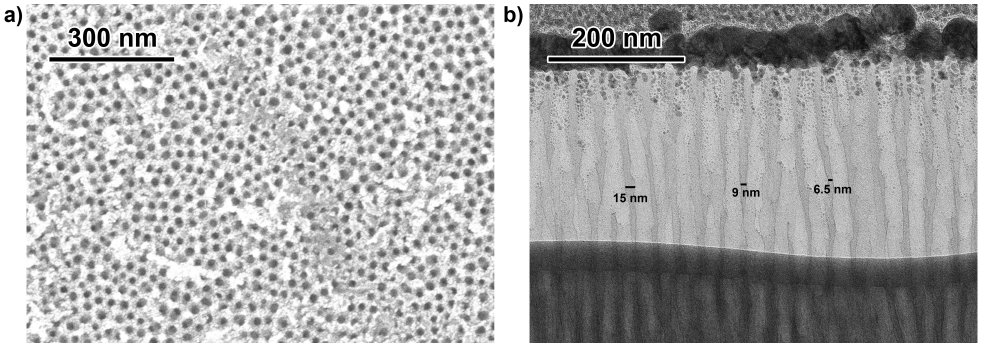

Figure 2.4: a) A SEM image of the AAO membrane surface shows a 10-nm pore at 120,000× magnification. b) A TEM image shows a cross-section of the same membrane at 150,000× magnification; nanopore morphology can be observed in the light gray area in the middle portion of the figure.

Figure 2.4a shows the SEM image of the surface of the AAO membrane with 10-nm pores. The membrane has a highly ordered, dense array of pores of similar size. These properties deem it suitable to function as an IEM. Figure 2.4b shows the transmission electron microscopy (TEM) image of the same membrane's cross-section. At the top of the figure, a darker area with circular shapes represents the gold nanoparticles deposited for the FIB cut that prepared the sample for TEM. The figure's lighter middle section shows the nanopores, which do not appear to be perfectly cylindrical; they sometimes narrow or widen and at some points converge and diverge, causing a wider pore size distribution than expected. We can also observe how the pores often widen at the top, giving them a slightly funneled shape (Figure S2.7).

Figure 2.5a shows the size distribution on the AAO membrane with 10-nm pores determined by three different methods. All methods resulted in a wider pore size distribution

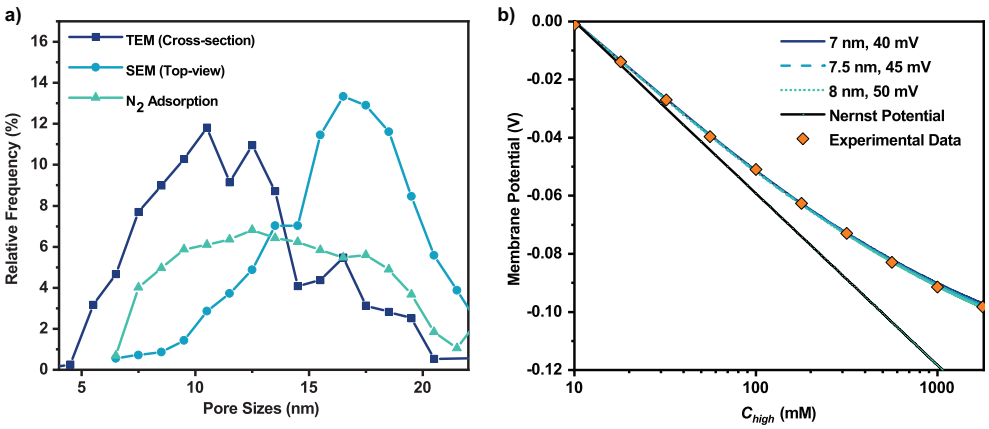

Figure 2.5: a) Pore size distributions are shown. b) Membrane potential data is fit with the ITM software. The three lines have a combination of pore sizes of 7, 7.5, and 8 nm and 40, 45, and 50 mV of ζpotential.

than expected or provided by the supplier. Since the pores slightly widen at the top (Figures 2.4b and S2.7), the entire distribution curve determined by SEM is shifted toward larger pore sizes. On each of the membrane's two sides (see Figures S2.8 and S2.9), we also observe a different morphology and perhaps even a different pore density. This further explains the large pore size distribution. Average pore size determined by treating the TEM data is 10.6 ± 3.5 nm; by fitting the nitrogen desorption curve, the average pore size obtained was determined at 13.5 nm. However, because the larger pore size (near the surface) and narrow pore size (in the middle) were connected in series, we expected the narrower parts to determine the membrane's selectivity. Because the TEM data showed pore sizes starting at 5 nm and an average pore size of roughly 10 nm, we expected the effective pore size for determining the selectivity in these samples to be somewhere between 5 and 10 nm.

To further elucidate the effective pore size and understand the experimental results, we compared the experiments with simulated values from the ITM software. For model validation over a broad range in membrane potential, we performed a new set of permselectivity experiments keeping C_{low} at 10 mM while increasing C_{high} stepwise. According to the literature, the ζ-potential of an AAO surface in aqueous solutions ranges between 40 and 50 mV at neutral pH, depending on the electrolyte concentration.[59, 67, 68] Figure 2.5b shows the comparison of the experimentally obtained membrane potential values with simulation data. Combinations of pore sizes between 7 and 8 nm and ζ-potentials between 40 and 50 mV were shown to fit the experimental data perfectly. For the remaining simulations, we used 7 nm as the pore size and 40 mV as the surface potential boundary condition.

We observed that the experimental data fit remarkably well when using a constant membrane potential. Using a constant surface charge density instead (Figure S2.10) did not yield good fits; this was because the surface charge density depended on the electrolyte concentration, which vary along the length of the pore, especially when the membrane is between two solutions of different concentrations.[60] This shows the simulations

can accurately predict the selectivity of AAO when using constant membrane potential. It is important to note that although the simulation perfectly fit the experimental data using C_{low} = 10 mM, shown in Figure 2.5b, it failed at higher concentrations for the samples labeled 10 nm (and with effective pore size of 7 nm) (Figure S2.11a). This discrepancy was even more pronounced at low concentration ratios (Figure S2.11b). To some extent, experimental data was subject to sample-to-sample variation, not least because of the broad pore size distribution. ζ-potential could also vary along the pore, notably at the elevated electrolyte concentrations at low ratios.[59] Pore size and length also determined the diffusion flux through the pore and therefore influenced the concentration polarization, which was not taken into account by the model. Nevertheless, since the simulations were consistent with a large portion of the experimental data, they were considered a useful tool to further explore the concept of nanofluidic IEM selectivity.

2.4.3. SIMULATIONS

In order to explain the relationship between membrane properties and operating conditions, we used the ITM model to simulate the effect of these parameters. This model enabled simulation of different membrane properties and operation conditions that were not possible to verify experimentally and offered further insight into the executed experiments.

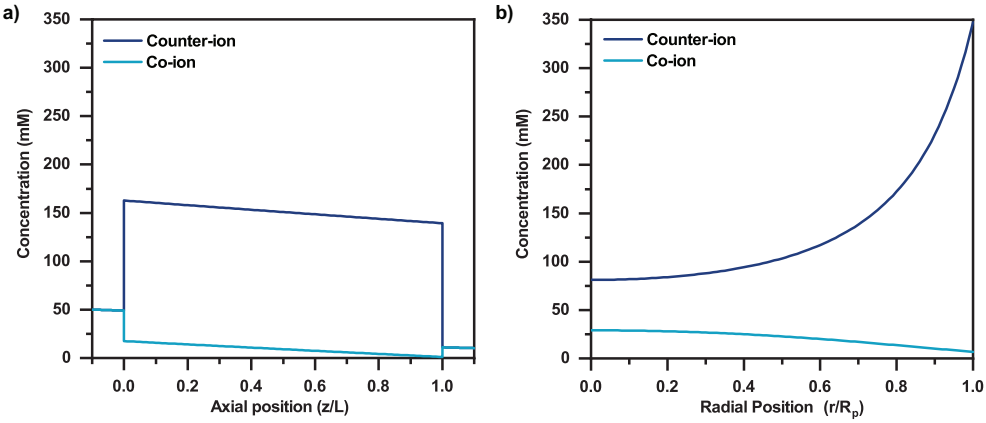

Figure 2.6: 5 Ion concentration profiles inside a pore with a 7-nm diameter (effective R_p = 3 nm) and a 1-µm length are shown placed between two reservoirs with 10 mM and 50 mM of KCl. a) Longitudinal ion concentration profiles are shown with averaged concentration at each z position. b) Radial ion concentration profiles are shown at z/L = 0.5, where 0 is the center of the pore and 1 is the pore wall.

Firstly, to gain deeper insight into the selectivity mechanism, we plotted the simulated ion concentration profiles within a nanopore. Figures 2.6a and 2.6b show the longitudinal and radial ion profiles, respectively. Figure 2.6a shows a jump in ion concentration occurring at the entrances of the pore, together with a sudden jump in Donnan potential (Figure S2.12a). The pronounced jump is partly due to the SCM's use of jump boundary conditions. In a real scenario, the electric field increases more progressively, which can only be captured by a model with continuous change of potential and ion concentration

at the interfaces. Nevertheless, when such a model is used, although smoother, a pronounced jump in potential and concentration is still observed at the interfaces.[53] Since the surface potential is positive, the concentration of anions inside the pore is higher than in the bulk. Concentration and surface charge density (Figure S2.12b) inside the nanopore vary almost linearly along the length of the pore (from $z = 0$ to $z = L$). The jump in potential and concentration suggests that the selectivity is mainly created by these interfaces. The largest counter to co-ion ratio is observed a $z/L = 1$, which suggests this interface plays a significant role in the selectivity.

The radial profiles (Figures 2.6b) show that the largest ion concentrations are close to the pore wall, with counter-ion concentration exceeding co-ion concentration even in the center of the pore. This shows that the entirety of the nanopore has a certain degree of selectivity even though there is no EDL overlap at this concentration. Moreover, both the highest conductivity and highest counter- / co-ion separation were observed close to the pore wall. This provides evidence for the surface conductance mechanism described earlier. The high counter-ion concentration close to the pore wall also clarifies that higher selectivities can be achieved with smaller nanopores.

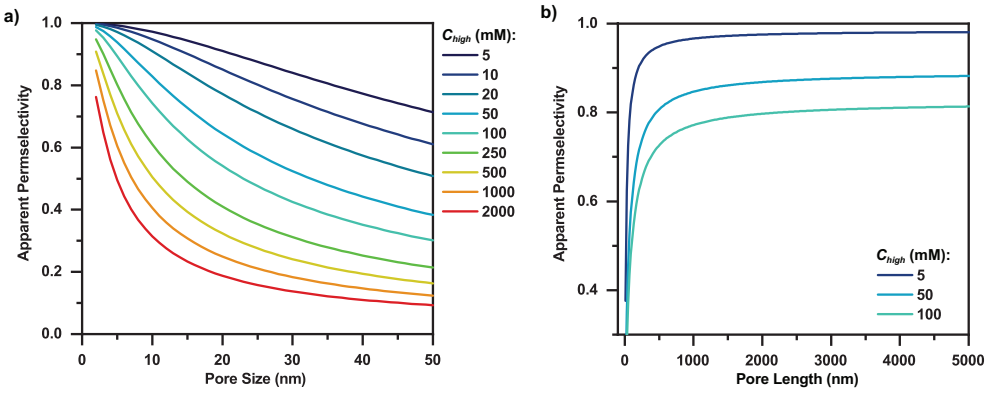

Figure 2.7: a) Effect of pore size vs. different concentrations is shown. b) Effect of pore length on apparent selectivity is shown. C_{high}:C_{low} ratio is fixed at 5.

To investigate the relationship between pore geometry and selectivity, we plotted permselectivity against pore size and length at various C_{high} concentrations (Figure 2.7). Smaller pore sizes led to much higher selectivity, and this effect was more pronounced at higher concentrations (Figure 2.7a). This highlights the sensitivity of the pore size as a parameter; an increase in just 5 nm could mean a 30% selectivity decrease for concentrations above 100 mM. It also shows that small pores can be selective even at high concentrations. This result underscores the importance of precise fabrication of NFMs, as a wider pore size distribution can have negative impacts on selectivity, which could be a challenge for large-scale (m^2) fabrication. To reiterate, pores smaller than 3 nm were not modeled because the continuum assumption becomes questionable at those scales. In addition, pores smaller than 1 nm are expected to lose the advantage of enhancing transmembrane transport since, at that level of confinement, the Stern layer covers the majority of the pore, where the water's viscosity greatly increases and the diffusion coefficient of the ions

decreases.[56, 69, 70]

Figure 2.7b shows the effect of pore length on selectivity. An increase in pore length from a couple tens of nm to a couple hundreds of nm can substantially improve the selectivity, while selectivity is not very sensitive to pore length in the micrometer range. Based on our results, a minimum length is thus required, though pore lengths above several µms are unnecessary for selective AAO IEMs.

On the other hand, 2D or atomically thin materials have also been shown to be selective up to over 80%.[44] To explain this occurrence, we made a separate model in COMSOL Multiphysics, which included not only the nanopore itself, but also the surface of the membrane. The result (Figures S2.13 and S2.14) showed that for longer pores ($L >> R_p$), the surface does not affect selectivity; but for short or 2D pores, the surface itself has a significant effect. Therefore, we attribute the selectivity of 2D materials (typically graphene) to EDL overlap, their large surface potential, and the surface itself, which is more prominent since the pore density is typically lower. For materials with a lower surface potential and high pore density, however, 2D materials are expected to remain selective only when there is EDL overlap, which is already at sub-nanometer level for concentrations above 100 mM (Equation 2.1).

To further understand the effect of surface potential and electrolyte concentration, we plotted the effect of the changing ζ-potential (Figure 7a) and electrolyte concentration (Figure 7b) on selectivity.

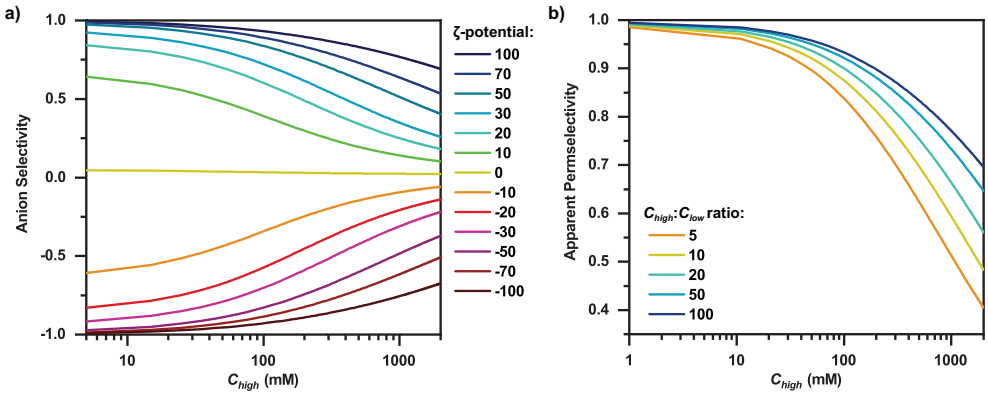

Figure 2.8: Simulations performed for a 7-nm pore with boundary conditions of 40-mV surface potential. a) Effect of the surface potential boundary conditions on permselectivity is shown, with a negative "anion selectivity" representing selectivity toward cations. b) Effect of the ratio between C_{high} and C_{low} on permselectivity is shown.

Figure 2.8a shows that selectivity was strongly enhanced for higher ζ-potential. The ζ-potential can be viewed as a material property, but it is also strongly affected by the pH. Therefore, 0 potential can also be interpreted as the isoelectric point, the higher potentials as the effect of a more acidic pH and vice versa. Actual potential values would naturally depend on material, structure, and environment. In addition, this is also a highly sensitive parameter (for direct comparison with pore size, see Figure S2.15), so the surface potential or choice of material represents an important lever in achieving ion selectivity.

Surface potential could also be externally altered by applying a potential to the membrane itself.[71–73] This can be particularly beneficial, for example to switch between anion and cation selectivity or in electrolysis applications where the membrane can be placed in contact with one of the electrodes. In the latter, a small overpotential can be required to greatly improve membrane selectivity, but it is only feasible if Faradaic reactions that occur on the surface of the NFM can be prevented. Fortunately, these materials are often dielectric, they exhibit low catalytic activity, and the required potential window to make the membrane selective is quite low. However, for applications where stacks of membranes are used, such as RED, this approach may be unsuitable since each membrane would need its own source of external charge and likely a reference electrode, which is impractical.

The final parameter studied was the concentration ratio. Figure 2.8b displays the simulations performed for a pore with a 7-nm diameter and a 40-mV surface potential for different C_{high}:C_{low} ratios. Naturally, the selectivity was highest for a low electrolyte concentration (low C_{high}) and for a higher ratio (which implies low C_{low}). The impact of the concentration ratio was more pronounced at higher concentrations. To study which side (C_{low} or C_{high}) had a larger impact on selectivity, we plotted the apparent permselectivity against the arithmetic, the harmonic, and the geometric average of C_{high} and C_{low} (Figure S2.16). For the geometric average, the lines for all concentration ratios were almost coincident, indicating that the geometric average in electrolyte concentration is determining the selectivity. Geometric average is always lower than (or equal to) arithmetic average, which means the lower side has a quadratically larger impact on selectivity than the higher concentration side. This property makes these membranes a good option for applications where the electrolyte concentration is very high on one side and very low on the other side, such as RED.

In order to look into their peak perfomance, we simulated a membrane with 2-nm pores and 5-µm length and considered one scenario in which the membrane had 40 mV of ζ-potential and one with 100 mV. We conservatively assumed that the membrane was being used for power generation through a salinity gradient, between a river with a 17-mM salt concentration and seawater (0.6 M) (see Figure S2.17b). The results show that this membrane would have a 97.7% selectivity at 100 mV and 93.3% with 40 mV of surface potential. The result with 100-mV surface potential surpassed many of the polymeric IEMs used for this application; these values can be even higher since this simulation was done with a ratio C_{high}:C_{low} of 35 while in practical RED processes, it can be as high as 500. We want to highlight that this prediction is based on the space-charge model, which has not yet been experimentally proven to accurately predict the selectivity for membranes with a pore size as low as 3-5 nm. Experimental proof of this prediction would be highly valued.

In terms of conductivity, the currently commercially available NFM materials, do not perform well enough to compete with polymeric IEMs. The AAO membranes we tested experimentally, have at least a 100 $\Omega\,cm^2$ ionic resistance when placed between two compartments with 0.1 M KCl. This is because the membrane thickness is not optimized and the effective porosity is very low – see Figure 2.4b, many channels have a dead end. Laboratory-made NFMs in other works have shown ionic resistances as low as 1 $\Omega\,cm^2$, which is lower than many polymeric IEMs.[50, 74, 75] We will look further into this topic in chapter 3.

In this chapter, we've shown that nanofluidic IEMs can act as a selective ion separator, reaffirming their potential for applications such as RED and electrolysis.[51, 73, 76] Anodized metal oxides can be fabricated with fine-tuned pore sizes and geometries, adaptable for different applications.[77] The inorganic nature of these materials also brings the advantage of no swelling. Swelling of polymeric IEMs can be a challenge when assembling a large stack of membranes, since it is dependent on ion concentration and temperature, among other parameters. Additionally, creating an ultrathin (5 µm or less) nanofluidic IEM can enhance ion conductivity without compromising selectivity. It would be insightful if these results were verified experimentally by creating membranes with different thicknesses (i.e. pore lengths).

On the other hand, the inorganic nature of the materials also means that these membranes can be extremely brittle, especially when ultrathin. This could pose practical and transportation challenges, therefore requiring the use of a support material. The chemical stability of AAO membranes is also very limited, especially at alkaline pH and in aqueous solutions. Over time, the pores become clogged due to formation of aluminum hydroxide.[78] However, other materials, such as titanium, can also be anodized to create the same geometries in a controlled manner. Anodized metal oxides can be easily coated, for example with atomic layer deposition, electroless deposition, or simple functionalizations with organic acids to manipulate their chemical stability.[77] This can improve chemical stability and also change the material's surface potential to enhance selectivity. Anodized metal oxide membranes are currently commercially available exclusively in cm^2 scale. Their defect-free production in m^2 scale remains a major challenge. Other methods to produce materials with a dense array of cylindrical nanopores include plating polycarbonate membranes and synthesis of nanoporous silica films via sol-gel techniques.[72, 79, 80]

Another challenge is related to the surface potential being affected by pH. Most materials have a negative surface potential at high pHs, thus making it very difficult to create anion-exchange membranes in highly alkaline environments, or cation-exchange membrane in acidic environments. Although this is not a problem for most RED processes, it can be relevant for electrocatalytic applications, such as CO_2 electrolysis or water electrolysis. In that case, the external charging can be used to circumvent loss of anion selectivity at high pH in electrolysis applications.

NFMs could also have an increased water and gas permeability due to their comparatively more open structure, which could compromise the energy efficiency in RED or induce gas crossover risks in electrolysis. However, the water transport through the AAO membranes was negligible in our experiments ($< 10^{-12}$ m^2/s). For reference, we measured the water permeability of the Selemion AMV membrane at $(5 \pm 1) * 10^{-10}$ m^2/s and and $(2.2 \pm 0.3) * 10^{-9}$ m^2/s for Zirfon Perl UTP500, which is close to other reported values in literature.[65, 81] The extremely low water permeability of NFMs, despite the porous structure, is likely related to their low effective porosity. Other values in literature suggest that their water permeability is in the same order of magnitude,[82] or slightly higher than of polymeric IEMs.[83] A more open and thinner NFM would likely enhance the water transport, and reduce the ionic resistance at the same time. Because the water transport is currently orders of magnitude lower than polymeric IEMs, there is room for increasing the effective porosity of NFMs.

This study has also reaffirmed that the space-charge model can predict the selectivity of the nanofluidic IEMs. We recommend that future models include finite ion size, as this can change the total concentration inside the nanopore, especially at larger concentrations. For very small pore sizes, they should also include a variable diffusion coefficient since it is known that in a nanoconfined fluid, the diffusion coefficient will be affected, especially when close to the pore walls.[69, 70] The diffusion coefficient is of great importance when simulating the conductivity of the membranes. It is good practice to consider the Stern layer thickness, where virtually no ion transport occurs as described in [71]. For 2D materials or very short nanopores, the membrane surface should also be included for accurate simulations.

2.5. CONCLUSIONS

In this study, we tested commercial AAO membranes with different pore sizes on their functionality as IEMs. We measured the apparent permselectivity of the membranes by placing them between two compartments of different electrolyte concentrations and measuring the potential across the membrane. The results showed that up to electrolyte concentrations of $\tilde{0}.15$ vs. 0.75 M, the AAO membranes with $\tilde{7}$-nm pores had a selectivity above 90%, which is comparable to polymeric IEMs. To our knowledge, this is the highest reported selectivity for nanofluidic IEMs in the literature, thus proving the concept's potential. Anisotropic membranes with a thin selective layer of 3-nm and 5-nm pores did not achieve high selectivities. Further, we used the space-charge model to explain these results and gain further understanding on how pore geometry can be modified to optimize selectivity.

Our simulations showed that pore size and surface potential are the most sensitive parameters for selectivity. Smaller nanopores can potentially achieve even higher selectivities, especially if a material with a higher surface potential or ζ-potential is used. However, the ζ-potential is not only dependent on the material but on the environment and pH as well. The simulations also showed that a minimum pore length is necessary to achieve selectivity although increasing the pore length in the μm scale has no significant effect. The concentrations on the two sides of the membrane were also found to have a large impact on selectivity, with the geometric average between the two being the determining parameter for selectivity.

Although challenges still restrict large-scale fabrication and implementation of nanofluidic membranes, we have shown that these materials can act as selective IEMs. Ultimately, the development of nanofluidic membranes as a replacement of polymeric IEMs could improve the performance of many electrochemical membrane processes, ranging from RED to electrolysis.

BIBLIOGRAPHY

1. Varcoe, J. R. *et al.* Anion-exchange membranes in electrochemical energy systems. *Energy & Environmental Science* **7,** 3135–3191 (2014).
2. Xia, R., Overa, S. & Jiao, F. Emerging Electrochemical Processes to Decarbonize the Chemical Industry. *JACS Au* **2,** 1054–1070 (2022).
3. Luo, T., Abdu, S. & Wessling, M. Selectivity of ion exchange membranes: A review. *Journal of Membrane Science* **555,** 429–454 (2018).
4. Strathmann, H. B. T. *Ion-Exchange Membrane Separation Processes* ISBN: 0927-5193 (Elsevier, 2004).
5. Silva, V., Poiesz, E. & van der Heijden, P. Industrial wastewater desalination using electrodialysis: evaluation and plant design. *Journal of Applied Electrochemistry* **43,** 1057–1067 (2013).
6. Strathmann, H. Electrodialysis, a mature technology with a multitude of new applications. *Desalination* **264,** 268–288 (2010).
7. Oehmen, A., Viegas, R., Velizarov, S., Reis, M. A. M. & Crespo, J. G. Removal of heavy metals from drinking water supplies through the ion exchange membrane bioreactor. *Desalination* **199,** 405–407 (2006).
8. Güler, E., Elizen, R., Vermaas, D. A., Saakes, M. & Nijmeijer, K. Performance - determining membrane properties in reverse electrodialysis. *Journal of Membrane Science* **446,** 266–276 (2013).
9. Vermaas, D. A., Saakes, M. & Nijmeijer, K. Power generation using profiled membranes in reverse electrodialysis. *Journal of Membrane Science* **385-386,** 234–242 (2011).
10. Dekel, D. R. Review of cell performance in anion exchange membrane fuel cells. *Journal of Power Sources* **375,** 158–169 (2018).
11. Jiao, K. *et al.* Designing the next generation of proton-exchange membrane fuel cells. *Nature* **595,** 361–369 (2021).
12. Schwenzer, B. *et al.* Membrane Development for Vanadium Redox Flow Batteries. *ChemSusChem* **4,** 1388–1406 (2011).
13. Chen, D., Hickner, M. A., Agar, E. & Kumbur, E. C. Optimized Anion Exchange Membranes for Vanadium Redox Flow Batteries. *ACS Applied Materials & Interfaces* **5,** 7559–7566 (2013).
14. Lakshmanan, S. & Murugesan, T. The chlor-alkali process: Work in Progress. *Clean Technologies and Environmental Policy* **16,** 225–234 (2014).
15. Grigoriev, S. A., Fateev, V. N., Bessarabov, D. G. & Millet, P. Current status, research trends, and challenges in water electrolysis science and technology. *International Journal of Hydrogen Energy* **45,** 26036–26058 (2020).
16. Fortin, P. *et al.* High-performance alkaline water electrolysis using Aemion™ anion exchange membranes. *Journal of Power Sources* **451,** 227814 (2020).

17. Blommaert, M. A., Subramanian, S., Yang, K., Smith, W. A. & Vermaas, D. A. High Indirect Energy Consumption in AEM-Based CO_2 Electrolyzers Demonstrates the Potential of Bipolar Membranes. *ACS Applied Materials & Interfaces,* 557–563.

18. Sata, T. & Jones, G. N. *Ion Exchange Membranes* X001–X004. ISBN: 978-0-85404-590-7 (The Royal Society of Chemistry, 2004).

19. Donnan, F. G. Theorie der Membrangleichgewichte und Membranpotentiale bei Vorhandensein von nicht dialysierenden Elektrolyten. Ein Beitrag zur physikalisch-chemischen Physiologie. *Zeitschrift für Elektrochemie und angewandte physikalische Chemie* **17,** 572–581 (1911).

20. Molau, G. E. Heterogeneous ion-exchange membranes. *Journal of Membrane Science* **8,** 309–330 (1981).

21. Tufa, R. A. *et al.* Bipolar Membrane and Interface Materials for Electrochemical Energy Systems. *ACS Applied Energy Materials* **4,** 7419–7439 (2021).

22. Dischinger, S. M., Gupta, S., Carter, B. M. & Miller, D. J. Transport of Neutral and Charged Solutes in Imidazolium-Functionalized Poly(phenylene oxide) Membranes for Artificial Photosynthesis. *Industrial & Engineering Chemistry Research* **59,** 5257–5266 (2020).

23. Stenina, I., Golubenko, D., Nikonenko, V. & Yaroslavtsev, A. Selectivity of Transport Processes in Ion-Exchange Membranes: Relationship with the Structure and Methods for Its Improvement. *International Journal of Molecular Sciences* **21** (2020).

24. Galama, A. H., Post, J. W., Cohen Stuart, M. A. & Biesheuvel, P. M. Validity of the Boltzmann equation to describe Donnan equilibrium at the membrane–solution interface. *Journal of Membrane Science* **442,** 131–139 (2013).

25. Geise, G. M., Hickner, M. A. & Logan, B. E. Ionic Resistance and Permselectivity Tradeoffs in Anion Exchange Membranes. *ACS Applied Materials & Interfaces* **5,** 10294–10301 (2013).

26. Kingsbury, R. S., Wang, J. & Coronell, O. Comparison of water and salt transport properties of ion exchange, reverse osmosis, and nanofiltration membranes for desalination and energy applications. *Journal of Membrane Science* **604,** 117998 (2020).

27. Kitto, D. & Kamcev, J. The need for ion-exchange membranes with high charge densities. *Journal of Membrane Science* **677,** 121608 (2023).

28. Daniilidis, A., Vermaas, D. A., Herber, R. & Nijmeijer, K. Experimentally obtainable energy from mixing river water, seawater or brines with reverse electrodialysis. *Renewable Energy* **64,** 123–131 (2014).

29. Abidin, M. N. Z., Nasef, M. M. & Veerman, J. Towards the development of new generation of ion exchange membranes for reverse electrodialysis: A review. *Desalination* **537,** 115854 (2022).

30. Yaroslavtsev, A. B. & Stenina, I. A. Current progress in membranes for fuel cells and reverse electrodialysis. *Mendeleev Communications* **31,** 423–432 (2021).

31. Gubler, L. Membranes and separators for redox flow batteries. *Current Opinion in Electrochemistry* **18,** 31–36 (2019).

32. Machado, C. A. *et al.* Redox Flow Battery Membranes: Improving Battery Performance by Leveraging Structure–Property Relationships. *ACS Energy Letters* **6,** 158–176 (2021).

33. Salvatore, D. A. *et al.* Designing anion exchange membranes for CO_2 electrolysers. *Nature Energy* **6,** 339–348 (2021).

34. Garg, S., Giron Rodriguez, C. A., Rufford, T. E., Varcoe, J. R. & Seger, B. How membrane characteristics influence the performance of CO_2 and CO electrolysis. *Energy & Environmental Science* **15,** 4440–4469 (2022).

35. Zhang, Z., Wen, L. & Jiang, L. Nanofluidics for osmotic energy conversion. *Nature Reviews Materials* **6,** 622–639 (2021).

36. Merle, G., Wessling, M. & Nijmeijer, K. Anion exchange membranes for alkaline fuel cells: A review. *Journal of Membrane Science* **377,** 1–35 (2011).

37. Ghalloussi, R. *et al.* Ageing of ion-exchange membranes in electrodialysis: A structural and physicochemical investigation. *Journal of Membrane Science* **436,** 68–78 (2013).

38. Wang, L. *et al.* Fundamental transport mechanisms, fabrication and potential applications of nanoporous atomically thin membranes. *Nature Nanotechnology* **12,** 509–522 (2017).

39. Kayvani Fard, A. *et al.* Inorganic Membranes: Preparation and Application for Water Treatment and Desalination. eng. *Materials (Basel, Switzerland)* **11,** 74 (2018).

40. Rollings, R. C., Kuan, A. T. & Golovchenko, J. A. Ion selectivity of graphene nanopores. *Nature Communications* **7,** 11408 (2016).

41. Ishimatsu, R. *et al.* Ion-Selective Permeability of an Ultrathin Nanoporous Silicon Membrane as Probed by Scanning Electrochemical Microscopy Using Micropipet-Supported ITIES Tips. *Analytical Chemistry* **82,** 7127–7134 (2010).

42. Zhou, K., Perry, J. M. & Jacobson, S. C. Transport and Sensing in Nanofluidic Devices. *Annual Review of Analytical Chemistry* **4,** 321–341 (2011).

43. Vlassiouk, I., Kozel, T. R. & Siwy, Z. S. Biosensing with Nanofluidic Diodes. *Journal of the American Chemical Society* **131,** 8211–8220 (2009).

44. Ghosh, M., Jorissen, K. F. A., Wood, J. A. & Lammertink, R. G. H. Ion Transport through Perforated Graphene. *The Journal of Physical Chemistry Letters* **9,** 6339–6344 (2018).

45. Lebedev, D. *et al.* Focused ion beam milling based formation of nanochannels in silicon-glass microfluidic chips for the study of ion transport. *Microfluidics and Nanofluidics* **25,** 51 (2021).

46. Xiao, K. *et al.* A Tunable Ionic Diode Based on a Biomimetic Structure-Tailorable Nanochannel. *Angewandte Chemie International Edition* **56,** 8168–8172 (2017).

47. Ali, M. *et al.* Single Cigar-Shaped Nanopores Functionalized with Amphoteric Amino Acid Chains: Experimental and Theoretical Characterization. *ACS Nano* **6,** 3631–3640 (2012).

48. Lee, M.-Y. *et al.* Current achievements and the future direction of electrochemical CO_2 reduction: A short review. *Critical Reviews in Environmental Science and Technology* **50,** 769–815 (2020).

49. Li, A. P., Müller, F., Birner, A., Nielsch, K. & Gösele, U. Hexagonal pore arrays with a 50–420 nm interpore distance formed by self-organization in anodic alumina. *Journal of Applied Physics* **84,** 6023–6026 (1998).

50. Kim, D.-K., Duan, C., Chen, Y.-F. & Majumdar, A. Power generation from concentration gradient by reverse electrodialysis in ion-selective nanochannels. *Microfluidics and Nanofluidics* **9,** 1215–1224 (2010).

51. Kim, J., Kim, S. J. & Kim, D.-K. Energy harvesting from salinity gradient by reverse electrodialysis with anodic alumina nanopores. *Energy* **51,** 413–421 (2013).

52. Lee, Y., Kim, H. J. & Kim, D.-K. *Power Generation from Concentration Gradient by Reverse Electrodialysis in Anisotropic Nanoporous Anodic Aluminum Oxide Membranes* 2020.

53. Ryzhkov, I. I., Lebedev, D. V., Solodovnichenko, V. S., Minakov, A. V. & Simunin, M. M. On the origin of membrane potential in membranes with polarizable nanopores. *Journal of Membrane Science* **549,** 616–630 (2018).

54. Stern, O. ZUR THEORIE DER ELEKTROLYTISCHEN DOPPELSCHICHT. *Zeitschrift für Elektrochemie und angewandte physikalische Chemie* **30,** 508–516 (1924).

55. Braus, M. J. *'The theory of electrolytes. I. Freezing point depression and related phenomena' (Debye & Hückel, 1923)* in (2019).

56. Bocquet, L. & Charlaix, E. Nanofluidics, from bulk to interfaces. *Chemical Society Reviews* **39,** 1073–1095 (2010).

57. Poggioli, A. R., Siria, A. & Bocquet, L. Beyond the Tradeoff: Dynamic Selectivity in Ionic Transport and Current Rectification. *The Journal of Physical Chemistry B* **123,** 1171–1185 (2019).

58. in. *Solid-Liquid Interfaces* (ed Lyklema, J. B. T.) 3–232 (Academic Press, 1995). ISBN: 1874-5679.

59. Reyes Bahena, J. L., Robledo Cabrera, A., López Valdivieso, A. & Herrera Urbina, R. Fluoride adsorption onto α-Al_2O_3 and its effect on the zeta potential at the alumina–aqueous electrolyte interface. *Separation Science and Technology* **37,** 1973–1987 (2002).

60. Butt, H.-J., Graf, K. & Kappl, M. in *Physics and Chemistry of Interfaces* 42–56 (2003). ISBN: 9783527602315.

61. Morrison, F. A. & Osterle, J. F. Electrokinetic Energy Conversion in Ultrafine Capillaries. *The Journal of Chemical Physics* **43,** 2111–2115 (1965).

62. Masliyah, J. & Bhattacharjee, S. in *Electrokinetic and Colloid Transport Phenomena* 537–611 (2006). ISBN: 9780471799740.

63. Ryzhkov, I. I., Vyatkin, A. S. & Mikhlina, E. V. Modelling of Conductive Nanoporous Membranes with Switchable Ionic Selectivity. *Membranes and Membrane Technologies* **2,** 10–19 (2020).

64. Hartkamp, R. *et al.* Measuring surface charge: Why experimental characterization and molecular modeling should be coupled. *Current Opinion in Colloid & Interface Science* **37,** 101–114 (2018).

65. Veerman, J., de Jong, R. M., Saakes, M., Metz, S. J. & Harmsen, G. J. Reverse electrodialysis: Comparison of six commercial membrane pairs on the thermodynamic efficiency and power density. *Journal of Membrane Science* **343,** 7–15 (2009).

66. Liu, Z., Yang, H., Kutz, R. & Masel, R. I. CO_2 Electrolysis to CO and O_2 at High Selectivity, Stability and Efficiency Using Sustainion Membranes. *Journal of The Electrochemical Society* **165,** J3371–J3377 (2018).

67. Novak, S. & Kalin, M. The Effect of pH on the Wear of Water-Lubricated Alumina and Zirconia Ceramics. *Tribology Letters* **17,** 727–732 (2004).

68. Choudhary, R., Khurana, D., Kumar, A. & Subudhi, S. Stability analysis of Al_2O_3 / water nanofluids. *Journal of Experimental Nanoscience* **12,** 140–151 (2017).

69. Döpke, M. F. & Hartkamp, R. The importance of specifically adsorbed ions for electrokinetic phenomena: Bridging the gap between experiments and MD simulations. *The Journal of Chemical Physics* **154,** 94701 (2021).

70. Hartkamp, R., Siboulet, B., Dufrêche, J.-F. & Coasne, B. Ion-specific adsorption and electroosmosis in charged amorphous porous silica. *Physical Chemistry Chemical Physics* **17,** 24683–24695 (2015).

71. Ryzhkov, I. I., Shchurkina, M. A., Mikhlina, E. V., Simunin, M. M. & Nemtsev, I. V. Switchable ionic selectivity of membranes with electrically conductive surface: Theory and experiment. *Electrochimica Acta* **375,** 137970 (2021).

72. Nishizawa, M., Menon, V. P. & Martin, C. R. Metal Nanotubule Membranes with Electrochemically Switchable Ion-Transport Selectivity. *Science* **268,** 700–702 (1995).

73. Kapitonov, A. A. & Ryzhkov, I. I. Modelling the Performance of Electrically Conductive Nanofiltration Membranes. *Membranes* **13,** 596 (2023).

74. Zhang, Z. *et al.* Mechanically strong MXene/Kevlar nanofiber composite membranes as high-performance nanofluidic osmotic power generators. *Nature Communications* **10,** 2920 (2019).

75. Aixalà-Perelló, A. *et al.* Scalable and highly selective graphene-based ion-exchange membranes with tunable permselectivity. *npj 2D Materials and Applications* **7,** 46 (2023).

76. Cao, L. *et al.* Towards understanding the nanofluidic reverse electrodialysis system: well matched charge selectivity and ionic composition. *Energy & Environmental Science* **4,** 2259–2266 (2011).

77. Md Jani, A. M., Losic, D. & Voelcker, N. H. Nanoporous anodic aluminium oxide: Advances in surface engineering and emerging applications. *Progress in Materials Science* **58,** 636–704 (2013).

78. Jeong, J. & Hwang, W. Communication—Facile and Rapid Fabrication of Highly Oleophobic Surfaces with Anodized Alumina Nanofiber and Nanoparticles. *Journal of The Electrochemical Society* **164,** E158 (2017).

79. Al-Harbi, T., Al-Hazmi, F. & Mahmoud, W. E. Synthesis and characterization of nanoporous silica film via non-surfactant template sol–gel technique. *Superlattices and Microstructures* **52,** 643–647 (2012).

80. Zhao, D. *et al.* Triblock Copolymer Syntheses of Mesoporous Silica with Periodic 50 to 300 Angstrom Pores. *Science* **279,** 548–552 (1998).

81. Schaep, J., Vandecasteele, C., Leysen, R. & Doyen, W. Salt retention of Zirfon® membranes. *Separation and Purification Technology* **14,** 127–131 (1998).

82. Petukhov, D. I., Buldakov, D. A., Tishkin, A. A., Lukashin, A. V. & Eliseev, A. A. Liquid permeation and chemical stability of anodic alumina membranes. eng. *Beilstein journal of nanotechnology* **8,** 561–570 (2017).

83. Lee, S. W., Shang, H., Haasch, R. T., Petrova, V. & Lee, G. U. Transport and functional behaviour of poly(ethylene glycol)-modified nanoporous alumina membranes. *Nanotechnology* **16,** 1335–1340 (2005).

2.6. SUPPORTING INFORMATION

MEMBRANE CHARACTERIZATION

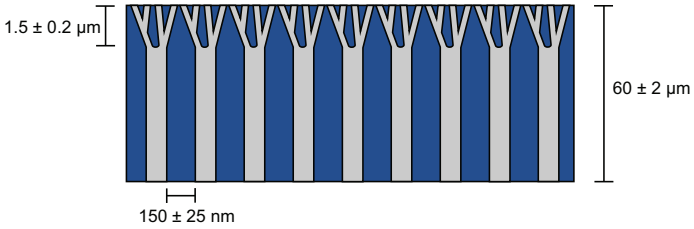

Figure S2.1: Schematic illustration of branched structure in asymmetric AAO membranes. The pore size at the top of the active layer is (2-4) ± 1 and 5 ± 2 nm.

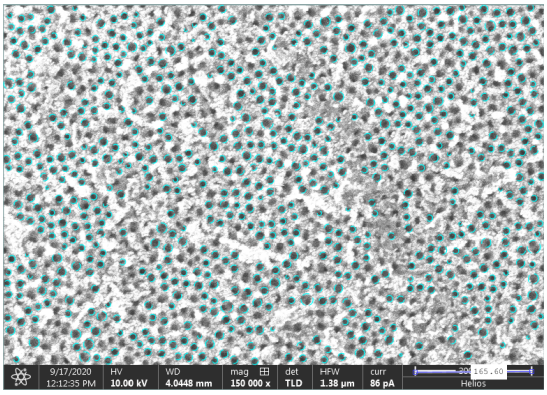

Figure S2.2: Pore detection on SEM image using CircleFinder tool in MatLab.

The circle finder tool in MatLab was used to determine the pore sizes in the SEM images (Figure S2.2). This gave the size of each circle in pixels and the scale bar was used to convert the pixels to nm. The few largest circles were not considered in the distribution, since in a few cases the circle finder considers two pores as one.

Figure S2.2 shows the procedure to determine the pore size distribution from the TEM images. The clear pores were first traced and then horizontal strokes were intersected with the traced line. The length in pixels of each of these lines was taken as the pore size. The 200 nm scale was used to convert pixels to nm.

Figures S2.4a and b show the result from the N_2 adsorption experiments onto the AAO membranes, described in section 2.3.2. Figure S2.4c shows the fitting of the cumulative pore volume which was then used to obtain the pore size distribution shown in Figure S2.4d. From the obtained pore size distribution, only the values up to 22 nm were considered. Since the AAO membranes had to be broken in order to insert in the equipment, it was considered that higher values could have been caused by cracks during the sample preparation. Moreover, it was obtained by fitting the cumulative pore volume which is more accurate in the lower range, the higher values could carry a significant error.

We also measured the water permeability of our membranes. This was performed by adding two thin pieces of transparent tubing to the each of the two compartments if the setup shown in Figure

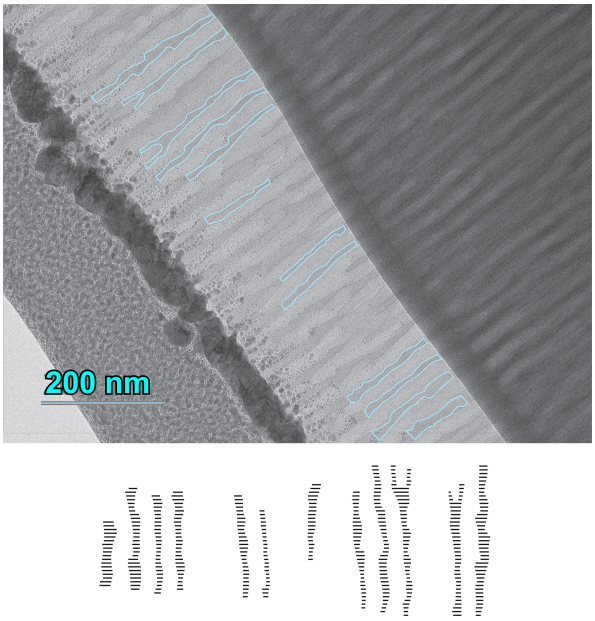

Figure S2.3: Pore size determination from TEM microscopy image. a) step 1, pore tracing. b) step 2, length determination.

2.2a. Water was then pumped into the setup so that the water level in the two tubes is different, and the inlets and outlets were closed off. A camera was set in front of the transparent tubing to monitor the water level change over time. As the pressure difference in the two compartments drives the water through the membrane, the water in the tubing slowly reaches the same level. By measuring the height difference we calculate the pressure difference in the two compartments, and by measuring the time and water level change we can estimate the water flow through the membrane. With this information we can use Darcy's law to estimate the permeability, or use the Van 't Hoff equation to convert this pressure difference into an estimated water concentration gradient and calculate a water diffusion coefficient, as described in [65]. A schematic of this setup is shown in Figure S2.5.

PARAMETERS USED FOR SIMULATIONS

The parameters used for the simulations in the ITM software are summarized in Table S2.1. Additionally, a Stern layer of 0.5 nm was considered, but since the boundary condition was the ζ-potential, which is measured at the shear plane, the Stern layer was then added to the pore size as a correction. The assumption behind this method is that no ion transport occurs through the Stern layer, which is stagnant.

EXPERIMENTAL DATA PLOTTED VS C_{low}

Figure S2.6 shows the data displayed in Figure 2.3b, against C_{low}.

ASYMMETRY OF THE MEMBRANES

On the bottom left of Figure S2.7, is the top of the AAO membrane. It can be observed, that the widen at the top. This can cause the pore size obtained from top-view images to be larger than reality.

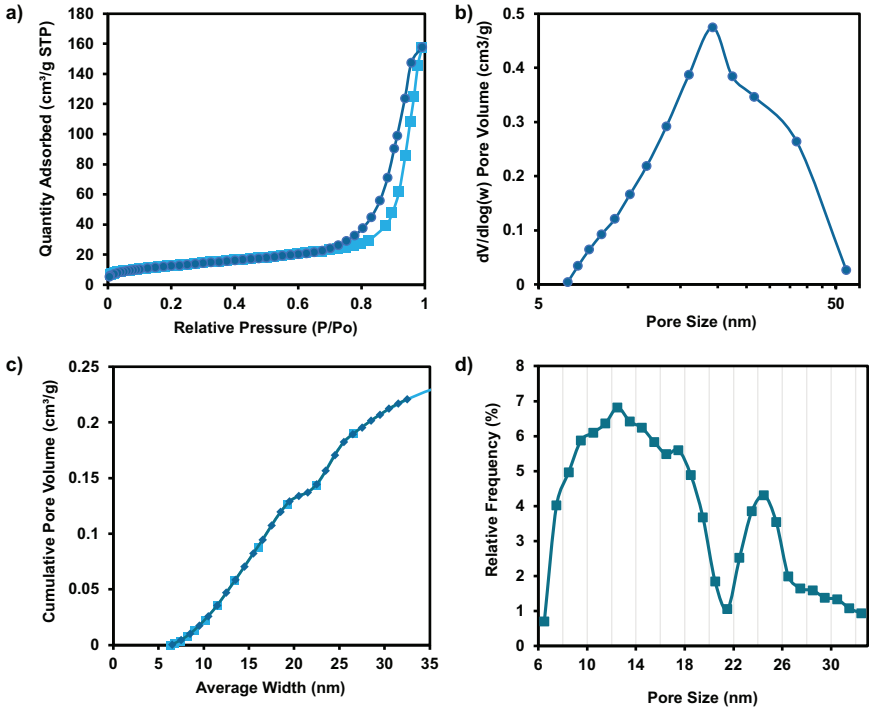

Figure S2.4: a) Adsorption (light squares) and desorption (dark circles) isotherms b) standard BJH plot based on the desorption curve c) cumulative pore volume based on the desorption curve (light squares) and respective fitting (dark diamonds) d) relative pore size frequency obtained based on the fitting of the cumulative pore volume.

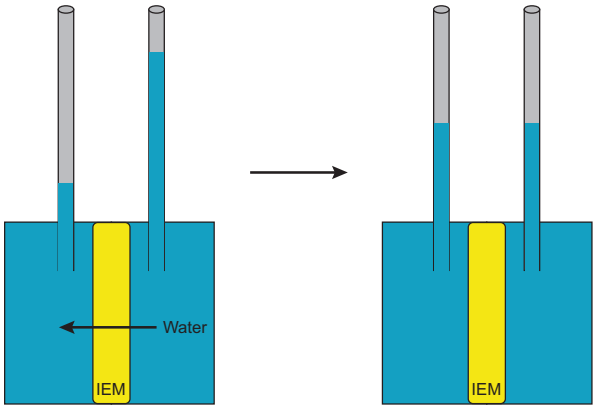

Figure S2.5: Schematic illustration of water permeability setup. Deionized water was used to fill both compartments and a camera was used to monitor the water level in the tubing over time.

Table S2.1: Variables and Parameters used in the ITM software for simulations.

Pore Size	Varied / fitted	2 to 50 nm / 6 nm
Pore Length	Varied	10 to 5000 nm
Surface Potential	Varied / fitted	35 to 50 mV / 40 mV
Electrolyte concentration	Varied	0.001 to 4 M
Temperature	Parameter	298.15 °K
Viscosity	Parameter	0.888×10-3 Pa.s
Relative Permittivity	Parameter	78.49
K^+ diffusion coefficient	Parameter	1.957×10^{-9} m^2/s
Cl^- diffusion coefficient	Parameter	2.032×10^{-9} m^2/s

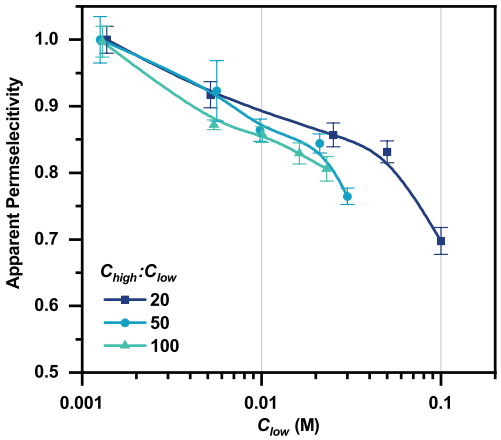

Figure S2.6: Apparent permselectivity results showcasing the effect of concentration and concentration ratio on permselectivity of the 10 nm pore sized AAO membrane, plotted against C_{low}. See vs C_{high} on Figure 2.3b.

Figure S2.8 shows the pictures taken with SEM, of the same AAO membrane, as it was delivered. The stark difference in contrast could be due to the imaging software, and not per se a significant difference in morphology, but the figure also shows an apparent pore size difference on the two sides of the membrane.

The contact angle is an indication for porosity, meaning while 20 nm pore sized AAO has more or less uniform pores throughout the membrane thickness, the 10 nm has quite a large difference on the two sides. In addition to the pore size and morphology shown on the SEM images, here it can be seen that the wettability is also different. Figure S2.9 shows that the 20 nm pore size is more uniform between the two sides.

COMPARISON OF SIMULATIONS AND EXPERIMENTAL DATA

Figure S2.10 shows the fitting of the membrane potential data when C_{low} is kept at 10 mM using a constant surface charge density in the ITM software. The fitting is poor in comparison to the fitting obtained when using a constant surface potential (Figure 2.5).

On Figure S2.11a, it can be observed that the simulations have a good level of agreement with the experimental data relating to the 20 nm and 50 nm pore sizes, but do not agree so well with the data relating to the 10 nm pore size (Figure S2.11a and b), especially at lower concentration ratios.

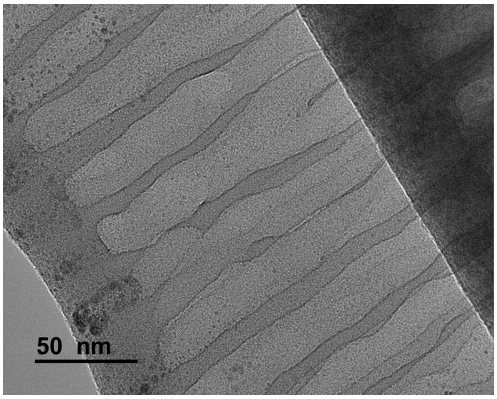

Figure S2.7: Zoom-in to the cross-section of the nanopores, close to the membrane surface. Image taken at 60k times magnification.

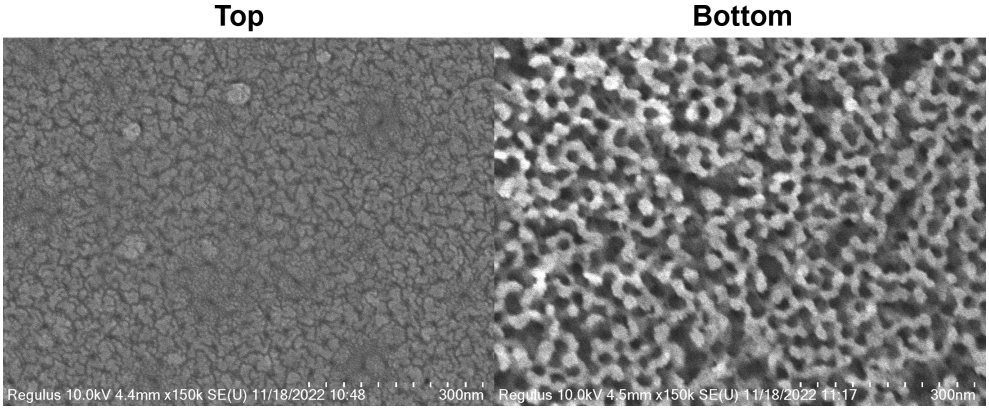

Figure S2.8: SEM pictures of the two different sides of an AAO membrane, as delivered.

ELECTRICAL POTENTIAL AND SURFACE CHARGE DENSITY PROFILES

Figure S2.12 shows the electric potential profile and surface charge density along the length of the pore. The membrane potential can be seen at $z = 1$, on Figure S2.12a. Figure S2.12b shows that the surface charge density is decreasing along the length of the pore, toward the low concentration side.

EFFECT OF MEMBRANE SURFACE

Figure S2.13 shows the effect on co-ion rejection of including charge on the surface of the membrane. It shows that the surface has a role in rejecting co-ions away from the entrances of the pore. Therefore, the co-ion concentration is lower close to the pore entrance in the case the charge of the surface is included.

Figure S2.14 shows the same 20 nm wide nanopore, but with increasing pore lengths. The result implies that the surface only has an impact for short pores. At 100 nm length, it no longer has an effect, which means that long pores ($L >> R_p$) are not affected by the surface of the membrane.

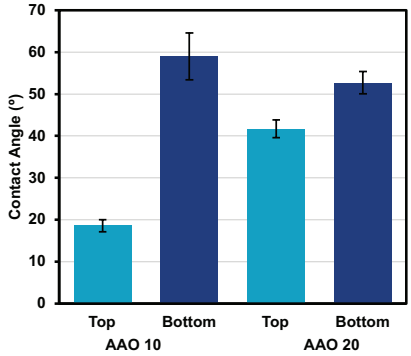

Figure S2.9: Contact angles of the two sides of AAO membranes with 10 nm and 20 nm pore sizes.

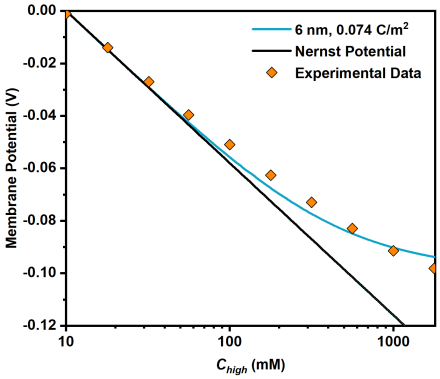

Figure S2.10: Membrane potential data fit with the ITM software, using a constant surface charge density of 0.074 C/m^2.

COMPARISON OF WHICH VARIABLE HAS LARGER IMPACT

Figure S2.16 shows that when plotted against the geometric average, the lines corresponding to different concentration ratios are nearly coincident. Therefore, it is the geometric mean of the low and high concentration sides that determines selectivity.

SIMULATING OPTIMAL PORE PROPERTIES

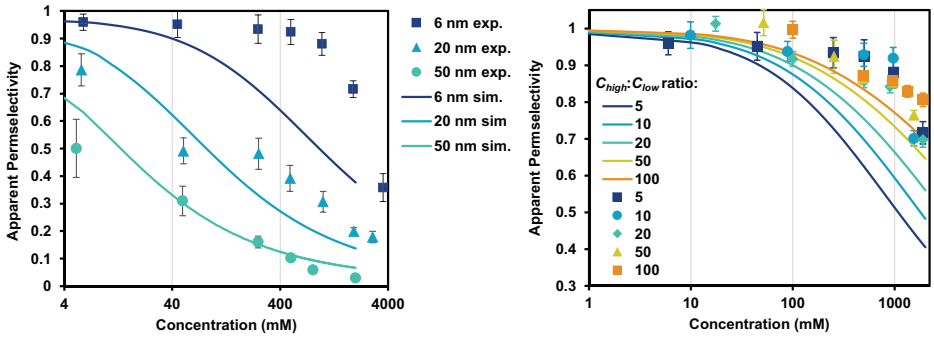

Figure S2.11: a) Comparison between pore size data and simulation. b) Comparison between concentration ratio data and simulations. Legend shows the C_{high}:C_{low} ratio, with the lines corresponding to the simulation results and the markers corresponding to the experimental data.

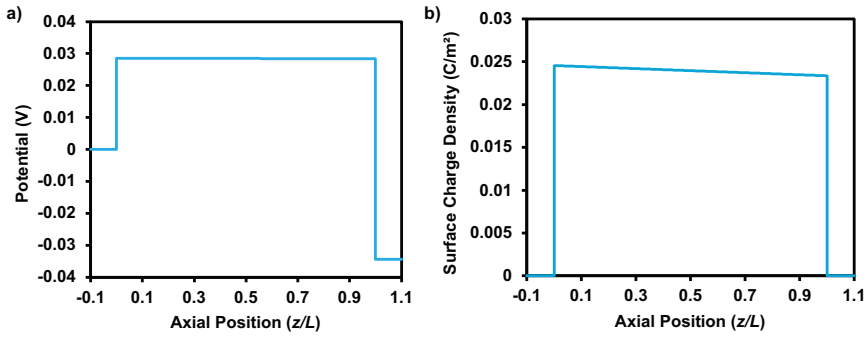

Figure S2.12: a) Electric potential profile along the length pore b) surface charge density along the length of the pore.

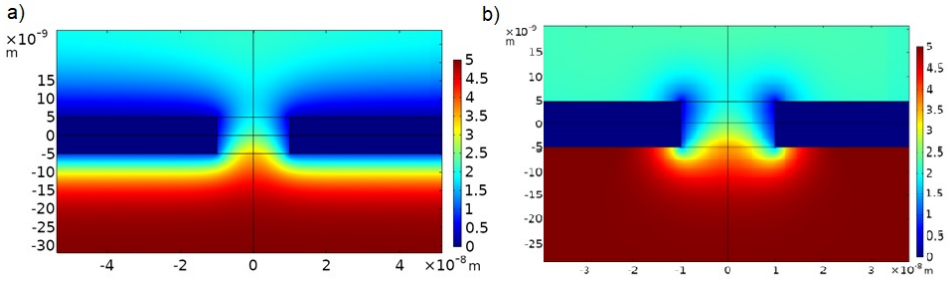

Figure S2.13: Co-ion profiles of 20 nm wide, 10 nm long pore between two reservoirs of 5 and 1 mM of KCl. The color scale shows the co-ion concentration in mM. a) entire membrane has a surface potential. b) only the pore walls have a surface potential of 45 mV.

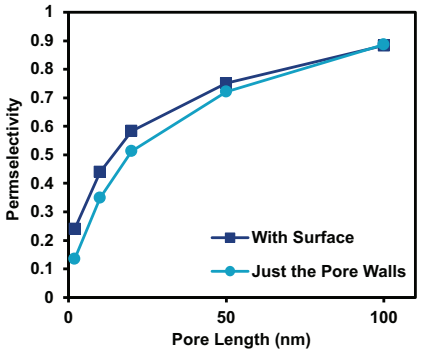

Figure S2.14: Simulated effect of presence of surface potential on the entire membrane vs pore length.

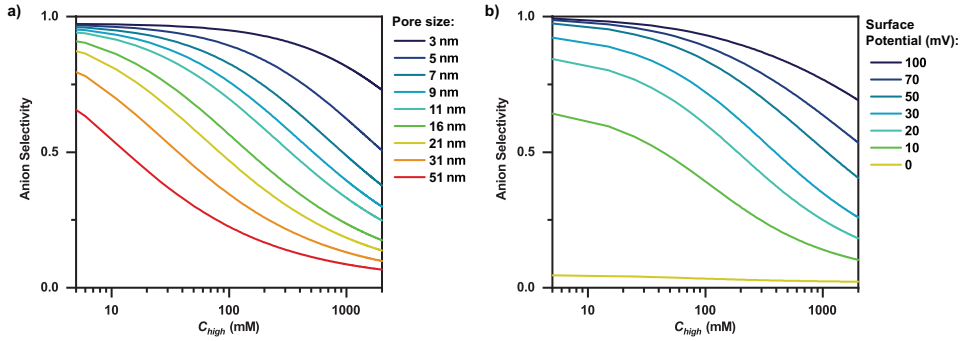

Figure S2.15: a) different pore sizes (shown in legend) vs C_{high} with 40 mV surface potential b) pore size of 7 nm but at different potentials (shown in legend) vs C_{high}.

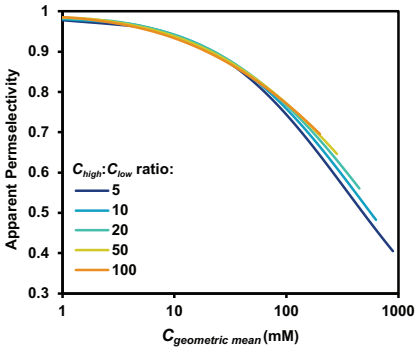

Figure S2.16: Different C_{high}:C_{low} ratios plotted vs the geometric mean of C_{high} and C_{low}.

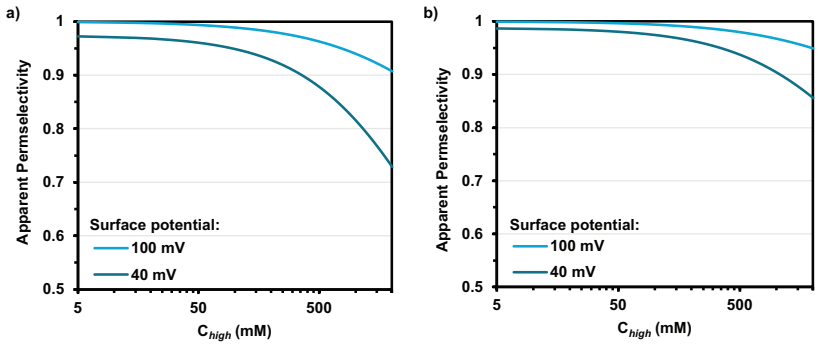

Figure S2.17: a) C_{high}:C_{low} ratio = 5 b) C_{high}:C_{low} ratio = 35 with different surface potentials. Pore size of 3 nm and pore length of 5 µm.

3

NANOFLUIDIC ION-EXCHANGE MEMBRANES: CAN THEIR CONDUCTANCE COMPETE WITH POLYMERIC ION-EXCHANGE MEMBRANES?

Nanofluidic membranes (NFMs) are becoming increasingly recognized as viable alternatives to traditional ion-exchange membranes, because of their distinct selectivity mechanism, which does not rely on functional groups on a polymeric backbone but rather on charged nanopores that allow straight ion-conductive pathways for efficient ion transport. We measured the conductivity of commercial anodized aluminum oxide membranes with different pore sizes under different current densities and electrolyte concentrations. We also simulated a nanopore channel with charged walls between two electrolyte reservoirs. Our findings indicate that electrolyte concentration is the main parameter that determines NFM conductivity, with a linear dependence at least up to 1 M. Our study shows that the optimal pore length is between 0.5 to 5 µm considering the trade-off between selectivity and conductance. On the other hand, the conductance is not sensitive to the pore diameter. Conical nanopores are a way to increase conductance, but according to our results, this increase comes at the expense of selectivity. Our findings suggest that NFMs can outperform polymeric ion-exchange membranes in certain electrochemical applications, such as reverse electrodialysis, but not in applications that use low electrolyte concentrations on both sides of the membrane.

Parts of this chapter have been submitted for publication as "Nanofluidic ion-exchange membranes: can their conductance compete with polymeric ion-exchange membranes?" by K.V. Petrov, JW. Hurkmans, R. Hartkamp, D.A. Vermaas.

3.1. INTRODUCTION

With the pressing need to reduce our reliance on fossil fuels and mitigate the environmental impact of traditional industrial processes, electrochemical membrane technologies have taken center stage in addressing these multifaceted challenges.[1–3] Ion-exchange membranes (IEMs), are a key component for technologies such as the chlor-alkali process,[4] fuel cells,[5] electrodialysis and redox-flow batteries,[6, 7] due to their ability to selectively transport ions.

IEMs are usually thin films (100 µm) of a polymeric backbone structure with charged functional groups, which are responsible for the ion-selectivity.[8, 9] These polymeric materials offer several advantages, including flexibility, cost-effectiveness, and ease of fabrication. However, they do present certain intrinsic issues, such as swelling of the backbone structure, which leads to a limited charge density and a trade-off between conductivity and selectivity.[10, 11] Most IEMs have a fixed charge density of 0.5 to 3 M, which limits their selectivity, especially in at high electrolyte concentrations.[12] Additionally, the interstitial space within the dense polymeric structure where ion transport takes place, are often comparable in size to the ions themselves (Figure 3.1a). As a result, tortuosity and electrostatic effects cause a high resistance to ion transport in polymeric IEMs.[13–15] These drawbacks hinder the scale-up possibilities of technologies such as reverse electrodialysis (RED), redox flow batteries, and CO_2 electrolysis.[16–20]

Nanofluidic membranes (NFMs) have recently gained attention as an alternative to polymeric IEMs.[13, 21] They are made from inorganic materials, with nanopores typically between 1 and 20 nm in size. Since this size is in of the same order of magnitude as the electrical double layer thickness, the fluid will have a non-zero charge density throughout the pore due to electric double layer overlap.[22] This overlap causes an increased (Donnan) potential within the pore, which is responsible for rejecting co-ions (ions with the same charge as the pore surface) and allowing counter-ions (oppositely charged) to permeate.[23] Because of their inorganic nature, NFMs do not suffer from the swelling issues that IEMs have. The pores in NFMs are much larger than the ion size, which promotes ion transport, and the ionic pathway can be optimized to increase ionic conductivity.[13]

In Chapter 2 we, and previous,[24, 25] works have shown that NFMs can achieve a good ion-selectivity, if optimized. However, little is known about what parameters enhance their conductivity. Nanofluidics literature often uses single nanochannels showing ionic resistances in the $k\Omega cm^2$ range, which is too high to be applied in practical electrochemical applications. NFMs have seen development, mostly for power generation through RED, which has slightly decreased their ionic resistance.[26, 27] Graphene oxide (GO) membranes are an example of a material that has recently been developed to exhibit ionic resistance as low as 3.9 Ωcm^2.[28] However, GO membranes are made of stacked 2D sheets, which leads to a non-optimal and tortuous ionic pathway (Figure 3.1b) and makes it harder to optimize the trade-off between selectivity and conductance. Cylindrical nanopores that directly connect one side of the membrane to the other have promise to further reduce ionic resistance, since this geometry allows the ions to travel the shortest path (Figure 3.1c).[13]

In this work, we study the conductivity of nanofluidic membranes under different operational parameters, such as current density and electrolyte concentration. We use anodized aluminum oxide (AAO) membranes with different pore sizes and a Poisson-Nernst-Planck model to better understand the conductivity of nanofluidic membranes. AAO is a commercial material with a dense array of cylindrical nanopores, which make it an ideal model material to study NFMs. We examine and discuss their potential for practical applications.

3.2. METHODS

3.2.1. EXPERIMENTAL METHODS

This section describes the measurements of the ionic resistance of AAO membrane discs with a diameter of 1.3 ± 0.1 cm, a thickness of 50 µm, and an array of cylindrical nanopores with differ-

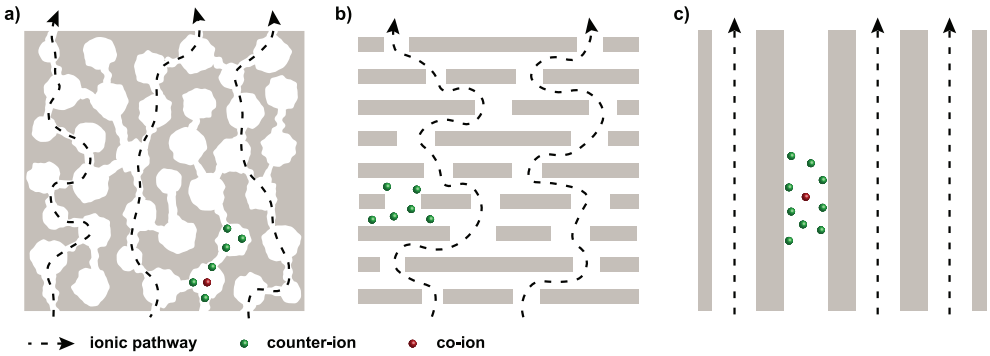

Figure 3.1: Schematic illustration of ion transport through the cross-section of a) polymeric IEMs, according to the microheterogeneous model,15 b) GO membranes and c) NFMs with cylindrical nanopores. The membrane structure is in grey, and the edges are charged surfaces.

ent pore sizes (InRedox, Colorado, USA), in different KCl concentrations. The membranes act as an anion-exchange membrane (AEM) at neutral pH, and their detailed characterization can be found in Chapter 2. We found that these membranes have a low effective porosity due to the non-uniform size and convergence and divergence of numerous nanochannels along their length, resulting in dead-end pores and a lack of direct connection between the two sides of the membrane. Additionally, our characterization of the AAO membranes revealed a wider pore size distribution than provided by the supplier, with the effective pore size being 8 nm for the samples labeled as 10 nm.

The ionic resistance was measured in a 6-compartment, 4-electrode setup, as illustrated in Figure 3.2a. In this setup, two platinum-coated titanium electrodes were used to apply a current over the whole setup (in compartments 1 and 6), and two double-junction Ag/AgCl electrodes were connected to Luggin capillaries, placed very close (< 0.5 mm) to the membrane. The latter electrodes allowed the measurement of membrane potential, which was corrected by a blank measurement, without a membrane, after every experiment. Each compartment has a volume of approximately 130 mL and the electrolyte within was kept flowing at 40 mL/min to mitigate concentration polarization. 0.1 M K_2SO_4 was flowed in compartments 1 and 6 to avoid any undesired Faradaic reactions – only the hydrogen and oxygen evolution reactions occurred. Since these reactions produce OH^- and H^+, respectively, a buffer solution (0.1 M K_2PO_4) was flowed in compartments 2 and 5. In compartments 3 and 4, KCl solutions were circulated, and the respective concentrations are stated along with the results. The AAO membranes were placed in a holder with 0.64 cm^2 of open area, between two flat O-rings. Cation-exchange membranes were placed between the remaining compartments, since the cation is the same in the whole setup, and anion crossover should be avoided. Current was applied and the voltage was measured using an Autolab PGSTAT 128 N potentiostat (Metrohm, Switzerland).

Since the resistance was dependent on the applied current, it was measured using the current interrupt method.[29] A constant current was applied for 300 seconds, to observe a stable voltage, and then it was set to 0. The immediate voltage drop corresponds to the ohmic resistance. The resistance value was then simply calculated by Ohm's law, using the difference between average voltage of the last 30-60 seconds and the voltage value right after interrupt (very close to 0), and the applied current. Positive currents were measured first, followed by a re-equilibration time of at least 2 hours with the electrolyte solutions, after which the negative currents were measured.

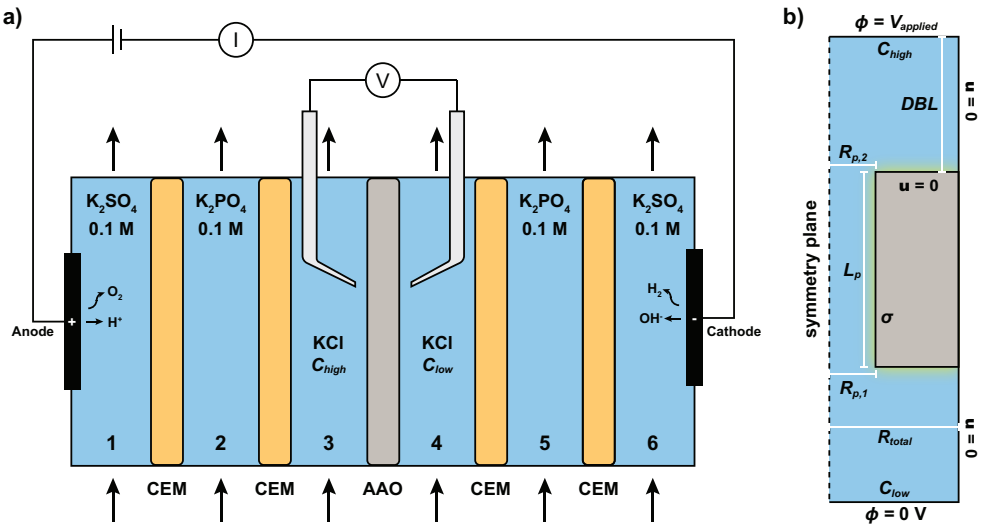

Figure 3.2: a) Schematic illustration of the 6-compartment setup used for electrical resistance measurements, b) geometry modelled in COMSOL Multiphysics

3.2.2. SIMULATIONS

This section describes the modelling methods, governing equations, and assumptions used to implement the space-charge model (also known as the Poisson-Nernst-Planck theory), used to describe ionic transport through a cylindrical nanopore. The modeled geometry consists of two electrolyte compartments separated by a single nanopore, as shown in Figure 3.2b.

The system is modeled as a continuum system with the Poisson-Nernst-Planck (PNP) theory coupled to the Navier-Stokes equation. The model has been implemented in COMSOL Multiphysics 5.6.

Through assumption of a dilute electrolyte, the transport of dissolved species is modelled through the steady-state Nernst-Planck equation:

$$\nabla \cdot \left(-D_i \nabla c_i - D_i \frac{z_i e}{k_B T} c_i \nabla \phi + c_i u \right) = 0 \tag{3.1}$$

Whereby D_i is the diffusion coefficient, c_i the concentration and z_i the valence of species i, k_B is Boltzmann's constant, e is the elementary charge, T is the temperature, ϕ is the electrolytic potential and u is the velocity field. The electrostatic potential ϕ is resolved through the Poisson equation:

$$-\varepsilon \varepsilon_0 \nabla^2 \phi = \rho_e \tag{3.2}$$

Here, ε is the relative permittivity, ε_0 is the vacuum permittivity and ρ_e is the charge density of the solution, defined as $\rho_e = c_{K^+} - c_{Cl^-}$ for the binary system under investigation. The velocity field is simulated through the Navier-Stokes equations for an incompressible Newtonian fluid which has been reduced to the steady-state Stokes equation since inertial effects on the length scales of a single nanopore are near zero. A Coulombic body force is added to account for electro-osmotic flow:

$$\mu \nabla^2 u - \nabla p + \rho_e E = 0 \tag{3.3}$$

Here, μ is the dynamic viscosity, p is the pressure and E is the electric field, which can be expressed as $-\nabla\phi$. Conservation of mass is ensured through the continuity equation:

$$\nabla \cdot u = 0 \tag{3.4}$$

The axisymmetric computational domain (Figure 3.2b) consists of two reservoirs containing KCl electrolyte, separated by a nanopore of length L_p. The nanopore can be varied between a cylindrical pore with radius R_p ($R_{p,1} = R_{p,2}$) or a conical pore, with $R_{p,1} < Rp,2$, where $R_{p,1}$ and $R_{p,2}$ are the radii at the outer ends of the channel. The electrolyte concentrations are fixed at their bulk concentrations ($c_i = c_{i,0}$) at the extremities of the electrolyte compartments. These boundaries are positioned at 10 µm away from the nanoporous membrane. This is a realistic thickness for the diffusion boundary layer (DBL) in flow applications (especially when a spacer is used) and is sufficiently far away to ensure electroneutrality. An external electric field is applied over the membrane by setting the electrostatic potential at these far-end boundaries as $\phi = V_{applied}$ and $\phi_L = 0$. The non-solid boundaries orthogonal to the membrane surface (on the right side in Figure 3.2b) are sufficiently far-away from the nanopore to prevent edge effects ($R_{total} >> R_{pore}$), with R_{total} also serving as a lever to obtain desired membrane porosity . At these boundaries, zero charge is enforced ($\nabla \cdot D = 0$, where D is the electric displacement field), and a no-flux boundary was also employed to ensure a constant DBL thickness.

At the interface of the membrane surface and the electrolyte, a surface charge density (σ_S) is defined. Although many models use σ_S as a fitting parameter, this simplification can reduce the accuracy of the model since σ_S depends on the local electrolyte concentration and on also the pore size due to double layer overlap, which are parameters that may vary along the pore length. Therefore, we followed the work of Berg and Ladipo,[30] who derived an analytical solution for the Poisson-Boltzmann equation and σ_S. They assumed that the surface charge density is entirely screened by counter-ions, which is a reasonable assumption for highly charged surfaces ($\phi_0 > \frac{e}{k_B T}$). In this way, the surface charge was defined as:

$$\sigma_S = \frac{4\frac{\varepsilon\varepsilon_0 k_B T}{eR_p}\left[1 - exp\left(-\frac{e\phi_0}{2k_B T}\right)\right]}{2 - exp\left(-\frac{e\phi_0}{2k_B T}\right)} \tag{3.5}$$

where ϕ_0 is the surface potential, for which we used the ζ-potential value for aluminum oxide in neutral solutions (40 mV).[31, 32] By assuming the ζ-potential as the boundary potential, the modeled boundary is located at the shear plane and the model does not solve for the Stern layer. The underlying assumption is that no ion transport occurs through the Stern layer,[33] which we assume to have a thickness of 0.5 nm and use a correction to the modelled pore size.

For the fluid flow, the outer ends of the electrolyte compartments are set at atmospheric pressure, thereby preventing pressure- driven flow through the nanopores. No-slip boundary conditions ($u = 0$) and no-flux boundary conditions are employed for the fluid and species transport at the pore surface, since it is assumed to be impermeable ($-n \cdot J_i = 0$).

We varied the pore radii ($R_{p,1}$ and $R_{p,2}$), pore length (L_p), electrolyte concentrations (C_{high} and C_{low}), surface potential (ϕ_0), and porosity. Pores smaller than 5 nm were not simulated because the continuum approach likely would not hold for lower values.[22, 33] The base conditions were with a pore size of 8 nm (7 nm effectively due to the Stern layer), a pore length of 1 µm, a surface potential of 40 mV, a porosity of 12 %, a DBL thickness of 10 µm, and either 50 mM KCl on both sides of the membrane or 10 mM on one side and 50 mM on the other side. The parameters were varied one at a time, keeping the remaining ones constant. The current-voltage data (minimum 15 points) was fit in MATLAB using a 3rd degree polynomial function, and its first derivative was taken as the ionic resistance.

3.3. RESULTS AND DISCUSSION

3.3.1. AXIAL PROFILES

To gain insight into the selectivity mechanism and the entrance effects, we simulated a pore with an 8 nm diameter and 50 nm length, with a 40 mV surface potential, between two compartments of 50 mM concentration, and plotted the concentration, potential and ion flux profiles along the pore length (Figure 3.3). For clarity, Figure 3.3a shows the cross-section of a nanopore, the normalized z/L_{pore} position, and the direction of the most significant migration and diffusion contributions of both ion species when a positive potential is applied across the anion-selective nanopore.

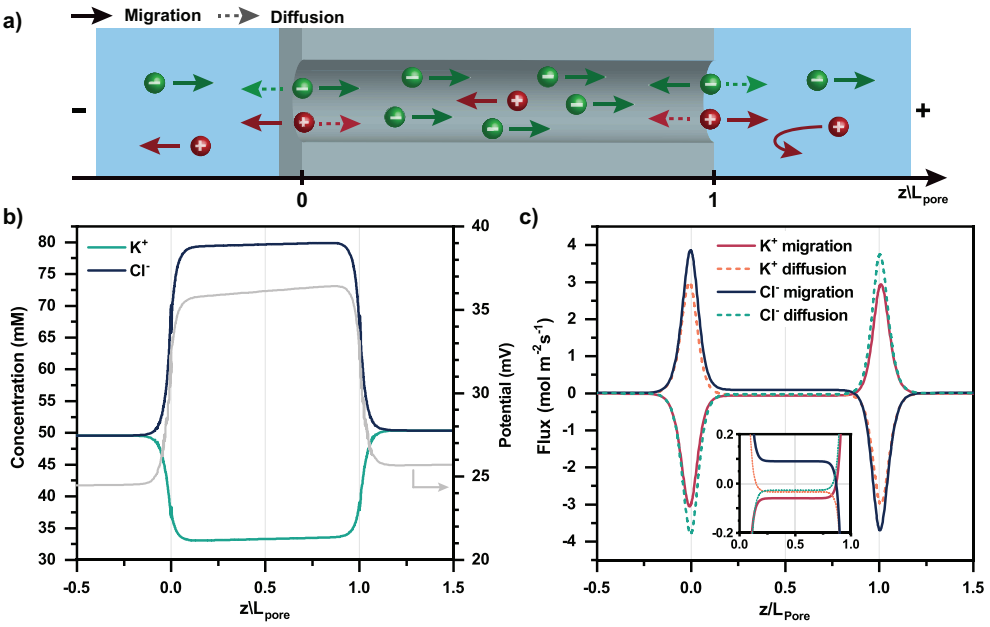

Figure 3.3: Simulations for an 8 nm in diameter and 50 nm in length pore with a 40 mV ζ-potential at 0.05 V applied potential. The pore was placed between two compartments with 50 mM solution. a) schematic illustration showing the anion-selective nanopore, the z/L_{pore} position and the direction of ion migration under positive potentials ($V_{applied}$), b) average concentration and potential (grey line, secondary axis) within the pore, and c) flux contributions of diffusion and migration in the z-direction for K^+ and Cl^- ions. The insert shows a zoom-in on the fluxes within the pore.

Figure 3.3b shows a clear Donnan potential at the entrance and exit of the pore, and a corresponding abrupt increase in counter-ion concentration and decrease in co-ion concentration. This Donnan potential is responsible for the selectivity, which means that the pore entrances have a significant role.23 Inside the pore, the concentration has a slight linear increase in the direction toward which Cl^- are migrating (more positive potentials).

Figure S3.11 depicts another important transport mechanism in NFMs, which is surface conductance. Surface conductance is related to the higher concentration of ions close to the pore wall, where the fluid is both more conductive and more selective, due to the increased local charge. In other words, when a driving force is applied across the NFM, ion migration preferentially occurs close to the pore walls.[34]

3.3.2. EFFECT OF CONCENTRATIONS

Figure 3.4a shows the experimentally obtained ionic resistances for the 10 nm pore sized AAO membranes. Firstly, the observed values, especially at low concentrations, are significantly higher than expected based on the pore geometry and initial modeling results. This is caused by the low effective porosity of the commercial AAO membranes. In Chapter 2 we saw that the nanopores contract, widen and even diverge and converge within the first few tens of nm from the surface, which means that most pores do not connect the two sides of the membrane as we show in Figure 3.1c. Figure 3.4b shows the simulated ionic resistance where the porosity of the membrane was used as a fitting parameter. The obtained porosity was 0.09 %, and it can be observed that the data fits well with experimental data, except for the peak around 0 mA/cm^2. A similar simulation but for 12 % porosity (realistic value for AAO membranes) can be found in Figure S3.2a. It shows that the ionic conductivity of these membranes can be improved by more than two orders of magnitude.

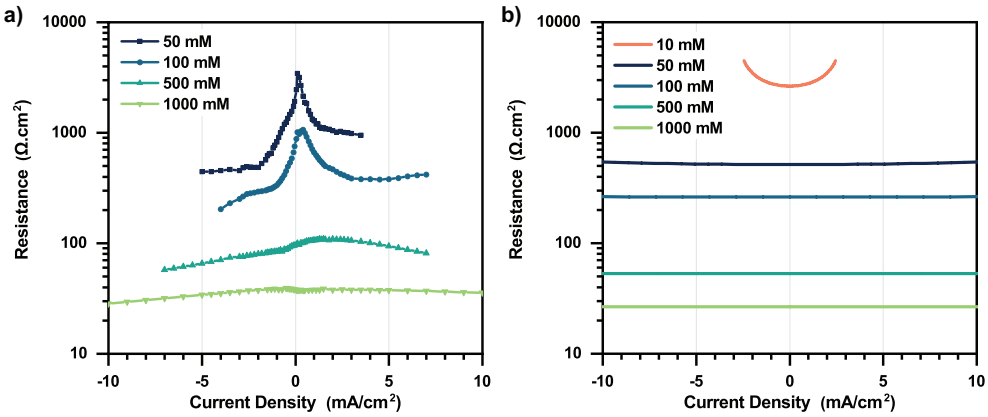

Figure 3.4: a) Ionic resistance of 10 nm pore sized AAO membranes when placed between two compartments with the same concentration on both sides. b) Simulated ionic resistance for a nanopore with a 10 nm pore size, 50 µm in length, 40 mV of surface potential, with porosity as a fitting parameter (0.09 %).

The experimentally obtained ionic resistances (Figures 3.4a and 3.5a) show a peak in resistance at low current densities. This peak in resistance does not seem to be solely explained by the current density, since the peak is shifted to about 2 mA/cm^2 for the 500 mM case. Rather, the peak in resistance is observed when the membrane voltage is approximately 0.2 V (Table S3.1). To our knowledge, this has not been observed in the literature, and it is not captured by analytical/numerical models. While we are not certain why this peak occurs, it could be related to the voltage contribution of the ζ-potential of the material, which is more significant at lower potentials. Even though the potential over the membrane is a floating potential that should not alter the membrane charge, it is remarkable that the electrolyte potential affects the resistance. Alternatively, it could be related to electric-field induced changes to the ζ-potential and electro-osmotic flows.[35] In the field of nanofluidics, similar nanochannels are often used at very low ionic currents.[36, 37] If this effect extends to other nanochannel systems, it could be causing an under-estimation of the conductivity of the nanochannels for larger-scale applications.

Perhaps the most important observation from Figure 3.4 is the linear relationship between conductivity and electrolyte concentration (plotted in Figure 3.6). This is unlike polymeric ion-exchange membranes where the measured conductivity plateaus after 0.3 M of external electrolyte concentration. Ion transport in polymeric IEMs occurs through microcavities and microchannels in series (Figure 3.1a),[38] where conductivity in the microchannels is determined by the counterions, which

have a fixed concentration. Meanwhile, in NFMs, the surface charge density, and thus the membrane conductivity, is affected by the local electrolyte concentration within the pores. Therefore, the conductivity of NFMs increases with increasing reservoir concentration, without a plateau. However, the ion selectivity reduces at higher concentrations, as seen in Chapter 2 of this thesis.

In more detail, the simulations shown in Figure 3.4b demonstrate a higher resistance at higher current density, especially at low concentrations, which indicates a substantial impact of concentration polarization. Figure S3.3a shows the concentration profiles of the entire geometry, at 5 mM bulk electrolyte and large applied voltages. The figure demonstrates that on the depleting side, the electrolyte concentration is significantly reduced close to the membrane surface, which is the cause for the observed limiting current density. Similar limiting currents are observed in polymeric IEMs.[39, 40] Such effects are difficult to observe in the experimental results due to the limited current densities we can reach experimentally at low electrolyte concentrations.

In practical conditions (e.g. in electrodialysis and reverse electrodialysis), the concentration may differ at either side of the membrane. Previous work showed that the resistance of polymeric membranes is dependent on both concentrations, more dominantly on the lower concentration.[38] Moreover, as we know that the AAO membrane is asymmetric, we additionally add the direction of the concentration gradient as a parameter to study for nanofluidic ion-exchange membranes. Figures 3.5a and 5b show the experimental and simulation results of placing an AAO membrane between two compartments with different concentrations – in this case, the higher concentration side (C_{high}), is 5 times more concentrated than the lower concentration (C_{low}).

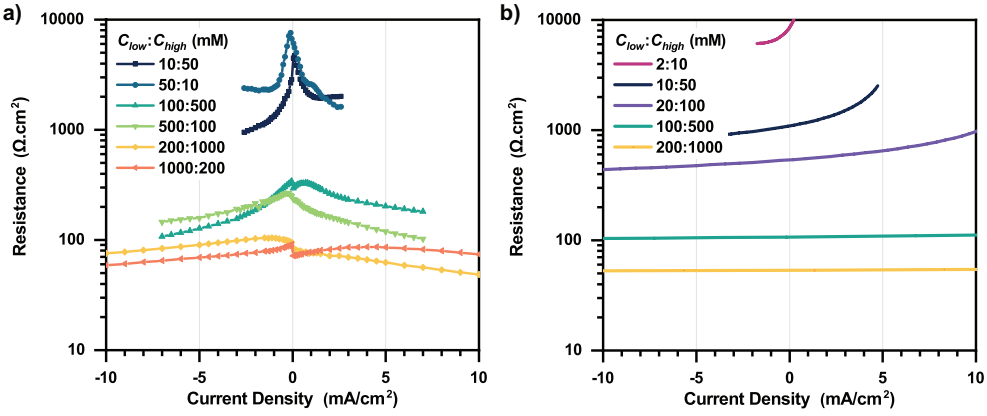

Figure 3.5: a) Ionic Resistance of 10 nm pore sized AAO membranes when placed between two compartments with different concentrations the two sides, a C_{high}:C_{low} ratio of 5. The membranes were also inverted to account for non- idealities in the pore geometry. b) Simulated ionic resistance, with porosity as a fitting parameter.

The results for distinct concentrations (Figure 3.5) indeed show asymmetric resistance plots. When the counter-ions migrate against the concentration gradient (i.e., for C_{low}:$C_{high} > 1$ at positive current density), the resistance is higher than when the current or concentration gradient is reversed. Although the concentration gradient itself plays a role, this is mostly a consequence of concentration polarization. The concentration profiles in Figure S3.3b show that the concentration on the C_{low} side is close to 0 at the highest applied voltage. At high concentrations, the concentration gradient is larger in magnitude, but the resistance has a less pronounced increase – this is mostly because concentration polarization is less pronounced at high concentrations, but also because the NFM is less selective, allowing both ion species to migrate across further reducing concentration polarization. Concentration polarization can be reduced for example by increased mixing of

the electrolyte, which reduces the diffusion boundary layer thickness.

Figure 3.5a provides further evidence that the commercial AAO membranes do not have perfectly symmetrical channels. For each concentration, when the concentration gradient was inverted, the resulting resistance (and in particular the peak) differs depending on the orientation. This is evidence for asymmetry, such as conicity of the nanopores.[41]

Larger C_{high}:C_{low} ratios were also simulated. Figure S3.4a shows the result of a simulation with a fixed C_{low} at 10 mM and increasing C_{high}. The figure shows an increased resistance at positive current densities, even at higher C_{high} concentrations. However, contrary to the previous scenario at low concentrations, C_{low} doesn't deplete – the concentration on the C_{low} side actually increases closer to the NFM (Figure S3.4b). In this case, the resistance is only increased because counterion migration occurs in opposite direction of the concentration gradient.

When the concentration is different on the two sides of the membrane, the question arises, which concentration, C_{high} or C_{low}, drives the conductivity? By taking the values at 2 mA/cm^2 and -2 mA/cm^2 from Figures 3.4a and 3.5a, we plotted the area conductivity against concentration (Figure 3.6a). The data relating to the experiments with equal concentrations on both sides of the membrane fits into a linear relationship. Interestingly, when taking the data where the concentrations on the two sides differ, it reasonably fits the same linear relationship only when plotted against the geometric average of the concentrations - shown with individual points in Figure 3.6a. Figure S3.5 shows that the same conductivity data plotted against the arithmetic average or the harmonic average of the concentrations do not fit the linear relationship established by the $C_{high} = C_{low}$ experiments.

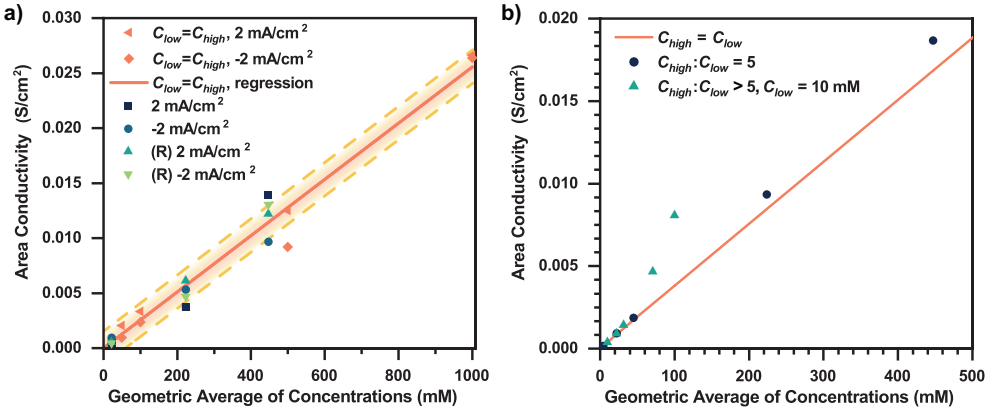

Figure 3.6: a) Ionic Resistance of 10 nm pore sized AAO membranes when placed between two compartments with different concentrations the two sides, a C_{high}:C_{low} ratio of 5. The membranes were also inverted to account for non- idealities in the pore geometry. b) Simulated ionic resistance, with porosity as a fitting parameter.

To further understand the effect of different concentrations on the membrane resistance, Figure 6b shows the same analysis for the simulation results (from Figures 3.4b, 3.5b and S3.4a). This analysis shows that there is a good agreement between the $C_{high} = C_{low}$ line and the geometric average of the concentrations at low concentration ratios, but the fit deviates when the ratio between C_{high} and C_{low} is very high. Nevertheless, these results indicate that once the relationship between conductivity and concentration is known, the geometric average of C_{high} and C_{low} can be used to estimate the conductivity for when the NFM is placed between two different electrolyte concentrations. Moreover, in Chapter 2, we found that the selectivity is also governed by the geometric average of the concentrations on both sides.

3.3.3. EFFECT OF PORE SIZE AND SHAPE

We further studied the impact of pore size on membrane resistance. Figure 3.7a shows the resistance of AAO membranes with different pore sizes against current density. Other pore sizes also show the same peak in resistance close to 0 mA/cm^2 as observed with the 10 nm AAO membrane. The discontinuity for the 3/150 nm membrane is unclear, but this could be an artifact due to the order of measurements (i.e., hysteresis from previous potential due to capacitance). All the nearly-symmetric pores (10, 20, 50 nm) have similar conductivities – the observed differences in resistance are more likely to stem from differences in porosity, ageing and the slight asymmetry of the AAO. Therefore, it can be stated that for cylindrical nanopores the pore size does not have a notable impact on conductivity. This is consistent with the results of our simulations (Figures 3.7b, 3.7c) and implies that the ion mobility within the nanopores is not significantly affected by the increased confinement in smaller nanopores. The simulations in Figure 3.7c also show that cylindrical pores with a smaller diameter (< 8 nm) are more conductive, due to the higher average electrolyte concentration in small charged channels. On the other hand, the model does not consider a varying diffusion coefficient within the nanopore in the radial direction, which has been shown to decrease within the electrical double layer.[42] Not accounting for the decrease in diffusivity in the diffuse layer could result in a small overprediction of the conductance, but this would in part be compensated by the stagnant Stern layer in our model, whereas molecular simulations indicate that ion mobilities are small but finite in the Stern layer.[35, 43] The effect of these modeling choices on the result can become more significant as the pore radius decreases.

The asymmetric channels with 3 and 5 nm pore sizes (Figure 3.7a) show an increased conductivity in one direction. A lower resistance is observed when a negative current is applied, which corresponds to when the anions first enter the large pore size and then reach the selective layer. When this is the case, the area resistance drops below 10 Ωcm^2, which means that their conductivity is even comparable to polymeric IEMs. In the previous chapter, we have shown that this pore geometry was not able to ensure sufficient permselectivity because the narrow part is too short (few nanometers) to create charge selectivity. However, the enormous decrease in membrane resistance suggests that the pore geometry is an important lever, and probably asymmetric pores with a somewhat longer neck could be useful to balance a good conductivity and selectivity of NFMs.

Therefore, we simulated conical nanopores, while keeping in mind the manufacturing possibilities and methodology. In practice, to create conical nanopores AAO membranes are anodized multiple times to create a larger pore size variation along the membrane thickness, e.g. for the fabrication of nanoneedles. Therefore, we used a fixed pore diameter of 8 nm at the lower pore size ($D_{p,1}$), and progressively increased the larger pore size, without changing the size of the geometry (which means that the porosity also increases with increasing $D_{p,2}$).

Figure 3.7c shows the resistance of both cylindrical and conical nanopores with the varying pore size. In the case of conical nanopores, the smaller pore size was kept constant at 8 nm and the larger pore size was increased. The figure shows that the resistance significantly decreases with an increasing pore size, and therefore also porosity.

However, our simulation did not fully produce the expected results for conical nanopores – this pore geometry typically induces the current rectification effect,35,42 which was not the case in our simulation. In Figure 3.7b, for the conical nanopores, a lower resistance should have been observed at negative current than at positive ones. At positive currents, the resistance was expected to be closer to the resistance of cylindrical nanopores, because of the entrance effects.[44] On the other hand, we did observe a “rectified” ion transport, with higher transport numbers at negative currents (Figure S3.6a). This effect was especially pronounced at low concentrations, because of the increased selectivity.

The decreased conductivity of conical nanopores comes at a price: an equal decrease is observed in the permselectivity (Figure 3.7d). Despite surface conductance, the selectivity of the NFMs

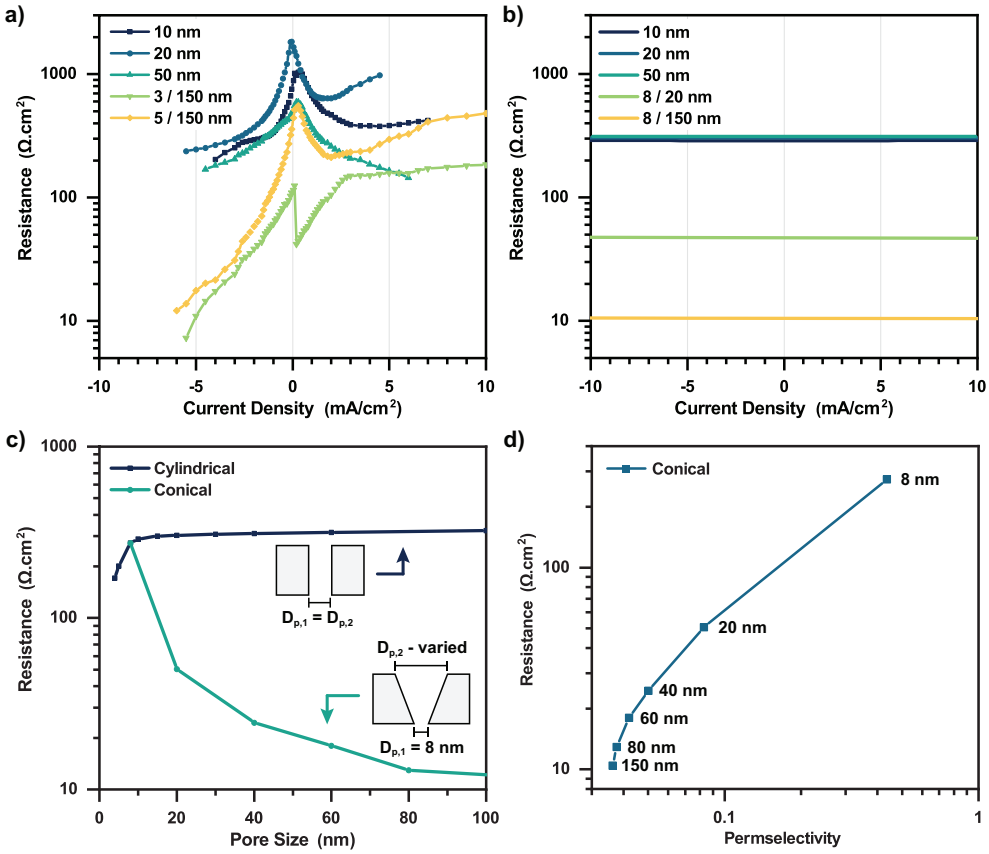

Figure 3.7: a) Membranes with different pore sizes – two asymmetric membranes with a thin selective layer and 150 nm pore size and three membranes with uniform pore sizes (10, 20 and 50 nm), placed between two compartments with 0.1 M KCl. b) Simulated ionic resistance for three cylindrical nanochannels (10, 20 and 50 nm) and two conical nanochannels with 8 nm as the smaller diameter, and 20 and 150 nm at the larger side. c) comparison of the ionic resistance of conical and cylindrical channels when varying the pore size, at -5 mA/cm^2. Only the larger pore size ($D_{p,2}$) was varied in conical nanopores, while keeping the smaller one ($D_{p,1}$) at 8 nm. d) Ionic resistance plotted against the permselectivity (at -5 mA/cm^2) of conical nanopores. $D_{p,2}$ is indicated on the figure for each point.

largely stems from the entrance effects. Therefore, when ions enter the membrane through the larger pore size, where the selectivity is significantly decreased, the total membrane selectivity is compromised. Figure S3.6b shows the concentration and potential profiles for the conical nanopores, and there is a notable absence of a Donnan potential on the large pore size side.

Therefore, in the next section we will simulate parameter values that could not be experimentally verified, but whose optimization could aid in the manufacturing of a conductive NFM, without the loss of selectivity.

3.3.4. EFFECTS OF POROSITY, PORE LENGTH AND SURFACE POTENTIAL

To understand the effect of parameters that could not be studied experimentally, and to predict the possibilities of NFMs with optimal performance, the porosity, pore length and surface potential effects are plotted on Figure 3.8.

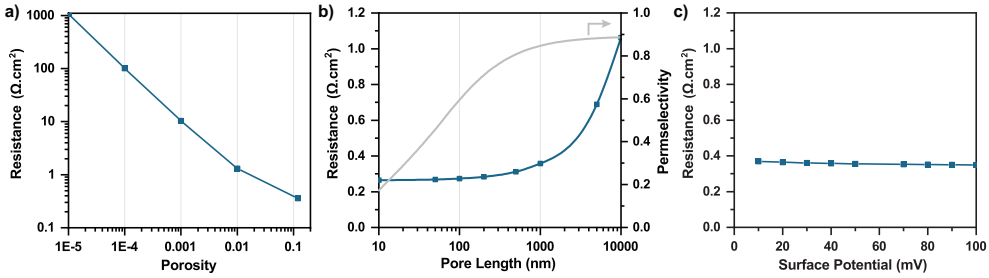

Figure 3.8: A pore of 1 µm length, 12 % porosity 3.5 nm pore size, and with a 40 mV zeta potential was simulated between two compartments of 50 mM KCl. The figure shows the result of varying a) porosity, b) pore length and c) surface potential.

Figure 3.8a shows the effect of porosity, which is as expected – the resistance increases with the decrease in porosity, or in other words, the conductivity increases linearly with the increase in porosity. The deviation from linearity observed at higher porosities is caused by concentration polarization and fluid velocity differences close to the pore entrance. When an NFM has a higher pore density, a higher current can be achieved, and naturally the concentration polarization will be more significant. However, this result also indicates that the concentration polarization must be considered when going to high pore densities and high currents densities.

Since resistance and selectivity of the membrane both scale with its thickness, the pore length is an important parameter to optimize. Figure 3.8b shows the effect of pore length on resistance. Although it is not as pronounced as the effect of concentration, we observe a linear relationship between resistance and pore length past 1 µm. Increasing the length up to 1 µm, does not show a dramatic increase in resistance. At lower pore lengths, the concentration gradient within the channel plays a role - although the resistance is proportional to the length, the decrease in concentration gradient in longer nanochannels reduces back diffusion and makes the ion transport more efficient. In Chapter 2, we showed that increasing the pore length from a couple of tens of nanometers to a couple of hundreds of nanometers greatly improved the selectivity, but increasing it beyond an a couple of micrometers does not further affect the selectivity significantly (shown in Figure 3.8b, secondary axis). Considering the trade-off between conductivity and selectivity, the optimum pore length likely lies in the 0.5 – 5 µm range, depending on the application and remaining membrane and fluid properties. The surface potential shown in Figure 3.8c, has an almost negligible effect on conductivity, which can be counter intuitive. A larger surface potential increases the surface charge density and therefore the fluid charge inside the nanopore, which has a major impact on selectivity. However, despite the larger charge separation, the total concentration of charge carriers inside the nanopore does not significantly increase, thus the conductivity remains almost unaffected by the magnitude of the surface potential. Additionally, surface charge density reaches a plateau at surface potentials close to 100 mV (Equation 5).

Galama et al.[38] have shown that when a polymeric IEM is placed between two solutions of different concentrations, it is the lower concentration side that determines the conductivity, due to the influence of (electro)osmotic flows on the concentration profile inside the membrane. In this work, we have shown that for NFMs, it is the geometric average of the concentrations that dictates the conductivity, and not C_{low}. Therefore, (electro)osmosis certainly plays a different role on the con-

centration profiles inside NFMs. According to our model and other models in literature,[23] the concentration changes linearly along the length of the NFM, a very different concentration profile than those observed in polymeric IEMs. Moreover, in polymeric IEMs, ions typically lose part of their hydration shell upon entering the polymeric structure.[45] In NFMs, since the pore size is larger, and no interactions with fixed charged groups take place, it is likely that ions will predominantly remain hydrated. Additionally, since electroosmotic mobility can be reduced within the electrical double layer relative to bulk electrolyte,[46] we expect that due to the larger pore size of NFMs, electroosmosis will be larger than in polymeric IEMs. Electroosmosis can have positive effects on the conductivity, since it can reduce concentration polarization, and enhance ionic transport. On the other hand, for applications, such as electrodialysis, where the objective is to obtain a concentrated stream, a larger water transport due to electroosmosis will limit the achievable concentration in the stream.

In this work, we have shown that electrolyte concentration is the main driver for NFM conductivity. However, at high electrolyte concentrations NFMs also lose selectivity, which means that optimizing their performance is hindered by a similar conductance-selectivity trade-off as in polymeric IEMs.. Nevertheless, they can potentially outperform polymeric IEMs in specific applications. An example of such an application is power generation through RED, where the membrane is placed between a concentrated salt stream and a pure water or river water stream. This particular combination allows the membrane to be both selective and sufficiently conductive. Using our model, we simulated a nanochannel of 1 μm in length, 5 nm in pore size and 40 mV of ζ-potential, between two concentrations of 17 mM and 600 mM (river and sea water), and the resulting area resistance was found to be 0.11 Ωcm^2 (at -100 mA/cm^2). This is lower than most of the currently used polymeric IEMs, and previous works have shown that such a channel can also surpass them in terms of selectivity. Additionally, NFMs also offer the possibility of custom-tailored pore sizes and surface chemistries which is a promising avenue for specific functionalities, such as lithium extraction and separation.

Since conductivity is dependent on electrolyte concentration, standard NFMs are mostly not suitable for applications that require dilute solutions on both sides of the membrane. For such applications, the background conductivity of fixed charges is required for an energy efficient process. We believe that strategies that combine the benefits of polymeric IEMs and NFMs – oriented nanochannels which promote transmembrane transport surrounded by fixed charges, hold promise to significantly improve IEM conductivity. Such strategies include: the orientation of polymeric chains with fixed charges during polymerization to create ionic pathways in between, e.g. by an external electric field,[47, 48] or by controlling the hydrophobicity of the polymeric backbone and hydrophilicity of the functional groups;[49] using metal-organic frameworks or covalent-organic frameworks with charged functional groups and defined nanochannels,[50, 51] or functionalizing inorganic material-based NFMs.[52, 53]

3.4. CONCLUSIONS

We have studied experimentally and numerically the conductivity of AAO membranes with different pore sizes, under different operational conditions such as current density and electrolyte concentrations. Experimentally, we observed that the conductivity is affected by membrane voltage with the lowest conductivity found close to 0.2 V. When using cylindrical nanopores, no significant effect of pore size on conductivity was observed, both in the experiments and simulations. However, using conical nanopores significantly improves the conductivity, although it is at the expense of selectivity, which is largely determined by entrance effects (when ions enter through a large pore entrance, the selectivity is compromised).

The pore length, or membrane thickness, is also a sensitive parameter – we estimate that the

optimal value, considering the trade-off with selectivity lies in the 0.5 to 5 µm range, depending on the application. Surprisingly, the surface potential of the material has a low impact on conductivity. Although a membrane with a higher surface potential ensures better selectivity and charge separation within the fluid, our simulations show that since the total concentration of charge carries doesn't change; the conductivity is not affected. The membrane conductivity is dictated by the bulk electrolyte concentration, with a linear relationship even up to 1 M. When the NFM separates two compartments of different electrolyte concentrations, the geometric average of the concentrations determines the conductivity. Therefore, NFMs are suitable for applications such as RED, where a dilute solution and a highly concentrated solution are used on either side – this ensures both their selectivity and conductivity. However, since NFMs do not have the background conductivity of fixed charges, they may not be suitable for applications where low electrolyte concentrations are used.

BIBLIOGRAPHY

1. Varcoe, J. R. *et al.* Anion-exchange membranes in electrochemical energy systems. *Energy & Environmental Science* **7,** 3135–3191 (2014).
2. Xia, R., Overa, S. & Jiao, F. Emerging Electrochemical Processes to Decarbonize the Chemical Industry. *JACS Au* **2,** 1054–1070 (2022).
3. Sharifian, R., Wagterveld, R. M., Digdaya, I. A., Xiang, C. & Vermaas, D. A. Electrochemical carbon dioxide capture to close the carbon cycle. *Energy & Environmental Science* **14,** 781–814 (2021).
4. Lakshmanan, S. & Murugesan, T. The chlor-alkali process: Work in Progress. *Clean Technologies and Environmental Policy* **16,** 225–234 (2014).
5. Jiao, K. *et al.* Designing the next generation of proton-exchange membrane fuel cells. *Nature* **595,** 361–369 (2021).
6. Strathmann, H. Electrodialysis, a mature technology with a multitude of new applications. *Desalination* **264,** 268–288 (2010).
7. Schwenzer, B. *et al.* Membrane Development for Vanadium Redox Flow Batteries. *ChemSusChem* **4,** 1388–1406 (2011).
8. Sata, T. & Jones, G. N. *Ion Exchange Membranes* X001–X004. ISBN: 978-0-85404-590-7 (The Royal Society of Chemistry, 2004).
9. Tanaka, Y. *Ion Exchange Membranes Fundamentals and Applications* ISBN: 978-0-444-63319-4 (Elsevier Science, 2015).
10. Park, H. B., Kamcev, J., Robeson, L. M., Elimelech, M. & Freeman, B. D. Maximizing the right stuff: The trade-off between membrane permeability and selectivity. *Science* **356,** eaab0530 (2017).
11. Espinoza, C., Kitto, D. & Kamcev, J. Counter-ion Conductivity and Selectivity Trade-Off for Commercial Ion-Exchange Membranes at High Salinities. *ACS Applied Polymer Materials* **5,** 10324–10333 (2023).
12. Kitto, D. & Kamcev, J. The need for ion-exchange membranes with high charge densities. *Journal of Membrane Science* **677,** 121608 (2023).
13. Zhang, Z., Wen, L. & Jiang, L. Nanofluidics for osmotic energy conversion. *Nature Reviews Materials* **6,** 622–639 (2021).
14. Nichka, V. S. *et al.* Modified Microheterogeneous Model for Describing Electrical Conductivity of Membranes in Dilute Electrolyte Solutions. *Membranes and Membrane Technologies* **1,** 190–199 (2019).
15. Kamcev, J., Paul, D. R., Manning, G. S. & Freeman, B. D. Predicting Salt Permeability Coefficients in Highly Swollen, Highly Charged Ion Exchange Membranes. *ACS Applied Materials & Interfaces* **9,** 4044–4056 (2017).
16. Daniilidis, A., Vermaas, D. A., Herber, R. & Nijmeijer, K. Experimentally obtainable energy from mixing river water, seawater or brines with reverse electrodialysis. *Renewable Energy* **64,** 123–131 (2014).

17. Abidin, M. N. Z., Nasef, M. M. & Veerman, J. Towards the development of new generation of ion exchange membranes for reverse electrodialysis: A review. *Desalination* **537,** 115854 (2022).

18. Machado, C. A. *et al.* Redox Flow Battery Membranes: Improving Battery Performance by Leveraging Structure–Property Relationships. *ACS Energy Letters* **6,** 158–176 (2021).

19. Gubler, L. Membranes and separators for redox flow batteries. *Current Opinion in Electrochemistry* **18,** 31–36 (2019).

20. Salvatore, D. A. *et al.* Designing anion exchange membranes for CO_2 electrolysers. *Nature Energy* **6,** 339–348 (2021).

21. Nanofluidics is on the rise. *Nature Materials* **19,** 253 (2020).

22. Bocquet, L. & Charlaix, E. Nanofluidics, from bulk to interfaces. *Chemical Society Reviews* **39,** 1073–1095 (2010).

23. Ryzhkov, I. I., Lebedev, D. V., Solodovnichenko, V. S., Minakov, A. V. & Simunin, M. M. On the origin of membrane potential in membranes with polarizable nanopores. *Journal of Membrane Science* **549,** 616–630 (2018).

24. Nishizawa, M., Menon, V. P. & Martin, C. R. Metal Nanotubule Membranes with Electrochemically Switchable Ion-Transport Selectivity. *Science* **268,** 700–702 (1995).

25. Vlassiouk, I., Smirnov, S. & Siwy, Z. Ionic Selectivity of Single Nanochannels. *Nano Letters* **8,** 1978–1985 (2008).

26. Kim, J., Kim, S. J. & Kim, D.-K. Energy harvesting from salinity gradient by reverse electrodialysis with anodic alumina nanopores. *Energy* **51,** 413–421 (2013).

27. Ahmed, Z., Bu, Y. & Yobas, L. Conductance Interplay in Ion Concentration Polarization across 1D Nanochannels: Microchannel Surface Shunt and Nanochannel Conductance. *Analytical Chemistry* **92,** 1252–1259 (2020).

28. Aixalà-Perelló, A. *et al.* Scalable and highly selective graphene-based ion-exchange membranes with tunable permselectivity. *npj 2D Materials and Applications* **7,** 46 (2023).

29. Wruck, W. J., Machado, R. M. & Chapman, T. W. Current Interruption—Instrumentation and Applications. *Journal of The Electrochemical Society* **134,** 539 (1987).

30. Berg, P. & Ladipo, K. Exact solution of an electro-osmotic flow problem in a cylindrical channel of polymer electrolyte membranes. *Proceedings of the Royal Society A: Mathematical, Physical and Engineering Sciences* **465,** 2663–2679 (2009).

31. Reyes Bahena, J. L., Robledo Cabrera, A., López Valdivieso, A. & Herrera Urbina, R. Fluoride adsorption onto α-Al_2O_3 and its effect on the zeta potential at the alumina–aqueous electrolyte interface. *Separation Science and Technology* **37,** 1973–1987 (2002).

32. Novak, S. & Kalin, M. The Effect of pH on the Wear of Water-Lubricated Alumina and Zirconia Ceramics. *Tribology Letters* **17,** 727–732 (2004).

33. Qiao, R. & Aluru, N. R. Ion concentrations and velocity profiles in nanochannel electroosmotic flows. *The Journal of Chemical Physics* **118,** 4692–4701 (2003).

34. Poggioli, A. R., Siria, A. & Bocquet, L. Beyond the Tradeoff: Dynamic Selectivity in Ionic Transport and Current Rectification. *The Journal of Physical Chemistry B* **123,** 1171–1185 (2019).

35. Döpke, M. F., van der Meij, F., Coasne, B. & Hartkamp, R. Surface Protolysis and Its Kinetics Impact the Electrical Double Layer. *Phys. Rev. Lett.* **128,** 56001 (2022).

36. Haywood, D. G., Saha-Shah, A., Baker, L. A. & Jacobson, S. C. Fundamental Studies of Nanofluidics: Nanopores, Nanochannels, and Nanopipets. *Analytical Chemistry* **87,** 172–187 (2015).

37. Cheng, L.-J. & Guo, L. J. Nanofluidic diodes. *Chem. Soc. Rev.* **39,** 923–938 (2010).

38. Galama, A. H. *et al.* Membrane resistance: The effect of salinity gradients over a cation exchange membrane. *Journal of Membrane Science* **467,** 279–291 (2014).

39. Krol, J. J., Wessling, M. & Strathmann, H. Concentration polarization with monopolar ion exchange membranes: current–voltage curves and water dissociation. *Journal of Membrane Science* **162,** 145–154 (1999).

40. Długołecki, P., Anet, B., Metz, S. J., Nijmeijer, K. & Wessling, M. Transport limitations in ion exchange membranes at low salt concentrations. *Journal of Membrane Science* **346,** 163–171 (2010).

41. Lan, W.-J. *et al.* Voltage-Rectified Current and Fluid Flow in Conical Nanopores. *Accounts of Chemical Research* **49,** 2605–2613 (2016).

42. Hartkamp, R., Siboulet, B., Dufrêche, J.-F. & Coasne, B. Ion-specific adsorption and electroosmosis in charged amorphous porous silica. *Physical Chemistry Chemical Physics* **17,** 24683–24695 (2015).

43. Döpke, M. F. & Hartkamp, R. The importance of specifically adsorbed ions for electrokinetic phenomena: Bridging the gap between experiments and MD simulations. *The Journal of Chemical Physics* **154,** 94701 (2021).

44. Karimzadeh, M., Seifollahi, Z., Khatibi, M. & Ashrafizadeh, S. N. Impacts of the shape of soft nanochannels on their ion selectivity and current rectification. *Electrochimica Acta* **399,** 139376 (2021).

45. Epsztein, R., Shaulsky, E., Qin, M. & Elimelech, M. Activation behavior for ion permeation in ion-exchange membranes: Role of ion dehydration in selective transport. *Journal of Membrane Science* **580,** 316–326 (2019).

46. Haywood, D. G., Harms, Z. D. & Jacobson, S. C. Electroosmotic Flow in Nanofluidic Channels. *Analytical Chemistry* **86,** 11174–11180 (2014).

47. Lee, J.-Y., Lee, J.-H., Ryu, S., Yun, S.-H. & Moon, S.-H. Electrically aligned ion channels in cation exchange membranes and their polarized conductivity. *Journal of Membrane Science* **478,** 19–24 (2015).

48. Hyun, J. *et al.* Magnetic Field-Induced Through-Plane Alignment of the Proton Highway in a Proton Exchange Membrane. *ACS Applied Energy Materials* **3,** 4619–4628 (2020).

49. Chen, X.-C., Zhang, H., Liu, S.-H., Zhou, Y. & Jiang, L. Engineering Polymeric Nanofluidic Membranes for Efficient Ionic Transport: Biomimetic Design, Material Construction, and Advanced Functionalities. *ACS Nano* **16,** 17613–17640 (2022).

50. Lu, X. *et al.* In Situ Observation of the pH Gradient near the Gas Diffusion Electrode of CO_2 Reduction in Alkaline Electrolyte. *Journal of the American Chemical Society* **142,** 15438–15444 (2020).

51. Lu, J. & Wang, H. Emerging porous framework material-based nanofluidic membranes toward ultimate ion separation. *Matter* **4,** 2810–2830 (2021).

52. Shi, W. *et al.* Functionalized anodic aluminum oxide (AAO) membranes for affinity protein separation. *Journal of Membrane Science* **325,** 801–808 (2008).

53. Xie, L. *et al.* Surface Charge Modification on 2D Nanofluidic Membrane for Regulating Ion Transport. *Advanced Functional Materials* **33,** 2208959 (2023).

3.5. SUPPORTING INFORMATION

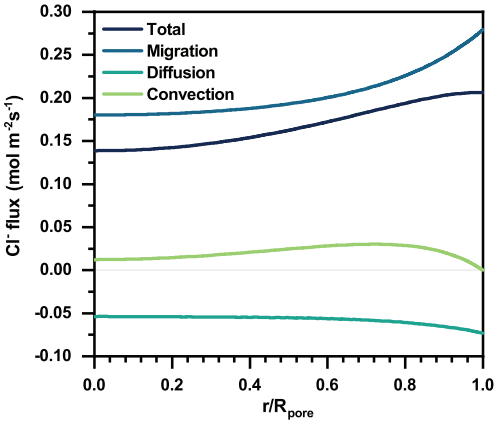

Figure S3.1: Simulations for an 8 nm in diameter and 50 µm in length pore with a 40mV ζ-potential at 0.05 V applied potential. The pore was placed between two compartments with 50 mM solution. Total flux, and flux contributions of migration, diffusion, and convection in the r-direction for Cl^- ions. $r = 0$ shows the center of the pore, and at $r = 1$ is the pore wall. The fluxes are indicated in the middle of the pore, at $z/L_{pore} = 0.5$

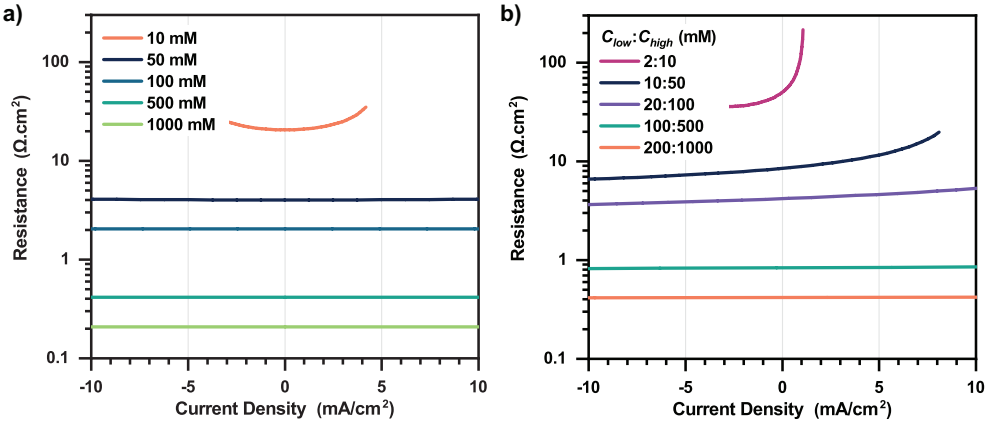

Figure S3.2: Simulation of 50 µm long pore, with 40 mV of surface charge, and 12 % porosity at different electrolyte concentrations.

Table S3.1: Concentration vs the current at which the peak of resistance (shown in Figure 4a) occurs.

Concentration (mM)	i **at peak resistance** (mA/cm^2)	V_M **at peak resistance (V)**
50	0.1	0.31
100	0.2	0.23
500	1.6	0.22
1000	3.5	0.19

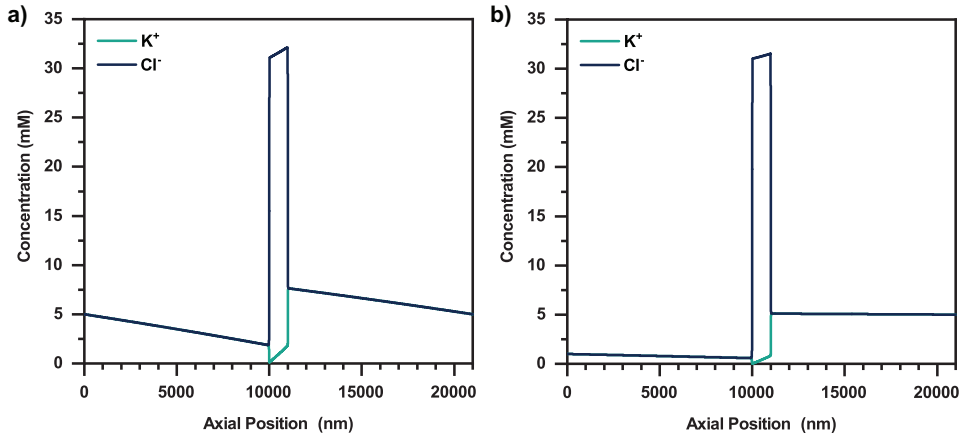

Figure S3.3: Concentration profiles for Cl^- and K^+ along the center of the geometry (symmetry axis). L_p = 1000 nm, $V_{applied}$ = 0.1 V. a) for $C_{high} = C_{low}$ = 5 mM, b) C_{low} = 1 mM, C_{high} = 5 mM

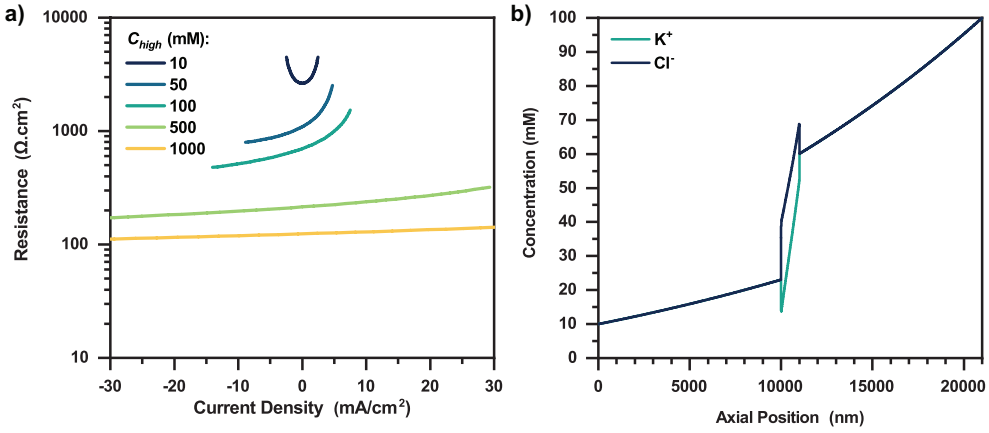

Figure S3.4: a) simulation of the real AAO nanopore, with 0.09 % porosity, 50 µm pore length, 8 nm pore size and with fixed C_{low} at 10 mM. C_{high} varied (legend). b) concentration profiles in the entire geometry at 0.1 V and C_{high} = 100 mM

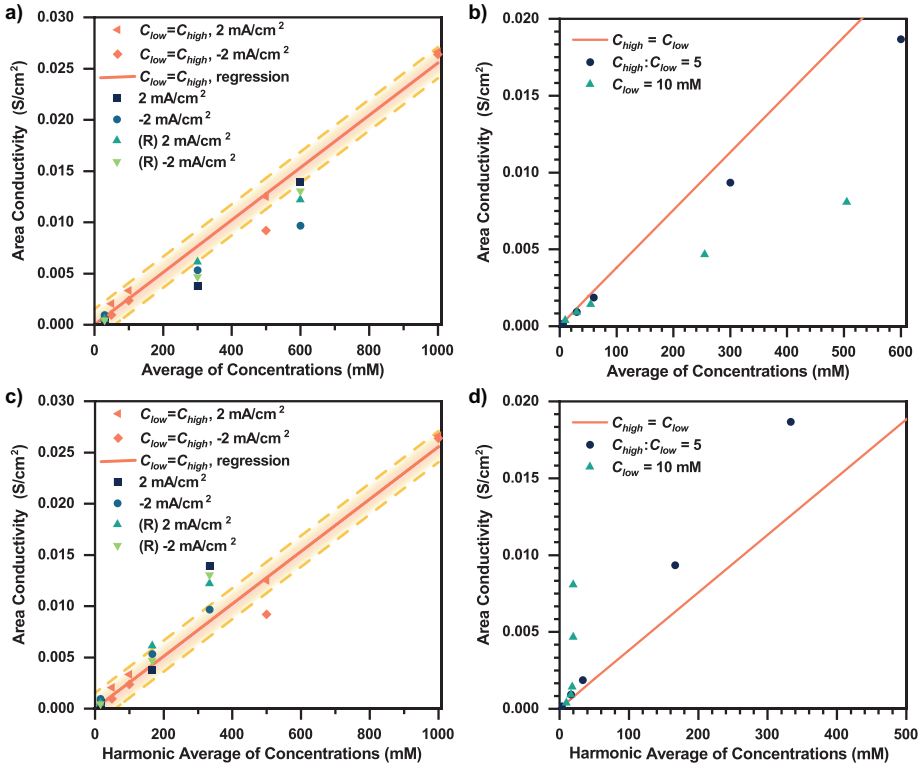

Figure S3.5: Data relating to $C_{low} \neq C_{high}$ (in symbols), plotted against arithmetic average and harmonic average. a) Experimental data, arithmetic average; b) simulation data vs arithmetic average; c) experimental data vs harmonic average; d) simulation data vs harmonic average. The data relating to $C_{low} = C_{high}$ fits into a linear regression shown as a line, with its respective standard error shown as a dotted line. Note that Figures a and c have a different scale from figure b and d.

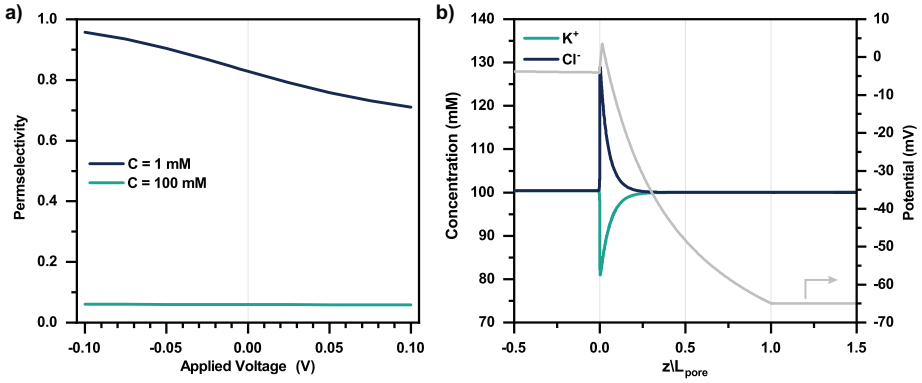

Figure S3.6: a) Permselectivity of conical nanopore with 8 nm of $D_{p,1}$ and 50 nm of $D_{p,2}$, 50 µm in length with a 40 mV ζ-potential. Electrolyte concentration displayed in legend. b) Average ion concentration and potential (secondary axis) within a conical nanochannel with 8 nm of $D_{p,1}$ and 20 nm of $D_{p,2}$, 50 µm in length with a 40mV ζ-potential, at approximately -5 mA/cm^2. Pore placed between two compartments with 100 mM solution.

4

Anion-exchange Membranes with Internal Microchannels for Improved Water Management

Electrochemical reduction of carbon dioxide poses substantial promise to convert abundant feedstocks (water and CO_2) to value-added chemicals and fuels using solely renewable energy. However, recent membrane-electrode assembly (MEA) devices that have been demonstrated to achieve high rates of CO_2 reduction are limited by water management within the cell, due to both consumption of water by the CO_2RR and electro-osmotic fluxes that transport water from the cathode to the anode. Additionally, crossover of potassium (K^+) ions poses concern at high current densities where saturation and precipitation of the salt ions can degrade cell performance. Herein, a device architecture incorporating an anion-exchange membrane (AEM) with internal water channels to mitigate MEA dehydration is proposed and demonstrated. A macroscale, two-dimensional continuum model is used to assess water fluxes and local water content within the modified MEA, as well as to determine the optimal channel geometry and composition. The modified AEMs are then fabricated and tested experimentally, demonstrating that the internal channels can both reduce K^+ cation crossover as well as improve AEM conductivity and therefore overall cell performance. This work demonstrates the promise of these materials, and operando water-management strategies in general, in handling some of the major hurdles in the development of MEA devices for CO_2 electrolysis.

This chapter has been published as "Anion-exchange membranes with internal microchannels for water control in CO_2 electrolysis" by K.V. Petrov, J.C. Bui, L. Baumgartner, L. Weng, S.M. Dischinger, D.M. Larson, D.J. Miller, A.Z. Weber, D.A. Vermaas, Sustainable Energy & Fuels, **6**, 5077-5088 (2022).

4.1. INTRODUCTION

Large-scale carbon dioxide (CO_2) electrolysis could be the key for storage of renewably-generated energy through sustainable production of fuels and chemicals.[1–3] By applying an electric potential to an electrolyzer, CO_2 and water can be electrochemically reduced at the cathode to form carbon monoxide (CO), formate, ethylene, methane, and other products, depending on the chosen catalyst.[4–9] At the anode, oxygen is typically produced by oxidation of water.[10, 11] State-of-the-art scalable electrolyzers operate in a zero-gap configuration, where porous gas-diffusion electrodes (GDEs) are directly pressed against an ion-exchange membrane (also known as a membrane-electrode assembly (MEA)),[2, 12] thereby minimizing transport losses. The GDE used on the cathode side facilitates direct supply of gaseous CO_2 to the catalyst, which is advantageous because CO_2 is sparingly soluble in water. If the reactor were to be operated in a fully aqueous medium, the CO_2 reduction reaction (CO_2RR) would quickly become mass-transport limited.[2, 13] Since a high current density is required for process scale-up, the membrane is a critical component since it must selectively conduct desired ions between the electrodes. The best reported results employ an anion-exchange membrane (AEM), which is shown to improve the Faradaic efficiency (FE) of the process by enabling operation at alkaline pH.[14, 15]

One of the challenges with this system is that the CO_2RR consumes water in neutral or alkaline environments.[16] This phenomenon can lead to the dehydration of the membrane surface close to the cathode, thereby inhibiting ionic transport and reducing overall efficiency. Additionally, the electro-osmotic flux of water away from the cathode when using an AEM, as well as the consumption of water by the CO_2RR both can lead to reduced water availability for the electrochemical reactions within the cathodic catalyst. Therefore, water management is of utmost importance to ensure optimized conductivity of the membrane and ionomer materials, as well as to promote the desired CO_2RR by negating the aforementioned challenges.[15, 17] Liu et al.[18] demonstrated that several factors influence membrane water content, including reaction rate, water diffusion from the anode and the hydrated CO_2 gas stream, and electro-osmotic flow. When the anolyte was deionized water, their cell lacked operational stability beyond 100 h. However, with 10 mM $KHCO_3$ anolyte, their electrolyzer was able to operate at a stable voltage for 4000 h. This result reveals that water diffusion from the anode is not sufficient by itself to maintain membrane hydration at the cathode/membrane interface, but the contribution of the water molecules in the hydration shell of K^+ ions, which cross over via electro-osmosis, ensured stable membrane hydration and water availability by the cathode surface. In a broader framework, the management of water transport in these devices has shown to be a strong lever for boosting the energy efficiency in alkaline water electrolyzers and increasing the stability of CO_2 electrolyzers.[14, 16, 19–22]

Another phenomenon that can be detrimental to CO_2RR is salt deposition on the cathode, which can block diffusion pathways and/or the catalyst surface.[15, 23] $KHCO_3$, and K_2CO_3 salts deposition occurs at high K^+ concentrations near the cathode, where CO_2 also reacts with OH^- (produced in the CO_2RR) to form (bi)carbonate.[18] A decreased water content near the cathode surface will also promote salt deposition. To mitigate the crossover of K^+, researchers have opted to limit the anolyte concentration to 10 mM.[18, 24] Such low cation concentrations in the anolyte minimize crossover, not only because they decrease the driving force for crossover (i.e., electrochemical potential gradient), but also increase the membrane selectivity due to more effective Donnan exclusion.[25] However, low anolyte concentrations may also result in poor ionic conductivity in the catalyst region.

This work aims to address these challenges by introducing internal microchannels into the AEM (Figure 4.1) that enable the circulation of water or electrolyte within the AEM. Using a mixture of continuum-scale modeling and experiments, our work demonstrates that these internal microchannels maintain AEM hydration by providing a direct supply of water to the cathode, enabling higher current densities for CO_2RR. Furthermore, the impact of the flowing electrolyte inside these chan-

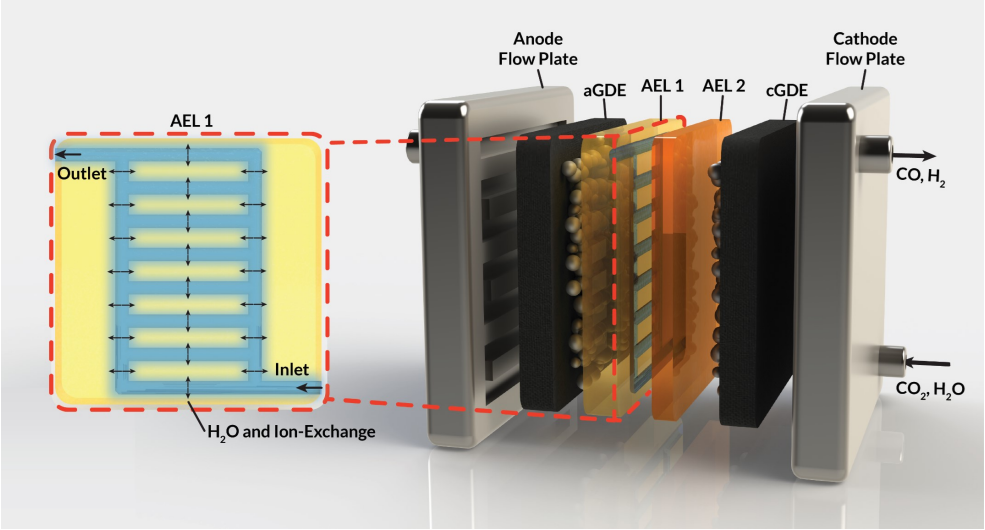

Figure 4.1: Schematic representation of an MEA cell for CO2RR that employs a bilayer AEM with internal channels to manage water fluxes. Inset (red box): Cross-section depicting internal water channels in the AEM.

nels on the overall AEM conductivity and selectivity is assessed. Specifically, the impact of the channel geometry, position, and composition on the electrochemical performance of a CO_2 electrolyzer is studied, expressed in terms of ohmic losses and observed ion crossover. Ultimately, this study sets the stage for the development of membrane materials with operando water-management strategies that will be critical in the deployment of CO_2RR devices at scale.

4.2. METHODS

4.2.1. MACROSCALE MODELING

This section describes the modeling methods, governing equations, and assumptions used to model the electrochemical performance and local hydration of MEA devices employing AEMs with internal microchannels. Because hydration gradients are greatest for a full MEA, (i.e., one with a vapor phase anodic feed), the AEM-MEA is modeled with a 100% relative-humidity (RH) water vapor feed in a nitrogen (N_2) carrier gas. The domain modeled is a two-dimensional (2-D) representation of the full MEA device (Figure 4.2a), including both anodic and cathodic porous-transport layers (PTLs), where the gaseous species diffuse through and distribute to the porous anodic and cathodic catalyst layers (which are modeled to be comprised of porous catalyst particles in an ionomer binder, see Figure S4.1) (catalyst layers (CLs)), where the electrochemical reactions occur. It is important to note that multiphase transport exists within the CL domains, where there is ionic transport within the ionomer in the CL, bulk vapor and liquid phase transport in the pore space of the CL, and electronic transport in the solid domain of the CL.[17]

In between the anodic and cathodic CLs is the AEM with internal microchannels, which is modeled with quarter-circular channels. The geometry of the channel is chosen to match the membrane fabricated by the process depicted in (Figure 4.2b) and detailed in the following subsections. Because the embedded channels are symmetrically patterned, half of a repeating unit is selected to be simulated (red box in Figure 4.2a). While this treatment does neglect edge effects, by applying symmetry conditions at the upper and lower boundaries of the modeled domain, the AEM can be

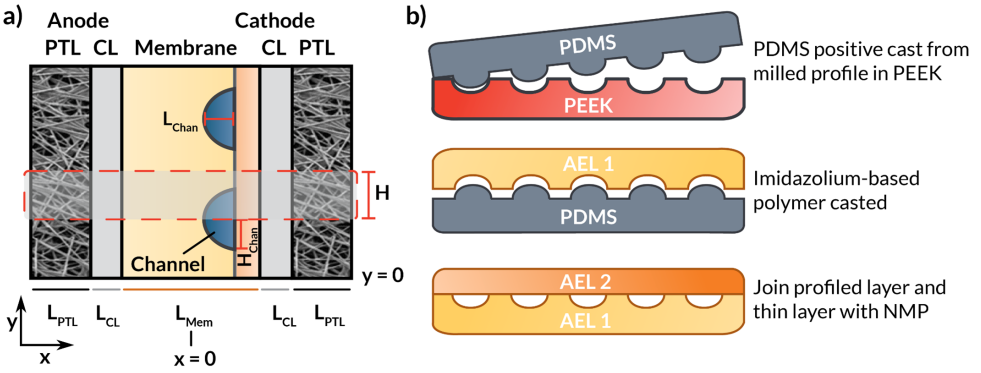

Figure 4.2: (a) Schematic representation of the simulated AEM-MEA in which the AEM has internal microchannels. (b) Schematic representation of the fabrication process and cross section of the entire bilayer AEM. The dashed box represents the modeled domain.

more efficiently simulated in 2-D, greatly reducing computational cost.

The model captures the gradients in electrostatic potential and bulk ionic current through a secondary current distribution, the diffusive transport of concentrated gas species in the CLs and PTLs, bulk aqueous and vapor fluid flow through the porous media, and water transport throughout the CL and AEM domains. The governing equations describing these phenomena are discussed in detail in the following subsections.

CHARGE TRANSPORT

Charge transport within the ionomer, membrane, and electrode domains is modeled by use of a secondary current distribution, which accounts for the effect of hydration-dependent solution resistance as well as the effects of electrode kinetics. Secondary current distributions neglect concentration-dependent kinetics, such as the migration and diffusion of ionic species, and the consumption and generation of CO_2, carbonate, and bicarbonate through buffer reactions. These effects are, of course, important to consider in the simulation of devices for the electrochemical CO_2RR.[17, 26, 27] However, due to the complex 2-D geometry of the simulated system, convergence is challenging when a complete treatment of all ions in the electrolyte is employed due to the immense increase in the number of degrees of freedom calculated when the ionic species are included, as well as the sharp concentration gradients generated by the nonlinear buffer source terms. Therefore, because the primary aim of the study is to explore membrane hydration in these systems, a secondary current distribution, which still enables the capture of hydration-dependent charge transport and electro-osmosis on bulk water transport, is adequate to describe the essential physics. When using the secondary current distribution, the ionic current in the electrolyte is calculated by Ohm's law,

$$i_l = -\kappa_M \nabla \phi_l \tag{4.1}$$

where κ_M is the ionic conductivity of the membrane (see Supplementary Methods for definition of transport properties in the model), ϕ_l is the ionic potential, and i_l is the ionic current density. The electronic current in the porous electrodes is defined also through Ohm's law,

$$i_s = -\sigma_s \nabla \phi_s \tag{4.2}$$

where σ_S is the electronic conductivity of the solid phase of the porous electrodes, ϕ_S is the electrostatic potential, and i_s is the ionic current density. The ionic and electrostatic potentials are related

by Tafel kinetics for the CO_2RR and hydrogen evolution reaction (HER) at the cathode, as well as the acidic or alkaline oxygen evolution reaction (OER) at the anode. Employing Tafel kinetics assumes all reactions are irreversible, which is likely true for the high applied potentials modeled. Standard potentials are evaluated at a pH of pH_0=8.14.

For cathodic reactions, the kinetics are modeled using the following expression:

$$i_k = -A_s i_{o,k} \prod_{r=1}^{c} \left(\frac{c_r}{c_{ref}} \right)^{\gamma_{r,k}} \exp\left(-\frac{\alpha_{c,k} F}{RT} \left(\phi_s - \phi_l - U^0_{k,\ pH_0} \right) \right) \tag{4.3}$$

For anodic reactions, the kinetics are modeled using the following expression:

$$i_k = A_s i_{o,k} \prod_{p=1}^{a} \left(\frac{c_p}{c_{ref}} \right)^{\gamma_{p,k}} \exp\left(\frac{\alpha_{a,k} F}{RT} \left(\phi_s - \phi_l - U^0_{k,\ pH_0} \right) \right) \tag{4.4}$$

In the Tafel expression, A_s is the surface area to volume ratio of the porous electrode, $i_{o,k}$ is the exchange current density of heterogeneous reaction k, $\gamma_{i,k}$ is the rate order of reaction k with respect to species i. The subscript c denotes a cathodic reaction, and subscript r denotes the reactant species in a given cathodic reaction. The subscript a denotes an anodic reaction, and subscript p denotes reactant species in a given anodic reaction. c_{ref} is a reference concentration set to the concentration at unit activity (1 M). $\alpha_{a/c,k}$ is the transfer coefficient of the given anodic or cathodic half reaction, R is the ideal gas constant, F is Faraday's constant, T is the temperature (assumed to be a constant 298 °K), and U^0_{k,pH_0} is the equilibrium potential of the given half reaction evaluated at pH_0.

The concentration of CO_2 in the electrolyte is determined using Henry's Law,

$$c_{CO_2,l} = p_{CO_2,g} H_{CO_2} \tag{4.5}$$

where $p_{CO_2,g}$ is the partial pressure of CO_2 in the gas phase, and H_{CO_2} is the Henry's Law constant for CO_2 dissolution in water.

Concentrated Species Transport in the Gas Phase

The gas phase contains CO_2, H_2O, H_2, CO, N_2, and O_2. The mole fractions in the gas phase are calculated from,

$$\nabla N_i = R_{CT,i} + R_{PT,i} \tag{4.6}$$

The flux, N_i is defined by the following relationship,

$$N_i = \frac{1}{M_i} \left(-\rho_G D_i^{eff} \nabla \omega_i - \frac{\rho_G D_i^{eff} \omega_i \nabla M_A}{M_A} + \rho_i u_G \right), \tag{4.7}$$

where u_G is the bulk velocity of the gaseous mixture, M_A is the average molecular weight of the mixture, and ρ_G is the gaseous mixture density. Additionally, Mi is the molar mass of species i, ω_i is the mass fraction of species i, and D_i^{eff} is the effective diffusion coefficient of species i in the gaseous mixture.

Water Transport in the Ionomer Phase

The molar flux of water, Nw, through the ionomer occurs by two mechanisms: diffusion and electro-osmosis.

$$N_w = \alpha_W^M \nabla \mu_w + \frac{\xi_A^M i_L}{F} \tag{4.8}$$

where $\alpha_W^{eff,M}$ is the water transport coefficient in the AEM, which is itself a function of the water activity,[28] and ξ_A^M is the electro-osmotic coefficient. Anions carry current in the AEM, so the sign is negative because water flows in the direction opposite to the current density. The chemical potential of water, μ_w, is defined by

$$\mu_w = RTln(a_w) + \underline{V_{w,L}}(p_{L,M} - p_{ref}) \tag{4.9}$$

where $\underline{V_{w,L}}$ is the molar volume of liquid water, and $a_w = p_v / p_w^{vap}$ is the activity of water vapor referenced to its vapor pressure. The water chemical potential is solved for by solving the mole balance:

$$\nabla N_w = R_{CT,i} + R_{PT,i} \tag{4.10}$$

It is important to note that the water in both the GDE and membrane, as modeled, are within ionomer environments; in other words, the simulated GDE possesses Ag catalyst particles suspended within an anion-exchange ionomer. This is crucial, because the ionomer in the GDE plays an important role in water management for the system. The ionomer is crucial in the case of excess water, because it mitigates flooding and enables improved transport of the reactant CO_2 to the catalyst sites.[26] However, it is also notable that the presence of the ionomer will change the local microenvironment in the catalyst layer, particularly, with respect to the local CO_2 to H_2O ratio due to the lower water availability in the anion-exchange ionomer compared to the liquid water present in a flooded GDE catalyst layer.[29] Ultimately, the ionomer microenvironment is beneficial for CO_2RR because it enables enhances the local CO_2 to water ratio, mitigates flooding, and provides improved ionic pathways for the transport of ions to and from the reactive sites. However, at higher current densities, the reduced water availability in the catalyst layer ionomer can become limiting. Therefore, for the case of simulation, we choose to model the system with an ionomer in the catalyst layer because it possesses the most opportune microenvironment for potential application in CO_2RR devices, as well as the most severe case of potential catalyst layer dry-out.

BULK FLUID FLOW IN POROUS MEDIA

The gas and liquid pressures in the porous media domains (PTLs and CLs) are calculated using mass conservation and Darcy's Law as follows.

$$\nabla \rho_p u_p = Q_p \tag{4.11}$$

$$u_p = -\frac{\psi_{m,p}^{eff}}{\mu_p} \nabla p_p \tag{4.12}$$

In the above expressions, u_p is the mass-averaged velocity field of phase p, $\psi_{m,p}^{eff}$ is the effective permeability of phase p in a porous medium, m, and p_p is the bulk pressure of phase p. μ_p and ρ_p are the viscosity and density of phase p, respectively.

BOUNDARY CONDITIONS

The boundary conditions are detailed in Table 4.1. At the leftmost boundary of the anodic PTL (the interface of the anode channel (CH) and the PTL), the potential is set to the applied cell potential. At this boundary, the gas pressure is set to 1 bar. The liquid-phase Darcy's Law boundary is defined as follows: if the liquid pressure, p_L, is less than or equal to the gas pressure, then a no-flux boundary condition is applied. Conversely, if the liquid pressure exceeds the gas pressure, there is an outward flux of liquid water with an arbitrarily high mass-transfer coefficient (k_{MT} = 1 $kgm^{-2}s^{-1}$) to maintain the pressure balance at the boundary. At the interface of the cathode CH and PTL, the gas and liquid pressures remain the same as for the anode side, but the solid-phase potential is now set to ground (0 V). At the interface of the PTL and the CLs, the ionomer water flux and the ionic flux are both set to 0. Lastly, at the interface of the internal channel and the membrane, the chemical

potential of water in the membrane is set to 0 (i.e., the liquid pressure in the membrane is set to its reference pressure of 1 bar).

Table 4.1: Boundary conditions for the continuum simulation.

	Anode CH|PTL	**Cathode CH|PTL**
ϕ_S	V_{cell}	$0\ V$
p_G	1 bar	
p_L	$n\rho_L u_L = \frac{k_{MT}(p_L - p_G)}{1\ Pa}\text{step}(\frac{p_L - p_G}{1\ Pa})$	

	Anode PTL|CL	**Cathode PTL|CL**	**Internal CH|Mem**
ϕ_L	$\nabla\phi_L = 0$	$\nabla\phi_L = 0$	$\mu_0 = 0$
μ_0	$\nabla N_w = 0$	$\nabla N_w = 0$	

NUMERICAL METHODS

All governing equations were solved using COMSOL Multiphysics 5.6 software with the PARDISO solver with a relative tolerance of 0.001. The modeling domain was adaptively refined, with element size decreased sharply near domain boundaries to capture gradients in the simulated quantities.

4.2.2. EXPERIMENTAL

MEMBRANE FABRICATION

For the preparation of the AEM, an imidazolium-functionalized poly(phenylene oxide) (ImPPO) polymer with 13 % of functionalized methyl pendants was synthesized as described elsewhere [30]. To fabricate a membrane with internal microchannels, a mold with these channels was first milled in polyether ether ketone (PEEK). Afterwards, a positive mold was made in polydimethylsiloxane (PDMS). 0.26 g of ImPPO was then dissolved in ≈4.5 mL of NMP, the solution was cast in the PDMS mold, and left in the oven at 70°C for ≈36 H until the solvent had completely evaporated. This resulted in a membrane material with the profiled channels (Figure 4.2b). The inlet and outlet holes were reamed into the sides (Figure 4.1). To enclose the channels, a 40 µm thin film of ImPPO without channels was attached with a minimal amount of NMP. For additional tests and comparison, two membranes without channels were fabricated: a 32 µm-thick membrane, and a membrane with the same thickness (170 µm) as the one with internal microchannels.

ELECTROCHEMICAL CELL TESTS FOR FLAT MEMBRANE

The ImPPO membrane conductivity and CO_2 reduction characteristics were tested using a 5 cm^2 electrolyzer from Dioxide Materials, with 0.1 M KOH anolyte and a humidified CO_2 stream at the cathode. The cathode was a carbon paper GDE (Sigracet 38 BC) sputtered with 100 nm-thick silver layer, and the anode was a nickel foam electrode. Using an IviumStat.f potentiostat, a current of 100 mA/cm^2 was applied for 30 minutes, while measuring the voltage. The gas outlet was analyzed using a gas chromatograph (CompactGC, Interscience).

ELECTROCHEMICAL CELL TESTS FOR MEMBRANE WITH INTERNAL MICROCHANNELS

A 2.25 cm^2 electrolyzer was custom-made with an inlet and outlet for the membrane's internal microchannels (Figure S4.3). It was first used to measure the membrane resistance with deionized (DI) water or different electrolyte concentrations inside the channels using the fast current-interrupt method. On the two sides of the cell, 0.1 M $KHCO_3$ was used as catholyte and anolyte.

Two micro reference electrodes (Ag/AgCl) from Alvatek were placed near the inlets of the catholyte and anolyte in the cell and a current of 5 mA/cm^2 was applied until a stable voltage was observed (Figure S4.4). By interrupting the current, the drop in voltage corresponding to the ohmic resistance was immediately observed. The electrolyte inside the channels was pumped at 0.2 mL/min using a syringe pump and the anolyte and catholyte were flowed at 1.3 mL/min. The concentration of $KHCO_3$ inside the channels was varied between 0 and 0.5 M.

For the electrolysis experiments, a humidified (89-95 % humidity) CO_2 gas stream was used on the cathode side, while the anolyte was either 0.1 M KOH or a humidified N_2 stream. The liquid flow rates were the same as those used in the resistance experiments and the gas flow rates were set at 50 sccm. Initially, a voltage of 3 V was applied to the cell for 30 minutes in order to ensure that the membrane was equilibrated with the ions produced during CO_2 electrolysis, such as HCO_3^- and CO_3^{2-}. The voltage was then swept linearly at 0.1 V/s up to 3.75 V and the current was recorded continuously.

For the K^+ crossover experiments, a constant current of 5 mA/cm^2 was applied for 70 minutes. A sample was taken from the electrolyte in the membrane microchannels before and after the experiment, and the cathode GDE was immersed in acidified water with 15% isopropanol and stirred overnight. Both solutions were then filtered and analyzed using ion chromatography (Metrohm 881 Compact IC Pro). This method allows the estimation of the amount of K^+ ions which have crossed from the anolyte to the cathode surface.

4.3. RESULTS AND DISCUSSION

4.3.1. MACROSCALE SIMULATIONS

EFFECT OF INTERNAL CHANNEL GEOMETRY AND LOCATION

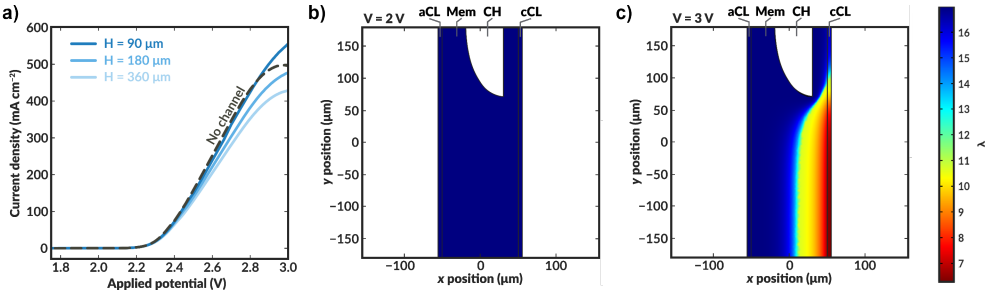

Figure 4.3: (a) Simulated polarization curves for bilayer AEM-MEA systems (red solid lines) with various distances between the centers of the internal microchannels (see schematic in Figure 4.2 for definition of H), as well as for an AEM-MEA with no internal channel (black dashed line). Simulated water content distribution within the MEA for a bilayer MEA with H = 360 µm at applied voltages of (b) 2 V and (c) 3 V. For these simulations, the aspect ratio of H to the channel height (H_{chan}) is constant. If H is scaled by 0.5, H_{chan} is similarly scaled by 0.5. The thickness of the channel is constant. The simulated water content and intermediate applied potential of 2.5 V can be found in Figure S4.6.

To explore how the implementation of an internal membrane channel impacts the performance of a vapor-fed MEA CO_2 electrolyzer, the local water content and current densities were simulated for various applied potentials in a macroscale model of the device. Considering the low conductivity of the DI-filled internal channel and the expected improved hydration, the size and spacing of the internal channels are important parameters. As shown in Figure 4.3a, when a channel with half-distance of the channel centers (H) of 360 µm is incorporated into the membrane (i.e., 720 µm

spacing, 218 µm channel height), the current density is lower than that of a device with no channel at potentials greater than approximately 2.4 V. This reduction is a result of the increased ohmic resistance incurred due to loss of direct ionic pathways between the anode and cathode when a DI water-filled channel is incorporated into the cell. However, the hydration of the membrane is substantially improved (Figures 4.3b-c, S4.7), thus there is a tradeoff between ionic path tortuosity and membrane hydration. Notably, sections of the cathode catalyst layer (cCL) closest to the internal channel are fully hydrated, with the AEM being fully liquid equilibrated with a water content (λ) of 17, where the water content is defined to be the moles of water in the membrane or CL ionomer domain per moles of fixed charge.[31] This improvement in the membrane hydration could potentially lead to longer AEM lifetimes.[32, 33]

When H is decreased proportionally along with the channel height (H_{chan}) (i.e., the channel spacing is decreased), the polarization characteristics improve (Figure 4.3a). When the channel spacing decreases by a factor of four (H = 90 vs H = 360 µm), the MEA can achieve a substantial 100 mA/cm^2 enhancement in the current density at an applied potential of 3 V. This enhancement results from improved hydration reducing the ohmic losses incurred in the cell. For this case, the improved ionic conductivity through the membrane due to increased hydration around the channels outweigh the low conductivity of the DI water in the channels themselves. The water content distributions for the no channel, along with the H = 90 and 180 µm cases can be found in Figures S4.7-S4.9. As simulated, for a given applied potential, bilayer AEMs with lower channel spacings possess larger, more uniform water content values.

To further highlight the role of hydration in these ionomers, it is instructive to calculate the average tortuosity of these modified AEMs. These tortuosities are calculated using power loss analysis[34, 35] for the fully hydrated AEM at low applied potentials to calculate an effective conductivity of the AEM that accounts for the increased average path length required to traverse around the water channel (see Supporting Information). The ratio of the conductivity of the membrane without the water channels to the effective conductivity of the membrane with the water channels represents the increase in the tortuosity of the ion conduction pathways. The tortuosities of all three AEMs with channels are greater than one, meaning that the ionic conductivities through these AEMs should be lower than that of an AEM with no channels due to the increase in the average path length at the same level of hydration. This increased tortuosity may explain the reduced current density supported by the bilayer AEMS with H = 180 and 360 µm, despite their higher hydration than the AEM without channels. However, for the bilayer AEM with H = 90 µm, the increased hydration overcomes the losses due to increased tortuosity, and the AEM with channels supports a higher current density at 3 V than the AEM without channels.

Further insight into how the internal channels impact local water content in the CO_2RR catalyst environment can be gained by exploring the water content and local current density distributions within the CLs for the various simulated bilayer AEMs (Figure 4.4). The water content in the cathode CL is critical to simulate, as it represents the availability of water to the catalyst to perform CO_2RR. Previous work has demonstrated that the water content of the cathode CL impacts both the activity and selectivity of the CO_2RR.[17, 36] Additionally, work by Disch et al. has used neutron-imaging to experimentally demonstrate that the loss of water content is prevalent in Ag-AEMEAs performing the reduction of CO_2 to CO, and the simulated water content profiles for the no-channel case are consistent with the trends shown experimentally, wherein upon increases in current density, the water content near the membrane-GDE interface is substantially reduced.[37] Interestingly, the average water content at the CL at a given applied potential is reduced at lower channel spacings, particularly around the channels themselves (Figure 4.4b-c). This behavior can be rationalized as follows. For the bilayer AEM with H = 360 µm, the internal channels are relatively large, and ionic current does not readily pass around the channel, essentially making a portion of the catalyst layer inactive for CO_2RR, as evidenced by the low to negligible local current densities observed near the

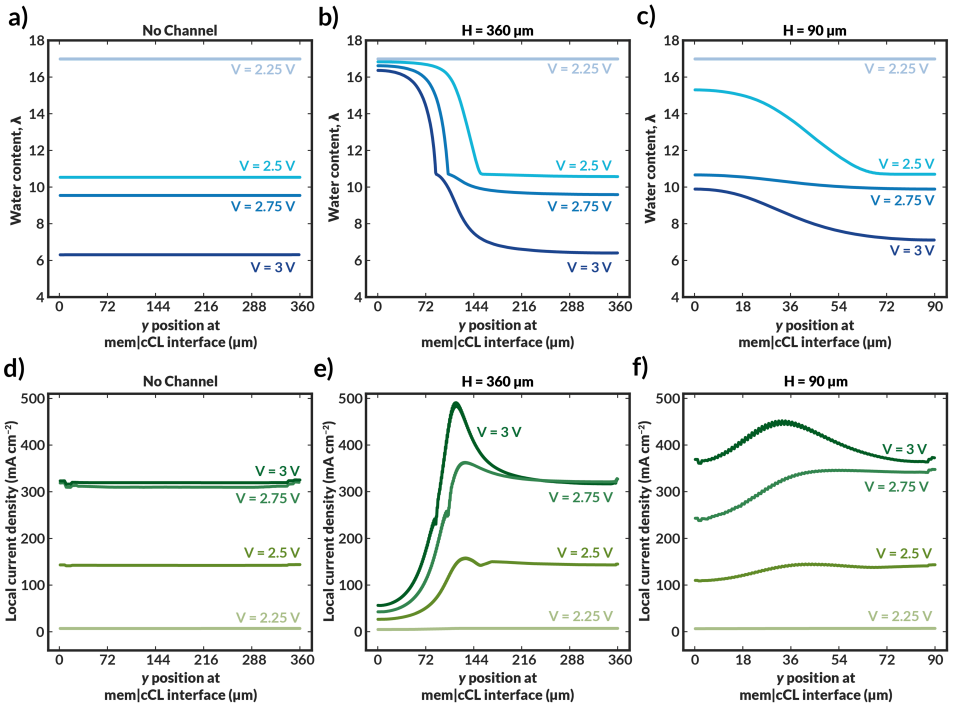

Figure 4.4: (a-c) Local water content of the ionomer within the cathodic CL averaged across thickness of the CL for varying channel geometries and spacings. (d-f) Local current density within the cathodic CL averaged across thickness of the CL for varying channel geometries and spacings.

internal channel (Figure 4.4e). Therefore, a portion of the CL near the internal channel remains well hydrated because water is not consumed by the CO_2RR.

Conversely, the CL adjacent to channels with H = 90 µm remains active for CO_2RR because the ionic transport pathways are less impeded around the smaller channels and ionic current can pass through the bulk AEM. While the improved CL utilization is promising, high water consumption is observed due to the CO_2RR and water content is reduced as the applied potential is increased. Nonetheless, for both bilayer AEMs with H = 90 and 360 µm, the water content at a given applied potential within the CL is markedly higher than in the AEM with no channel, and in the H = 90 µm case, the local current densities are also enhanced due to improved CL utilization. The analysis of these water content and current density profiles reveals two challenges with these materials: the low conductivity of the internal water channels can lead to poor CL utilization, and water consumption in the CL remains a challenge even at low channel spacings. A potential solution to these issues is to use the thinnest possible channel in the in-plane direction to mitigate loss of active area, and to position the channel as close to the CL as possible to better maintain hydration in the vicinity of water consumption.

To confirm these theorized impacts of variations in the channel size and location, additional geometries were simulated. For these models, H_{chan} was fixed to 10 µm (representing a small channel that could be reasonably be manufactured with techniques such as additive manufacturing [38–40]) and H was varied independently of H_{chan}, with the channel positioned directly adjacent to the CL.

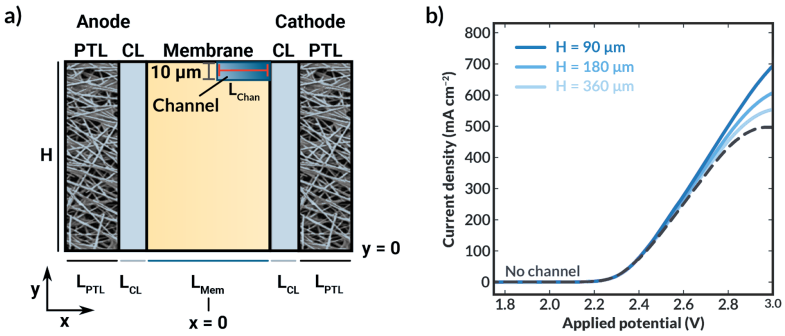

Figure 4.5: (a) Schematic of 2-D geometry employed to model an AEM with the internal channel placed adjacent to the cathode CL. Contrary to the prior simulations where the channel height was scaled proportionally to the channel spacing, the channel height was fixed at 10 µm in these simulations, representing the smallest height reasonably manufacturable. (b) Polarization curves of bilayer AEMs with cathode-adjacent channels of varying channel spacings.

Additionally, due to challenges with convergence with the curved channel implemented for previous simulations, the geometry was made rectangular while retaining the same L_{chan} (Figure 4.5a). Following the hydration patterns in case of curved internal channels (e.g. (Figure 4.3c), we expect little effect on the current density when changing to a rectangular channel shape. As shown in the simulated polarization curves in Figure 4.5b, this implementation of the channel exhibits higher current density at all channel spacings (H = 90, 180, and 360 µm) than in the prior implementation or for the AEM with no channel. Because the channel is so thin, ion transport to the CL is blocked very little, which minimizes the locally low current density as was the case in Figure 4.4e-f (see Figure S4.10). In addition, positioning the channel directly adjacent to the CL maintains better AEM hydration than the implementation wherein there is a polymer layer between the channel at the CL. Although the fabrication of such a thin channel is challenging and its positioning directly at the interface of the AEM and the CL may pose structural challenges, the simulations presented herein demonstrate the utility of geometric levers that can control the activity and performance of CO_2RR devices employing operando water management strategies.

EFFECT OF INTERNAL CHANNEL ELECTROLYTE CONDUCTIVITY

We also simulated the case in which the internal channel is extending through the full height of the membrane. Such a case is relatively straightforward to manufacture by, for example, using spacers in between thin flat membrane layers. Moreover, it collapses the computationally costly 2-D model to a 1-D model as shown schematically in Figure 4.6a.

Simulations demonstrate that, as the concentration (and, consequently, conductivity) of supporting electrolyte within the channel increases, the cell current density also increases (Figure 4.6b). Additionally, the membrane is more highly hydrated (as evidenced by the average polymer conductivity, Figure 4.6c) in all cases where the channel is included than in the case where no channel is included. Interestingly, when the channel contains 0.1 or 0.05 M $KHCO_3$, the cell largely exhibited lower current densities than the no-channel case at potentials greater than approximately 2.3 V (Figure 4.6b), despite the observed increase in conductivity of the ionomer domains when the channel was included (cf., Figure 6c). In these systems, performance is limited by the low conductivity of the aqueous electrolyte in the channel.

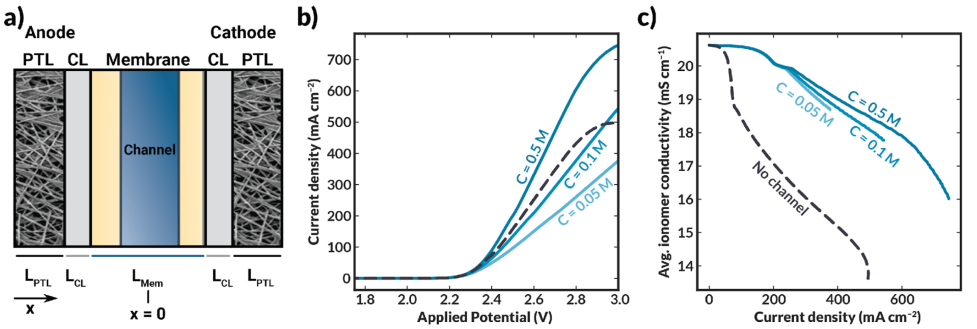

Figure 4.6: (a) Schematic of 1-D geometry modeled (channel thickness of 50 µm) to determine the impact of channel electrolyte concentration on cell performance. (b) Current-voltage characteristics of bilayer AEM cells with an internal channel with varying $KHCO_3$ concentration. (c) Average ionomer conductivity within the bilayer AEM with varying $KHCO_3$ concentration as a function of total cell current density.

4

4.3.2. EXPERIMENTAL RESULTS

EFFECT OF INTERNAL CHANNEL IMPLEMENTATION AND COMPOSITION ON CELL RESISTANCE AND PERFORMANCE

The previously synthesized imidazolium-functionalized poly(phenylene oxide) was cast into a 32 µm-thick membrane to test its conductivity under electrolysis conditions. As shown in Figure S4.2, a CO_2 electrolyzer containing this membrane exhibited a stable cell voltage of approximately 3.6 V when a current of 100 mA/cm^2 was applied, with an average FE for CO of 74%. While this device incorporating ImPPO does not outperform state-of-the-art membranes such as Sustainion and PiperION in terms of conductivity, they greatly outperform devices incorporating other commercial membranes like Fumasep and Selemion.[14, 41]

The microchannels resulting from casting the AEM as described previously are shown in Figure 4.7a. This film was subsequently joined with another thin AEM layer using a minimal amount of NMP to create a bilayer membrane with internal microchannels. The resulting channels were 59 µm deep, 216 µm high, and were spaced 502 µm apart. The center-to-center spacing (502+216 = 718 µm) is approximately the same as the geometry of the first simulated AEM with H_{chan} = 360 µm (2×360 = 720 µm spacing). The total hydrated membrane thickness was 170 µm, which is significantly thicker than the 25 - 50 µm thickness of state of the art membranes.[14, 18]

Improved fabrication methods, such as sterolithography or techniques involving additives [38–40] may be needed to achieve such dimensions with the presence of internal microchannels. Nonetheless, this membrane facilitates the experimental study of how the electrolyte concentration inside the channels influences the membrane properties and observables within the electrolysis process, such as the current density, applied voltage, and salt crossover/deposition.

Figure 4.7b displays the ionic resistance of the membrane as a function of the $KHCO_3$ concentration in the internal microchannels. Consistent with the simulated results displayed above, the ionic resistance greatly increases with decreasing electrolyte concentration in the channels. Only at the highest tested concentration of 0.5 M, the membrane exhibited approximately the same conductivity as a membrane of equal thickness without channels. Therefore, in fully hydrated conditions, the presence of channels does not improve the membrane conductivity. Future work should aim to quantify the ohmic resistance of the bilayer AEM at high current densities, potentially via in situ high-frequency resistance measurements or the current interrupt method.[42] Additionally, future work should seek to use in situ techniques of water management, such as neutron imaging,[43] x-ray tomography,[44] and magnetic resonance imaging [45] that have been used to measure water

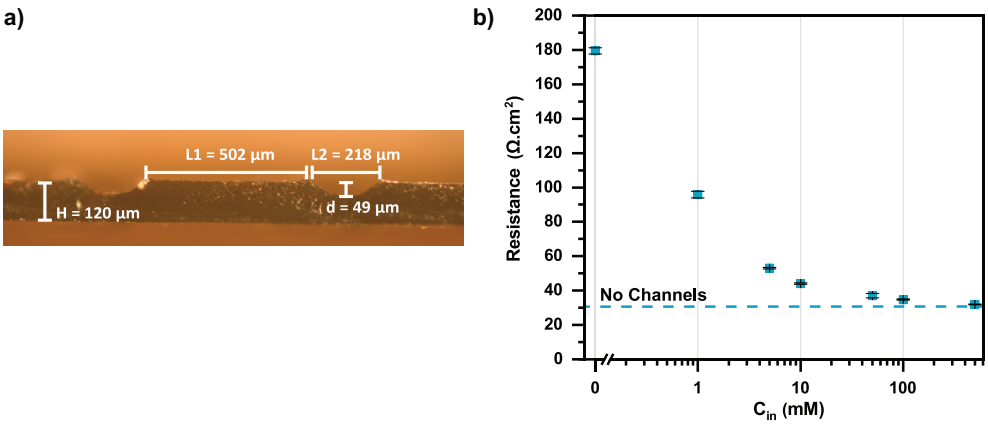

Figure 4.7: (a) Optical micrograph of ImPPO layer with channels in hydrated state. For the experiments, a thin ImPPO layer was attached (not shown) to cover the top side of the channels. (b) Ionic resistance of the membrane vs the concentration of $KHCO_3$ in the microchannels (C_{in}). The concentration outside of the membrane was 0.1M $KHCO_3$ at either side.

content in fuel cells to better relate changes in conductivity to changes in water content.[46]

It is important to note that all the observed resistance values are higher than expected, with typical values for membranes of this thickness being between 4 to 10 Ωcm^2, [47, 48] and that the resistance is highly sensitive to the electrolyte concentration in the internal channels. Although electrolyte concentration is known to affect polymer conductivity,[49] the internal channels are small relative to the distance between them, and hence the external electrolyte should not dominate the membrane's conductivity. The thin (32 µm) AEM without channels had an ionic resistance of 6.2 Ωcm^2, which means that the polymer's bicarbonate conductivity should be improved. This can be achieved by, for example, tuning the polymer degree of functionalization.[30] Another aspect, which could be affecting the results is the contact resistance between the electrodes and the membrane, since this measurement was performed in the zero-gap electrolyzer.

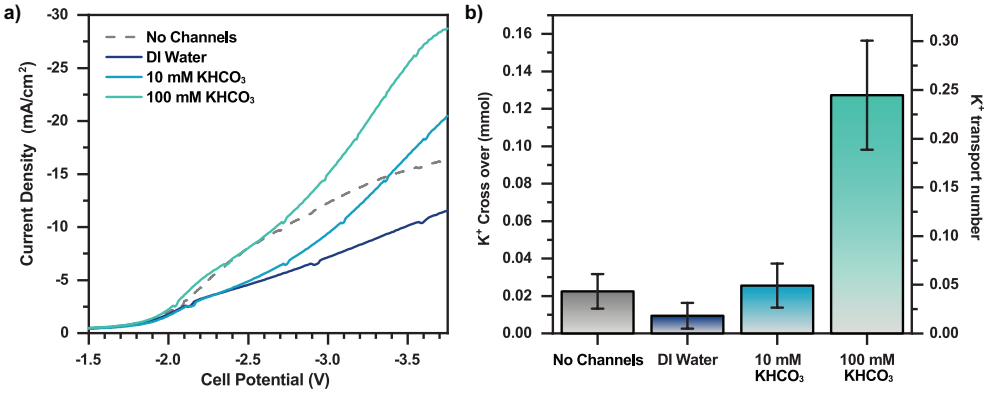

Figure 4.8: (a) galvanostatic linear sweep experiments with different electrolyte concentrations inside the AEM channels. (b) K+ crossover to the cathode side in function of the KHCO3 concentration inside the microchannels of the AEM.

Carbon dioxide reduction experiments were performed to validate the effect of internal channels on the cell's energy efficiency and ion crossover. Figure 4.8a and S9 show the current response to a linear voltage sweep with 0.1 M KOH as an anolyte and in a full MEA configuration, respectively, as a function of the concentration of $KHCO_3$ in the microchannels.

Figure 4.8a and S4.11 show that for this channel geometry, flowing DI water in the internal microchannels reduces the current density at a fixed voltage. This result is due to the very low conductivity of the DI water, which increases the overall ohmic resistance while also reducing CL activity as observed in the simulations. Employing a 10 mM $KHCO_3$ concentration in the microchannels substantially increases conductivity with respect to DI water when operating in aqueous solutions at both sides (see Figure 4.7b), and this trend is also observed when fed with humidified CO_2 gas (Figure 4.8a). The required cell potential is less negative compared to that of the standard AEM (i.e, without microchannels) beyond a current density of $\approx$15 mA/cm^2. This result further highlights that the role of the internal channels is more pronounced at higher current densities. A 100 mM $KHCO_3$ concentration inside the microchannels increases the current density even further, well beyond that of the standard AEM (Figure 4.8a). Because it has previously been established that the bilayer AEM is not more conductive than the standard AEM under fully hydrated conditions (Figure 4.7), it is likely that increased membrane hydration under the applied potential is critical to this result. Unfortunately, the maximum achievable current density was 30 mA/cm^2 due to the membrane thickness and conductivity. Nonetheless, we expect that at higher current densities the (de)hydration effect would be even more prominent. This result suggests that membrane hydration could limit CO_2 electrolysis efficiency as current densities are increased.

EFFECT OF INTERNAL CHANNELS ON SALT CROSSOVER

Because K^+ ion availability has also been reported to increase the activity of the catalyst layer, the microchannels could improve the selectivity of the catalyst toward CO by supplying cations.[50–52] Conversely, an excess supply of K^+ can lead to salt deposition and deactivation of the catalyst.[17] Thus, MEAs for CO_2RR will need to manage salt fluxes.[34] Figure 4.8b shows the K^+ crossover to the cathode GDE as a function of the $KHCO_3$ concentration in the internal microchannels. Consistent with prior CO_2RR literature,[15, 17, 23] a significant amount of K^+ crosses over through the AEM from the anolyte (100 mM KOH) in the absence of internal channels. Interestingly, the presence of an internal microchannel filled with DI water reduces the amount of K^+ that reaches the cathode. The K^+ concentration of the internal channel feed increased at time progressed during the experiment, implying K^+ is captured in the internal channel and washed away along with the outlet water.

A dilute solution in the internal microchannels is also likely to make the surrounding membrane material more selective to counter-ions, as the Donnan exclusion is most effective at low electrolyte concentrations.[25] The classical Donnan model predicts that the ratio between co-ions (K^+) and counter-ions (HCO_3^-, CO_3^{2-} or OH^-) in the membrane decreases when the $KHCO_3$ concentration in the aqueous phase decreases (see supporting information Equation S4.22). Therefore, a low $KHCO_3$ concentration in the internal channel not only reduces the driving force for K^+ crossover to the CL, but also causes an increased selectivity due to the relatively low sorption coefficient of K^+ in the membrane. Hence, this would imply that the total K^+ crossover (to cathode and internal feed together) would be lower compared to having a membrane without internal channels. We calculate from Equation S4.22 that changing the $KHCO_3$ concentration from 100 mM to 10 mM, assuming a membrane charge density of 5 M, the potassium concentration in the membrane decreases by a factor 100. Although the effect of increased selectivity cannot be distinguished from the ions being removed by the internal feed at this scale of experiments (the channel volumes do not allow for an accurate mass balance), it is clear that the actual decrease is crossover is less extreme (0.13 at 100 mM to 0.025 at 10 mM). We conclude that the distance between the microchannels is too large to fully leverage the effect of increased selectivity.

The internal microchannel feed concentration was also expected to have an influence on the FE for CO, since literature shows that the presence of K^+ in the catalyst layer also increases the selectivity of the process.[24, 53] However, the FE remained constant (≈58 %, Table S4.3), since such changes in selectivity cannot be observed in the current density range in our experiments.

Utilizing a 10 mM $KHCO_3$ electrolyte concentration in the microchannel had an insignificant impact on the K^+ crossover compared to the K^+ crossover through a membrane without internal channels. However, substantial salt deposition on the cathode was observed when 100 mM $KHCO_3$ was used. Therefore, there is a balance between the current density that can be feasibly achieved in this system and the salt deposition, which both depend on the electrolyte concentration in the microchannels. Our results suggest that electrolyte concentrations up to 10 mM $KHCO_3$ could be advantageous since they promote membrane hydration at high current densities, improve its conductivity, and do not contribute significantly to salt deposition.

This concept of incorporating microchannels into an AEM exhibits great potential, but some practical challenges remain. These challenges are primarily linked membrane thinness requirements and the need for reduced spacing of the channels within the AEM to enhance conductivity. Altogether, for this system to be feasible, the channels must be fabricated with a channel height on the order of 10 µm. Although it is possible to fabricate such a channel, the pressure drop would be substantial (≈1.7 bar per cm of channel at 50 µL/min). However, the small radii of such channels would make them ideal for leveraging capillary forces by connecting the channels to a water or electrolyte tank.[19] In this case, if any water were consumed, it would be replenished without requiring pumping. Similarly, recent work has demonstrated 3-D printed cellular fluidics that provide programmable management of gas and liquid flows via capillary action.[39]

4.4. CONCLUSIONS

In summary, we have simulated and experimentally quantified the transport properties of an AEM with internal microchannels for CO_2 electrolysis. Both our simulations and experiments indicate that membrane hydration is a major challenge in AEMs due to electro-osmotic fluxes and catalytic consumption of water in the CO_2RR. The presence of internal microchannels helps to maintain membrane hydration, which can increase the current density. These channels, however, can impede ionic pathways, especially if a low conductivity fluid is flowing through, effectively deactivating portions of the catalyst blocked by the channels. We conclude that internal channels should be on the order of 10 µm in size. Furthermore, they should be positioned close to the cathode surface to better hydrate and provide water for the catalytic CO_2RR that occurs within the cathode CL. Modeling reveals that the distance between channels should not exceed 90 µm, and that a membrane with channels of optimal geometry can increase the current density by up to 40% compared to a standard AEM. It is important to note that this value will likely change with the material properties of the AEM(e.g., thickness, ion exchange capacity, electro-osmotic coefficient, etc.), and further work should aim to design optimized ionomer chemistry for this specialized application. Modeling and experimental results have shown that current density increases with increasing electrolyte concentration inside the channels. Furthermore, experimentally, a membrane with microchannels (H_{chan} = 360 µm, L_{chan} = 50 µm) containing 0.1 M $KHCO_3$ electrolyte exhibited a significant increase in current density compared to a membrane without these microchannels. Since the presence of channels does not make the overall membrane more conductive in fully hydrated state, this result provides further evidence for the importance of water management in an electrolyzer. Lastly, we have also observed experimentally that electrolyte concentrations in the channels higher than 10 mM promote K^+ crossover to the cathode. Nonetheless, concentrations lower than 10 mM inside the channels do not meaningfully contribute to salt deposition, but promote membrane hydration and increasing its overall conductivity.

While there are still substantial challenges with regard to the fabrication and implementation of these bilayer AEMs, particularly with regard to making channels small and close enough such that they result in substantive gains in performance. Recent work in additive manufacturing provides great promise for ameliorating these concerns by enabling the generation of cellular fluidics with well-defined and geometrically controlled capillary flow in unit cells,[39] and capillary fluidics may enable the implementation of internal microchannels without induced flow. This work could initiate the development of a new class of materials with in operando water management that can alleviate dehydration in MEA CO_2RR devices, and could potentially be critical in the implementation of electrolyzer technology at scale.

BIBLIOGRAPHY

1. Küngas, R. Review - Electrochemical CO_2 Reduction for CO Production: Comparison of Low- and High-Temperature Electrolysis Technologies. *Journal of The Electrochemical Society* **167,** 44508 (2020).
2. Burdyny, T. & Smith, W. A. CO_2 reduction on gas-diffusion electrodes and why catalytic performance must be assessed at commercially-relevant conditions. *Energy Environtal Science* **12,** 1442–1453 (2019).
3. Lee, M.-Y. *et al.* Current achievements and the future direction of electrochemical CO_2 reduction: A short review. *Critical Reviews in Environmental Science and Technology* **50,** 769–815 (2020).
4. Gabardo, C. M. *et al.* Continuous Carbon Dioxide Electroreduction to Concentrated Multicarbon Products Using a Membrane Electrode Assembly. *Joule* **3,** 2777–2791 (2019).
5. Hatsukade, T., Kuhl, K. P., Cave, E. R., Abram, D. N. & Jaramillo, T. F. Insights into the electrocatalytic reduction of CO_2 on metallic silver surfaces. *Phys. Chem. Chem. Phys.* **16,** 13814–13819 (2014).
6. Bui, J. C., Kim, C., Weber, A. Z. & Bell, A. T. Dynamic Boundary Layer Simulation of Pulsed CO_2 Electrolysis on a Copper Catalyst. *ACS Energy Letters* **6,** 1181–1188 (2021).
7. Gu, Z. *et al.* Nanostructured Copper-Based Electrocatalysts for CO_2 Reduction. *Small Methods* **2,** 1800121 (2018).
8. Jouny, M., Luc, W. & Jiao, F. Correction to "General Techno-Economic Analysis of CO_2 Electrolysis Systems". *Industrial & Engineering Chemistry Research* **59,** 8121–8123 (2020).
9. Shin, H., Hansen, K. U. & Jiao, F. Techno-economic assessment of low-temperature carbon dioxide electrolysis. *Nature Sustainability* **4,** 911–919 (2021).
10. Blommaert, M. A. *et al.* Orientation of a bipolar membrane determines the dominant ion and carbonic species transport in membrane electrode assemblies for CO_2reduction. *Journal of Materials Chemistry A* **9,** 11179–11186 (2021).
11. Subramanian, S., Middelkoop, J. & Burdyny, T. Spatial reactant distribution in CO_2 electrolysis: balancing CO_2 utilization and faradaic efficiency. *Sustainable Energy & Fuels* **5,** 6040–6048 (2021).
12. Garg, S. *et al.* Advances and challenges in electrochemical CO_2 reduction processes: an engineering and design perspective looking beyond new catalyst materials. *Journal of Materials Chemistry A* **8,** 1511–1544 (2020).
13. Merino-Garcia, I., Alvarez-Guerra, E., Albo, J. & Irabien, A. Electrochemical membrane reactors for the utilisation of carbon dioxide. *Chemical Engineering Journal* **305,** 104–120 (2016).
14. Endrődi, B. *et al.* High carbonate ion conductance of a robust PiperION membrane allows industrial current density and conversion in a zero-gap carbon dioxide electrolyzer cell. *Energy & Environmental Science* **13,** 4098–4105 (2020).
15. Salvatore, D. A. *et al.* Designing anion exchange membranes for CO_2 electrolysers. *Nature Energy* **6,** 339–348 (2021).

16. De Mot, B., Ramdin, M., Hereijgers, J., Vlugt, T. J. H. & Breugelmans, T. Direct Water Injection in Catholyte-Free Zero-Gap Carbon Dioxide Electrolyzers. *ChemElectroChem* **7,** 3839–3843 (2020).

17. Weng, L.-C. C., Bell, A. T. & Weber, A. Z. Towards membrane-electrode assembly systems for CO_2 reduction: a modeling study. *Energy Environ. Sci.* **12,** 1950–1968 (2019).

18. Liu, Z., Yang, H., Kutz, R. & Masel, R. I. CO_2 Electrolysis to CO and O_2 at High Selectivity, Stability and Efficiency Using Sustainion Membranes. *Journal of The Electrochemical Society* **165,** J3371–J3377 (2018).

19. Hodges, A. *et al.* A high-performance capillary-fed electrolysis cell promises more cost-competitive renewable hydrogen. *Nature Communications* **13,** 1304 (2022).

20. Sánchez, O. G. *et al.* Recent advances in industrial CO_2 electroreduction. *Current Opinion in Green and Sustainable Chemistry* **16,** 47–56 (2019).

21. Vass, Á., Kormányos, A., Kószo, Z., Endrődi, B. & Janáky, C. Anode Catalysts in CO_2 Electrolysis: Challenges and Untapped Opportunities. *ACS Catalysis* **12,** 1037–1051 (2022).

22. Reyes, A. *et al.* Managing Hydration at the Cathode Enables Efficient CO_2 Electrolysis at Commercially Relevant Current Densities. *ACS Energy Letters* **5,** 1612–1618 (2020).

23. Leonard, M. E., Clarke, L. E., Forner-Cuenca, A., Brown, S. M. & Brushett, F. R. Investigating Electrode Flooding in a Flowing Electrolyte, Gas-Fed Carbon Dioxide Electrolyzer. *ChemSusChem* **13,** 400–411 (2020).

24. Endrődi, B. *et al.* Operando cathode activation with alkali metal cations for high current density operation of water-fed zero-gap carbon dioxide electrolysers. *Nature Energy* **6,** 439–448 (2021).

25. Galama, A. H., Post, J. W., Cohen Stuart, M. A. & Biesheuvel, P. M. Validity of the Boltzmann equation to describe Donnan equilibrium at the membrane–solution interface. *Journal of Membrane Science* **442,** 131–139 (2013).

26. Weng, L. C., Bell, A. T. & Weber, A. Z. Modeling gas-diffusion electrodes for CO_2 reduction. *Physical Chemistry Chemical Physics* **20,** 16973–16984 (2018).

27. Hashiba, H. *et al.* Effects of electrolyte buffer capacity on surface reactant species and the reaction rate of CO_2 in Electrochemical CO_2 reduction. *Journal of Physical Chemistry C* **122,** 3719–3726 (2018).

28. Weng, L. C., Bell, A. T. & Weber, A. Z. A systematic analysis of Cu-based membrane-electrode assemblies for CO_2reduction through multiphysics simulation. *Energy and Environmental Science* **13,** 3592–3606 (2020).

29. Kim, C. *et al.* Tailored catalyst microenvironments for CO_2 electroreduction to multicarbon products on copper using bilayer ionomer coatings. *Nature Energy* **6,** 1026–1034 (2021).

30. Dischinger, S. M., Gupta, S., Carter, B. M. & Miller, D. J. Transport of Neutral and Charged Solutes in Imidazolium-Functionalized Poly(phenylene oxide) Membranes for Artificial Photosynthesis. *Industrial & Engineering Chemistry Research* **59,** 5257–5266 (2020).

31. Peng, J., Roy, A. L., Greenbaum, S. G. & Zawodzinski, T. A. Effect of CO_2 absorption on ion and water mobility in an anion exchange membrane. *Journal of Power Sources* **380,** 64–75 (2018).

32. Kusoglu, A. & Weber, A. Z. New Insights into Perfluorinated Sulfonic-Acid Ionomers. *Chemical Reviews* **117,** 987–1104 (2017).

33. Fornaciari, J. C. *et al.* The Role of Water in Vapor-fed Proton-Exchange-Membrane Electrolysis. *Journal of The Electrochemical Society* **167,** 104508 (2020).

34. Bui, J. C. *et al.* Continuum modeling of porous electrodes for electrochemical synthesis. *Chemical Reviews* (2022).

35. Gerhardt, M. R. *et al.* Method—Practices and Pitfalls in Voltage Breakdown Analysis of Electrochemical Energy-Conversion Systems. *Journal of The Electrochemical Society* **168,** 074503 (2021).

36. Wheeler, D. G. *et al.* Quantification of water transport in a CO_2 electrolyzer. *Energy & Environmental Science* **13,** 5126–5134 (2020).

37. Disch, J. *et al.* High-resolution neutron imaging of carbonate precipitation and water transport in zero-gap CO_2 electrolysis. *Nature Communications* **13** (2022).

38. Ambrosi, A. & Pumera, M. 3D-printing technologies for electrochemical applications. *Chemical Society Reviews* **45,** 2740–2755 (2016).

39. Dudukovic, N. A. *et al.* Cellular fluidics. *Nature* **595,** 58–65 (2021).

40. Peighambardoust, S. J., Rowshanzamir, S. & Amjadi, M. Review of the proton exchange membranes for fuel cell applications. *International Journal of Hydrogen Energy* **35,** 9349–9384 (2010).

41. Kutz, R. B. *et al.* Sustainion Imidazolium-Functionalized Polymers for Carbon Dioxide Electrolysis. *Energy Technology* **5,** 929–936 (2017).

42. Cooper, K. R. & Smith, M. Electrical test methods for on-line fuel cell ohmic resistance measurement. *Journal of Power Sources* **160,** 1088–1095 (2006).

43. Yang, K., Kas, R. & Smith, W. A. In Situ Infrared Spectroscopy Reveals Persistent Alkalinity near Electrode Surfaces during CO_2 Electroreduction. *Journal of the American Chemical Society* **141,** 15891–15900 (2019).

44. Sinha, P. K., Halleck, P. & Wang, C. Y. Quantification of Liquid Water Saturation in a PEM Fuel Cell Diffusion Medium Using X-ray Microtomography. *Electrochemical and Solid-State Letters* **9,** A344 (2006).

45. Gong, X. *et al.* Self-diffusion of water, ethanol and decafluropentane in perfluorosulfonate ionomer by pulse field gradient NMR. *Polymer* **42,** 6485–6492 (2001).

46. Das, G., Choi, J.-H., Nguyen, P. K. T., Kim, D.-J. & Yoon, Y. S. Anion Exchange Membranes for Fuel Cell Application: A Review. *Polymers* **14** (2022).

47. Karpenko, L. V. *et al.* Comparative Study of Methods Used for the Determination of Electroconductivity of Ion-Exchange Membranes. *Russian Journal of Electrochemistry* **37,** 287–293 (2001).

48. Van Geluwe, S. *et al.* Evaluation of electrodialysis for scaling prevention of nanofiltration membranes at high water recoveries. *Resources, Conservation and Recycling* **56,** 34–42 (2011).

49. Galama, A. H. *et al.* Membrane resistance: The effect of salinity gradients over a cation exchange membrane. *Journal of Membrane Science* **467,** 279–291 (2014).

50. Bui, J. C. *et al.* Engineering Catalyst–Electrolyte Microenvironments to Optimize the Activity and Selectivity for the Electrochemical Reduction of CO_2 on Cu and Ag. *Accounts of Chemical Research* (2022).

51. Resasco, J. *et al.* Promoter Effects of Alkali Metal Cations on the Electrochemical Reduction of Carbon Dioxide. *Journal of the American Chemical Society* **139,** 11277–11287 (2017).

52. Yang, K. *et al.* Cation-driven increases of CO_2utilization in a bipolar membrane electrode assembly for CO_2electrolysis. *ACS Energy Letters* **6,** 4291–4298 (2021).

53. Erick, H. J. *et al.* CO2 electrolysis to multicarbon products in strong acid. *Science* **372,** 1074–1078 (2021).

54. Weber, A. Z. & Newman, J. Modeling transport in polymer-electrolyte fuel cells. *Chemical Reviews* **104,** 4679–4726 (2004).

55. Singh, M. R., Goodpaster, J. D., Weber, A. Z., Head-Gordon, M. & Bell, A. T. Mechanistic insights into electrochemical reduction of CO_2 over Ag using density functional theory and transport models. *Proceedings of the National Academy of Sciences of the United States of America* **114,** E8812–E8821 (2017).

56. *CRC Handbook of Chemistry and Physics* (ed Haynes, W.) (CRC Press, Cleveland, 1977).

4.5. Supporting Information

4.5.1. Supplementary Computational Methods

Definition of Transport Properties

In the ionomer domains, the conductivity of the electrolyte is

$$\kappa_M = (1 - S_M)\kappa_V + \kappa_L S_M \tag{S4.1}$$

In the above expression, κ_L is the conductivity of a liquid-equilibrated AEM, which is set to a constant value of 20.6 mS/cm (See Table S4.1 for a summary of parameter values used in the simulation).[17] κ_V is the conductivity of a vapor-equilibrated AEM, which is a function of the vapor activity (a_w) by

$$\kappa_V = 0.003 \exp(8.1432 a_w) \tag{S4.2}$$

S_M is defined by an empirical relationship roughly related to the interior surface energies and water-phase network. When S_M is 1, the ionomer is fully liquid equilibrated, when SM is 0, the ionomer is fully vapor equilibrated.

σ_S of the porous electrode is defined to be 220 S/m for the diffusion medium, and 100 S/m for the catalyst-layer domains.

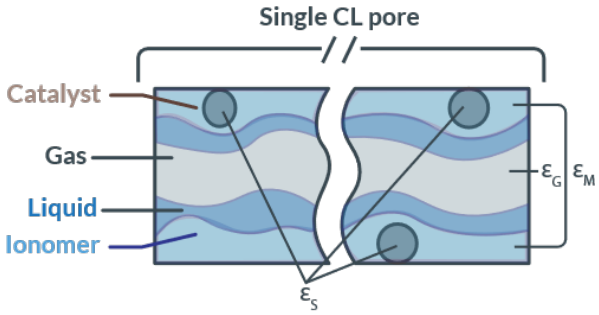

Figure S4.1: Schematic of a single pore within the porous catalyst layer in the electrochemical model. As simulated, the porous catalyst layer is assumed to be a homogeneous continuum of CL pores with volumes defined as shown above.

Lastly, all conductivities in the porous-electrode domains (shown schematically in Figure S4.1) are corrected for tortuosity and porosity using the Bruggeman correlation,

$$\kappa^{eff} = \varepsilon_p^{1.5} \kappa \tag{S4.3}$$

where ε_p is the volume fraction of the phase of interest. For the ionomer or membrane phase,

$$\varepsilon_M = (1 - \varepsilon_s) f_M \tag{S4.4}$$

where f_M is the volume fraction of ionomer in the pore space and ε_s is the volume fraction of the solid volume of the porous electrode.

The diffusion coefficients in the gaseous phase are:

$$D_i^{eff} = \varepsilon_G^{1.5} \frac{1 - \omega_i}{\sum_{k \neq i} \frac{x_k}{D_{ik}}} \tag{S4.5}$$

where x_k is the mole fraction of species i. The gas phase volume fraction, ε_G , is:

$$\varepsilon_G = (1 - \varepsilon_s)(1 - f_M)(1 - S) \tag{S4.6}$$

where S is the CL or PTL liquid saturation.

Lastly, because water activity or chemical potential in the ionomer cannot be readily measured or observed, the simulated water activities are converted to membrane water content, λ, by the following semi-empirical expression:[54]

$$\lambda = (1 - S_M)\,\lambda_V + \lambda_L S_M \tag{S4.7}$$

$$\lambda_V = 30.752 a_v^3 - 41.194 a_v^2 + 21.141 a_v \tag{S4.8}$$

where λ_V is the water content of vapor equilibrated AEM and λ_L is the water content of a liquid equilibrated AEM (set to a constant value of 17).[31]

SOURCE TERM DEFINITIONS

$R_{CT,i}$, represents the molar source terms of species i due to charge transfer reactions, respectively,

$$R_{CT,i} = -\sum_k \frac{s_{i,k} i_k}{n_k F} \tag{S4.9}$$

where $s_{i,k}$ is the stoichiometric coefficient of species i in reaction k, and n_k is the number of electrons transferred in reaction k.

For water vapor, an additional phase-transfer term related to the modeled transfer of water from the liquid or ionomer to the gas phase is required,

$$R_{PT,w,G} = -A_s k_{MT,v}\left(\frac{RH}{100} - a_w\right) - k'_{MT}(RH - 100\%)\left[H_0\left(\frac{p_L}{p_{ref}}\right) + H_0\,(RH - 100\%)\right] \tag{S4.10}$$

where $k_{MT,v}$ is the mass-transfer coefficient between the vapor phase and hydrated ionomer phase, RH is the relative humidity, and p_L is the bulk pressure of the liquid phase. The first term in the above equation describes mass transfer between vapor phase and the hydrated CL ionomer. The second term describes water evaporation or condensation in both the CL and PTL. A mass transfer coefficient of $k'_{MT} = 10^7$ mol m^{-3}s^{-1} and implementation of the Heaviside step function $H_0(x)$ ensure that RH is always 100% when liquid water is present and that the RH never exceeds 100%. Similarly, for liquid phase water:

$$R_{PT,w,L} = -A_s k_{MT,L}\left(p_L - p_{L,M}\right) + k'_{MT}(RH - 100\%)\left[H_0\left(\frac{p_L}{p_{ref}}\right) + H_0\,(RH - 100\%)\right] \tag{S4.11}$$

where $p_{L,M}$ is the pressure of liquid water in the membrane. Again, the first term describes transfer between the liquid and ionomer phases, and the second term describes evaporation or condensation.

Additionally, the phase-transfer source term associated with water in the ionomer phase is given as

$$R_{PT,w,M} = A_s k_{MT,L}\left(p_L - p_{L,M}\right) + A_s k_{MT,v}\left(\frac{RH}{100} - a_w\right) \tag{S4.12}$$

It is important to note that, while for vapor- or liquid-phase water there was no charge-transfer source term, there is a source term associated with the consumption of water by charge-transfer reactions in the ionomer phases. The phase-transfer source term associated with water in the ionomer phase is given as

$$R_{PT,w,M} = A_s k_{MT,L}\left(p_L - p_{L,M}\right) + A_s k_{MT,v}\left(\frac{RH}{100} - a_w\right) \tag{S4.13}$$

Q_p describes the source term into or out of a given phase p. For the gas phase, the expression is

$$Q_G = M_W R_{PT,w,G} + \sum_{i \neq CO_2, H_2O, N_2} M_i R_{CT,i} \tag{S4.14}$$

For liquid phase,

$$Q_L = M_W R_{PT,w,L} \tag{S4.15}$$

Table S4.1: Parameter values for simulation.

Parameter	Value	Unit	Ref
Geometry			
H	360	µm	
H_{chan}	109	µm	
L_{CL}	5	µm	
L_{PTL}	100	µm	
L_{mem}	100	µm	
L_{chan}	50	µm	
Charge Transport			
k_L	20.6	mS/cm	[28]
σ_S	220 (PTLs) 100(CLs)	S/m	[28]
ε_S	0.47(PTLs) 0.5(CLs)		[28]
f_M	0.4		[28]
Reaction Kinetics			
A_S	1×10^6	m^{-1}	[28]
$i_{o,CO}$	3.48×10^{-14}	mA/cm^2	[17]
$\alpha_{c,CO}$	1		[17]
$\gamma_{CO_2,CO}$	1.5		[55]
$U_{0,CO}$	-0.11	V vs. RHE	[34]
i_{o,H_2}	5.09×10^{-10}	mA/cm^2	[17]
α_{c,H_2}	0.44		[17]
γ_{CO_2,H_2}	0		[55]
U_{0,H_2}	0	V vs. RHE	[34]
$i_{o,O_2,base}$	4.78×10^{-8}	mA/cm^2	[17]
$i_{o,O_2,acid}$	$1.11 \times 10^{-8} \exp(-0.4 pH_0)$	mA/cm^2	[17]
α_{a,O_2}	1.5		[17]
U_{0,O_2}	1.23	V vs. RHE	[34]
Species Transport			
H_{CO_2}	34	mM/atm	[56]
ξ_A^M	-1		[28]

TORTUOSITY CALCULATIONS

To calculate the tortuosity of the ionically conducting medium, we consider an applied potential for which the membrane is fully hydrated, and there are no variations in conductivity across the domain, $V_{app} = 1.6$ V. The ionomer conductivity at this potential is 20.6 mS/cm. The power loss due to ohmic losses throughout the modified ionomer domain is calculated as:[35]

$$P_{ohmic}^{real} = \int\int_{AEM} \frac{i_l \cdot i_l}{\kappa_{AEM}} dA \tag{S4.16}$$

where i_l is the local ionic current density vector, and κ_{AEM} is the local AEM conductivity. The calculated power loss represents the loss of power through the ionomer, accounting for the tortuous pathway of the ions around the water channel.

If there were no tortuous pathway, the power loss would be the ideal power loss:

$$P_{ohmic}^{ideal} = \frac{i_l^2 A}{\kappa_{AEM}} \tag{S4.17}$$

where A is the through-plane area of the AEM. We can use the above expression to determine an effective conductivity of the ionomer using the real ohmic power loss. Essentially, this value indicates the corresponding conductivity of a membrane without a channel that has the same ohmic power loss:

$$\kappa_{AEM}^{eff} = \frac{i_l^2 A}{P_{ohmic}^{real}} \tag{S4.18}$$

This value is reduced compared to the bulk AEM conductivity of 20.6 mS/cm. For the H = 360 µm case, κ_{AEM}^{eff}=8.6 mS/cm, for the H = 180 µm case, κ_{AEM}^{eff}=13.1 mS/cm, and for the H = 90 µm case, κ_{AEM}^{eff}=15.8 mS/cm.

To obtain the tortuosity (τ), we divide the bulk AEM conductivity of 20.6 mS/cm by the calculated effective conductivity. This value provides an average increase in the path length for each of the AEMs with internal channels.

$$\tau = \frac{20.6\ mS\ cm^{-1}}{\kappa_{AEM}^{eff}} \tag{S4.19}$$

The calculated effective conductivities and tortuosities for the bilayer AEM with varying channel spacings (H) can be found in Table S4.2.

Table S4.2: Table of effective conductivity and tortuosity as a function of table spacing as calculated by Equations S4.16-S4.19.

H **(Channel Spacing,** µm)	κ_{AEM}^{eff} **(Effective Condcutvity, mS/cm)**	τ **(Tortuosity)**
360	8.6	2.39
180	13.1	1.57
90	15.8	1.31

4.5.2. SUPPLEMENTARY EXPERIMENTAL METHODS

TESTING THE IONOMER

To test the imidazolium-functionalized poly(phenylene oxide) polymer's performance (conductivity and electrochemical response) under electrolysis conditions, an electrolyzer with 5 cm^2 area from Dioxide materials, which has a serpentine flow channel on both the anode and cathode endplates, was utilized. The cathode was a 6.25 cm^2 GDE sputtered with 100 nm-thick silver. A 100 nm thick Ag catalyst layer was sputtered on top of the microporous layer of a Sigracet 38 BC by direct-current magnetron sputtering. The anode was a Ni foam (3×3 cm). The cell voltage was stable at 3.6 V (see Figure S4.2) and the average faradaic efficiency was 74%.

CUSTOM-MADE ELECTROLYZER

Our custom-made electrolyzer chassis was assembled from two milled polyetheretherketone (PEEK) plates. One of the plates had four entrances: an inlet and outlet for the flow field, and two

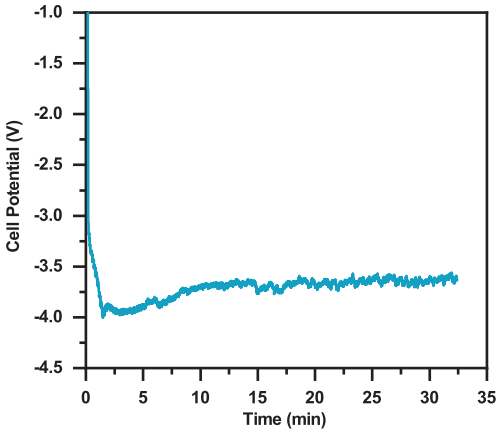

Figure S4.2: Electrolysis at 100 mA/cm^2, in zero-gap configuration using a 32 µm thick ImPPO membrane

connections for electrodes. Gold spring contact electrodes were used to apply voltage/current to the electrolyzer. The other plate (Figure S4.3) had six entrances: the same four as the first plate, and an extra inlet and outlet for the membrane internal microchannels. The cathode was a silver-coated GDE and the anode was an iridium-oxide coated GDE. Both of these GDEs were 2.25 cm^2 and were prepared by sputter coating (AJA International Sputter Machine) pure Ag and Ir, respectively, onto a Toray TGP-H-060 porous carbon paper (Alfa Aesar).

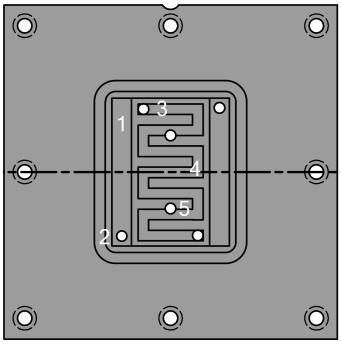

Figure S4.3: Schematic of one plate of the custom-made electrolyzer schematic. 1 - seat for gasket that ensures the fluid in the internal channels does not crossover to the flow-field; 2- inlet/outlet for internal membrane microchannels; 3 - inlet/outlet for plate flow-field; 4 – flow-field; 5 – entrance for electrode connection. The other plate is analogous, but does not have the inlet/outlet for membrane microchannels (2).

RESISTANCE MEASUREMENTS

To measure the membrane resistance with different electrolyte concentrations in the microchannels, two T-junctions were added in the inlet tubing close to the electrolyzer plates. In those junctions, two leakless Ag/AgCl reference electrodes were connected. This way, the voltage drop was measured between the electrolyte inlets. Since current flows only between the electrodes, and the membrane separates the electrodes, the voltage drop across the membrane is measured. The oper-

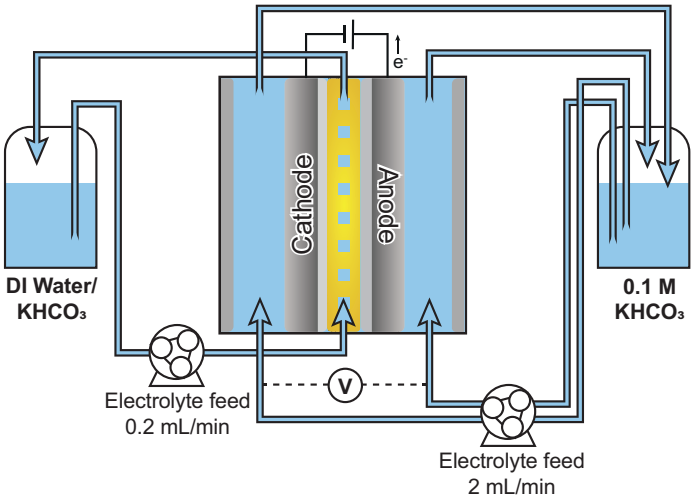

Figure S4.4: Schematic of the membrane resistance measurement. The AEM with internal microchannels (yellow) is between the anode and the cathode. $KHCO_3$ solutions of varying concentrations were introduced into the left electrolyte reservoir, and a 0.1 M $KHCO_3$ solution was introduced into the right reservoir.

ating conditions can be found in the main text. A schematic illustration of this setup is shown on Figure S4.4.

ELECTROLYSIS EXPERIMENTS

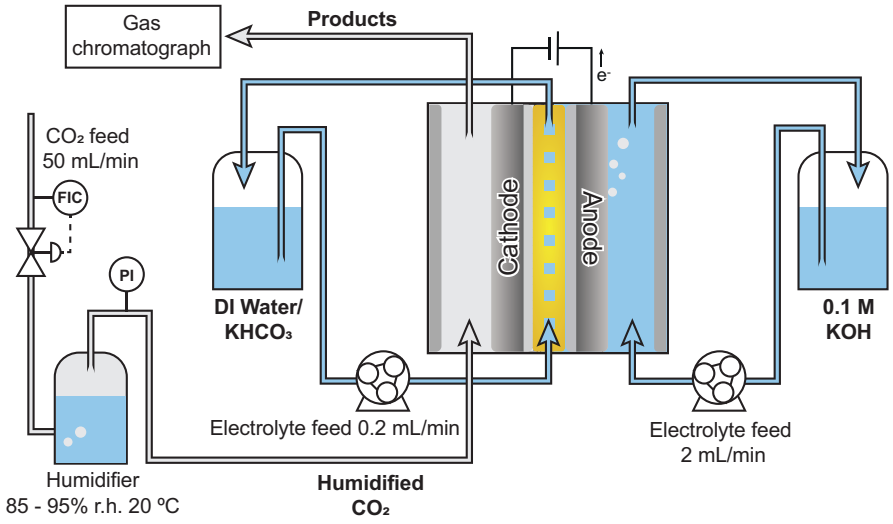

Figure S4.5: Schematic of the electrolysis setup. The AEM with internal microchannels (yellow) is between the anode and the cathode. During electrolysis, $KHCO_3$ solutions of varying concentrations were introduced via the left electrolyte reservoir into the microchannels.

A schematic illustration of the electrolysis setup is shown in Figure S4.5. A humidified CO_2 stream was introduced into the cathode side of the reactor for the electrolysis experiments. The gas stream was humidified by bubbling dry CO_2 through a sparger into a DI water column at room temperature, and the relative humidity was measured with a humidity sensor. A 0.1M KOH solution or a humidified N_2 stream were fed as reactants for the oxygen evolution reaction on the anode side. Linear sweeps of the voltage from 0 to -4 V, while measuring the current, were made in triplicate to assess the effect of the different electrolyte concentrations in the microchannels.

To quantify the K^+ crossover to the cathode side, 0.1 M KOH was fed into the anode channel, and a constant current of 5 mA/cm^2 was applied for 73 minutes. Aliquots of the anolyte and of the electrolyte in the internal membrane channels were taken before and after current was applied. At the end of the experiment, the serpentine flow channels in the cathode plate were rinsed (collecting the liquid), and the cathode GDE was placed in 30 mL of aqueous solution containing 5 mL isopropanol and approximately 1.5 mL of concentrated HCl. This solution was chosen to counter the GDEs hydrophobicity and to dissolve any potassium salts that had deposited. Five aliquots were analyzed using ion chromatography and a mass balance on the K^+ was made.

4.5.3. SUPPLEMENTARY RESULTS

WATER CONTENT DISTRIBUTION AT 2.5 V FOR BASE CASE (SPACING OF 360 µm)

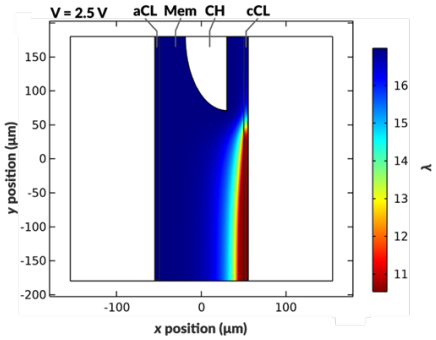

Figure S4.6: Water content distribution in the bilayer AEM with a curved channel geometry and spacing of H = 360 µm. The applied potential for this simulation is 2.5 V.

Figure S4.6 displays the intermediate applied potential of 2.5 V, not shown in Figure 4.3.

WATER CONTENT DISTRIBUTION IN AEMS AT VARIOUS APPLIED VOLTAGES

Figures S4.7, S4.8 and S4.9 show the water content distributions for the AEM without internal microchannels, for the H = 90 µm, and the H = 180 µm cases, respectively.

LOCAL WATER CONTENT AND CURRENT DENSITY FOR AEMS WHERE THE MICROCHANNEL CONTACTS THE CL

Figure S4.10 displays the local water content of the ionomer and the local current density within the across the membrane - catalyst layer boundary, for the case when the channel is modelled adjacent to the catalyst layer (as shown in Figure 4.5a).

ELECTROLYSIS EXPERIMENTS

Note that Figure 4.8 and S4.11 have different scales. The current density achieved for the full MEA is much lower.

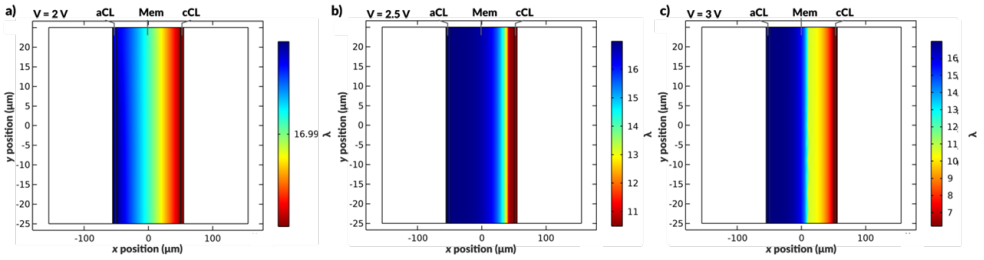

Figure S4.7: Water content distribution in the AEM with no internal microchannels for (a) 2 V, (b) 2.5 V (c) 3 V applied potentials. Note that the figures have different scales.

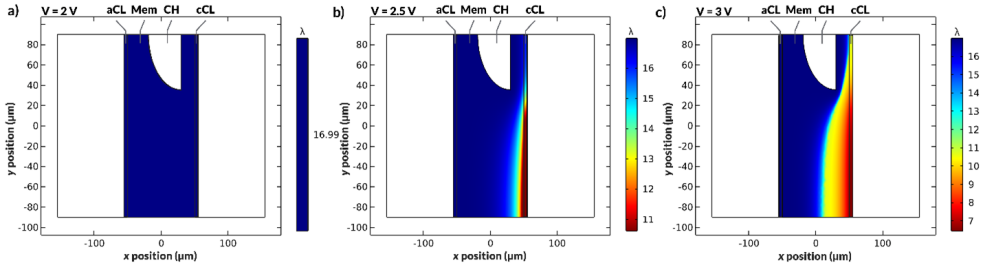

Figure S4.8: Water content distribution in the bilayer AEM with a curved internal channel with channel spacing of H = 180 µm for (a) 2 V, (b) 2.5 V (c) 3 V applied potentials. Note that the figures have different scales. Note that the figures have different scales.

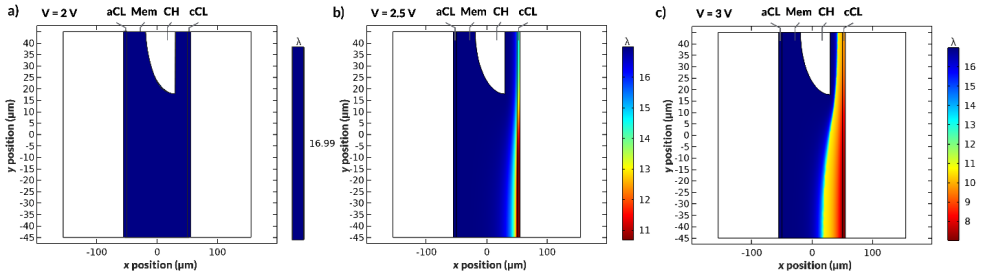

Figure S4.9: Water content distribution in the bilayer AEM with a curved internal channel with channel spacing of H = 90 µm for (a) 2 V, (b) 2.5 V (c) 3 V applied potentials. Note that the figures have different scales.

DONNAN MODEL FOR K^+ CROSSOVER

We can consider an ion exchange membrane, with fixed charge density X, immersed in an aqueous solution with a salt concentration of c. Based on the classical Donnan model, the concentration of co-ions and counter-ions in the membrane, $c_{counter}$ and c_{co} satisfy the following two equations:

$$c_{counter} \cdot c_{co} = c^2 \tag{S4.20}$$

$$c_{counter} + c_{co} = \sqrt{X^2 + (2c)^2} \tag{S4.21}$$

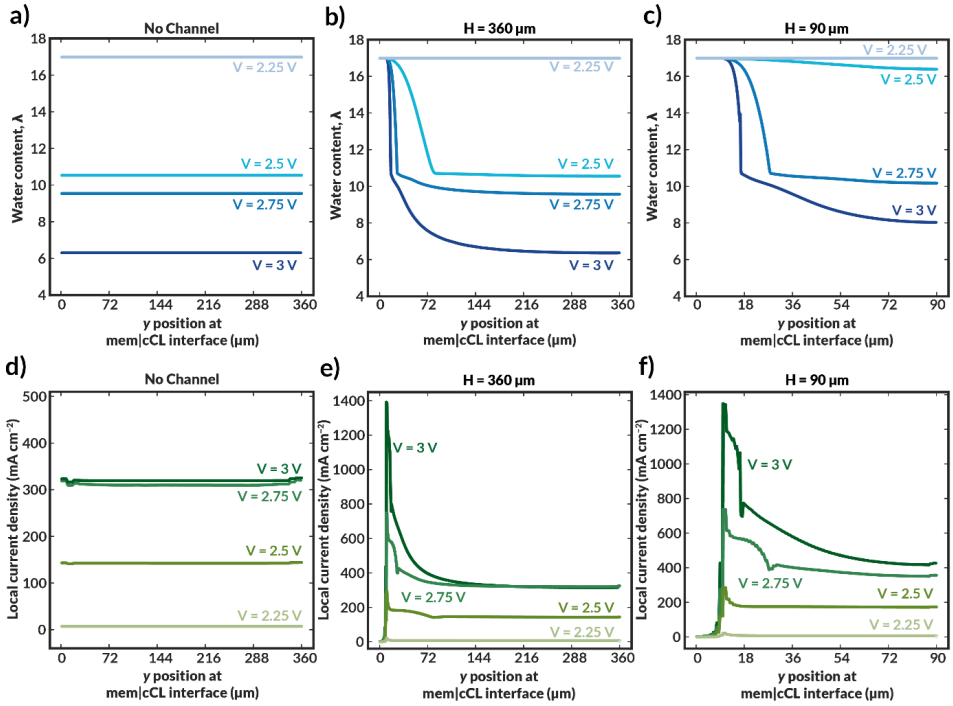

Figure S4.10: (a-c) Local water content of the ionomer within the cathodic CL averaged across the CL thickness for varying channel geometries and spacings for AEMs where the microchannel is in directly contact with the CL. (d-f) Local current density within the cathodic CL averaged across thickness of the CL for varying channel geometries and spacings for AEMs where the microchannel is in direct contact with the CL.

Table S4.3: Average faradaic efficiency observed during electrolysis with different electrolyte concentrations in the internal membrane channels, with a liquid anolyte and at 5 mA/cm^2.

C_{in} **(mM)**	**FE (Faradaic Efficiency, %)**
No Channels	58
DI Water	57
10	55
100	62
Average	58

That means the ratio between co-ions and counter-ions can be rewritten as:

$$\frac{c_{co}}{c_{counter}} = \frac{c^2}{X\sqrt{X^2+(2c)^2}-c^2} \tag{S4.22}$$

That means the ratio $\frac{c_{co}}{c_{counter}}$ increases as c increases, which is equivalent to a relatively high sorption coefficient of co-ions in the membrane at high external concentration. This has also been confirmed by experiments.[25]

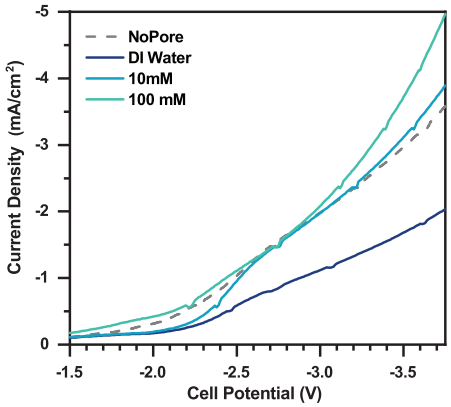

Figure S4.11: Galvanostatic linear sweep experiments with different electrolyate concentrations inside the membrane channels in full MEA configuration, with hydrated N_2 gas as anolyte.

5

THIN-FILM COMPOSITE MEMBRANES FOR CARBON EFFICIENT CO_2 ELECTROLYSIS

CO_2 electrolysis is a promising technology to produce sustainable fuels and chemicals out of air-captured carbon. However, most electrolyzers suffer from carbonate crossover, which limits the efficiency of the carbon usage and forces the use of rare-earth anode materials. In this chapter, we attempt to tackle this issue by fabricating a thin-film composite membrane (TFCM), with a selective layer to reject carbonate. The selective polyamide layers were synthesized on the surface of commercial anion-exchange membranes (AEMs). We studied the effect of different polyamide chemistries, the curing step and the monomer concentration on the CO_2 electrolysis process. Our preliminary experiments showed a significant increase in OH^-/CO_3^{2-} selectivity when using an AEM geared for electrodialysis as a support, but this result was not reproduced with electrolysis-suitable AEMs. Nevertheless, we show that the ionic conductance of these membranes can be optimized by manipulating the organic phase-monomer concentration. Lowering the aqueous phase monomer concentrations past a certain point (<0.2 %) no longer leads to polyamide film formation. Additionally, we unveiled other challenges related to the incorporation of TFCMs in CO_2 electrolyzers, such as the increased hydrogen production likely due to pH changes, and salt deposition due to increased carbonate concentrations in the catalyst microenvironment. Our results show that these challenges may be avoided by introducing a catholyte layer.

Parts of this chapter have been submitted for patenting by K.V. Petrov and D.A. Vermaas, as "Thin-film composite membrane for CO_2 electrolysis". 2022, Dutch Pat. App. No. 2033215.

5.1. INTRODUCTION

Electrochemical CO_2 reduction (CO_2R) stands as a promising avenue for the sustainable generation of carbon-based fuels and chemicals.[1] This process involves the application of an electric potential to an electrolyzer, enabling the cathodic electrochemical reduction of CO_2 and water to yield a spectrum of products such as carbon monoxide (CO), formate, ethylene, and other derivatives, depending on the catalyst employed.[2] Simultaneously, the anodic oxidation of water typically produces oxygen. State-of-the-art electrolyzers often use a zero-gap configuration, employing porous electrodes directly pressed against an anion-exchange membrane (AEM), also referred to as a membrane-electrode assembly (MEA), thereby significantly reducing inefficiencies in mass transport. The utilization of gas-diffusion electrodes (GDEs) on the cathode side allows the direct delivery of gaseous CO_2 to the catalyst layer, which is an advantageous feature given the limited solubility of CO_2 in water.[1]

Having achieved current densities and Faradaic effiencies (FEs) approximating commercial standards, the focus has now shifted to critical parameters such as stability, energy efficiency, CO_2 utilization, and the availability of materials. Serving as a conductive medium and a barrier between the CO_2 conversion at the cathode and the oxygen evolution reaction (OER) at the anode, the ion-exchange membrane (IEM) plays a central role in determining performance, selecting suitable materials, and ensuring the overall stability of the system configuration.

Ideally, the AEM would transfer hydroxide ions (OH^-) from the cathode to the anode, where they would be consumed in the oxygen evolution reaction (OER). However, AEM-based electrolyzers encounter a significant hurdle wherein the incoming CO_2 reacts with OH^- ions, resulting in the formation of (bi)carbonates.[3] Thus, carbonates are the main charge carrier, being transported through the AEM to the anode compartment.[4, 5] The carbonate crossover imposes limitations, preventing an alkaline environment at the anode without electrolyte regeneration, thereby mandating the use of iridium-based catalysts for the OER.[6] However, iridium's scarcity and escalating costs pose significant challenges for scaling up operations.[7] Furthermore, CO_2 crossover restricts the single pass utilization of CO_2 to 50% or less, depending on the product (CO – 50%, C_2H_4 – 25%).[8] This limitation incurs an indirect energy penalty since concentrated CO_2 is a valuable resource, and its separation from O_2 is not a straightforward process, due to the molecules' apolarity and similar size.[9]

Known alternatives for AEMs in CO_2 electrolyzers are cation-exchange membranes (CEMs) and bipolar membranes (BPMs), which can in turn be operated in reverse bias or forward bias.[10, 11] CEM and forward bias BPM systems require the use of acidic anode conditions, therefore, like the AEM, require the use of the scarce Ir as anode material. BPMs in reverse bias require a larger cell potential to sustain the water dissociation over the BPM and the pH gradient between the cation exchange layer and the catalyst layer (further elaborated upon in Chapter 6).

As a solution to the carbonate crossover issue in CO_2 electrolysis, we propose a multi-layer system comprising an AEM for OH- conductivity and a thin selective layer for CO_3^{2-} rejection (Figure 5.1). This TFCM, employs a polyamide selective layer, which is typically used in reverse-osmosis (RO) and nanofiltration (NF) applications. RO and NF are often used for water purification treatments, with RO aiming at producing pure water by removing virtually all solutes, and NF providing a high rejection for multivalent ions, but being mostly permeable to monovalent ions.[12, 13] Both these membranes reject solutes based on two mechanisms: size exclusion and charge repulsion (Donnan exclusion).

In order to optimize membrane performance we must maximize CO_3^{2-} rejection and OH^- permeability. It is possible to separate these molecules based on their size, since CO_3^{2-} has a hydrated radius of 3.94 Å, and OH^-, 3.0 Å.[14, 15] Alternatively, they can be separated by the charge since, e.g. NF membranes can reject bivalent ions but allow monovalent ions to permeate, or a combination of both size and charge. However, the polyamide layers were developed for vastly different applica-

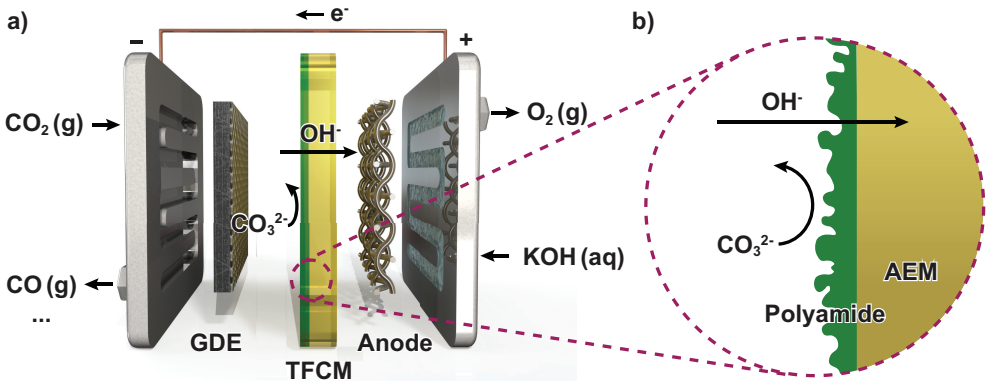

Figure 5.1: a) schematic illustration of a CO_2 electrolyzer employing a TFCM. b) zoom-in into the TFCM, showing its two comprising layers.

tions and their properties depend on local parameters such as pH and electrolyte concentrations. Both RO and NF are pressure-driven processes, therefore the polyamide layers are not optimized to be ion-conductive. Since in CO_2 electrolysis the driving force is the electric field and energy efficiency is a very important parameter, the polyamide layer's properties must be optimized for the new application.

Shi et. al.[16] used RO membranes for direct seawater electrolysis and found it performs decently in terms of ionic resistance and possessed promising selectivity for protons over other cations when using concentrated electrolytes. Similarly, Dai et. al.[17] used a TFCM for vanadium redox-flow batteries and observed both a higher conductivity and a higher selectivity than achieved with a Nafion 115 CEM. These studies underscore the potential of integrating such polyamide layers in electrolysis applications.

The goals of this work are: 1) to study how monomer concentrations and polyamide chemistry affect carbonate rejection and the membrane's ionic resistance; 2) how the polyamide layer and carbonate rejection influence the reaction microenvironment and overall CO_2 electrolysis process performance. This study was done by carrying out an interfacial polymerization reaction with different monomers and concentrations, to produce a polyamide layer on the surface of commercial AEMs, characterizing them, and testing their performance in CO_2 electrolysis.

5.2. EXPERIMENTAL METHODS

5.2.1. MEMBRANE MODIFICATION

Polyamide synthesis is generally done by an interfacial polymerization. It is called "intefacial" because it occurs between two phases - an aqueous and an organic phase. When coating a membrane, the amine monomer in the aqueous phase is embedded in the membrane itself, any excess is removed and then the organic phase with the acyl chloride monomer is added on top, so the interface is the membrane surface (Figure 5.2).[18] The interfacial polymerization reaction then occurs at the surface of the membrane itself, synthesizing a polyamide layer. This reaction is very fast and self-limiting, typically producing polyamide layers with 0.1 - 1 µm in thickness.

The support structure is generally a (micro)porous support, likely polysulfone.[18] However, in this study, the support was an AEM, which is a dense membrane. Additionally, the AEM has charged functional groups which have a counter-ion, and these charges could potentially interact with the

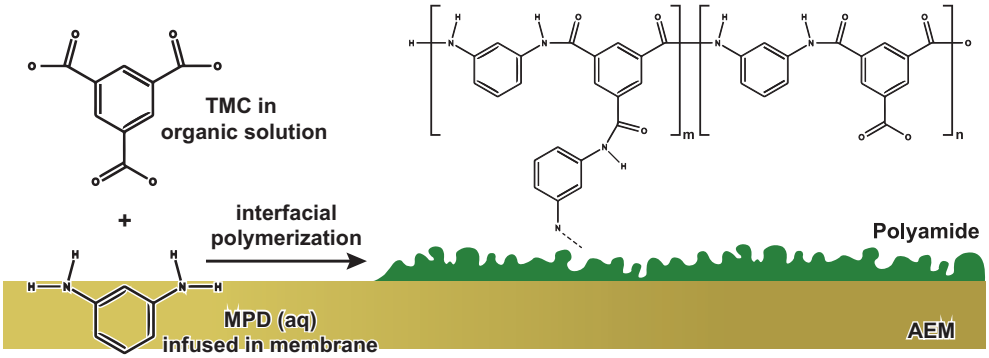

Figure 5.2: Schematic illustration of the interfacial polymerization process for modification of AEMs. [19]

monomers during the polymerization reaction.

In our case, the supporting membrane was a Selemion AMV (AGC, Japan) (in Cl^- form) for the preliminary experiments, and a Sustainion X37 (Dioxide Materials, Florida) (in OH^- form) for the remaining experiments. The membrane was initially rinsed with deionized (DI) water, placed on a flat surface, and completely covered by the aqueous amine solution for 7 minutes to allow it to diffuse into the membrane. For RO-based polyamides the amine is m-phenylenediamine (MPD), and for NF-based it is piperazine (PIP). After these 7 minutes the excess solution solution was removed by drying with nitrogen until it appeared dry but still shiny. This process was improved for later experiments by using a metal roller since uniform drying only with nitrogen proved to be a challenge. Next, the organic solution with the benzene-1,3,5-tricarbonyl chloride, also known as trimesoyl chloride (TMC), was added on top. The organic solvent for RO-based polyamides was cyclohexane and for NF-based polyamides it was n-hexane.[20, 21] After 1 minute of polymerization, the organic solution was removed and the membrane was cured in the oven at 55 °C for 7 minutes. Succeeding the curing procedure, the resulting TFCM was thoroughly rinsed to remove any remaining unreacted monomers and stored in DI water.

5.2.2. MEMBRANE CHARACTERIZATION

Fourier-transform infra red (FTIR) spectra were obtained using a Nicolet™ iS™ 10 FTIR Spectrometer, in order to confirm the presence of the polyamide layer.

Scanning electron microscopy (SEM) images were taken using the JSM-6010 electron microscope (JEOL). The majority of the images were taken at low accelerating voltages (5-8 kV). These images were used to examine the morphology and thickness of the formed structure.

IONIC RESISTANCE

The ionic conductivity was measured in a 4-electrode 6-compartment configuration setup, displayed in Figure 5.3. The electrodes at the outer ends of the setup were used to apply a current through the entire setup, and two reference were connected to Luggin capillaries which were placed very close (< 1 mm) to the membrane, to measure the membrane potential. An 0.1 M solution of K_2SO_4 was circulated in compartments 1 and 6 to avoid undesired reactions. At the anode and cathode, OER and HER occurred, respectively. Since these reactions produce OH^- and H^+ ions which can interfere with the measurement, a buffer solution (0.1 M K_2PO_4) was circulated in compartments 2 and 5. In compartments 3 and 4, the electrolyte in which the ionic conductivity was measured was circulated. This was either 0.1 M KOH or 0.1 M K_2CO_3. The expectation of this exper-

iment was that the polyamide layer would significantly increase the resistance in CO_3^{2-}, but not in OH^-.

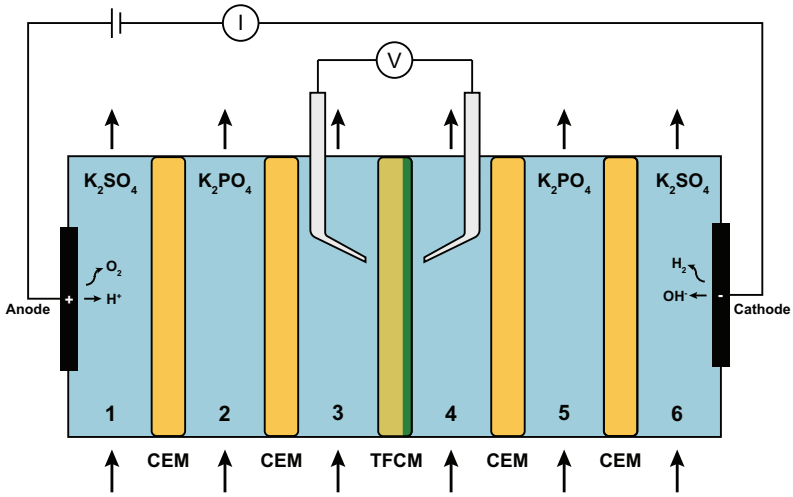

Figure 5.3: Schematic illustration of the 4-electrode, 6-compartment configuration setup used for ion crossover and ionic resistance measurements.

The membrane was placed between compartments 3 and 4, in a holder with 9.62 cm^2 open area. To avoid significant concentration polarization, the solutions were kept flowing at 40 mL/min. The electrodes were connected to an Autolab PGSTAT 128 N potentiostat (Metrohm, Switzerland), which was used to sweep the current with a scan rate of 10 mA/s. The linear sweep was performed 5 times, and subsequently, a blank measurement was taken of the electrolyte without a membrane in the holder.

OH^-/CO_3^{2-} SELECTIVITY

The setup shown in Figure 5.3 was also used for the OH^-/CO_3^{2-} selectivity experiments. In this case, a solution containing both OH^- and CO_3^{2-} was circulated in compartment 4, and a KCl solution in compartment 3. In the preliminary experiments, due to the high resistance of the membranes, the concentrations were 0.25 M NaOH and 0.25 M Na_2CO_3 in compartment 4, and 0.5 M KCl in compartment 3. In the remaining experiments, a solution with 0.0 5M KOH + 0.05 M K_2CO_3 was in compartment 4, and 0.1 M KCl was in compartment 3. A constant current was then applied to force the anions from compartment 4 to migrate into compartment 3, that has no initial alkalinity. Before the experiment a 20 mL sample was taken from the containers with the solutions pertaining to compartments 3 and 4. A constant current of 0.2 A was then applied for a calculated amount of time necessary to observe a 50% change in OH^- concentration. The time-frames necessary were between and 1.5 and 2.5 hours, depending on the concentrations of the solutions and the resistance of the membrane. At the end of the experiment, two more 20 mL samples were taken from compartments 3 and 4.

The obtained samples were titrated using an 848 Titrino plus (Metrohm, Switzerland) with an 0.05 M HCl solution. The titration curve allowed the estimation of the OH^- and CO_3^{2-} amounts which crossed through the membrane into compartment 3.

5.2.3. CO_2 ELECTROLYSIS

A schematic illustration of the electrolysis setup is shown in Figure 5.4. The electrolyzer, similar to what has been described by Montfort et. al.[22], consists of: two backplates with a flow channel - on one side the humidified CO_2 (85-95% humidity) was flown at 50 mL/min, and on the other side the 0.1 M KOH anolyte, circulated at 20 mL/min; a GDE coated with 1.05±0.1 mg/cm^2 of Ag nanoparticles, and 10 wt% Sustainion ionomer used as cathode; a Ni foam or Ti coated with Ir mesh as anode; the TFCM; and an optional catholyte (3M K_2CO_3) layer, with 1.8 mm thickness, which can be placed between the cathode and the TFCM. The TFCM was stored in DI water before usage. Once everything is assembled, the backplates are tightened to 3.0 Nm. A constant current was applied using an Ivium XP20 potentiostat, while measuring the cell potential. The gas products from the cathode compartment were analyzed using a CompactGC4.0 (Interscience, the Netherlands) gas chromatograph (GC), which was connected in-line.

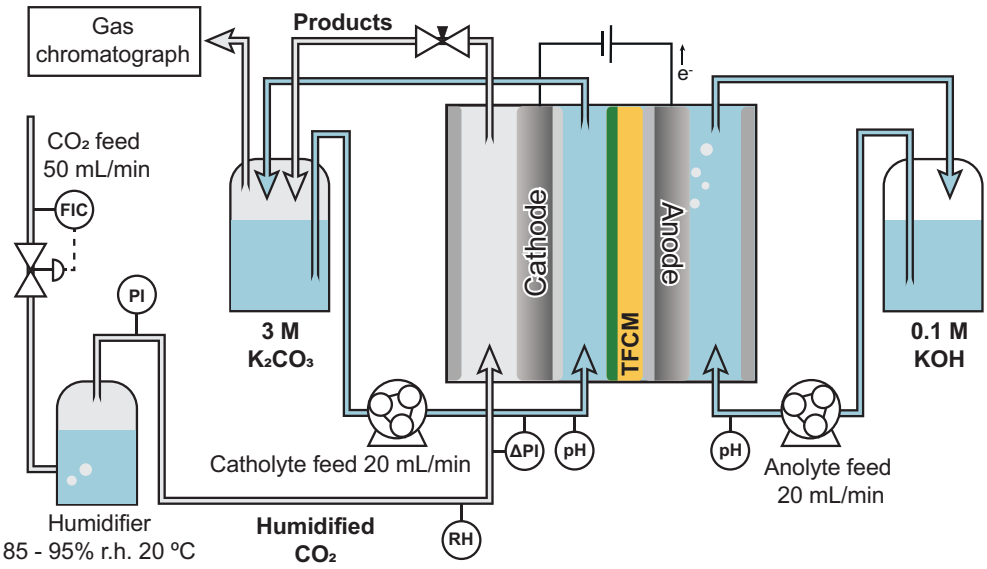

Figure 5.4: Schematic of the CO_2 electrolysis setup.

In the initial CO_2 electrolysis experiments, the gas produced by the anode was also measured by the GC. However, since we start with 0.1 M KOH, CO_2 evolution only begins after about 1 hour. Therefore, in later experiments we added in-line pH meters in both the catholyte (when used) and anolyte. In order to avoid flooding when a catholyte was used, the back pressure in the gas-channel was controlled using a needle valve at the outlet, and a differential pressure meter between the catholyte and gas channel inlets.

5.3. RESULTS AND DISCUSSION

5.3.1. PRELIMINARY EXPERIMENTS

Because this is a novel concept, we initially did not know if the polyamide synthesis would be possible on a dense membrane, as is the AEM. Therefore, we started by using a Selemion AMV membrane because of its lower price, higher mechanical strength and anion selectivity compared to the membranes typically used for electrolysis.[23] Nevertheless, the first synthesis of an RO-based

polyamide layer was faintly observable by the naked eye and seemed to not be easily removed by handling and rinsing.

We then measured the ionic resistance in 0.1 M $KHCO_3$ and saw an approximately 30 times increase in resistance after addition of the polyamide layer (Figure S5.1). After this clear indication that a modification had occurred, we measured the crossover of CO_3^{2-} and OH^- through a non-modified AEM, and TFCMs synthesized with different monomer concentrations (Figure 5.5).

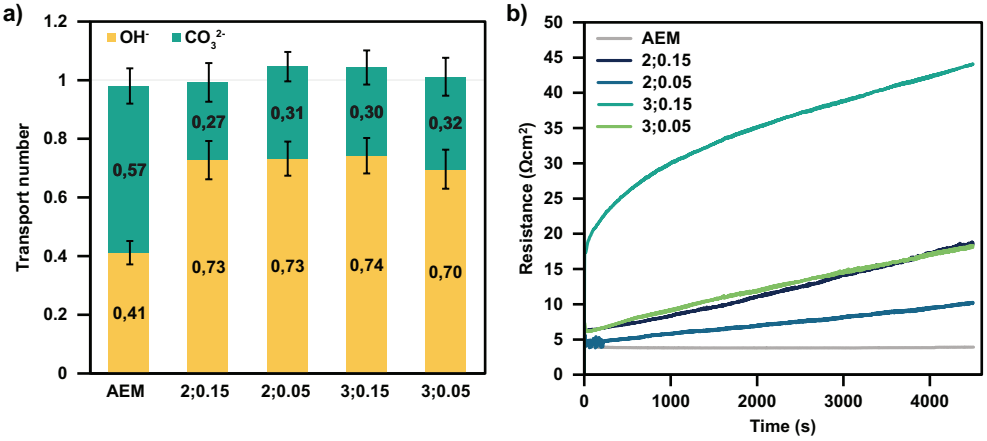

Figure 5.5: a) transport numbers of OH^- and CO_3^{2-} ions resulting from crossover experiments. The *x*-axis shows the monomer concentration with which the TFCM was fabricated, in MPD;TMC format, in w/v%. b) ionic resistance during the crossover experiments, with the legend indicating the monomer concentrations.

Figure 5.5a shows that the transport number of OH^- increases from 41 % to approximately 73 % for all modified membranes. This proves that the polyamide layer can influence the transport through the membrane, and increase OH^- selectivity. However, no relationship was observed between the concentration of monomers and the transport numbers, since all of the TFCMs show similar transport numbers.

Figure 5.5b shows the change in ionic resistance during the crossover experiments. We observe that the resistance of TFCMs is much larger than the non-modified AEM's throughout the entire experiment. Additionally, while the AEM resistance remains constant, the TFCM resistance is increasing over time. This could be because of accumulation of CO_3^{2-} within the polyamide structure. Such an accumulation would imply that operation with these membranes requires a backwashing step, as done in RO.

Although the concentration of monomers did not influence the OH^- selectivity, it seems to have a large effect on resistance. The polyamide layers made with more concentrated monomer solutions clearly show a larger resistance, with both monomers having a contribution.

It is important to note that over time, we found oxidation evidence of the MPD monomer. Figure S5.2 shows a 2 to 5 times increase in resistance (depending on the used MPD concentration) of the later batches of TFCMs, after a new MPD flask had been purchased. Therefore, the resistance values shown in Figure 5.5b are possibly under-estimated and not completely reliable.

As an attempt to increase the rejection of CO_3^{2-}, the membranes were dip-coated to obtain a coating on both sides, instead of only applying the coating on one side. The resulting OH^-/CO_3^{2-} selectivity and resistance are shown in Figures 5.6a and 5.6b, respectively. It can be observed that dip-coating also did not have a significant impact on the selectivity, but it did approximately double the ionic resistance. Therefore, the membranes were only coated on one side in the remaining

studies. The higher resistance observed in this graph compared to Figure 5.5 is owed to the renewed monomer.

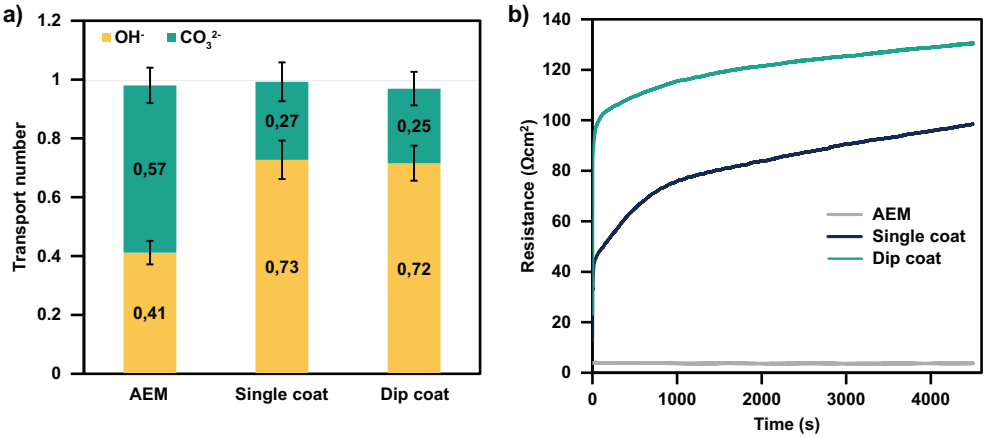

Figure 5.6: a) transport numbers of OH^- and $CO_3{}^{2-}$ ions resulting from crossover experiments of dip-coated and single-coated TFCMs. b) ionic resistance during the crossover experiments, of non-modified AEMs, and single-coated and dip-coated TFCMs.

Because these RO-based TFCMs showed increased OH^- selectivity, the preliminary experiments were deemed successful. However, the resistance of the TFCM was considerably high, which is not convenient for application in electrolysis, as the larger ohmic resistance will significantly decrease the energy efficiency of the process. Therefore, in the following projects we manipulated the monomer concentration in a larger span of concentrations, to study how much the resistance can be optimized.

Although the interfacial polymerization reaction is very hard to study because of its fast kinetics and very thin (50-200 nm) resulting films, it is described to occur mostly in the organic phase since MPD has a higher mobility in the organic solvent than TMC in aqueous solutions. As the polyamide polymer forms, further diffusion of MPD into the organic phase is limited, resulting in the thin-film. However, the final step of this reaction is cross-linking which can take longer time and is known to be influenced by the monomer concentration, reaction time and curing temperature, among other parameters.[19, 24] Since cross-linking can determine salt rejection and water permeability for RO membranes, we believe we should further study the impact of the monomer concentration despite not having observed noticeable effect within the range shown in Figure 5.5.

5.3.2. STUDY OF MONOMER CONCENTRATION

After the proof of concept, Sustainion X37 membranes were modified with different monomer concentrations in order to optimize the conductivity, and to increase the OH^- selectivity.

Firstly, a membrane was modified with typical monomer concentrations found in literature (1% MPD and 0.1% TMC), to prove that the expected structure was formed. The resulting TFCM was characterized using FTIR spectroscopy and SEM. The FTIR results confirmed the expected polyamide presence (Figure S5.3). SEM images can be seen in Figure 5.7.

Figure 5.7a shows the SEM picture of the non-modified AEM. It has a smooth surface without any visible features, even at higher magnifications. Meanwhile, the modified AEM, shown on Figure 5.7b, has a distinguished rugged surface. This structure is similar to other polyamide structures shown in literature.[13, 20] Combined with the preliminary experiments and the FTIR results

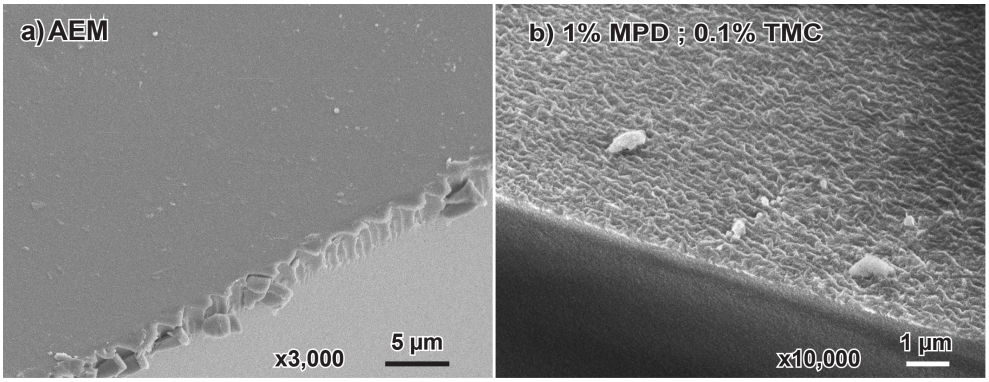

Figure 5.7: SEM images at a 45 ° angle of a) a non-modified AEM and b) a TFCM made with 1 % MPD and 0.1 % w/v TMC. The magnification and the scale are indicated on the legends.

(Figure S5.3), this proves that polyamide structures can be synthesized on dense IEMs, despite the uncertainty of the amount of amine monomer that actually gets embedded in the support.

Next, a set of membranes were modified with a low MPD concentration, to see its effect on the polyamide structure. Figures 5.8a and 5.8b show the structure obtained with 0.1 w/v% MPD and 0.02 w/v% TMC, and 0.1 w/v% and 0.06 w/v%, respectively. Both polyamide layers do not cover the entirety of the surface, and did not form a uniform film. Instead, they show smaller agglomerated structures. The first TFCM has round agglomerates of approximately 5 µm in size. The second TFCM which has the same MPD concentration but a higher TMC concentration, shows smaller and more dispersed agglomerates. Structures without a uniform film coating were not expected to show any carbonate rejection, and therefore were not electrochemically characterized.

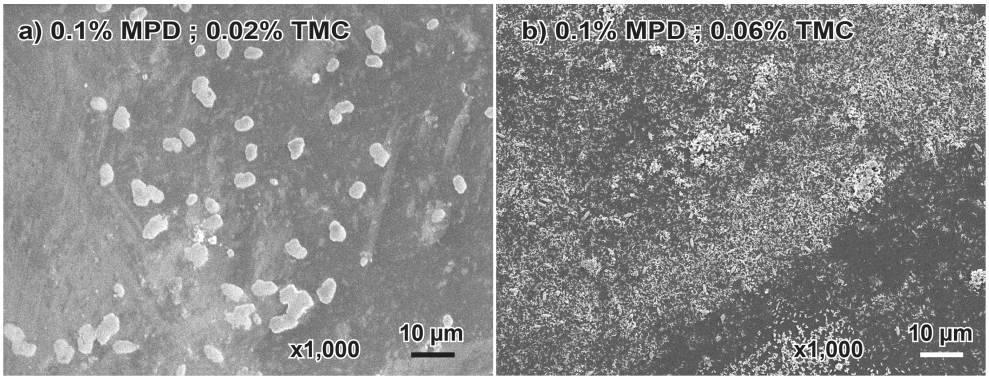

Figure 5.8: Top view SEM images at 1000 times magnification, of TFCMs made with 0.1 w/v% MPD and a) 0.02 w/v% TMC, and b) 0.06 w/v% TMC.

Afterwards, we fixed the MPD at 2 w/v% and lowered the TMC concentration from 0.2 to 0.002 w/v%. Figure 5.9 displays the result of these modifications, showing that all of them produced uniform films that cover the surface of the AEM, even at the lowest tested TMC concentration. This is evidence that TMC is a better lever to manipulate ionic resistance than MPD, since lowering its concentration doesn't prevent the polyamide layer from forming.

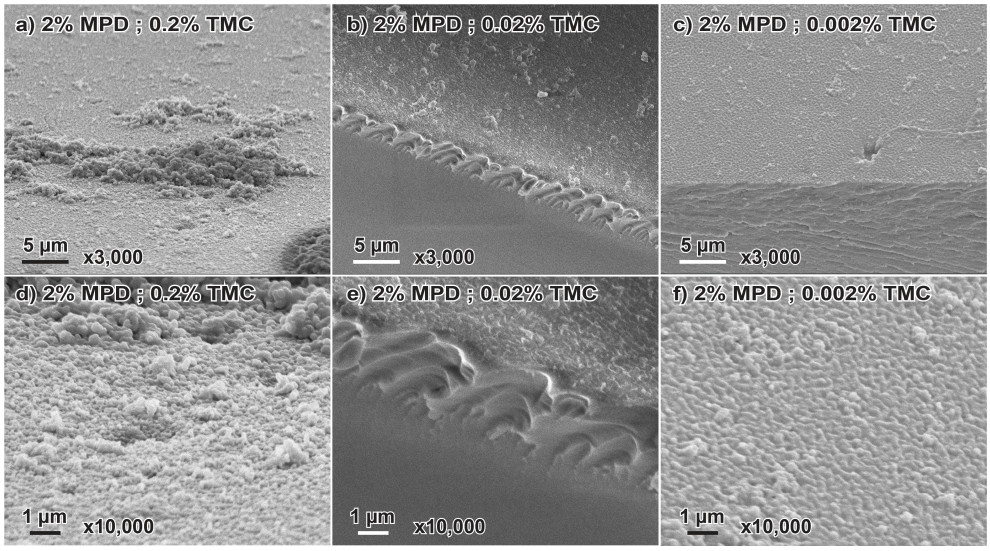

Figure 5.9: SEM images at a 45° angle of of TFCMs made with 2 w/v% MPD and: a) and d) 0.2 w/v% TMC; b) and e) 0.02 % w/v TMC; c) and f) 0.002 w/v% TMC. Figures a-c) are at 3,000× magnification, while figures d-f) show a zoom-in at 10,000× magnification.

At the highest concentration of TMC (shown in Figures 5.9a and 5.9d), cauliflower-like structures which sit on top of the polyamide films were observed. We hypothesize that these structures can be formed by improper drying - if microdroplets of water remain on the surface of the membrane before the addition of the organic phase, the interface where the polymerization will take place will be the surface of these microdroplets and not the membrane surface. We believe that the removal of the water phase is more challenging than in porous supports and that it is imperative to do it thoroughly to avoid such imperfections. Alternatively, the structures can be formed by local mixing when adding the organic phase, or in places where the initial film had defects which allow the amine monomer to pass through the film and react with unreacted TMC - which would likely not be the case at lower TMC concentrations.

The three monomer concentrations lead to slightly different polyamide morphologies with the lowest TMC concentrations originating larger less sharp structures. Although this appears beneficial for carbonate rejection, this film also has more defects which can compromise its selectivity.

The SEM images were taken at a 45° angle to allow the estimation of the selective layer thickness. Although the boundaries of the layer were not clearly visible even when looking at the cross-section of the membrane (Figures 5.9b and 5.9e), the thickness of is less than 200 nm, with some variations due to the irregular structure (see Figure S5.4). This value is in line with other reported values in literature (50 - 200 nm), and likely indicates a multi-layer void structure.[25]

In summary, the SEM images indicate that there is a limit in monomer concentration below which the polyamide layer no longer forms, and this limit is mainly governed by the MPD concentration. Therefore, we believe it is best to ensure sufficient MPD concentration, and use TMC as a lever to control polyamide structure properties. Nevertheless both monomer concentrations should be optimized based on the TFCM performance.

We measured the ionic resistance of the TFCMs made with 0.2 or 2 w/v% MPD with varying TMC concentrations in 0.1 M KOH and in 0.1 M K_2CO_3. The expectation is that if the membranes reject

CO_3^{2-} but allow OH^- to permeate, they will exhibit a much lower resistance in KOH.

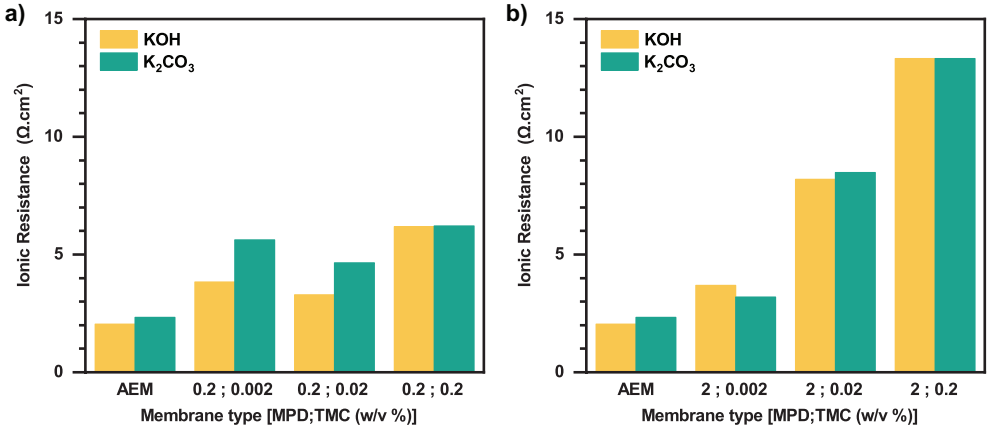

Figure 5.10: Ionic resistances of a non-modified AEM and TFCMs with made with varying TMC concentrations from 0.002 to 0.2 w/v%, and a) 0.2 % MPD, b) 2 % MPD.

Unlike the preliminary experiments (Figure 5.5), the TFCMs prepared on Sustainion membranes showed a constant resistance over time, even when measured in K_2CO_3 solutions. Figure 5.10 shows the ionic resistances of different TFCMs in KOH and K_2CO_3. The ionic resistance has been successfully decreased to values close to those of a non-modified AEM by changing the support membrane and reducing the TMC concentration used to synthesize the polyamide layer. The resistance increases with increasing TMC concentration. However, contrary to expectation based on the presence of the polyamide layer and the preliminary experiments, no significant improvement in OH^- selectivity was observed after the modification of these membranes, but two cases may be promising due to their relative higher resistance in . The largest difference in resistance between KOH vs. K_2CO_3 was observed for the 0.2;0.002 and 0.2;0.02 membranes - 47 and 41%, respectively, compared to 14% for the bare AEM. It appears the ratio between monomer concentrations also plays a role, with the MPD monomer being 100 times more concentrated than the TMC monomer leading to larger carbonate rejection, but these small differences scan also be within the experimental error margins. While we are not sure why no significant carbonate rejection was observed for the other cases, it is that it is related to large pore size distributions or defects. Perhaps the amount of defects observed in the SEM images is significant enough to not grant rejection of carbonate. Selectivity is highly influenced by defects, while ionic resistance is determined by area-averaged properties. Alternatively, it could be a chemical compatibility issue between the the Sustainion support and the formed layer or one of the monomers.

Nevertheless, CO_2 electrolysis experiments were performed with these membranes to study the influence of the polyamide layers on the reaction microenvironment and cell performance. These experiments are also an opportunity to test the membranes' OH^- selectivity in practical application. This is done by starting with a pure KOH anolyte, and monitoring its pH over time. If carbonate crosses over the membrane, the pH in the anolyte will be lowered, allowing us to quantify the carbonate transport number.

Figure 5.11a shows the cell potentials obtained when operating a CO_2 electrolyzer with an AEM or two different TFCMs. The operation with the non-modified membrane yielded stable cell potentials at each applied current density, and with consistent values to literature. Operating with a TFCM produced larger cell potentials, with the membrane made with higher monomer concentrations, be-

ing related to larger cell voltages, as expected from the resistance measurements. Interestingly, the increase does not have the linear relationship with current density as expected of an ohmic resistance. The increase in voltage seems linear between 10 and 50 mA/cm^2, but it is then reduced at larger current densities. In the previous experiment, the ionic resistance curve was measured only up to ≈ 20 mA/cm^2, so it is likely that the current-voltage curve is not linear past a certain current.

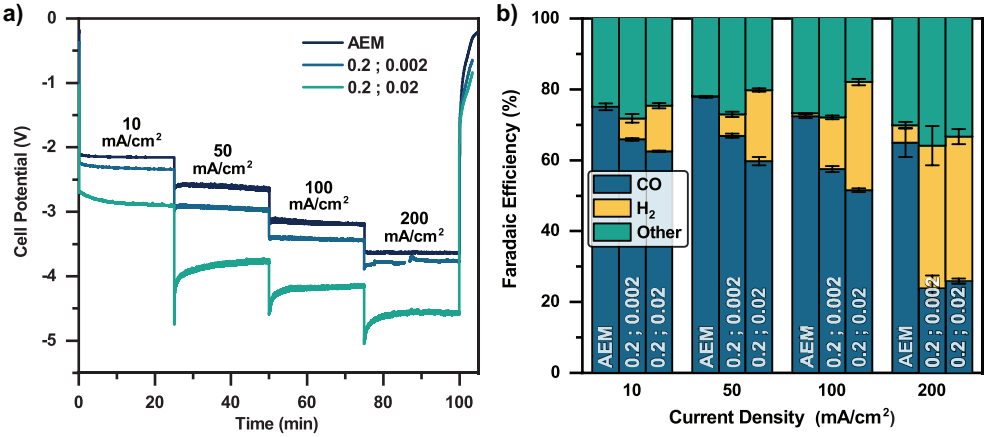

Figure 5.11: CO_2 electrolysis experiments performed with a non-modified AEM, the 0.2;0.002 and 0.2;0.02 TFCMs in a zero-gap configuration. a) cell potential, with the different current densities indicated, b) FEs.

Table 5.1: pH of the anolyte before and after the CO_2 electrolysis experiment.

	Starting pH	Final pH
AEM	12.98	9.51
0.2 ; 0.002	12.96	9.61
0.2 ; 0.02	12.95	9.33

Figure 5.11b shows the impact on the FE of using a TFCM, at different current densities. The products which were not quantified (marked as "other") are mostly composed by formate. Previous experiments in our group have shown that our spray-coated Ag GDEs produce a significant amount of formate. Hence, in this experiment, we expect that the "other" products are mainl formate, which cannot be quantified because it oxidizes back to CO_2 at the anode, due to the low pH of the anolyte. With the non-modified AEM, even at 200 mA/cm^2, only 6 % of hydrogen was produced, the remaining being CO_2R products. When using the TFCMs however, much more hydrogen was produced at all current densities, with the effect becoming increasingly more pronounced with increasing current density. The loss of selectivity to CO_2R products is related to the change in reaction microenvironment. The polyamide layer likely causes a decrease of local pH.[11]

Although a significant role of the polyamide layer was observed in the cell potential and FE, there was no significant change in carbonate crossover as shown by the pH of the anolyte before and after the experiment, as shown in Table 5.1. However, an increased salt deposition was observed at the back of the GDE when using TFCMs, which does indicate that the local carbonate concentration was increased. Another possible explanation for the increased salt deposition would be the less efficient water transport to the cathode from the anolyte.[26].

This section shows that even if the rejection of carbonate is not significant, the presence of the RO-based polyamide layer alters the reaction microenvironment favouring HER and salt deposition, which are undesired effects. In the next section, we will assess the effect of different polyamide chemistries.

5.3.3. STUDY OF POLYAMIDE CHEMISTRY

Different polyamide selective layers were synthesized to study their effect on CO_3^{2-} rejection and on the reaction microenvironment in a CO_2 electrolyzer. To improve the fabrication process, the aqueous solution was removed from the surface of the membrane using a metal roller, and then further dried with N_2. This should avoid the polymerization on the surface of microdroplets. The reaction time was also increased to 3 minutes in order to avoid defects.[27] The monomer concentrations were also increased to 1% of the amine monomer and 0.1% TMC, in order to reduce possible defects in the polyamide layer, and to facilitate the results comparison with literature. The synthesized polyamide layers were RO-based and NF-based, with MPD and PIP as the amine monomer, respectively (the chemical structures can be found in Figures 5.2 and S5.5). The curing step was either 7 minutes at 55 °C, or at room temperature for one week before usage. Heat curing is performed to increase cross-linking and help the termination of the polymerization reaction, which in the RO field is known to increase the water permeability.[19]

Figure 5.12 shows the SEM images of the different polyamide topologies. For both chemistries (NF and RO-based), the curing at room temperature originated much larger elongated structures (Figures 5.12f and 5.12h). These structures could be related to the subsequent polymerization on top of instabilities or defects.[28] Such large structures are not observed when TFCMs with porous supports are cured at (near-)room temperature.[19]

The RO-based layer which was cured in the oven at 55 °C shown on Figures 5.12a and 5.12e, has a very fine structure with small features, barely visible on the lower magnification. However, little to no defects can be observed even at larger magnifications. Meanwhile, the RO-based layer which was cured at room temperature (Figures 5.12b and 5.12f) does have defects - one can be observed near the centre of Figure 5.12b. A different impact was observed for the NF-based membranes. The membrane cured in the oven has plenty defects which are up to 3 µm in size - although they were not consistent, with parts of the membrane having fewer defects than others. Meanwhile, the membrane cured at room temperature has spherical structures of up to 10-20 µm size (Figures 5.12d and S5.6), with an apparent area of thinner polyamide layer around them. However, zooming in the thinner polyamide layer shows no defects.

The two membranes cured at 55 °C were tested in the CO_2 electrolyzer. A part of the NF-based membrane believed to have fewer defects (based on the SEM images) was chosen.

Figure 5.13a shows the cell potentials of the electrolyzer operated with the different membranes. Both TFCMs lead to a larger cell potential than the non-modified AEM. This is likely related to a lower carbonate conductivity, despite full rejection not being observed, since the pH in the anolyte still decreased (Table 5.2). The NF-based membrane exhibited a larger resistance to carbonate, contrary to expectations. RO membranes typically exhibit higher rejection % to all ions. This discrepancy is likely related to defects in the membrane, but the trend is also the opposite of the one observed in the SEM images. Therefore, we believe there is a low control of defects in our process, requiring further optimization.

Both TFCMs decrease the FE_{CO} when pressed against the GDE, as shown in Figure 5.13b. This metric also indicates a larger impact of using an NF- in comparison to the RO-based TFCM. This is likely related to the part of the membrane selected for this experiment, the NF-TFCM having relatively fewer defects. Alternatively, the lower carbonate conductance might be affecting the reaction environment more significantly, or even another reaction could be occurring related to degradation of the polyamide layer.

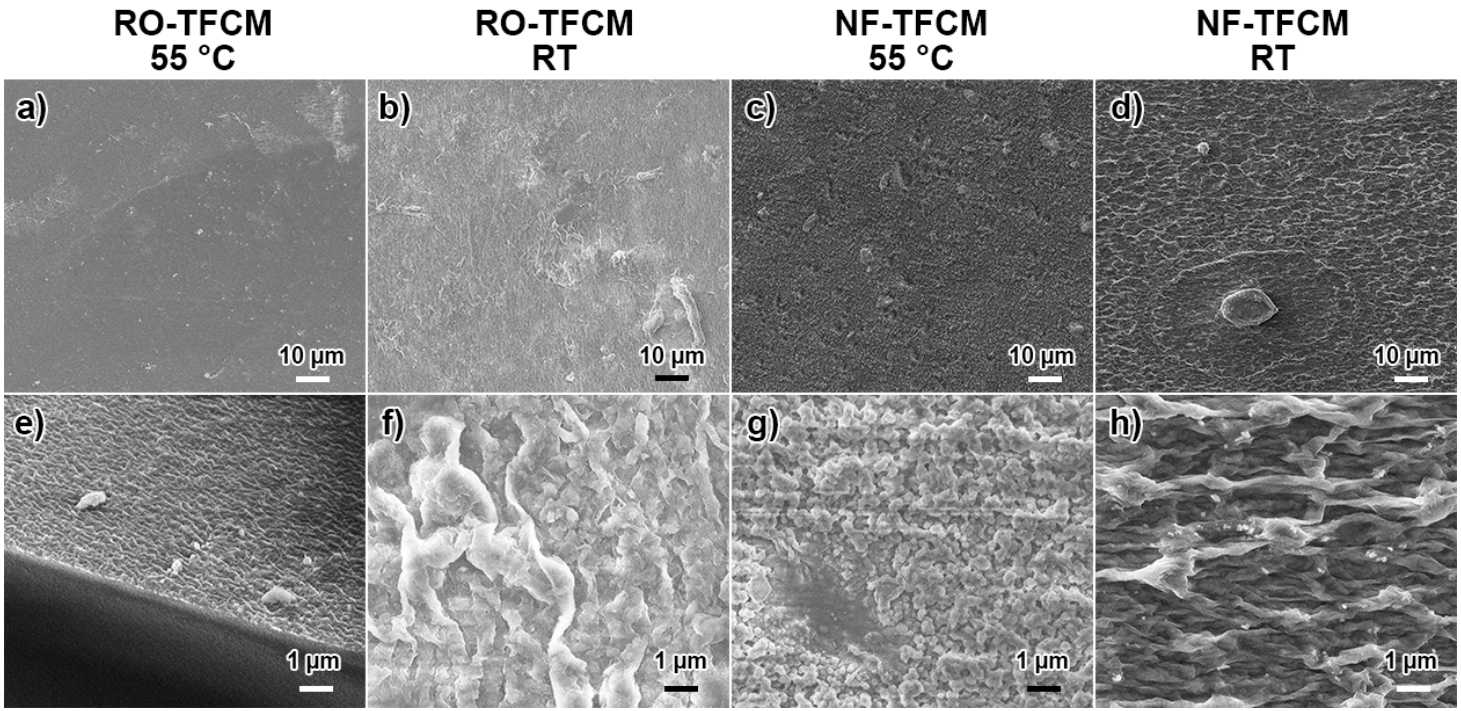

Figure 5.12: SEM images of TFCMs with different polyamide chemistry and curing methodologies (indicated on the top of the figure). Top row (a-d) show the image at 1,000× magnification and the bottom row of images (e-h) are at 10,000× magnification. Image e) was taken at a 45 ° angle at the cross-section

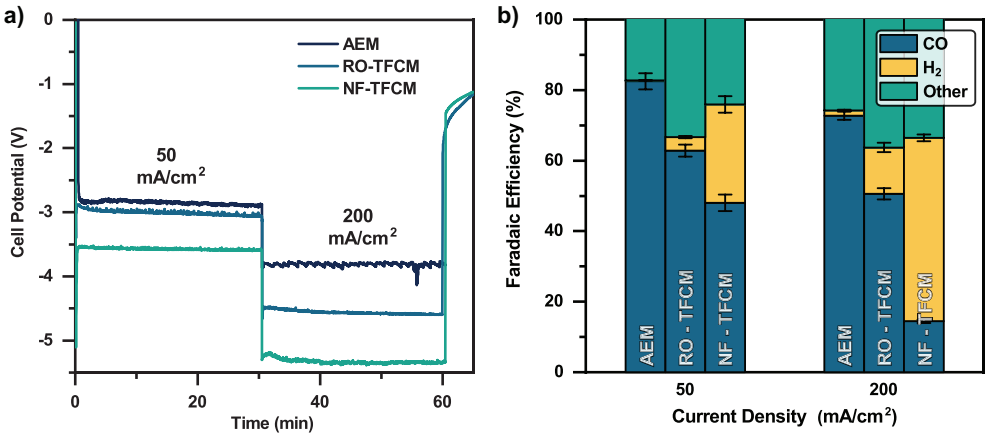

Figure 5.13: CO_2 electrolysis experiments performed with a non-modified AEM, the RO and NF-based TFCMs in a zero-gap configuration. a) cell potential, with the different current densities indicated, b) FEs for different current densities.

5

Table 5.2: pH of the anolyte before and after the CO_2 electrolysis experiment with RO and NF-based TFCMs.

	Starting pH	Final pH
AEM	12.94	7.69
RO-TFCM	13.03	7.34
NF-TFCM	13.04	7.22

Nevertheless, this experiment shows that both polyamide layers decrease the FE for CO_2R products as more hydrogen is produced. This is likely due to local pH changes of the reaction microenvironment or decreased CO_2 transport efficiency due to salt deposition, for example.

5.3.4. ADDING A CATHOLYTE LAYER TO RETRIEVE FARADAIC EFFICIENCY

The last two sections showed that the polyamide layer, independent of its chemistry and the fact that the OH^-/CO_3^{2-} selectivity is not very high, significantly affects the reaction microenvironment in the CO_2 electrolyzer, favoring H_2 production. In order to increase the FE to CO_2R products, we introduced a catholyte layer with 3 M K_2CO_3 in the electrolyzer, and tested all four membranes described in the previous section (Figure 5.14).

Figure 5.14a shows the cell potential of the electrolyzer operated with the different TFCMs. All of the TFCMs lead to a higher cell potential than the non-modified AEM. The two RO-based TFCMs showed a lower cell potential compared to the NF-based ones, as was the case for the zero-gap configuration. The membrane cured at room temperature also showed a lower cell potential compared to their counterparts cured at 55 °C. We can infer that the large structures observed for the room temperature membranes in Figure 5.12 lead to a higher ionic resistance and/or carbonate rejection. However, the membranes cured at 55 °C show an increase in potential over time, which could indicate an accumulation of ions on their surface. This effect is notably more pronounced in the NF-based TFCM.

Figure 5.14b displays the FEs obtained in the CO_2 electrolysis using a catholyte layer experiment. The NF-based membrane performed vastly different in the two configurations. When operat-

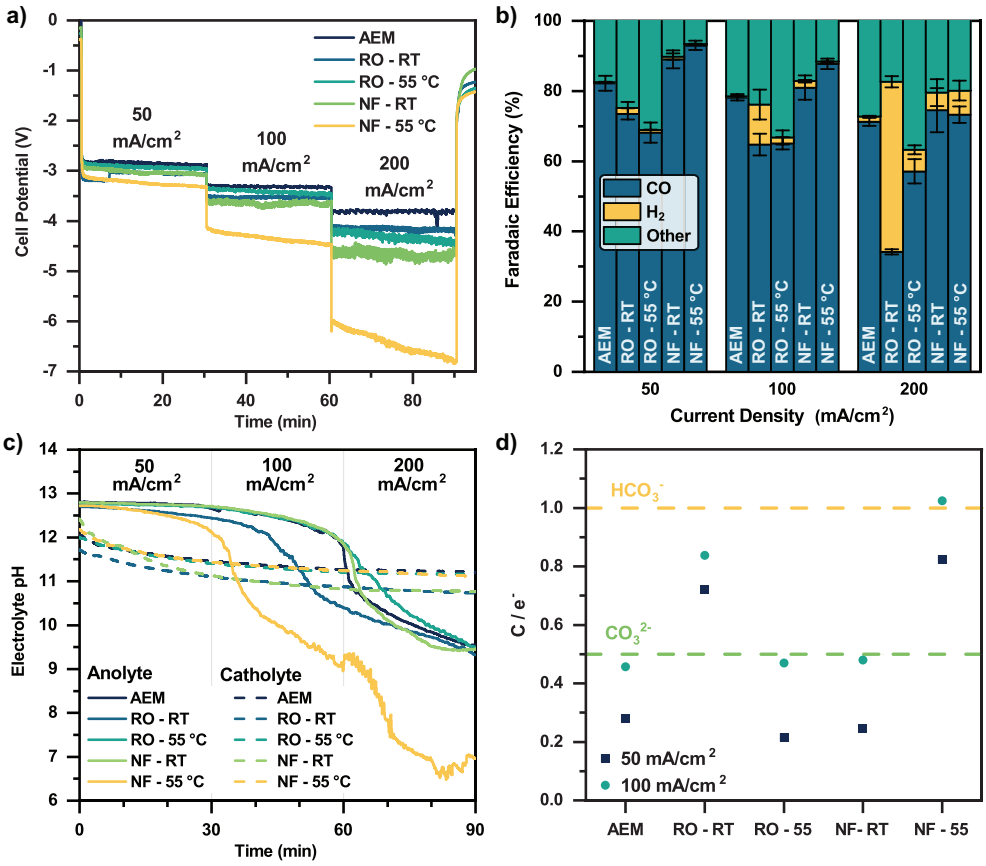

Figure 5.14: CO_2 electrolysis experiments performed with a catholyte layer, displaying the result with a non-modified AEM, the RO and NF-based TFCMs cured at room temperature (marked as RT) and at 55 °C. a) cell potential, with the different current densities indicated, b) FEs, c) pH profiles of the anolyte (solid lines) and catholyte (dashed lines) during the experiment and d) the calculated carbon transport numbers per electron, for 50 and 100 mA/cm^2.

ing the electrolyzer with NF-based TFCMs, the FE to CO_2R products was quite comparable to when using a non-modified AEM, with small differences likely stemming from the GDE. However, this FE was notably reduced when using RO-based TFCMs, especially the one cured at room temperature. The RO-based TFCM cured at 55 °C led to quite similar results as to when operated in a zero-gap configuration, but also without too significant deviations from when using a bare AEM. The notably increased hydrogen production when using the RO-TFCM cured at room temperature was an unexpected phenomenon, which could be caused by a contamination of the catholyte, possibly by remaining unreacted monomers within the polyamide structure.

Figure 5.14c shows the pH of the anolytes and catholytes over the duration of the experiment. The catholyte, which is initially 3 M K_2CO_3, has a relatively consistent pH around 11.5 with minor differences and slowly reducing throughout the experiment. Meanwhile, in the anolyte there is a clear steep reduction of the pH which is the point where most of the OH^- is consumed. The experiments with the bare AEM, the RO-TFCM cured at 55 °C and the NF-TFCM cured at room temper-

ature also have very similar pHs in the anolyte during the entire experiment, with the equivalence point being close to 65 min. Slight differences may occur due to different timing in the start-up of the experiment, where some carbonate diffusion may occur from the catholyte to the anolyte.

Based on these pH curves and the pK_as of the reactions, the rate of carbon crossover was calculated (more information in the supporting information, section 5.6). These rates were then converted to charge flows and normalized with the applied current. The result of this analysis is shown on Figure 5.14d, with an indication of the CO_3^{2-} and HCO_3^- dominated transport values. Only the values for 50 and 100 mA/cm^2 were reported because at 200 mA/cm^2, steady-state at a constant pH was reached for most experiments. The membranes which have a consistent pH profile over time among each other, also show CO_3^{2-} is the main charge carrier at 100 mA/cm^2, and a lower carbon transport at 50 mA/cm^2 - likely hydroxide ions are migrating at lower current density. However, the two membranes which have a different pH profile in Figure 5.14c - the NF-TFCM cured at 55 °C and the RO-TFCM cured at room temperature, also show a larger carbon transport per e^- than the rest, even at a lower current density. This could indicate that HCO_3^- is a major charge carrier, but we find this unlikely since the catholyte is composed of K_2CO_3 and at high current densities the produced OH^- should be sufficient to convert the HCO_3^- to CO_3^{2-}. On the other hand, polyamide layers are known to reject bivalent ions more than monovalent ions. Interestingly, these two membranes are also the membranes which show defects under the SEM, as shown on Figure 5.12. Therefore, diffusion could play a role as well, as long as K^+ ions can also travel through the membrane (due to electroneutrality). Although this is possible since Sustainion membranes are not very selective at high electrolyte concentrations (Figure 2.3), no diffusion contribution is observed with the non-modified AEM. Additionally, the steady-state anolyte pH is expected to be the pH of an 0.1 M $KHCO_3$ solution which is 8.13, and with the NF-TFCM cured at 55 °C, lower pHs are observed.

A possible explanation for the lower pH in the anolyte is the production of formate or acetate at the cathode, which can migrate and convert to formic and acetic acid, respectively, in the anolyte. If this hypothesis is true, it would imply that the use of the different TFCMs can also influence the resulting products, which would require further investigation.

SEM pictures of the TFCMs after CO_2 electrolysis, confirm the polyamide layer is still on the membrane and with the same morphology (Figure S5.8).

This section shows that a catholyte layer can guarantee a high FE to CO_2R products when using an NF-based TFCM. By placing the catholyte layer in between the catalyst layer and the polyamide layer on the membrane, one can ensure that the local pH of the reaction microenvironment is not affected. Additionally, salt deposition was observed on the back of the GDE in the zero-gap configuration but not when using a catholyte layer.

Overall, we did not achieve the goal of a CO_2 electrolyzer with stable anolyte pH. This is an indication that the polyamide layer synthesis is more challenging than it was found in our preliminary experiments (section 5.3.1). The polyamide layers' pore size can be affected by pH and electrolyte concentration, thus known values for these parameters from literature might be vastly different in this application. Future studies should be done in application-relevant conditions.

5.4. CONCLUSIONS

We have modified commercial AEMs with a polyamide selective layer in order to create an OH^- selective membrane for CO_2 electrolysis. Preliminary experiments showed that the resulting TFCMs had an increased OH^-/CO_3^{2-} selectivity, with the OH^- transport numbers increasing to 73 %, compared to 41 % of the non-modified AEM. However, these membranes also had an approximately 40 times increase in ionic resistance.

In order to decrease the ionic resistance, we studied the effect of the monomer concentration used in the interfacial polymerization reaction to synthesize the polyamide layers, with an

electrolysis-suitable AEM as support. Our findings showed that below a certain MPD concentration, the polyamide no longer forms. The TMC concentration can be significantly reduced and used as a lever to ionic conductance. However, we did not achieve significant OH^-/CO_3^{2-} selectivity with these membranes, with the carbonate rejection being increased by less than 10% with the addition of the polyamide layer.

We also tested a different polyamide layer chemistry and the effect of the curing step at 55 °C after the polyamide synthesis. According to our results, the curing step leads to finer structures in the polyamide layer and is essential for lower ionic resistance. The NF-based TFCMs lead to larger cell potentials when used in CO_2 electrolysis indicating they are less conductive and/or have a higher carbonate rejection.

CO_2 electrolysis with the TFCMs in a zero-gap configuration showed that the FE_{CO} is greatly reduced by the polyamide layer, which affects the reaction microenvironment. Adding a catholyte layer in the electrolyzer lead to the recovery of the FE when using an NF-TFCM.

However, the TFCMs still didn't prevent the decrease of anolyte pH. SEM images revealed defects in many of the used polyamide layers, which could be partly responsible for the lack of carbonate rejection. Additionally, these layers are typically applied in different environments and it is known that the pore size can be affected by electrolyte concentration and pH. Further and more detailed research must be done to achieve carbonate rejection in relevant conditions.

5.5. OUTLOOK FOR FABRICATING OH^- SELECTIVE ANION EXCHANGE MEMBRANES

In order to achieve size-based separation of OH^- and CO_3^{2-}, one must have a very fine control of the pore size. Liang et. al.[21] added surfactants to the solutions when synthesizing a NF membrane, which greatly improved the pore size control. With this method, they reduced the pore size distribution from 3 Å to less than 1 Å. Shen et. al.[29] showed that adding a salt to the water phase before the interfacial polymerization can also lead to narrower pore size distributions. Additionally, this method leads to thinner polyamide layer with more homogeneous structures, which are likely more conductive.

To avoid salt deposition in a zero-gap CO_2 electrolyzer, cation transport from the anolyte to the cathode must be avoided. A viable strategy is to use an anolyte with a larger cation than the pore size of the polyamide layer. This means that the generally used KOH or CsOH might not be suitable as their ion sizes (3.31 and 3.29 Å, respectively) are similar to the OH^- ion size.[30]

The pore size of polyamides has been shown to vary depending on the electrolyte concentration and the surrounding pH, which makes it imperative to conduct studies in relevant conditions. For membrane filtration applications, the pore size is typically derived from rejection of differently sized molecules,[21] but in that case, due to electroneutrality, both cations and anions must cross the membrane. For electrochemical applications, the pore size study must be studied under an applied electric field, allowing only one of the ion species to cross the membrane, which can affect the obtained rejection values.

Avoiding defects when using a non-porous support can also be challenging. One must ensure the surface is completely dry and free of microdroplets. However, the IEM must still be in hydrated form, because changes in its volume during synthesis may cause cracks in the polyamide layer. One way to avoid defects is to increase the reaction time, although this also increases cross-linking.[27, 31] Another method is to fabricate the polyamide layer separately from the support by synthesizing it between an aqueous phase and an organic phase which sit on top of the desired support, and then join the support and the selective layer by evaporating or draining the solvents.

To use AEMs as a support, the interaction between the monomers and the support should be studied. Most AEMs also have amine-based functional groups which could react with the TMC

monomer if insufficient amine monomer is present. Additionally, the polyamide layer can have charged groups depending on the pH (the isoelectric point being close to 6),[32] and electrostatic repulsions can compromise the stability of the added layer.

BIBLIOGRAPHY

1. Burdyny, T. & Smith, W. A. CO_2 reduction on gas-diffusion electrodes and why catalytic performance must be assessed at commercially-relevant conditions. *Energy Environtal Science* **12,** 1442–1453 (2019).
2. Sassenburg, M. *et al.* Characterizing CO_2 Reduction Catalysts on Gas Diffusion Electrodes: Comparing Activity, Selectivity, and Stability of Transition Metal Catalysts. *ACS Applied Energy Materials* **5,** 5983–5994 (2022).
3. Salvatore, D. A. *et al.* Designing anion exchange membranes for CO_2 electrolysers. *Nature Energy* **6,** 339–348 (2021).
4. Endrődi, B. *et al.* High carbonate ion conductance of a robust PiperION membrane allows industrial current density and conversion in a zero-gap carbon dioxide electrolyzer cell. *Energy & Environmental Science* **13,** 4098–4105 (2020).
5. Liu, Z., Yang, H., Kutz, R. & Masel, R. I. CO_2 Electrolysis to CO and O_2 at High Selectivity, Stability and Efficiency Using Sustainion Membranes. *Journal of The Electrochemical Society* **165,** J3371–J3377 (2018).
6. Blommaert, M. A., Subramanian, S., Yang, K., Smith, W. A. & Vermaas, D. A. High Indirect Energy Consumption in AEM-Based CO_2 Electrolyzers Demonstrates the Potential of Bipolar Membranes. *ACS Applied Materials & Interfaces,* 557–563.
7. Minke, C., Suermann, M., Bensmann, B. & Hanke-Rauschenbach, R. Is iridium demand a potential bottleneck in the realization of large-scale PEM water electrolysis? *International Journal of Hydrogen Energy* **46,** 23581–23590 (2021).
8. Rabinowitz, J. A. & Kanan, M. W. The future of low-temperature carbon dioxide electrolysis depends on solving one basic problem. *Nature Communications* **11,** 5231 (2020).
9. Perez-Carbajo, J. *et al.* Zeolites for CO_2–CO–O_2 Separation to Obtain CO_2-Neutral Fuels. *ACS Applied Materials & Interfaces* **10,** 20512–20520 (2018).
10. Blommaert, M. A. *et al.* Orientation of a bipolar membrane determines the dominant ion and carbonic species transport in membrane electrode assemblies for CO_2reduction. *Journal of Materials Chemistry A* **9,** 11179–11186 (2021).
11. Erick, H. J. *et al.* CO2 electrolysis to multicarbon products in strong acid. *Science* **372,** 1074–1078 (2021).
12. Mohammad, A. W. *et al.* Nanofiltration membranes review: Recent advances and future prospects. *Desalination* **356,** 226–254 (2015).
13. Habib, S. & Weinman, S. T. A review on the synthesis of fully aromatic polyamide reverse osmosis membranes. *Desalination* **502,** 114939 (2021).
14. Nightingale, E. R. J. Phenomenological Theory of Ion Solvation. Effective Radii of Hydrated Ions. *The Journal of Physical Chemistry* **63,** 1381–1387 (1959).
15. Dischinger, S. M., Miller, D. J., Vermaas, D. A. & Kingsbury, R. S. Unifying the Conversation: Membrane Separation Performance in Energy, Water, and Industrial Applications. *ACS ES&T Engineering* **4,** 277–289 (2024).

16. Shi, L. *et al.* Using reverse osmosis membranes to control ion transport during water electrolysis. *Energy Environ. Sci.* **13,** 3138–3148 (2020).

17. Dai, Q. *et al.* Thin-film composite membrane breaking the trade-off between conductivity and selectivity for a flow battery. *Nature Communications* **11,** 13 (2020).

18. Hailemariam, R. H. *et al.* Reverse osmosis membrane fabrication and modification technologies and future trends: A review. *Advances in Colloid and Interface Science* **276,** 102100 (2020).

19. Khorshidi, B., Thundat, T., Fleck, B. A. & Sadrzadeh, M. Thin film composite polyamide membranes: parametric study on the influence of synthesis conditions. *RSC Adv.* **5,** 54985–54997 (2015).

20. Ghosh, A. K., Jeong, B.-H., Huang, X. & Hoek, E. M. V. Impacts of reaction and curing conditions on polyamide composite reverse osmosis membrane properties. *Journal of Membrane Science* **311,** 34–45 (2008).

21. Polyamide nanofiltration membrane with highly uniform subnanometre pores for sub-1 Å precision separation. *Nature Communications* **11,** 2015 (2020).

22. Iglesias van Montfort, H.-P. *et al.* An Advanced Guide to Assembly and Operation of CO_2 Electrolyzers. *ACS Energy Letters* **8,** 4156–4161 (2023).

23. Espinoza, C., Kitto, D. & Kamcev, J. Counter-ion Conductivity and Selectivity Trade-Off for Commercial Ion-Exchange Membranes at High Salinities. *ACS Applied Polymer Materials* **5,** 10324–10333 (2023).

24. Chai, G.-Y. & Krantz, W. B. Formation and characterization of polyamide membranes via interfacial polymerization. *Journal of Membrane Science* **93,** 175–192 (1994).

25. Xu, J., Yan, H., Zhang, Y., Pan, G. & Liu, Y. The morphology of fully-aromatic polyamide separation layer and its relationship with separation performance of TFC membranes. *Journal of Membrane Science* **541,** 174–188 (2017).

26. Sassenburg, M., Kelly, M., Subramanian, S., Smith, W. A. & Burdyny, T. Zero-Gap Electrochemical CO_2 Reduction Cells: Challenges and Operational Strategies for Prevention of Salt Precipitation. *ACS Energy Letters* **8,** 321–331 (2023).

27. Zhou, S. *et al.* Unveiling the Growth of Polyamide Nanofilms at Water/Organic Free Interfaces: Toward Enhanced Water/Salt Selectivity. *Environmental Science & Technology* **56,** 10279–10288 (2022).

28. Li, C., Zhao, Y., Lai, G. S. & Wang, R. Investigation of aqueous and organic co-solvents roles in fabricating seawater reverse osmosis membrane. *Journal of Membrane Science* **645,** 120187 (2022).

29. Shen, L. *et al.* Polyamide-based membranes with structural homogeneity for ultrafast molecular sieving. *Nature Communications* **13,** 500 (2022).

30. Fan, S., Jiang, L., Jia, Z., Yang, Y. & Hou, L. Comparison of Adsorbents for Cesium and Strontium in Different Solutions. *Separations* **10** (2023).

31. Ali, Z. *et al.* Defect-free highly selective polyamide thin-film composite membranes for desalination and boron removal. *Journal of Membrane Science* **578,** 85–94 (2019).

32. Luo, J. & Wan, Y. Effects of pH and salt on nanofiltration—a critical review. *Journal of Membrane Science* **438,** 18–28 (2013).

33. Zhang, M. *et al.* The Intrinsic Parameters of the Polyamide Nanofilm in Thin-Film Composite Reverse Osmosis (TFC-RO) Membranes: The Impact of Monomer Concentration. *Membranes* **12** (2022).

5.6. SUPPORTING INFORMATION

Figure S5.1 shows the ionic resistance, measured in a 0.1 M K_2CO_3 solution, of a TFCM synthesized during preliminary experiments varying with the current density. The average resistance in this range of current density was 171 Ωcm^2.

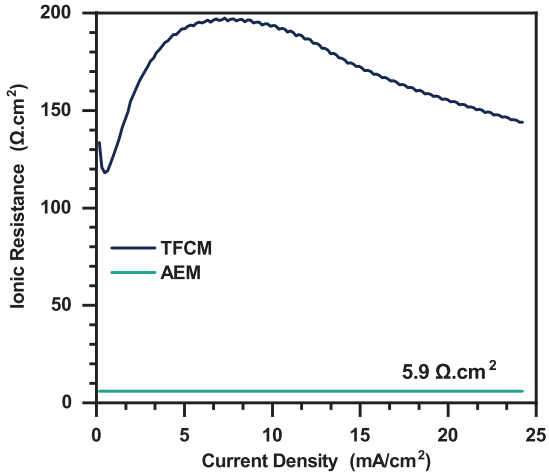

Figure S5.1: Ionic resistance in 0.1 M K_2CO_3 vs. current density of a non-modified AEM, and of a TFCM made with 1 w/v% MPD and 0.25 w/v% TMC

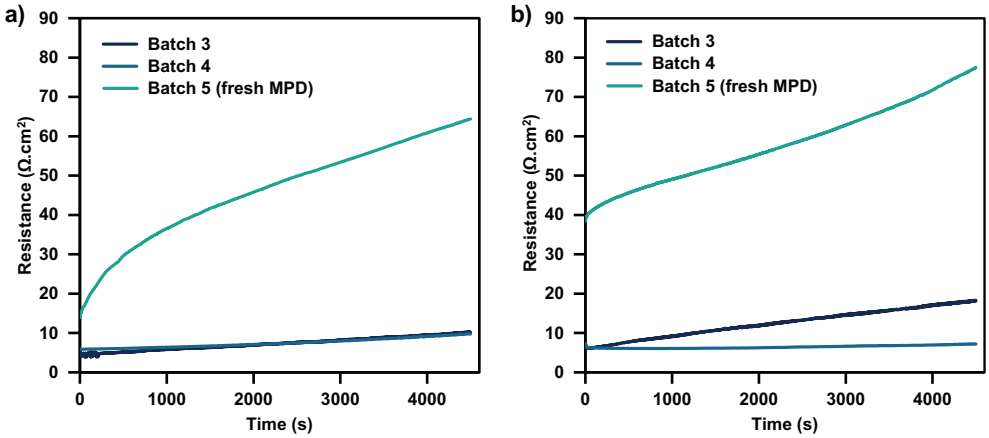

Figure S5.2: Resistance increase during the crossover experiments of the same membrane but in different batches. a) 2 w/v% MPD, 0.05 w/v% TMC, b) 3 w/v% MPD, 0.05 w/v% TMC

Figure S5.3 shows the FTIR spectra of a non-modified AEM, an RO-based polyamide, and the two TFCMs. The free-standing polyamide was created simply by mixing the two monomer solutions to obtain a larger polyamide structure. Identifying the peaks which are specific to polyamide can be a challenge on the TFCMs since the non-modified AEM has many of the same bonds and elements in its chemical structure. The peak identified at 1601 cm^{-1} is related to the N-C=O amide vibrations.

The peak identified at 1537 cm^{-1} is related to the C-N functional group. The peak identified at 1492 cm^{-1} indicates the "aromatic ring breathing" which is also specific to these polyamide functional groups according to literature.[33] These peaks are not observed on the non-modified membrane, but they were observed on the polyamide and TFCM spectra, confirming the presence of polyamide on the TFCMs.

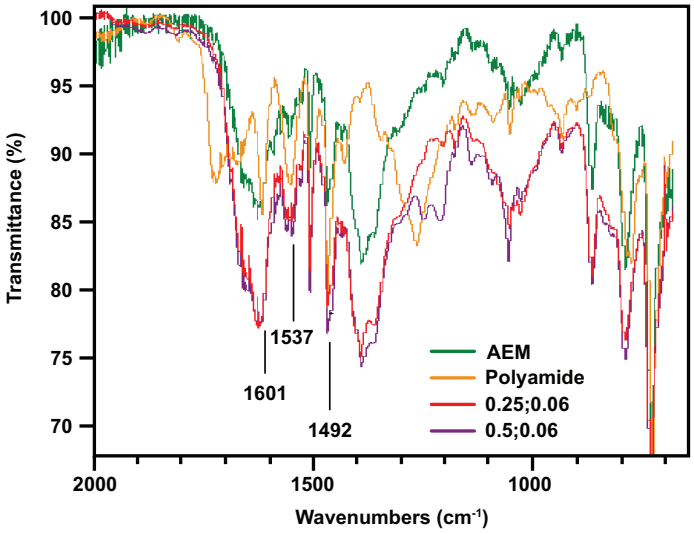

Figure S5.3: FTIR spectra of the non-modified AEM, an RO-based polyamide, and the two TFCMs with their monomer concentration indicated in the legend.

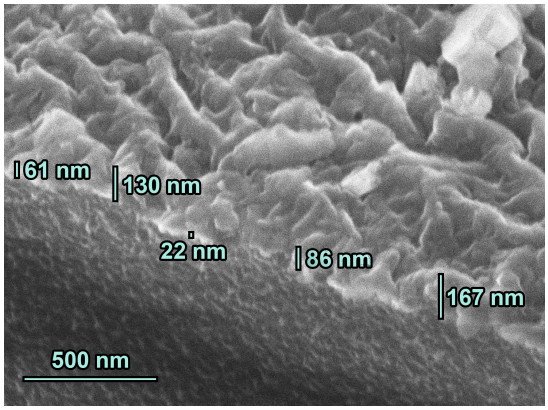

Figure S5.4: SEM image of an RO-based membrane cured at 55 °C. Image taken at 10,000 times magnification, at a 40degree angle.

Based on the pH of the anolyte shown in Figure 5.14c, we can identify the carbon species present therein. In addition to the OER, consuming OH^- ions, the following reactions were considered to occur in the anolyte:

$$CO_3^{2-} + H_2O \longrightarrow HCO_3^- + OH^- \tag{S5.1}$$

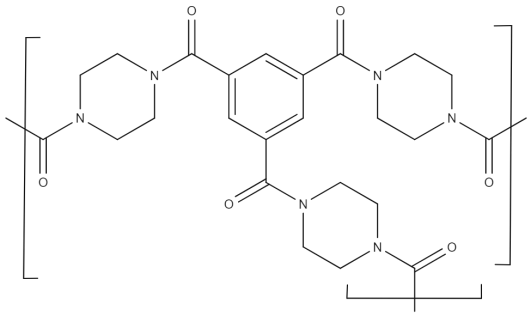

Figure S5.5: Chemical structure of the NF-based polyamide layer, with PIP used as the amine monomer.

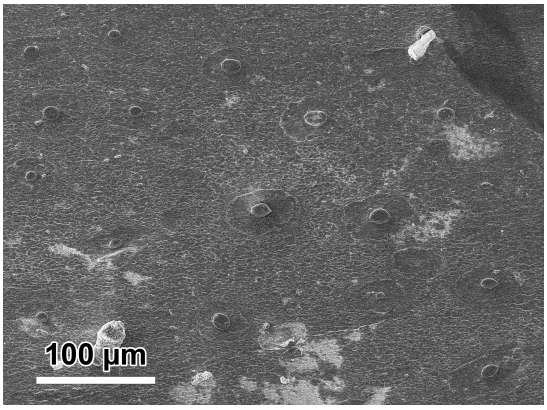

Figure S5.6: SEM image of an NF-based membrane cured at room temperature. 250× magnification.

$$HCO_3^- + H_2O \longrightarrow H_2CO_3 + OH^- \tag{S5.2}$$

$$H_2CO_3 \longrightarrow CO_2 + H_2O \tag{S5.3}$$

The pK_a of these reactions was obtained with Visual MINTEQ 3.1 software - 10.25 and 6.37 for reactions S5.1 and S5.2, respectively. The CO_2 concentration in the anolyte was considered to be 0, which was ensured in practice by bubbling N_2 gas into the anolyte reservoir.

Using the balance for the equations above, the electroneutrality equation with the initial K^+ concentration in the anolyte ($[K^+] = [OH-] + [HCO_3^-] + 2[CO_3^{2-}]$), and the water dissociation constant (K_w), the following equations were obtained:

$$[CO_3^{2-}] = K_{HCO_3^-} \frac{-K_w + [K^+][H^+]}{[H^+](2K_{HCO_3^-} + [H^+])} \tag{S5.4}$$

$$[HCO_3^-] = -\frac{K_w - [K^+][H^+]}{2K_{HCO_3^-} + [H^+]} \tag{S5.5}$$

$$[H_2CO_3] = [H^+]\frac{-K_w + [K^+][H^+]}{K_{HCO_3^-}(2K_{H_2CO_3} + [H^+])} \tag{S5.6}$$

These equations were then used to plot the individual species in the anolyte over time, using the pH in the anolyte as input - Figure S5.7a.

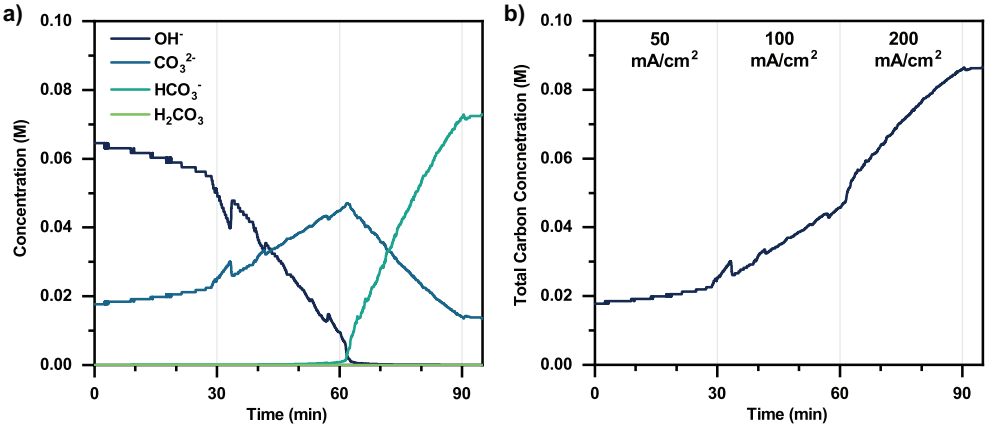

Figure S5.7: a) concentrations of OH^- and the different carbonate speciation species calculated based on the pH of the anolyte, b) calculated total carbon over time in the anolyte.

Figure S5.7b shows the sum of carbon species within the anolyte over time. Three clear slopes can be observed for the current densities. These slopes were used to calculate the rate of carbon transport, and then the transport numbers displayed in Figure 5.14d.

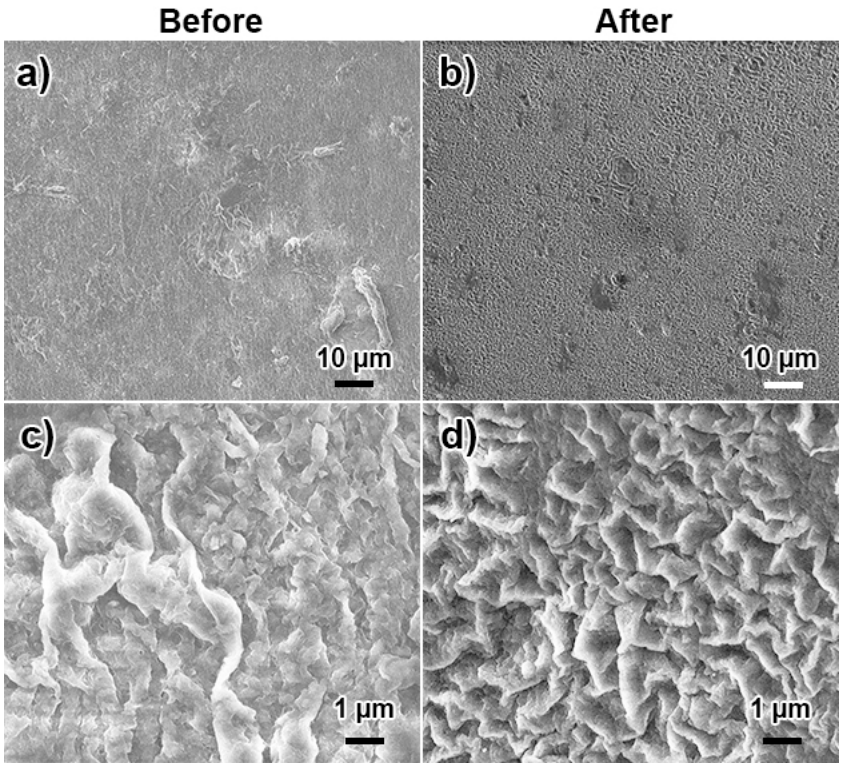

Figure S5.8: SEM pictures of the RO-based TFCM cured at room temperature before (a,c) and after (b,d) being used for CO_2 electrolysis.

6

RESEARCH IMPLICATIONS AND PERSPECTIVE ON BIPOLAR MEMBRANES FOR CO_2 ELECTROLYSIS

This chapter discusses the implications of our research and the further shortcomings and opportunities associated with the presented IEM developments. Aditionally, we argue that intrinsically stable and efficient CO_2 electrolysis without rare-earth metals is only possible using multilayer membrane systems, such as thin-film composite membranes or bipolar membranes (BPMs). While reverse- and forward-bias BPMs are both capable of inhibiting CO_2 crossover, forward-bias fails to solve the rare-earth metals requirement at the anode. Unfortunately, reverse-bias BPM systems presently exhibit comparatively lower Faradaic efficiencies and higher cell voltages than anion-exchange membrane based systems. Here we argue that these performance challenges can be overcome leading to superior BPM-based systems. Optimizing the catalyst, reaction microenvironment and alkali cation availability should be the primary areas of research. Furthermore, BPMs can be improved by using thinner layers and a suitable water dissociation catalyst, becoming the primary membrane separator of choice, alleviating core remaining challenges in CO_2 electrolysis to bring this technology to industrial scale.

Parts of this chapter have been submitted for publication as "Bipolar Membranes for Intrinsically Stable and Energy Efficient CO_2 Electrolysis" by K.V. Petrov, C.I. Koopman, S. Subramanian, M. Koper, T.E. Burdyny, D.A. Vermaas.

6.1. General Conclusions and Research Implications

The CO_2 electrolysis field has a very challenging goal since some of its target products, although having a vast market, do not have a high market value. Therefore, to incentivize the complete substitution of the oil alternatives of these products, the electrolysis process must be extremely energy efficient. Currently, the challenges reside in the efficiency of individual components, including catalysts, their interaction with the membrane, membrane conductivity, the efficient utilization of raw materials, long-term stability and downstream processing.

Requirements for Nanofluidic Membranes

In Chapters 2 and 3, we studied nanofluidic membranes (NFMs), an alternative to traditional ion-exchange membranes (IEMs) that can improve their conductivity and selectivity. We found that commercial NFMs still need further development because of their lack of conductivity, brittleness, and pore inhomogeneity. Nevertheless, our findings show that NFMs have potential for application as long as the electrolyte concentration is low on one side of the membrane and high on the other - which is the case for many CO_2 electrolyzers. Still their application faces quite a few challenges.

The inorganic nature brings the possibility of electrical conductivity, which is not acceptable in electrolyzers in a zero-gap configuration, since that would cause short-circuiting. Moreover, the surface charge, and consequently the ion selectivity, depends on pH. Therefore, since alkaline conditions impose a negative charge to most materials, it is very hard to fabricate an anion-exchange membrane (AEM) at high pH, and vice-versa. As demonstrated by Nishizawa et. al.,[1], it is possible to externally charge the membrane to alter its ion-selectivity. They have shown that a gold-coated porous membrane can act as a fully cation- or anion-selective IEM, by applying approximately -0.3 V or 0.3 V, respectively, vs. the open current voltage of the membrane. This brings the opportunity of having the membranes pressed to the anode in CO_2 electrolyzers to positively charge them, providing AEM functionality. However, this will bring the membrane to same potential as the anode, thus one must ensure that no Faradaic reactions can occur by carefully choosing a non-catalyst material.

Our modeling results in Chapters 2 and 3, show that a conductive and selective membrane ideally has cylindrical channels which directly connect one side to the other with a high channel density, it must be between 0.5 and 5 μm in thickness,(Figure 3.8) and the pore size should not be larger than ~ 5 nm (Figure 2.7). Additionally, the chosen material should have a very high isoelectric point, to ensure the positive charge at higher pH.

Nanofluidic Membrane Materials

Although fabricating such a membrane is not trivial, anodized aluminum oxide (AAO) and anodized titanium dioxide membranes have the type of structure specified above and have been vastly used for different applications, with fine control of the thickness and pore size. They are also dielectric materials, which can be polarized but do not easily conduct electrical currents. However, AAO is not stable for long periods of time in aqueous solutions, because of aluminum hydroxide formation,[2] which can block the nanochannels. Titanium dioxide is more stable and a good contender for an NFM material. However, it is a known catalyst for CO oxidation and photocatalyst, thus possible Faradaic reactions within the CO_2 electrolyzer need to be carefully studied.[3]

Other than anodization, options for NFMs involve graphene oxide (GO), ceramic membranes, zeolites, electroless plating and silica. GO membranes are not brittle, and are becoming more and more developed, but they lack the advantage of an optimal ionic pathway.[4] Ceramic membranes are also a good contender for NFMs because they can be produced in various geometries, by casting a particle suspension into a mold and sintering.[5] Zeolites have already been applied as proton-exchange membranes in fuel cells, but most zeolite materials lack stability in alkaline environments.[6] Electroless plating can be applied on virtually any type of support material, but the coating is typically made of metal-based materials which can bring issues in terms of undesired Faradaic

reactions.[1]

Finally, it is important to consider the inherent brittleness of most ceramic-type materials, which poses challenges in their fabrication, transportation, and the assembly of electrolyzers. Additionally, since the ideal thickness is less than 5 µm, it is likely they need a support structure.

Considering the challenges faced by NFMs and our research highlighting the significance of charged functional groups for conductivity, we have concluded that polymeric IEMs are more suitable for CO_2 electrolysis, at least in the near future.

IMPROVING POLYMERIC ION-EXCHANGE MEMBRANE CONDUCTIVITY

The achieved conductivity with NFMs does suggest a potential direction for improving polymeric IEMs conductivity: aligning the polymer chains to optimize the ionic pathway. In cation-exchange membranes (CEMs) (e.g. Nafion) this is mostly achieved by the polymer chemistry itself, where the polymer backbone is hydrophobic, but the side chains are hydrophylic, making them align toward each other during polymerization.[7] The downside of this approach is that the increased hydrophilicity leads to increased swelling.[8] Conductive AEMs (e.g. PiperION) are now being fabricated with the fixed charges on the polymeric backbone itself in order to increase the charge density.[8] To optimize the ionic pathway in such membranes, a possible strategy is to carry out the polymerization under an electric field.[9, 10]

Another concern about the conductivity of the polymer-based membranes in CO_2 electrolyzers is related to their hydration, which could be compromised at high current densities due to water consumption by the CO_2 reduction reaction (CO_2RR). In Chapter 4, we explored a microchannel structure within the membrane, that can supply water closer to the reaction environment. Our findings show that such a structure can significantly boost the energy efficiency of the process. However, it is imperative to optimize the size and location of the microchannels. According to our results, a microchannel of about 10 µm in size with at least 90 µm spacing in between each microchannel, adjacent to the catalyst layer, can improve the energy efficiency by up to 40% at high current densities. Profiled membranes have been shown in literature for other applications,[11, 12] and should also be considered for CO_2 electrolysis if hydration becomes a limiting factor at higher current densities. For now, for the sake of a less complicated system, we believe researchers should focus on using thin and water-permeable IEMs when using membrane-electrode assembly (MEA) configurations with a liquid anolyte.

RESOLVING THE CARBONATE CROSSOVER ISSUE

In addition to the direct energy efficiency of the electrolyzer, the role of indirect energy efficiencies is crucial. Carbonate crossover is perhaps the most important challenge of CO_2 electrolysis since it leads to at least 50 % CO_2 loss and its subsequent separation from O_2 is not trivial. Additionally, carbonate crossover lowers the pH of the anolyte - an undesired effect since it forces the use of one of the scarcest materials on earth (Ir) as anodic catalyst. However, it is not possible for a common IEM to reject/convert carbonate, allow stable operation with an alkaline anolyte and selectively conduct OH^- with low ionic resistance, all at the same time. Therefore, we considered multilayer membranes for the remainder of the work.

The goal of the work shown in Chapter 5, was to fabricate a membrane which allows OH^- to permeate, but rejects carbonate to allow the operation with an alkaline anolyte. To this end, we developed a thin-film composite membrane (TFCM), consisting of a selective polyamide layer and an ion conductive support. The polyamide layer's role is to reject carbonate which can be achieved based on both size and charge. This selective layer is synthesized on top of a commercial ion-exchange membrane instead of a porous support like seen in other applications because this ensures an ion-conductive support, without relying on electrolyte concentration for conductivity. Although we did not succeed in achieving high carbonate rejection, we successfully increased the conductivity of

these membranes and unveiled multiple challenges this strategy can bring. Namely, the increased carbonate concentration in the reaction microenvironment may lead to salt deposition, and subsequent decrease in Faradaic efficiency (FE).

Nevertheless, decoupling the functionalities by having two separate layers for selectivity and for conductivity is a strategy that holds great promise, not only for CO_2 electrolysis, but also for other applications, such as acid-base flow batteries, since it may produce an OH^-, or H^+ selective IEM. Since we have shown that the polyamide selective layer can be fabricated on an IEM, it is a matter of optimizing the coating process to achieve the selectivity. Effective drying, increased reaction times and additives (such as surfactants and salts) during the polymerization can ensure the formation of a defect-free selective layer with the desired pore size.[13, 14]

A key aspect for carbonate-rejecting membranes for CO_2 electrolysis, is to also prevent the crossover of cations from the anolyte to the cathode. Restricting the cation concentration cannot only avoid salt deposition, but also the formation of stable carbonate. In the absence of cations, dissolved inorganic carbon can only exist as CO_2 or H_2CO_3, and the latter dissociates to CO_2 and H_2O in alkaline mediums (as is the CO_2RR microenvironment).[15] In this way, an OH^- selective membrane combined with fine control of cation concentration in the reaction microenvironment can allow the operation with alkaline anolytes, with high product selectivities.

Another promising method of solving the carbonate crossover issue is to convert it back to CO_2 within the electrolyzer, by influx of protons. This can be achieved by using a cation-exchange membrane (CEM) coupled to an (undesired) acidic or neutral anolyte, or with bipolar membranes (BPMs). The following section explains in detail the shortcomings and the development possibilities of using BPMs for CO_2 electrolysis.

Overall, we see great promise in using multilayer membranes in CO_2 electrolyzers, as their adaptability presents a promising avenue for simultaneously addressing most challenges and improving the overall efficiency. Membranes with internal microchannels, TFCMs and BPMs exemplify the advantages of multilayer structures. The versatility of this approach extends to the possibility of integrating NFMs, such as GO, with fine tuned pore size to allow carbonate rejection with supporting polymers, offering potential solutions to issues such as brittleness. We envision the application of multilayer membranes in CO_2 electrolyzers for stable operation with alkaline anolytes, where the membranes can be composed of a selective layer, such as polyamide or an NFM-based layer on a support structure, or they can be BPMs which allow the conversion of carbonate.

6.2. BIPOLAR MEMBRANES FOR CO_2 ELECTROLYSIS

6.2.1. INTRODUCTION

Electrochemical CO_2 reduction (CO_2R) is a promising technology for the sustainable production of carbon-based fuels and chemicals. Having reached current densities and Faradaic efficiencies (FEs) that are near commercial standards, critical parameters of interest are now stability, energy efficiency, CO_2 utilization and material availability. As a modulator of the ionic current and a separation between the CO_2 conversion at the cathode and the oxygen evolution reaction (OER) at the anode, the ion-exchange membrane plays a central role in the performance, material selection and stability of the configuration.

Currently, the most efficient and high performing CO_2 electrolyzers employ anion-exchange membranes (AEMs) in a membrane-electrode assembly (MEA) configuration (Figure 6.1a). Ideally, the AEM facilitates the selective transport of hydroxide ions (OH^-) from the cathode to the anode. However, AEM-based electrolyzers face a major challenge since a large part of the input CO_2 reacts with OH^- to produce (bi)carbonates, which are then transported to the anode compartment through the AEM.[16]

To properly assess the industrial feasibility of AEM-based systems, we need to include the im-

plications of CO_2 crossover on the energy and material requirements. The crossover of CO_2 as (bi)carbonates does not allow an alkaline environment at the anode without electrolyte regeneration and thus necessitates the use of iridium-based OER catalyst at the anode.[17] However, iridium is one of the scarcest metals on earth, and its rising price is an impediment for scale-up.[18] Moreover, CO_2 crossover limits the (single-pass) CO_2 utilization to 50% or lower depending on the product (CO – 50%, C_2H_4 – 25%),[19] and is therefore an indirect energy penalty as concentrated CO_2 is a valuable feedstock. Conventional CO_2 capture processes have an energy consumption between 170 and 390 kJ/mol CO_2, depending on the source of CO_2.[20, 21] An energy consumption of 170 kJ/mol CO_2 would translate to a voltage of 0.88 V when recapturing CO_2 from the anode gas (assuming 100% FE and CO_3^{2-} as charge carrier).

As AEMs cannot prevent CO_2 crossover and its associated energy and material implications, we argue that bipolar membranes (BPMs) have the potential to be the primary option for CO_2 electrolysis. BPMs consist of a cation-exchange layer (CEL) and an anion-exchange layer (AEL) layer and depending on the orientation, can be used in forward or reverse bias. In reverse bias (Figure 6.1b), water dissociates into H^+ and OH^- at the CEL/AEL interface. The H^+ migrates to the cathode and the OH^- migrates to the anode, allowing operation at a steady-state pH difference between the electrodes. This offers the benefit of a theoretically stable alkaline anolyte, which is favourable for the OER and allows the use of more earth-abundant catalysts such as $NiFeO_x$.[22] Moreover, the CEL rejects carbonates and the generated H^+ recombines with carbonates to regenerate CO_2, impeding CO_2 crossover almost entirely.

However, a current bottleneck for reverse-bias BPMs is that the resulting acidic cathode environment has been associated with low FEs for CO_2R products, since the competitive hydrogen evolution reaction (HER) is promoted in the abundance of H^+.[23] Fortunately, recent advances in CO_2R in acidic media and the impact of cations on CO_2R have been better understood and offer strategies for suppressing the HER, providing interesting opportunities for reverse-bias BPM systems.[24–26] Conversely, an ideal forward bias BPM (Figure 6.1c), where OH^- from the cathode migrates through the adjacent AEL and recombines with H^+ from the anode, enables a neutral/alkaline environment at the cathode, but fails to provide anode conditions which permit earth-abundant catalysts. In this perspective, we assess the potential of BPMs for CO_2 electrolysis, with special attention to CO_2 utilization, energy consumption, and strategies to improve product selectivity and efficiency. We argue that for BPMs to be the new state of the art, their performance - in terms of conductance, BPM kinetics and stability - must be improved through innovation.

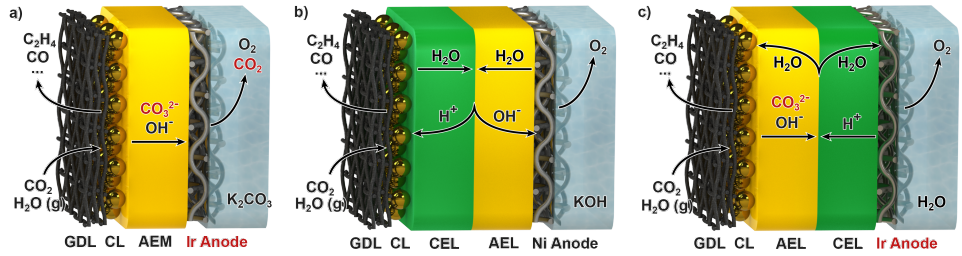

Figure 6.1: Schematic representation of cell configurations for electrochemical CO_2 reduction at a gas diffusion electrode paired with oxygen evolution at the anode in a liquid anolyte. The gas diffusion electrode consists of a gas diffusion layer (GDL) and a catalyst layer (CL). The three configurations highlighted here are: a) an (anion-exchange membrane-electrode assembly (AEMEA)), b) a BPM in reverse bias, and c) a bipolar membrane-electrode assembly (BPMEA) in forward bias.

6.2.2. Bipolar Membranes Inhibit Crossover Promoting CO_2 Utilization

The CO_2 crossover in AEM-based CO_2 electrolyzers proves to be an intrinsic limitation. Typically, AEM-based systems exhibit a crossover between 0.5 and 1 CO_2 per e- transferred, which corresponds to CO_3^{2-} and HCO_3^- as the dominant charge carrier, respectively (Figure 6.2a). Therefore, to achieve higher CO_2 utilization, (bi)carbonate formation/crossover must be suppressed which can only be done by replacing AEM separators with either a BPM or cation-exchange membrane (CEM) system.[27–29]

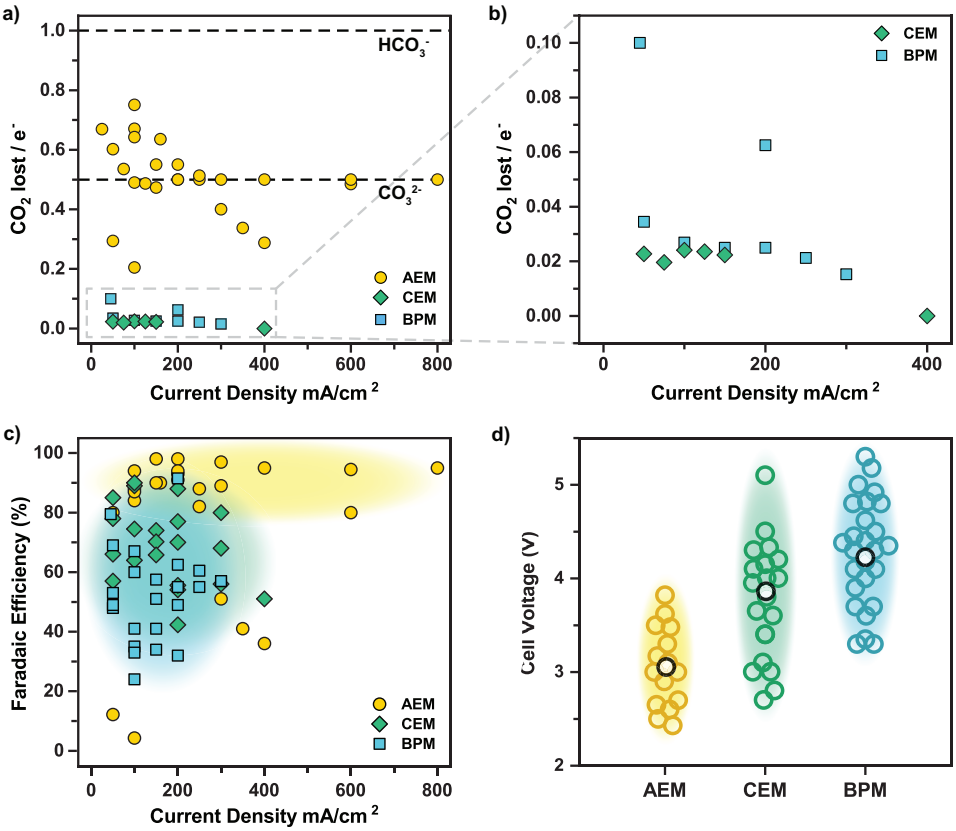

Figure 6.2: A comparison of AEM-, BPM-, and CEM-based CO_2 electrolyzers on different performance parameters: a,b) Relative CO_2 crossover per charge transferred. The data points represent values from several papers, while the lines represent the theoretical value when CO_3^{2-} or HCO_3^- are the main charge carriers. This assumes 1 OH^- per reaction electron (valid for most CO_2R reactions and HER) and no H_2CO_3 crossover. c) Faradaic efficiency for carbon-based products. d) cell voltages for the different membrane systems at current densities between 50 and 300 mA·cm-2. The highlighted (○) values show the average cell voltage of all data points.[17, 24, 25, 27–46]

CO_2 crossover is heavily reduced for BPM-based systems (Figures 6.2a-b) due to the presence of negatively charged groups in the CEL, which inhibits CO_2 crossover through Donnan exclusion of carbonates and negatively charged CO_2R products (formate).[47] Note that some crossover of co-ions can occur through uncharged membrane spaces (between charged phases),[48] which requires

mitigation against salt precipitation and electrolyte regeneration, but this issue is minor given the typical water dissociation (WD) efficiency > 99% at 100 mA/cm^2.[49] Additionally, reverse-bias BPMs reduce the crossover of neutral CO_2R products (methanol) through the outward flux of protons, which inhibits electroosmotic drag across the membrane in particular at higher current densities (Figure 6.2b).[50]

Although CEM-based electrolyzers are able to achieve low CO_2 crossover, they are more prone to instabilities due to co-ion crossover. Furthermore, their acidic/neutral anolyte conditions require the use of rare-earth metals, making the BPM-based system a more suitable candidate for large scale application.[18, 28]

BPM-based systems in both reverse or forward bias have been reported high single-pass CO_2 utilization values, up to 78%,[28, 51] surpassing the theoretical maximum of 50% for AEM-based systems for two-electron products.[27] The typically 0.02 CO_2 lost per electron (Figure 6.2b) implies a maximum of 96% CO_2 utilization, but high single-pass utilization is still expected to bring trade-offs in selectivity and energy efficiency through the concentration overpotential caused by reactant starvation.[52]

At the moment, the improved CO_2 utilization of reverse-bias BPM-based systems comes at the cost of lower FE and higher cell voltages (Figures 6.2c-d). However, unlike the intrinsic issues of CO_2 crossover and scarce anode materials for AEM-based systems, in this perspective, we argue that both the selectivity and cell voltage for BPM-based systems can be further improved through innovation.

6.2.3. THE KEY TO LOW CELL POTENTIALS IS MANAGING PH GRADIENTS

A large contribution to the high voltages observed in BPM and CEM electrolyzers that is often overlooked, stems from pH gradients within the electrolyzer. Assuming an electrolyzer is producing CO and O_2, the difference between the standard reduction potentials (E^0_{cell}) is 1.34 V. Because both reactions produce one H^+ or OH^- per electron, each pH unit causes a Nernstian shift of 59.2 mV. Theoretically, the voltage contribution of WD or recombination (0.83 V) at the BPM interface is counter-balanced by the Nernstian shift in redox potential at the electrodes, which would allow all configurations to operate at the same equilibrium cell voltage (1.34 V (see reference hydrogen electrode (RHE) panels in Figure 6.3).

In practice, however, pH gradients and buffering effects will change the local pH and therefore, the observed difference in redox potentials and cell potentials. Accurately determining the pH in the cathode reaction environment remains a challenge for zero-gap configurations, but for the sake of this discussion we will assume it to be 10.5 (close to the carbonate pK_a).[24, 53] In an AEM electrolyzer, where the anolyte will be composed of HCO_3^- or pure water (pH of ≈7-8.1), the pH gradient over the AEM increases the cell voltage by at least 0.14 V ((10.5-8.1)0.0592=0.14) (Figure 6.3a).

In a reverse-bias BPM electrolyzer, a large pH gradient is observed between the CEL and the catalyst layer, since the BPM interface produces H^+ while the produced OH^- and carbonate pin the pH to 10.5) (Figure 6.3b). This gradient does not allow the complete balancing of the WD voltage of 0.83 V. At a cathode pH of 10.5, only 0.21 V is compensated. Operating a cathode at acidic pH would be extremely beneficial for this configuration, since removing internal pH gradient would lower the overall cell potential by 0.62 V. Additionally, the BPM requires an overpotential for WD and increased ohmic resistance can be caused by the formation of bubbles at the CEL interface.[54]

For an electrolyzer with a forward-bias BPM (Figure 6.3c), the buffering effects occur both in the catalyst layer and at the BPM interface. The Nernstian pH shift added by the alkalinity in the cathode region in this scenario is 0.56 V. The forward-bias BPMEA configuration could potentially recover the this energy at the BPM junction, but recent work by Toh et. al.,[55] shows that the main recombining species is H_2CO_3 instead of water, lowering the maximum regained voltage to 0.38 V (0.0592pKa(H_2CO_3)).

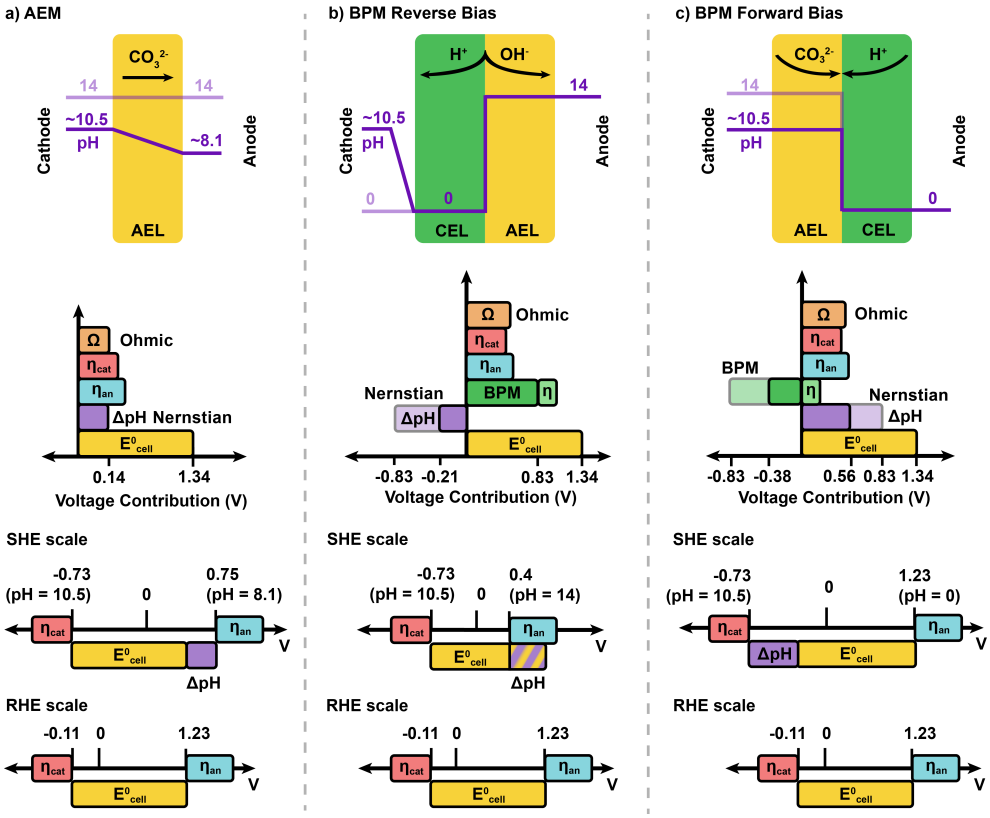

Figure 6.3: Schematic illustrations of the simplified different MEA configurations and the voltage contributions of the different components. η_{an} and η_{cat} represent the overpotentials of the anode and cathode respectively, Ω represents the ohmic resistance contribution, E^0_{cell} is the difference between the equilibrium redox potentials of the two reactions, ΔpH Nernstian represents the Nernstian pH shift, and WD is the voltage associated to the water dissociation reaction at the BPM interface. The voltage contributions of the reactions on the individual electrodes are also displayed on the standard hydrogen electrode (standard hydrogen electrode (SHE)), to highlight the effect of pH on the equilibrium redox potentials. Panel a) describes the AEMEA system; b), the reverse-bias BPMEA; and c), the forward-bias BPMEA.

6.2.4. Forward-bias Operation Requires Effective CO_2 Transport

The forward-bias BPMEA configuration (Figure 6.1c), has the advantages of maintaining an alkaline environment at the cathode, which ensures a high FE, and reducing CO_2 loss without a very high energy penalty. However, in addition to the incomplete recovery of the Nernstian pH shift due to carbonate formation, this configuration has additional challenges: 1) in forward-bias, the formation of water and gaseous CO_2 at the interface of the BPM causes blistering and delamination in commercial BPMs at current densities above 20 mA/cm^2, thus rendering them ineffective in practice; 2) as shown in recent works by Surendranath and co-workers,[55, 56] (bi)carbonate ions and weak acids can induce large neutralisation overpotentials, and the inefficient transport of the produced CO_2 leads to low limiting current densities.

Effective removal of CO_2 generated at the BPM interface is then essential, and future research should address this issue by smart membrane design strategies such as the use of a hybrid liquid-

membrane interface or using an AEL with a porous or micro-channelled structure.[57, 58] Disch et. al.[51] for example, successfully operated their electrolyser for 200 hours by using a porous AEL. Alternatively, designing BPMs with a high selectivity for OH^- ions over co-ions (such as carbonate, formate or acetate) can mitigate ionic blockades and elevate limiting current densities to industrially relevant rates (>100 mA/cm^2).

Although blistering and delamination can be overcome by engineering techniques, the forward bias case suffers from reduced voltage gain due to carbonic acid recombination, unfavourable pH conditions in the anode, and the necessity of scarce anode materials, which are difficult to overcome.

6.2.5. CONTROLLING CATALYST MICROENVIRONMENT TO ENHANCE FARADAIC EFFICIENCY

Until recently, the reverse-bias BPM-based MEA showed low FE due to the acidic microenvironment favouring HER. However, recent studies have demonstrated that manipulating cation concentrations, ionomer properties, and system configuration, promotes CO_2R relative to HER. The presence of alkali cations with small hydrated radii, like Cs^+ and K^+, were demonstrated to promote CO_2R even in strong acid.[25] Unlike HER, which involves a proton-coupled electron transfer, the rate-limiting step for CO_2R is the adsorption of CO_2 onto the catalyst by a cation-coupled electron transfer (formation of cation-stabilised CO_2 adsorbate [cat^+-*CO_2^-]).[59] Therefore, the cation concentration near the catalyst has an important role in determining the CO_2R kinetics.[60] Moreover, since cation-coupled CO_2R is a hydroxide-generating reaction instead of a proton-consuming reaction, it can neutralize incoming protons and thereby suppress HER from proton reduction.[26] In this way, water reduction is not suppressed, but this reaction happens at more negative potentials. The challenge is controlling the reaction microenvironment (including pH and alkali cations). We highlight 5 strategies for controlling the reaction microenvironment to achieve high FE in reverse bias.

1. Introducing an alkali cation-rich thin catholyte layer (Figure 6.4a), which provides the necessary cations in the vicinity of the catalyst particles, while the H^+ ions provided by the BPM react with OH^- so that carbonate production is minimize d. Xie et al.[28] added a 65 µm thin catholyte layer with 0.5 M K_2SO_4, and achieved a FE for CO_2R products of approximately 80 % at 300 mA/cm^2.
2. Pre-condition the BPM with K^+ or Cs^+ ions (Figure 6.4b). Similar to the previous strategy, infusing alkali cations in the CEL would ensure the presence of alkali cations in the vicinity of the catalyst, promoting CO_2R. Xiao et. al.[61] successfully exchanged the H^+ in a Nafion membrane with Na^+ or K^+ ions, which led to a FE_{CO} of 91.5 % in the initial stage of CO_2 electrolysis. The salt deposition problems that occur for the CEM case after one hour, may be resolved when applying this strategy to a BPM, as supply of new cations is blocked by the AEL.
3. Employing catalysts that are CO_2R-active in acidic media (Figure 6.4c). From a theoretical standpoint, a strongly acidic cathodic environment resembles the ideal electrode potentials (Figure 6.3b) and warrants a high ionic conductivity. Immobilized molecular catalysts have potential to catalyze CO_2 reduction in such acidic conditions. For example, Siritanaratkul et. al.[39] used [Ni(1,4,8,11 – tetraazacyclotetradecane)]$^{2+}$ to achieve 40 % higher FE_{CO} compared to an Ag catalyst in a zero-gap reverse-bias configuration. Also co-depositing Lewis acids, proven for local pH tuning in seawater electrolysis,[62] is inspiring to modify the local environment in CO_2 reduction.
4. Leveraging weak acids to reduce the acidity in the reaction microenvironment (Figure 6.4d). Weak acidic groups reduce the membrane charge at low pH, thus the H^+ concentration. Us-

ing alternating poly(acrylic acid) and poly(allylamine hydrochloride) as weakly acidic groups in the CEL demonstrated an increased FE_{CO} (40%).[63] When further optimizing this strategy, it must be considered that the near-neutral pH will shift the cathode potential (Fig. 3b). Theoretically, the WD could occur at <0.83 V if the H^+ concentration in the CEL is <1 M, but it seems unlikely to fully compensate for the cathode potential shift: for example, pH 4 would imply $[H^+]$=0.1mM, which will cause transport limitations in the CEL.

5. Periodic injection of cations from the back of the GDE (Figure 6.4e). This strategy has not been applied to BPM-based electrolyzers, but Endrődi et. al.[32] supplied Cs^+ ions (isopropanol/water with 1M CsOH) every 12h, and achieved a stable operation in an AEMEA electrolyzer (around 90% FE_{CO} for over 200 hours).

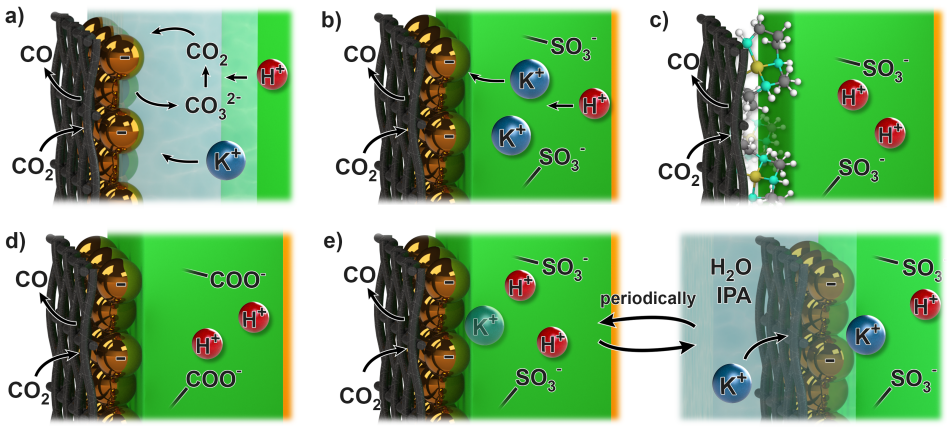

Figure 6.4: illustration of strategies to alleviate BPM-catalyst interaction: a) adding a catholyte layer, b) loading the CEL with K^+, c) employing CO_2R selective molecular catalysts, d) using CELs with weakly acidic groups or e) periodically injecting K^+ from the back of the GDE.

The first strategy is the most simple and proven effective at small scales.[28] However, introducing a catholyte layer can pose engineering challenges during scale-up, related to GDE breakthrough or flooding, and the formation of CO_2 gas bubbles near the BPM.[28, 64] Strategies 2 and 4 can also be applied on the ionomers often used in the catalyst layer to modify the reaction microenvironment. Strategies that ensure the presence of cations (1,2 and 5) could be largely affected by water evaporation at the GDE, causing the cations to be removed as aerosols in product stream and compromising the electrolyzer stability. To minimize cation loss, the humidity of the CO_2 gas stream, the process temperature and cation crossover (required at small rate to replenish cations) are key parameters to optimise.

Strategy #3, which involves using catalysts active in acidic media, has the added promise of reducing the cell potential by mitigating the pH gradient between the CEL and the catalyst layer. However, such catalysts are in an early stage of development and face challenges such as deactivation by CO, and degradation.[39] Nevertheless, we would urge the electrocatalysis field to focus more efforts in this direction, since a stable CO_2R catalyst which operates in acidic media would solve both main challenges associated with reverse-bias BPM operation.

6.2.6. OUTLOOK FOR IMPROVING BIPOLAR MEMBRANES FOR CO_2 ELECTROLYSIS

Known parameters to optimize BPMs are: 1) conductivity, 2) WD kinetics, 3) water permeability, 4) lifetime, and 5) counter-ion selectivity.[65] Ion-exchange membranes often exhibit a trade-off between conductivity and selectivity. Specifically for BPM-based CO_2 electrolysis, commercial BPMs should mainly improve in conductivity and BPM kinetics.

In order to improve conductivity and water permeability, the most straightforward method is to reduce the membrane thickness. Highly conductive polymers with sufficient mechanical stability for an ultrathin (< 30 µm) self-standing layer already exist for the individual polymers, e.g. the perfluorinated sulfonic acid based Nafion for CEMs, and quaternary ammonium based (such as Orion TMI and PiperION) for AEMs. Compatible chemistries, with similar swelling degrees, must be found for a stable BPM with a long lifetime. Additionally, since water can be easiest supplied from the anolyte and some AEMs, such as PiperION, have a low water permeability,[66] an asymmetric BPM with a thin AEL is a logical design strategy. Although reducing the thickness will increase co-ion crossover, we argue that a minor amount of cation crossover from the anolyte could actually be beneficial for the performance of the system,[35] or it could be tuned by using a larger cations. Moreover, crossover of (bi)carbonates will likely not be significant at high current densities (>1 A) due to the electroosmotic drag in the opposite direction.[37]

Simultaneously increasing both the conductivity and the selectivity of ion-exchange membranes is a widely known challenge, but it is a progressing field. Kamcev and co-workers are working on increasing the charge density by placing the charged functional groups in the polymeric backbone itself, to remove trade-off of cross-linking vs. functionality.[8] Other promising methods to increase the conductivity include the alignment of the polymeric chains in order to optimize ionic pathways, e.g. by conducting the polymerisation under an electric field.[10]

Solutions for enhanced WD kinetics include 3D interfaces and WD catalysts blended between the layers. A 3D interface can be created by, for example, electrospinning the two ionomers simultaneously, which increases the contact area and improves the adhesion between the layers.[67, 68] A catalyst blended in the interfacial layer enhances the kinetics of WD has been shown to largely reduce the ohmic resistance of BPMs.[69] Use of graphene oxide and thin layers has indeed demonstrated stable low overpotentials (<250 mV at 1 A/cm^2) and strongly asymmetric BPMs have even reached 9 A/cm^2,[70, 71] surpassing the 600 mA/cm^2 limiting current of existing commercial BPMs.

In summary, we argue that avoiding CO_2 crossover and ensuring favourable anode conditions are crucial steps toward the scale up of CO_2 electrolysis. Reverse-bias BPMs provide these conditions for a stable and scalable process, but need improvement in the cathode interaction and WDR efficiency. We have shown that the FE can be improved when the acidic CO_2R catalyst interfaces and proton mobility are controlled. Five strategies are available for that. When also implementing thickness optimisation, 3D interfaces with new WD catalysts and using available conductive polymers, the reverse-bias BPM system has high potential as the primary choice of separator for stable and scalable CO_2 electrolysis.

BIBLIOGRAPHY

1. Nishizawa, M., Menon, V. P. & Martin, C. R. Metal Nanotubule Membranes with Electrochemically Switchable Ion-Transport Selectivity. *Science* **268,** 700–702 (1995).
2. Jeong, J. & Hwang, W. Communication—Facile and Rapid Fabrication of Highly Oleophobic Surfaces with Anodized Alumina Nanofiber and Nanoparticles. *Journal of The Electrochemical Society* **164,** E158 (2017).
3. Dey, S. & Mehta, N. S. Synthesis and applications of titanium oxide catalysts for lower temperature CO oxidation. *Current Research in Green and Sustainable Chemistry* **3,** 100022 (2020).
4. Aixalà-Perelló, A. *et al.* Scalable and highly selective graphene-based ion-exchange membranes with tunable permselectivity. *npj 2D Materials and Applications* **7,** 46 (2023).
5. Kayvani Fard, A. *et al.* Inorganic Membranes: Preparation and Application for Water Treatment and Desalination. eng. *Materials (Basel, Switzerland)* **11,** 74 (2018).
6. Munavalli, B. B. & Kariduraganavar, M. Y. Development of novel sulfonic acid functionalized zeolites incorporated composite proton exchange membranes for fuel cell application. *Electrochimica Acta* **296,** 294–307 (2019).
7. Mauritz, K. A. & Moore, R. B. State of Understanding of Nafion. *Chemical Reviews* **104,** 4535–4586 (2004).
8. Kitto, D. & Kamcev, J. The need for ion-exchange membranes with high charge densities. *Journal of Membrane Science* **677,** 121608 (2023).
9. Lee, J.-Y., Lee, J.-H., Ryu, S., Yun, S.-H. & Moon, S.-H. Electrically aligned ion channels in cation exchange membranes and their polarized conductivity. *Journal of Membrane Science* **478,** 19–24 (2015).
10. Hyun, J. *et al.* Magnetic Field-Induced Through-Plane Alignment of the Proton Highway in a Proton Exchange Membrane. *ACS Applied Energy Materials* **3,** 4619–4628 (2020).
11. Pawlowski, S., Crespo, J. G. & Velizarov, S. Profiled Ion Exchange Membranes: A Comprehensible Review. *International Journal of Molecular Sciences* **20** (2019).
12. Vermaas, D. A., Saakes, M. & Nijmeijer, K. Power generation using profiled membranes in reverse electrodialysis. *Journal of Membrane Science* **385-386,** 234–242 (2011).
13. Polyamide nanofiltration membrane with highly uniform subnanometre pores for sub-1 Å precision separation. *Nature Communications* **11,** 2015 (2020).
14. Habib, S. & Weinman, S. T. A review on the synthesis of fully aromatic polyamide reverse osmosis membranes. *Desalination* **502,** 114939 (2021).
15. She, X. *et al.* Pure-water-fed, electrocatalytic CO_2 reduction to ethylene beyond 1,000 h stability at 10 A. *Nature Energy* **9,** 81–91 (2024).
16. Salvatore, D. A. *et al.* Designing anion exchange membranes for CO_2 electrolysers. *Nature Energy* **6,** 339–348 (2021).
17. Vass, Á., Kormányos, A., Kószo, Z., Endrődi, B. & Janáky, C. Anode Catalysts in CO_2 Electrolysis: Challenges and Untapped Opportunities. *ACS Catalysis* **12,** 1037–1051 (2022).

18. Minke, C., Suermann, M., Bensmann, B. & Hanke-Rauschenbach, R. Is iridium demand a potential bottleneck in the realization of large-scale PEM water electrolysis? *International Journal of Hydrogen Energy* **46,** 23581–23590 (2021).

19. Rabinowitz, J. A. & Kanan, M. W. The future of low-temperature carbon dioxide electrolysis depends on solving one basic problem. *Nature Communications* **11,** 5231 (2020).

20. Sharifian, R., Wagterveld, R. M., Digdaya, I. A., Xiang, C. & Vermaas, D. A. Electrochemical carbon dioxide capture to close the carbon cycle. *Energy & Environmental Science* **14,** 781–814 (2021).

21. McQueen, N. *et al.* A review of direct air capture (DAC): scaling up commercial technologies and innovating for the future. *Progress in Energy* **3,** 032001 (2021).

22. Xie, X. *et al.* Oxygen Evolution Reaction in Alkaline Environment: Material Challenges and Solutions. *Advanced Functional Materials* **32,** 2110036 (2022).

23. Kim, B., Ma, S., Molly Jhong, H.-R. & Kenis, P. J. A. Influence of dilute feed and pH on electrochemical reduction of CO_2 to CO on Ag in a continuous flow electrolyzer. *Electrochimica Acta* **166,** 271–276 (2015).

24. Monteiro, M. C. O., Philips, M. F., Schouten, K. J. P. & Koper, M. T. M. Efficiency and selectivity of CO_2 reduction to CO on gold gas diffusion electrodes in acidic media. *Nature Communications* **12,** 4943 (2021).

25. Erick, H. J. *et al.* CO2 electrolysis to multicarbon products in strong acid. *Science* **372,** 1074–1078 (2021).

26. Bondue, C. J., Graf, M., Goyal, A. & Koper, M. T. M. Suppression of Hydrogen Evolution in Acidic Electrolytes by Electrochemical CO_2 Reduction. *Journal of the American Chemical Society* **143,** 279–285 (2021).

27. O'Brien, C. P. *et al.* Single Pass CO_2 Conversion Exceeding 85% in the Electrosynthesis of Multicarbon Products via Local CO_2 Regeneration. *ACS Energy Letters* **6,** 2952–2959 (2021).

28. Xie, K. *et al.* Bipolar membrane electrolyzers enable high single-pass CO_2 electroreduction to multicarbon products. *Nature Communications* **13,** 3609 (2022).

29. Eriksson, B. *et al.* Mitigation of Carbon Crossover in 2 Electrolysis by Use of Bipolar Membranes. *Journal of The Electrochemical Society* **169,** 034508 (2022).

30. Jeng, E. & Jiao, F. Investigation of CO_2 single-pass conversion in a flow electrolyzer. *Reaction Chemistry & Engineering* **5,** 1768–1775 (2020).

31. Ma, M., Kim, S., Chorkendorff, I. & Seger, B. Role of ion-selective membranes in the carbon balance for CO_2 electroreduction via gas diffusion electrode reactor designs. *Chemical Science* **11,** 8854–8861 (2020).

32. Endrődi, B. *et al.* Operando cathode activation with alkali metal cations for high current density operation of water-fed zero-gap carbon dioxide electrolysers. *Nature Energy* **6,** 439–448 (2021).

33. Ma, M. *et al.* Insights into the carbon balance for CO_2 electroreduction on Cu using gas diffusion electrode reactor designs. *Energy & Environmental Science* **13,** 977–985 (2020).

34. Patru, A., Binninger, T., Pribyl, B. & Schmidt, T. J. Design principles of bipolar electrochemical co-electrolysis cells for efficient reduction of carbon dioxide from gas phase at low temperature. *Journal of the Electrochemical Society* **166,** F34–F43 (2019).

35. Liu, Z., Yang, H., Kutz, R. & Masel, R. I. CO_2 Electrolysis to CO and O_2 at High Selectivity, Stability and Efficiency Using Sustainion Membranes. *Journal of The Electrochemical Society* **165,** J3371–J3377 (2018).

36. Hansen, K. U., Cherniack, L. H. & Jiao, F. Voltage Loss Diagnosis in CO_2 Electrolyzers Using Five-Electrode Technique. *ACS Energy Letters* **7,** 4504–4511 (2022).

37. Yang, K. *et al.* Cation-driven increases of CO_2utilization in a bipolar membrane electrode assembly for CO_2electrolysis. *ACS Energy Letters* **6,** 4291–4298 (2021).

38. Khan, M. A. *et al.* Zero-crossover electrochemical CO_2 reduction to ethylene with co-production of valuable chemicals. *Chem Catalysis* **2,** 2077–2095 (2022).

39. Siritanaratkul, B. *et al.* Zero-Gap Bipolar Membrane Electrolyzer for Carbon Dioxide Reduction Using Acid-Tolerant Molecular Electrocatalysts. *Journal of the American Chemical Society* **144,** 7551–7556 (2022).

40. Jeanty, P. *et al.* Upscaling and continuous operation of electrochemical CO_2 to CO conversion in aqueous solutions on silver gas diffusion electrodes. *Journal of CO_2 Utilization* **24,** 454–462 (2018).

41. Del Castillo, A. *et al.* Sn nanoparticles on gas diffusion electrodes: Synthesis, characterization and use for continuous CO_2 electroreduction to formate. *Journal of CO_2 Utilization* **18,** 222–228 (2017).

42. Vennekoetter, J.-B., Sengpiel, R. & Wessling, M. Beyond the catalyst: How electrode and reactor design determine the product spectrum during electrochemical CO_2 reduction. *Chemical Engineering Journal* **364,** 89–101 (2019).

43. Mardle, P., Cassegrain, S., Habibzadeh, F., Shi, Z. & Holdcroft, S. Carbonate Ion Crossover in Zero-Gap, KOH Anolyte CO_2 Electrolysis. *The Journal of Physical Chemistry C* **125,** 25446–25454 (2021).

44. Blommaert, M. A., Subramanian, S., Yang, K., Smith, W. A. & Vermaas, D. A. High Indirect Energy Consumption in AEM-Based CO_2 Electrolyzers Demonstrates the Potential of Bipolar Membranes. *ACS Applied Materials & Interfaces,* 557–563.

45. Endrődi, B. *et al.* High carbonate ion conductance of a robust PiperION membrane allows industrial current density and conversion in a zero-gap carbon dioxide electrolyzer cell. *Energy & Environmental Science* **13,** 4098–4105 (2020).

46. Larrazábal, G. O. *et al.* Analysis of Mass Flows and Membrane Cross-over in CO_2 Reduction at High Current Densities in an MEA-Type Electrolyzer. *ACS Applied Materials & Interfaces* **11,** 41281–41288 (2019).

47. Aydogan Gokturk, P. *et al.* The Donnan potential revealed. *Nature Communications* **13,** 5880 (2022).

48. Pärnamäe, R. *et al.* Bipolar membranes: A review on principles, latest developments, and applications. *Journal of Membrane Science* **617,** 118538 (2021).

49. Blommaert, M. A., Verdonk, J. A. H., Blommaert, H. C. B., Smith, W. A. & Vermaas, D. A. Reduced Ion Crossover in Bipolar Membrane Electrolysis via Increased Current Density, Molecular Size, and Valence. *ACS Applied Energy Materials* **3,** 5804–5812 (2020).

50. Li, Y. C. *et al.* Bipolar Membranes Inhibit Product Crossover in CO_2 Electrolysis Cells. *Advanced Sustainable Systems* **2,** 1700187 (2018).

51. Disch, J. *et al.* High-resolution neutron imaging of carbonate precipitation and water transport in zero-gap CO_2 electrolysis. *Nature Communications* **13** (2022).

52. Subramanian, S., Middelkoop, J. & Burdyny, T. Spatial reactant distribution in CO_2 electrolysis: balancing CO_2 utilization and faradaic efficiency. *Sustainable Energy & Fuels* **5,** 6040–6048 (2021).

53. Liu, X., Monteiro, M. C. O. & Koper, M. T. M. Interfacial pH measurements during CO_2 reduction on gold using a rotating ring-disk electrode. *Physical Chemistry Chemical Physics* **25,** 2897–2906 (2023).

54. Bui, J. C. *et al.* Exploring Bipolar Membranes for Electrochemical Carbon Capture. *ChemRxiv* (2023).

55. Toh, W. L., Dinh, H. Q., Chu, A. T., Sauvé, E. R. & Surendranath, Y. The role of ionic blockades in controlling the efficiency of energy recovery in forward bias bipolar membranes. *Nature Energy* **8,** 1405–1416 (2023).

56. Dinh, H. Q., Toh, W. L., Chu, A. T. & Surendranath, Y. Neutralization Short-Circuiting with Weak Electrolytes Erodes the Efficiency of Bipolar Membranes. *ACS Applied Materials & Interfaces* **15,** 4001–4010 (2023).

57. Xu, Y. *et al.* A microchanneled solid electrolyte for carbon-efficient CO₂ electrolysis. *Joule* **6,** 1333–1343 (2022).

58. Kim, J. Y. T. *et al.* Recovering carbon losses in CO_2 electrolysis using a solid electrolyte reactor. *Nature Catalysis* **5,** 288–299 (2022).

59. Monteiro, M. C. O. *et al.* Absence of CO_2 electroreduction on copper, gold and silver electrodes without metal cations in solution. *Nature Catalysis* **4,** 654–662 (2021).

60. Birdja, Y. Y. *et al.* Advances and challenges in understanding the electrocatalytic conversion of carbon dioxide to fuels. *Nature Energy* **4,** 732–745 (2019).

61. Xiao, T. *et al.* Proton antagonist membrane towards exclusive CO_2 reduction. *Nano Research* (2022).

62. Guo, J. *et al.* Direct seawater electrolysis by adjusting the local reaction environment of a catalyst. *Nature Energy* **8,** 264–272 (2023).

63. Yan, Z., Hitt, J. L., Zeng, Z., Hickner, M. A. & Mallouk, T. E. Improving the efficiency of CO_2 electrolysis by using a bipolar membrane with a weak-acid cation exchange layer. *Nature Chemistry* **13,** 33–40 (2021).

64. Baumgartner, L. M., Koopman, C. I., Forner-Cuenca, A. & Vermaas, D. A. Narrow Pressure Stability Window of Gas Diffusion Electrodes Limits the Scale-Up of CO_2 Electrolyzers. *ACS Sustainable Chemistry & Engineering* **10,** 4683–4693 (2022).

65. Blommaert, M. A. *et al.* Insights and Challenges for Applying Bipolar Membranes in Advanced Electrochemical Energy Systems. *ACS Energy Letters* **6,** 2539–2548 (2021).

66. Khalid, H., Najibah, M., Park, H. S., Bae, C. & Henkensmeier, D. Properties of Anion Exchange Membranes with a Focus on Water Electrolysis. eng. *Membranes* **12** (2022).

67. Powers, D. *et al.* Freestanding Bipolar Membranes with an Electrospun Junction for High Current Density Water Splitting. *ACS Applied Materials & Interfaces* **14,** 36092–36104 (2022).

68. Xu, Q. *et al.* Enriching Surface-Accessible CO_2 in the Zero-Gap Anion-Exchange-Membrane-Based CO_2 Electrolyzer. *Angewandte Chemie International Edition* **62,** e202214383 (2023).

69. Chen, Y. *et al.* High-Performance Bipolar Membrane Development for Improved Water Dissociation. *ACS Applied Polymer Materials* **2,** 4559–4569 (2020).

70. Lucas, É. *et al. Asymmetric Bipolar Membrane for High Current Density Electrodialysis Operation with Exceptional Stability* Cambridge, 2023.

71. Mayerhöfer, B. *et al.* Bipolar Membrane Electrode Assemblies for Water Electrolysis. *ACS Applied Energy Materials* **3,** 9635–9644 (2020).

ACKNOWLEDGEMENTS

Although there were some minor challenges during my time in Delft (such as a global pandemic), I really enjoyed this period! I loved my topic and enjoyed doing the work I did, but I believe that the positive experience was primarily owed to the wonderful people around me. Here, I would like to thank some of them. I cannot mention everyone because I have easily met a hundred people who contributed to this positive experience so I apologise if I could not make a personal section for everyone!

Firstly a big thank you to my promotors, **David** and **Bernard**, for your vote of confidence in giving me the opportunity to work on this project and be part of your team. **David**, I really appreciate your guidance during these years! I can definitely say I have learned a lot from you, and you have inspired me to be a more creative scientist. You also taught me to question and boil down the importance of every single thing, which really helped keeping our priorities and key findings in the highlight. Thank you for the freedom you have given me to explore the new research directions I found most promising, and your many many puns (and also laughing at mine). **Bernard**, thank you for your constant availability, I found our meetings very helpful. I'm especially impressed how toward the end of this project, when we had to make some choices on what we want still to achieve and what to include, you ended up being absolutely right with all the advice you gave.

I also want to extend my gratitude to the committee members, **prof. Geerlings**, **prof. de Jong**, **prof. Lammertink**, **prof. Aili** and **dr. Hartkamp**. Thank you for your time and effort to assess my work and being a part of this PhD defense.

A massive thank you goes out to the TP group. Daily life in the office and working alongside you guys has been absolutely great, it made me genuinely excited to go to work in the mornings ♡. Thank you **Jorrit** for being the one who told me about this group in the first place, actually joining two years later, and bringing your friendly sillyness along. Thank you **Nathalie** for bringing a really fun, yet calming and relaxing vibe to the office! **Christel** (is geweldig), thank you for your very contagious good mood and the many foosball breaks and valuable teascussions. **Vojtech**, **Jan-Willem** and **Yu-Fan**, thank you guys for all the climbing sessions and the really fun times both in and outside the office, I never know what is coming out of our breaks! **Ai-Yu**, **Mäx** it was great to see you guys join and quickly become very integrated and a big part of the group! Thank you **Christiaan**, **Evert** and **Duco** not only for the technical support, which was absolutely vital during the experimental work, but I also loved the sarcastic "technician humour"! Special thanks go to **Matheus**, **Elise**, **Stef** and **Rens** for being some of the first people I really got along with at uni, and for sticking around for some great hangouts until today. I don't have space here to mention everyone, but I send a warm thank you to all other past and current TP members and students, for all the good times during coffee breaks, TP lunches and events!

Outside of the TP group, some e-Refinery and chemE department members have also been invaluable for great work discussions and fun times at events. Among many others, my gratitude goes to **Sid**, **Sorin**, **Hugo**, **Joe** and **Mark**! Although sometimes took me half of an hour to get from the lab to the office because I kept running into some of you guys.

A big thank you also goes to the students that I supervised during their projects: **Mark**, **Jochem**, **Veerle**, **Kaiyue**, **Jiska** and **Teise**. I enjoyed working together and have learned a lot from supervising you. Best of luck in your future endeavours!

Many others shaped my time in Delft. **May**, you had a major impact on social life, I can't thank you enough for welcoming me to your city! My one friend when I arrived, thank you for your great

energy, and all the awesome chillings (you should do a PhD in that). **Manas**, **Simone**, **Franceschi**, thank you guys for making Covid an actually fun time! Those Fridays were really precious. This extends to **Antonio**, **Alan**, **Maria**, **Jonas**, **Tjark**, and many others, we met in the least probable time to meet new people, yet you guys made Delft a great place to be at!

To my Portuguese friends in the Netherlands, **Bruno**, **Catarina**, and as of recently, **Bruna**, thank you for bringing a bit of Portugal here! **Bruno**, thank you for being my companion who for some reason decided to follow all my life decisions and go to all the same places. Na verdade não estou assim tão farto de ti.. **Catarina**, I've said this before but find it really amazing how we talked about coming to the Netherlands all those years ago in school, we enrolled in chemical engineering because "chemistry is cool" and now we're both here, and full chemical engineers!

Thanks again to **Christel**, **Catarina** and Bruno kind of, for all the help in this final stage and accepting to be my paranymphs!

Thank you to all the friends and family from Bulgaria and Portugal who visited me during the PhD! **Мама**, **Тати**, **Вальо**, **Рали**, **Леля Мария**, **Калина**, **Явор**, **Jóia**, **Patrícia**, **Gonçalo**, **Ramos**, **Cristiana**, **Atouguia**,**Nabais**, **Tubarão**, **Stijn**, **Teresinha**, **Hugo** and **Joinha**, you guys brought a piece of the homes to the Netherlands and it was an absolute pleasure having you here!

Много благодаря и на цялото семейство. Въпреки че ситуацията е такава от много години, не е лесно да съм далеч от вас, но винаги е голяма радост когато си дойда! Много ме радвате с вашето посрещане, и много благодаря за цялата подкрепа, която ми давате понякога дори без да знаете.

Inês, obrigado por aceitares embarcar nesta aventura comigo e por estares sempre ao meu lado. A tua ajuda foi fundamental em vários momentos, especialmente nesta reta final, onde tornaste todo o processo muito mais fácil. Estou ansioso pelos próximos passos da nossa vida, com o regresso a Portugal e o início do teu PhD! Aprecio imensamente tudo o que fazes por mim e amo-te muito ♡.

CURRICULUM VITÆ

Kostadin Veselinov PETROV

27-10-1994	Born in Sofia, Bulgaria.
2013 – 2018	**Integrated MSc course in Chemical & Biochemical Engineering** Faculty of Science and Technology NOVA University of Lisbon
2019	**Junior Researcher** Chemistry Department, Faculty of Science and Technology NOVA University of Lisbon
2019 – 2023	**Ph.D. in Electrochemical Engineering** Chemical Engineering Department, Faculty of Applied Sciences Delft University of Technology *Thesis:* Addressing CO_2 Electrolysis Challenges with Novel Ion-Exchange Membranes *Promotor:* Prof. dr. B. Dam *Promotor:* Dr.ir. D.A. Vermaas
2024 –	**Researcher** HyLab Sines, Portugal

LIST OF PUBLICATIONS

Publications in this thesis:

4. **K.V. Petrov**, C.I. Koopman, S. Subramanian, M.T.M. Koper, T. Burdyny, D.A. Vermaas, *Bipolar membranes for intrinsically stable and energy efficient CO_2 electrolysis*, Submitted.
3. **K.V. Petrov**, J.C. Bui, L. Baumgartner, L. Weng, S.M. Dischinger, D.M. Larson, D.J. Miller, A.Z. Weber, D.A. Vermaas, *Anion-exchange membranes with internal microchannels for water control in CO_2 electrolysis*, Sustainable Energy & Fuels, **6**, 5077-5088 (2022).
2. **K.V. Petrov**, JW. Hurkmans, R. Hartkamp, D.A. Vermaas, *Nanofluidic ion-exchange membranes: can their conductance compete with polymeric ion-exchange membranes?*, Submitted.
1. **K.V. Petrov**, M. Mao, A. Santoso, I. I. Ryzhkov, D.A. Vermaas, *Design criteria for selective nanofluidic ion-exchange membranes*, Journal of Membrane Science, **688**, 122156 (2023).

Publications not mentioned in this thesis:

3. K. Singh, A. Bondre, **K.V. Petrov**, D.A. Vermaas, *Tuning pH and Electrode Design to Enhance Power Density of H_2-I_2 Redox Flow Batteries* , Submitted.
2. A.S. Kumar, M. Pupo, **K.V. Petrov**, M. Ramdin, J.R. van Ommen, W. de Jong, R. Kortlever, *A Quantitative Analysis of Electrochemical CO_2 Reduction on Copper in Organic Amide and Nitrile-Based Electrolytes*, The Journal of Physical Chemistry C **127**, 27, 12857–12866 (2023).
1. **K.V. Petrov**, L. Paltrinieri, L. Poltorak, L.C.P.M. de Smet, E.J.R. Sudhölter, *Modified cation-exchange membrane for phosphate recovery in an electrochemically assisted adsorption – desorption process*, Chemical Communications **56**, 5046-5049 (2020).